

**THE STRUCTURAL ROLE OF SODIUM DITHIONATE
IMPURITY IN THE HABIT MODIFICATION OF
SODIUM CHLORATE SINGLE CRYSTALS**

By

Zhipeng Lan

Submitted in accordance with the requirements of the degree of
Doctor of Philosophy

The University of Leeds
School of Process, Environmental and Materials Engineering

September 2013

The candidate confirms that the work submitted is his/her own, except where work which has formed part of jointly authored publications has been included. The contribution of the candidate and the other authors to this work has been explicitly indicated below. The candidate confirms that appropriate credit has been given within the thesis where reference has been made to the work of others.

The calculations for structure factor of the $(\bar{3}\bar{4}3)(\bar{3}\bar{4}1)$ and $(343)(341)$ secondary planes were completed by Dr. Alan S. de Menezes, and will result in a jointly-authored publication listed (Lan et al., 2014), where the article will be written based on the experimental work by the author. The calculations for PDOS and molecular orbitals of $S_2O_6^{2-}$ were completed by Dr. Che Seabourne using CASTEP codes, and will result in a jointly-authored publication listed (Lan et al., 2014), where the article will be written based on the experimental work by the author. The work herein is the authors own analysis of the data, except where explicitly highlighted in the text. This is summarised below.

- (i) Chapter 7.5. The structure factor of the $(\bar{3}\bar{4}3)(\bar{3}\bar{4}1)$ and $(343)(341)$ secondary planes included in this section were calculated by Dr. Alan S. de Menezes.
- (ii) Chapter 8.3.3. The PDOS and molecular orbitals of $S_2O_6^{2-}$ included in this section were calculated by Dr. Che Seabourne.

Lan, Z., Lai, X., Roberts, K. J., de Menezes, A. S., dos Santos, A. O., Calligaris, G. A., & Cardoso, L. P. (2014). Determination of the Lattice Distortion in Dithionate-doped Sodium Chlorate Crystals using XRMD. *Crystal Growth and Design*, Manuscript in preparation.

Lan, Z., Lai, X., Seabourne, C. R., Scott, A. J., & Roberts, K. J. (2014). Determination of the Local Structure of the Orientational Dithionate Impurity in the Sodium Chlorate Crystals using Polarized XAFS. *Crystal Growth & Design*, Manuscript in preparation.

This copy has been supplied on the understanding that it is copyright material and that no quotation from the thesis may be published without proper acknowledgement.

ACKNOWLEDGEMENTS

Acknowledgements are due to Dr. Xiaojun Lai and Professor Kevin Roberts for their great supervision of this research and teaching of the fundamentals involved in this work. Professor Helmut Klapper, Professor Lisandro Cardoso and Dr. Alan S. de Menezes are acknowledged for their help in interpreting the results from X-ray topography and X-ray multiple-wave diffraction techniques, respectively. Dr. A. O. dos Santos, Guilherme Calligaris and Ian Rosbottom are acknowledged for their help in collecting the data at synchrotrons of LNLS and Diamond, respectively. Acknowledgments are due to Dr. Che Seabourne for providing training on the CASTEP analysis methods. Professor Fred Mosselmans is acknowledged for his kind mentoring on the technical details of XAFS during and after the data collection. Acknowledgements are due to Dr. Vasuki Ramachandran and Neepa Paul for their training on the molecular modelling techniques. Dr. Robert Hammond, Dr. Tim Comyn and Dr. Caiyun Ma are acknowledged for their kind support during this project. Simon Lloyd is acknowledged for his consistent assistance in organizing the local laboratories. The synchrotron facilities of Brazilian Synchrotron Light Laboratory and Diamond Light Source are acknowledged for providing the beamtime for the XRMD and XAFS experiments. Last, but also significantly, acknowledgements are due to my parents and my wife for their supporting me all the way.

ABSTRACT

A detailed study into the crystal habit modification of the $\text{NaClO}_3 / \text{Na}_2\text{S}_2\text{O}_6$ (host / impurity) system is presented. Ordinary morphology of NaClO_3 present faces of $\{001\}$, $\{110\}$ and $\{111\}$ types. The presence of impurity $\text{Na}_2\text{S}_2\text{O}_6$ has led to rapid development of new faces of $\{\bar{1}\bar{1}\bar{1}\}$ type on the NaClO_3 crystals grown from solution. Above 70ppm doping concentration, the morphology of NaClO_3 crystal is dominated by $\{\bar{1}\bar{1}\bar{1}\}$ faces. Crystal twinning occurred under 800ppm doping concentration and above. X-ray topography was used to investigate the growth history and defect configuration of the pure and doped crystals. Lattice distortions at various lattice planes within the pure and doped crystals were determined using X-ray multiple-wave diffraction (XRMD). The local structure of $\text{S}_2\text{O}_6^{2-}$ in NaClO_3 crystal was determined using X-ray absorption fine structure (XAFS). Molecular modelling was applied to investigate the molecular similarity between the impurity and the host.

Strong impurity incorporation in the $\{\bar{1}\bar{1}\bar{1}\}$ sectors was revealed by X-ray topography. The growth history of doped crystal was reconstructed and interpreted with respect to the inhibiting effect of $\text{S}_2\text{O}_6^{2-}$. Disturbance in lattice planes of doped crystals was investigated, which was attributed to the incorporation of $\text{S}_2\text{O}_6^{2-}$ on $\{\bar{1}\bar{1}\bar{1}\}$ faces. It also revealed different types of local strain on the $\{\bar{1}\bar{1}\bar{1}\}$ faces along two different directions. The three-dimensional orientation and the actual structure of $\text{S}_2\text{O}_6^{2-}$ impurity on the $\{\bar{1}\bar{1}\bar{1}\}$ faces of NaClO_3 crystal were obtained. A structural model for the impurity incorporation was established, showing good consistency with the experimental results. In addition, the segregation coefficient of the impurity was determined by elemental mapping, indicating strong impurity incorporation on the $\{\bar{1}\bar{1}\bar{1}\}$ faces rather than others. The incorporated $\text{S}_2\text{O}_6^{2-}$ was concluded to be capable of disrupting the proper packing structure of the $\{\bar{1}\bar{1}\bar{1}\}$ faces, obstructing the generation and propagation of growth steps, and decreasing of driving force for crystal growth.

Table of Contents

List of Figures	I
List of Tables	VIII
Abbreviations and Notation	X
1 Introduction	1
1.1 Introduction	2
1.2 Research Background	2
1.3 Aims and Objectives of This Thesis.....	4
1.4 Layout of This Thesis	5
2 Crystal Science and Characterization of Crystallization and Crystal Growth.	8
2.1 Introduction	9
2.2 Fundamental of Crystalline State	9
2.2.1 Crystalline Solid	9
2.2.2 Unit Cell	9
2.2.3 Miller Indices.....	10
2.2.4 Crystal Symmetry.....	11
2.2.5 Crystal Systems	12
2.2.6 Isomorphism and Polymorphism.....	14
2.2.7 Crystal Habit.....	14
2.2.8 Crystal Chemistry.....	18
2.2.9 Crystal Defect.....	19
2.3 Solubility and Supersaturation	20
2.3.1 Solubility	20
2.3.2 Supersaturation and the Meta-stable Zone	21
2.3.3 Effect of Impurities on Solubility.....	23
2.4 Nucleation.....	25
2.4.1 Introduction to Nucleation.....	25
2.4.2 Primary Nucleation.....	26
2.4.3 Secondary Nucleation.....	30
2.5 Crystal Growth	31
2.5.1 Introduction to Crystal Growth	31
2.5.2 Crystal Growth Theories	32
2.6 Characterization of Impurity Doped Single Crystal	38

2.6.1	Characterization of Defect Structure by X-Ray Topography.....	38
2.6.2	Synchrotron X-Ray Radiation	44
2.6.3	Micro-crystallography by X-Ray Multiple-wave Diffraction	45
2.6.4	Determination of the Local Structure of the Impurity by X-ray Absorption Fine Structure	51
2.7	Conclusions	61
3	Crystal Habit Modification	62
3.1	Introduction	63
3.2	Habit Modification of Inorganic Systems and Related Mechanisms	63
3.3	Previous Studies on the Crystal Growth of NaClO ₃	67
3.3.1	The Different Structures of NaClO ₃	67
3.3.2	Habit of Pure NaClO ₃ Crystal	68
3.3.3	Dislocations in Pure NaClO ₃	69
3.3.4	The Growth Mechanisms of NaClO ₃	71
3.3.5	The Effect of Strain on the Growth of NaClO ₃	71
3.4	Habit Modification of Sodium Chlorate by Impurities of RO ₄ ²⁻ type and Sodium Dithionate.....	72
3.5	Position of Sulphur K-edge and Profile of the XANES	74
3.6	Conclusions	77
4	Materials and Methodology	78
4.1	Introduction	79
4.2	Materials	79
4.3	Meta-stable Zone Width	80
4.3.1	Instrument.....	80
4.3.2	Experiment	81
4.4	Crystal Growth	82
4.4.1	Apparatus of Crystal Growth.....	82
4.4.2	Seed Preparation By Evaporation.....	84
4.4.3	Growth Solution Preparation.....	85
4.4.4	Seeding and Growth	86
4.5	ICP-OES	87
4.6	Powder X-Ray Diffraction (PXRD)	87
4.7	X-Ray Topography	88
4.7.1	Experiment Setup	88
4.7.2	Sample Preparation and Recording the Topograph.....	89
4.8	Polarized-light Microscopy	90

4.9	X-Ray Multiple-wave Diffraction	91
4.9.1	Experiment Setup	91
4.9.2	Renninger Scan and $\omega:\phi$ Mapping.....	93
4.9.3	Data Analysis.....	95
4.10	X-Ray Absorption Fine Structure.....	96
4.10.1	Experiment Setup	96
4.10.2	Sample and Data Acquisition	98
4.10.3	Data Analysis.....	101
4.11	Molecular Modelling	104
4.12	Conclusions	104
5	Crystal Growth and Habit Modification of NaClO₃.....	105
5.1	Introduction	106
5.2	Effect of Impurity on The Metastable Zone Width	107
5.3	Habit of Pure NaClO ₃ Crystal	108
5.4	Habit Modification of NaClO ₃ by The S ₂ O ₆ ²⁻ Impurity	111
5.4.1	Habit Modification of NaClO ₃ at Moderate S ₂ O ₆ ²⁻ Concentration	111
5.4.2	Twinned NaClO ₃ Crystal Formed at High S ₂ O ₆ ²⁻ Concentration.....	116
5.5	Transition Between Pure {111} and Doped $\{\bar{1}\bar{1}\bar{1}\}$	119
5.6	Segregation Coefficient	122
5.7	Discussions	124
5.8	Conclusion.....	126
6	Defect Structure, Growth History and Optical Activities of NaClO₃ in the Presence of S₂O₆²⁻	127
6.1	Introduction	128
6.2	Growth Defects.....	128
6.2.1	Growth Sectors and Growth Sector Boundaries.....	128
6.2.2	Growth Striations.....	131
6.2.3	Inclusions.....	132
6.2.4	Dislocations	134
6.2.5	Discussion on the Defects	135
6.3	Dislocation Characterization	136
6.3.1	Theoretical Burgers Vectors and Preferred Dislocation Line Directions.	136
6.3.2	Dislocation Lines in Pure NaClO ₃ Crystal	138
6.3.3	Dislocations in 40ppm S ₂ O ₆ ²⁻ -doped NaClO ₃ Crystal.....	143

6.3.4	Dislocation Lines in 160ppm $S_2O_6^{2-}$ -doped Crystal.....	151
6.4	Growth History of Impurity Affected Crystal.....	157
6.4.1	Introduction.....	157
6.4.2	190ppm Doped Crystal as Representative Case.....	159
6.5	Characterization of the Twinned Crystal.....	164
6.5.1	Optical Activity of The Twin Domains.....	164
6.5.2	Topograph of Twinned Crystal.....	167
6.6	Discussion.....	169
6.7	Conclusions.....	171
7	Determination of Lattice Distortion Induced by the Impurity Incorporation..	173
7.1	Introduction.....	174
7.2	Lattice Planes Disturbed by Impurity Incorporation.....	174
7.3	Different Strain at the Impurity Affected / Unaffected Regions.....	178
7.4	Evaluation of Crystal Quality by $\omega:\phi$ Mapping.....	182
7.5	Discussion.....	185
7.6	Conclusions.....	189
8	Determination of the Local Structure of Dithionate Impurity in $NaClO_3$ Crystal Using Polarized XAFS.....	191
8.1	Introduction.....	192
8.2	Quantitative Determination of the Molecular Orientation and the Structure of $S_2O_6^{2-}$ by EXAFS.....	193
8.2.1	EXAFS Data and the Fitting Model.....	193
8.2.2	Fit the isotropic EXAFS of powder crystalline $Na_2S_2O_6$	196
8.2.3	Fit the 190ppm Polarized EXAFS.....	199
8.2.4	Discussion on the Orientation of $S_2O_6^{2-}$	202
8.2.5	Discussion on the Local Structure of the $S_2O_6^{2-}$	204
8.3	Qualitative Determination of the Molecular Orientation of $S_2O_6^{2-}$ around Its 3-Fold Axis by Polarized XANES.....	209
8.3.1	Polarized XANES of 800ppm $S_2O_6^{2-}$ -doped $NaClO_3$ Crystal.....	209
8.3.2	The Isotropic XANES and the PDOS.....	211
8.3.3	The Polarized XANES and the PDOS.....	213
8.4	Determination of $S_2O_6^{2-}$ Distribution in Different Types of Growth Sectors by XRF-Mapping.....	217
8.5	Conclusions.....	219
9	A Structural Model for the Habit Modification of $NaClO_3$ by $Na_2S_2O_6$.....	220

9.1	Introduction	221
9.2	Molecular Model of Impurity Incorporation	221
9.2.1	Molecular Similarity between ClO_3^- and $\text{S}_2\text{O}_6^{2-}$	221
9.2.2	Surface Structure of NaClO_3 and Suitable Sites for Impurity Incorporation on the $\{\bar{1}\bar{1}\bar{1}\}$ Faces	224
9.2.3	The Structural Model and Its Correlations to All the Experimental Results	227
9.2.4	Charge Compensation Associated with Impurity Incorporation	230
9.3	Habit-modifying Effect of $\text{S}_2\text{O}_6^{2-}$ on the Crystal Growth of NaClO_3	232
9.3.1	Blocking Effect at the Growth Steps or Kink Sites	232
9.3.2	The Effect of Impurity-Induced Strain	233
9.4	The Origin of Twinning and the Structure of the Twin Boundary	233
9.4.1	Origin of the Twinning	233
9.4.2	The Structure of The Twin Boundary	236
9.5	Conclusions	237
10	Conclusions and Future Work.....	239
10.1	Conclusions	240
10.2	Review of the Aims and Objectives	244
10.3	Recommendations for Future Work	244
	References.....	246
	Appendix I.....	259
	Appendix II.....	262
	Appendix III.....	264

List of Figures

Figure 1.1	(1 $\bar{1}0$) projection of the structure of NaClO ₃ .	3
Figure 1.2	The route map illustrating the layout of this thesis.	7
Figure 2.1	The three-dimensional unit cell, with three crystallographic axes, the lattice parameters (a, b, c and α , β , γ).	10
Figure 2.2	Intercepts of planes with defined crystallographic axes.	11
Figure 2.3	Schematic illustration of an example of symmetry operations for a simple cube unit.	12
Figure 2.4	The schematic illustration of Bravais lattices - cubic types.	13
Figure 2.5	Several typical crystal habits of magnetite (Fe ₃ O ₄).	15
Figure 2.6	Schematic illustration for the surface structure according to the Hartman–Perdok theory for a cubic crystal.	17
Figure 2.7	Schematic illustration of the directions of Burgers vector and dislocation line for screw dislocation (a) and edge dislocation (b).	20
Figure 2.8	A typical solubility–supersolubility diagram.	21
Figure 2.9	An illustration of nucleation classification.	26
Figure 2.10	Free energy diagram relating to the “critical nucleus” in nucleation.	27
Figure 2.11	Effect of supersaturation on the nucleation rate.	28
Figure 2.12	Schematic illustration of the angular relationship among the three phases.	29
Figure 2.13	Schematic representation of stages involved in crystal growth	32
Figure 2.14	A mode of crystal growth without dislocations.	34
Figure 2.15	The schematic illustration of Kossel’s Model of a growing crystal surface.	34
Figure 2.16	Schematic illustration of the development of crystal growth on a screw dislocation	35
Figure 2.17	Schematic illustration of the criteria for vertical resolution. The beam source, specimen and film are arranged horizontally, with distance between them as indicated.	41
Figure 2.18	Schematic illustration of the directions of Burgers vector and dislocation line for screw dislocation (a) and edge dislocation (b).	44
Figure 2.19	The brief structure of a synchrotron machine.	45
Figure 2.20	(a) Geometry of X-ray multiple-diffraction in reciprocal space using a three-beam case as example. (b) Section projection view for the indicated part.	47

Figure 2.21	An example Renninger Scan pattern using 004 primary reflection, showing different peaks with their index numbers.	48
Figure 2.22	Schematic representation for the beam propagation paths of a typical three-beam case under X-ray multiple-wave diffraction in real crystal space.	49
Figure 2.23	X-ray absorption spectrum for Pb, covering three edges which are K, L and M.	52
Figure 2.24	A typical X-ray absorption spectrum composed of three components, i.e. Pre-edge, XANES and EXAFS.	53
Figure 2.25	Illustration of the photoelectric effect in which the incident X-ray is absorbed by a core-level electron and the electron is excited out of its original level.	54
Figure 2.26	The two mechanisms for decay of the excited states: X-ray fluorescence (left) and the Auger effect (right).	55
Figure 2.27	Interference of the photoelectron among atoms after its ejection from the core atom.	57
Figure 3.1	Locations of absorbed impurity particles on the crystal face, Kossel model. ...	65
Figure 3.2	Sulphur K-edge XANES of different reference compounds.....	76
Figure 4.1	The main components of the AUTOMATE units.....	80
Figure 4.2	Schematic illustration of the apparatus for crystal growth.....	83
Figure 4.3	Photo of the apparatus for seed preparation by evaporation and the crystal seed	84
Figure 4.4	Schematic representation and photograph of the employed Lang's Camera for X-ray topography.	88
Figure 4.5	The instrumental set up of polarized optics for determining the optical activity of a single crystal plate.	91
Figure 4.6	The instrumental set-up at beamline XRD1 at the Brazillian Synchrotron Radiation Facility (LNLS).....	92
Figure 4.7	Schematic illustration of the beamline set-up for measuring XRMD at XRD1, LNLS.	93
Figure 4.8	Schematic representation for the beam propagation paths of a typical three-beam case under X-ray multiple-wave diffraction condition in real crystal space..	94
Figure 4.9	The instrumental set-up at beamline I18 of Diamond Light Source.	97
Figure 4.10	Photograph of the sample environment filled with helium gas.....	97
Figure 4.11	Schematic illustration of the beamline set-up for measuring XAFS at Diamond I18.....	98

Figure 4.12 The ($\bar{1}10$) crystal plate was cut from 190ppm $S_2O_6^{2-}$ -doped $NaClO_3$ crystal for polarized EXAFS..	98
Figure 4.13 The crystal was first aligned to make the sulphur-sulphur bond (along $[\bar{1}\bar{1}\bar{1}]$ axis) parallel to the electric field vector \vec{e} of beam (position I), in order to enhance the EXAFS signal from second shell atom sulphur (first shell atom is oxygen).....	99
Figure 4.14 The geometries used for XANES measurement on an 800ppm sample..	100
Figure 4.15 The molecular orientation of ClO_3 on ($\bar{1}\bar{1}\bar{1}$) surface of $NaClO_3$ crystal.....	103
Figure 5.1 The variation of metastable zone width of $NaClO_3$ in the presence of $S_2O_6^{2-}$ impurity.	107
Figure 5.2 (a) Pure $NaClO_3$ crystal grown from aqueous solution without impurity at the cooling rate of 1.0 °C/day. Habit faces are of {001} type. (b) Schematic illustration for the crystal shown in (a).	109
Figure 5.3 (a) Pure $NaClO_3$ crystal grown from aqueous solution without impurity at the cooling rate of 1.0 °C/day. Parasitic crystals formed in the solution at the bottom of the flask. Habit faces are six {001} faces and five {110} faces. (b) Schematic illustration for the crystal shown in (a).	110
Figure 5.4 (a) Pure $NaClO_3$ crystal grown from aqueous solution without impurity at the cooling rate of 0.5 °C/day. Habit faces are of {001} and {110} types. (b) Schematic illustration for the crystal shown in (a).....	110
Figure 5.5 (a) Pure $NaClO_3$ crystal grown from aqueous solution without impurity at the cooling rate of 0.125 °C/day. The (111) face of the crystal is highlighted by tracing with dotted lines since the contrast of the photo is low due to large volumes of inclusions in the crystal. (b) Schematic illustration for the crystal shown in (a).....	111
Figure 5.6 (a) $NaClO_3$ crystal grown from aqueous solution doped with 40ppm $S_2O_6^{2-}$ at the cooling rate of 1.0 °C/day. Predominant habit faces are of $\{\bar{1}\bar{1}\bar{1}\}$, {001} and {110} types. (b) Schematic illustration for the crystal shown in (a).....	112
Figure 5.7 The same $NaClO_3$ crystal doped with 40ppm $S_2O_6^{2-}$ as shown in Figure 5.6....	112
Figure 5.8 (a-d) $NaClO_3$ crystals grown from aqueous solutions doped with 130ppm – 220ppm $S_2O_6^{2-}$ impurity..	113
Figure 5.9 Schematic illustration for a typical process of crystal morphology changing from the cubic seed (a) to the tetrahedron (d).	115
Figure 5.10 Photograph of the twinning case of $NaClO_3$ formed in the solution doped by 800ppm $S_2O_6^{2-}$	117
Figure 5.11 Photographs of the twinned $NaClO_3$ crystals grown at the bottom of the growth vessel..	118

- Figure 5.12 (a) Doped seed with $\{\bar{1}\bar{1}\bar{1}\}$ faces prepared by evaporating 160ppm doped solution. The thread has been drawn onto the photograph as a coloured line for illustration. The position and direction of the drawn thread is identical to that used in the experiment. (b) The as-grown pure crystal with $\{111\}$ faces, grown from the $S_2O_6^{2-}$ -doped seed. (c) Sketch of the doped seed in (a). (d) Sketch of the as-grown pure crystal in (b). 120
- Figure 5.13 (a) Pure seed with $\{111\}$ faces prepared by evaporating $NaClO_3$ aqueous solution. (b) The as-grown doped crystal with $\{\bar{1}\bar{1}\bar{1}\}$ faces grown from 160ppm doped solution. (c) Sketch of the pure seed in (a). (d) Sketch of the as-grown doped crystal in (b). 121
- Figure 5.14 Segregation coefficient of $S_2O_6^{2-}$ in crystals grown from aqueous solution doped with various impurity concentrations. 123
- Figure 6.1 Schematic illustration of the typical growth sectors and growth sector boundaries of the pure and doped $NaClO_3$ crystals. 129
- Figure 6.2 (a) Topograph of (010) plate of pure crystal. Reflection 002, film D7. It shows no contrast at the boundaries between different growth sectors. Small black dots: surface damages. (b) Sketch of the topograph in (a) in which I and I' represent solvent inclusions. 130
- Figure 6.3 (a) Topograph of the ($\bar{1}\bar{1}0$) plate of 40ppm $S_2O_6^{2-}$ -doped $NaClO_3$ crystal. Reflection 002, film D7. (b) Sketch for the topograph in (a) 130
- Figure 6.4 (a) Topograph of ($\bar{1}\bar{1}0$) plate of 160ppm $S_2O_6^{2-}$ -doped $NaClO_3$ crystal. Reflection 002, film D4. (b) Sketch for the topograph in (a). 131
- Figure 6.5 (a) Topograph of (010) plate of pure $NaClO_3$ crystal. Reflection 002, film D7. (b) Sketch for the topograph in (a). 133
- Figure 6.6 (a) Topograph of ($\bar{1}\bar{1}0$) plate of 160ppm $S_2O_6^{2-}$ -doped $NaClO_3$ crystal. Reflection 002, film D4. (b) Sketch for the topograph in (a). 133
- Figure 6.7 (a) Topograph of ($\bar{1}\bar{1}0$) plate of 40ppm $S_2O_6^{2-}$ -doped $NaClO_3$ crystal. Reflection 002, film D4. (b) Sketch for the topograph in (a). 134
- Figure 6.8 (a) Topograph of the (010) plate of pure $NaClO_3$ crystal. Reflection 002, film D4. (b) Sketch for the topograph in (a). 139
- Figure 6.9 (a) Topograph of the ($\bar{1}\bar{1}0$) plate of 40ppm $S_2O_6^{2-}$ -doped $NaClO_3$ crystal. Reflection 002, film D4. (b) Sketch for the topograph in (a). 143
- Figure 6.10 (a) ($\bar{1}\bar{1}0$) plate of 40ppm $S_2O_6^{2-}$ -doped $NaClO_3$ crystal. Reflection $11\bar{1}$, film D4. (b) Sketch for the topograph in (a). 146
- Figure 6.11 (a) ($\bar{1}\bar{1}0$) plate of 40ppm $S_2O_6^{2-}$ -doped $NaClO_3$ crystal. Reflection 012, film D4. (b) Sketch of the topograph in (a). 149

- Figure 6.12 (a) Topograph of $(\bar{1}10)$ plate of 160ppm $S_2O_6^{2-}$ -doped $NaClO_3$ crystal. The upper and left margins of 160ppm plate $(\bar{1}10)$ are not integral due to previously artificial cutting of the crystal. Reflection 002, film D7. (b) Sketch for the topograph in (a).. 153
- Figure 6.13 (a) Topograph of $(\bar{1}10)$ plate of 160ppm $S_2O_6^{2-}$ -doped $NaClO_3$ crystal. Reflection $11\bar{1}$, film D7. (b) Sketch of the topograph in (a)..... 156
- Figure 6.14 Illustration of the relation between growth velocities of v_1 and v_2 of the $(\bar{1}\bar{1}\bar{1})$ and $(00\bar{1})$ sectors..... 158
- Figure 6.15 (a) Topograph of $(\bar{1}10)$ plate of 190ppm $S_2O_6^{2-}$ -doped $NaClO_3$ crystal. Reflection 002, film D4. (b) Sketch for the topograph in (a). 160
- Figure 6.16 (a) Topograph of $(\bar{1}10)$ plate of 460ppm $S_2O_6^{2-}$ -doped $NaClO_3$ crystal. Reflection 002, film D4..... 163
- Figure 6.17 Photograph of plate I (i.e. (110) plate) in polarized white light. (a) Analyser A rotated anticlockwise by about 20° from the crossed-polarizer position (dotted line). (b) Analyser A rotated clockwise by roughly the same angle with respect to the crossed-polarizer position (dotted line)..... 165
- Figure 6.18 Photograph of plate II (i.e. $(1\bar{1}0)$ plate) in polarized white light. All the data and labels are analogous to Figure 6.17. 165
- Figure 6.19 (a) The D- structure of $NaClO_3$. (b) The L- structure of $NaClO_3$. (c) The Miller indices for habit faces of doped $NaClO_3$ of D- structure. (d) The Miller indices for habit faces of doped $NaClO_3$ of L- structure. 166
- Figure 6.20 (a) X-ray topograph of (110) plate I, reflection 002, Mo- $K\alpha$ radiation. (b) Schematic illustration of growth sectors with their indices and twin domains. 168
- Figure 6.21 (a) X-ray Topograph of (110) plate II, reflection 002, Mo- $K\alpha$ radiation. (b) Schematic illustration of growth sectors with their indices and twin domains. 168
- Figure 7.1 Renninger Scans using (004) primary reflection around $\varphi=0$ for various samples, i.e. pure $NaClO_3$, 70ppm, 160ppm, 190ppm and 220ppm $S_2O_6^{2-}$ -doped $NaClO_3$ 175
- Figure 7.2 Expanded view around 0° of the RSs showing four peaks of different four-beam cases. 177
- Figure 7.3 Schematic illustration for the tetrahedral faces of pure crystal in (a) and doped crystal in (b)..... 178
- Figure 7.4 Calculation fitting of the BSD peaks (111) and $(\bar{1}\bar{1}\bar{1})$ in the 002 RS for all crystals of various doping concentrations. 179
- Figure 7.5 Calculation fitting of the BSD peaks $(1\bar{1}\bar{1})$ and $(\bar{1}11)$ in the 002 RS for all crystals of various doping concentrations. 179
- Figure 7.6 Illustration of the beam transmission path for the BSD cases..... 181

Figure 7.7 Lattice parameters as a function of impurity concentration obtained from the XRMD four-beam cases and the Powder-XRD Rietveld analysis.	182
Figure 7.8 High-resolution $\omega:\phi$ mapping of (012) BSD reflection using the 004 reflection as primary diffraction..	183
Figure 7.9 Mosaic spread for the perpendicular and in-plane directions as a function of impurity concentration.	184
Figure 7.10 Proposed molecular model of $S_2O_6^{2-}$ incorporation on the $(\bar{1}\bar{1}\bar{1})$ face of $NaClO_3$ crystal, with an extra sub-layer above the surface.	186
Figure 7.11 The variation of structure factor of particular reflection planes as a function of the displacement of specific oxygen atoms in the $NaClO_3$ sample.	188
Figure 8.1 The isotropic EXAFS spectra of $Na_2S_2O_6$ powder and the polarized EXAFS spectra of 190ppm doped crystal collected at the two orientations.....	194
Figure 8.2 Molecular structure of the model used in fitting EXAFS.	195
Figure 8.3 Illustration of the structure of the $S_2O_6^{2-}$ ion.....	196
Figure 8.4 The $k^3\chi$ curve, Fourier transformed $k^3\chi$ curve and the best-fit for powder $Na_2S_2O_6$	197
Figure 8.5 The $k^3\chi$ curve, Fourier transformed $k^3\chi$ curve and the best-fit for 190ppm doped $Na_2S_2O_6$	200
Figure 8.6 The back Fourier Transformed (FT) spectra of different EXAFS.	204
Figure 8.7 The measuring method for bond angle $\langle R-O,R-R \rangle$ of RO_3 and RO_4 ions..	206
Figure 8.8 Illustration of the the structure of $S_2O_6^{2-}$ with dimensions obtained from 190ppm EXAFS..	208
Figure 8.9 The XANES spectra of 800ppm doped crystal sample at various orientations, together with that measured on powder $Na_2S_2O_6$	210
Figure 8.10 The S K-edge XANES of $Na_2S_2O_6$ powder and the theoretical p-symmetry PDOS.....	212
Figure 8.11 The S K-edge XANES of 800ppm doped crystal at various orientations and the unoccupied p-symmetry PDOS.	213
Figure 8.12 Projection map of the unoccupied orbitals of $S_2O_6^{2-}$ ion within specific energy region “C”, i.e. 2479.30 – 2480.37 eV.	215
Figure 8.13 Projection map of the unoccupied orbitals of $S_2O_6^{2-}$ ion within specific energy range “D”.....	216
Figure 8.14 (a) XRF-map of sulphur across part of the 190ppm doped crystal plate. (b) The topograph for the same plate used for XRF-mapping.	218

Figure 9.1 The structure and the atomic charges of the ClO_3^- and the $\text{S}_2\text{O}_6^{2-}$	222
Figure 9.2 The dimensions of chlorate and dithionate ions.....	223
Figure 9.3 The visualization of the molecular arrangement on different surfaces of NaClO_3	225
Figure 9.4 The structural model of the incorporation of $\text{S}_2\text{O}_6^{2-}$ on the $\{\bar{1}\bar{1}\bar{1}\}$ type faces of NaClO_3	228
Figure 9.5 The structure of the $(\bar{1}\bar{1}\bar{1})$ face after impurity incorporation, showing the surface where impurity incorporation occurred and one sub-layer after that.....	231
Figure 9.6 Projection of the structure of surface epitaxial twinning NaClO_3 along the cube diagonal $[110]$	234
Figure 9.7 Schematic illustration of a pair of ions on the interface between the twin domains.	235
Figure 9.8 Projected views of the (001) twin boundary, where the $\text{S}_2\text{O}_6^{2-}$ impurity is incorporated.....	237

List of Tables

Table 2.1 Four classes of crystallographic symmetric elements.....	11
Table 2.2 General parameters of the seven crystal systems.....	13
Table 3.1 The critical concentrations for different impurity species to modify the habit of NaClO ₃ from cube into total tetrahedral.	73
Table 3.2 Peak positions of K-edge XANES.....	75
Table 5.1 Segregation coefficient of S ₂ O ₆ ²⁻ in crystals grown from aqueous solution doped with various impurity concentrations.....	122
Table 5.2 Segregation coefficient of S ₂ O ₆ ²⁻ in different growth sectors of 40ppm doped crystal.....	123
Table 5.3 Type of final habit faces of NaClO ₃ crystals grown from solutions doped with different impurity concentrations.....	125
Table 6.1 Calculation of the preferred dislocation lines with their related crystallographic details.....	138
Table 6.2 The observed dislocation lines in the {001} type growth sectors of pure NaClO ₃ crystal and their characterizations. Reflection 002.	141
Table 6.3 The observed dislocation lines in {101} type growth sectors of pure NaClO ₃ crystal and their characterizations. Reflection 002.	142
Table 6.4 The observed dislocation lines in the ($\bar{1}10$) plate of 40ppm S ₂ O ₆ ²⁻ -doped NaClO ₃ crystal and their characterizations. Reflection 002.	146
Table 6.5 The observed dislocation lines in the plate ($\bar{1}\bar{1}0$) of 40ppm S ₂ O ₆ ²⁻ -doped NaClO ₃ crystal and their characterizations, as well as the calculated values. Reflection $11\bar{1}$	148
Table 6.6 The observed dislocation lines in the plate ($\bar{1}\bar{1}0$) of 40ppm S ₂ O ₆ ²⁻ -doped NaClO ₃ crystal and their characterizations. Reflection 012.....	151
Table 6.7 The observed dislocation lines in the plate ($\bar{1}\bar{1}0$) of 160ppm S ₂ O ₆ ²⁻ -doped NaClO ₃ crystal and their characterizations. Reflection 002.....	155
Table 6.8 The observed dislocation lines in the plate ($11\bar{1}$) of 160ppm S ₂ O ₆ ²⁻ -doped NaClO ₃ crystal and their characterizations. Reflection $11\bar{1}$	158
Table 6.9 The β angles measured at the three sampling points on the growth sector boundary shown in Figure 6.15a.....	160
Table 8.1 Results of the fit to 190ppm doped crystal EXAFS at orientation I, i.e. <i>e</i> //S-S. The data was fitted by considering the two SO ₃ groups of S ₂ O ₆ ²⁻ as <i>identical</i>	198

Table 8.2 Results of the best-fit to 190ppm doped crystal EXAFS at orientation I (i.e. $\vec{e} // \text{S-S}$) and at orientation II (i.e. $\vec{e} \perp \text{S-S}$).....	201
Table 8.3 The experimental and the theoretical values of the $N_{\text{effective}}$ and the angle $\langle \text{S-O,S-S} \rangle$	206
Table 8.4 The angle between the R-O bond and the three-fold axis of the investigated ion .	207

Abbreviations and Notation

NaClO ₃	Sodium chlorate
Na ₂ S ₂ O ₆	Sodium dithionate
MSZW	Meta-stable zone width
XRMD	X-Ray multiple-wave diffraction
BSD	Bragg surface diffraction
RS	Renninger Scan
XAFS	X-ray absorption fine structure
PXAFS	Polarized X-ray absorption fine structure
XANES	X-Ray absorption near edge structure
EXAFS	Extended X-ray absorption fine structure
FT	Fourier transform
PDOS	Partial density of states
XRF-map	X-ray fluorescence map
D-	is short for dextrorotatory in crystallography, describing the properties of rotating plane polarized light clockwise
L-	is short for levorotary in crystallography, describing the properties of rotating plane polarized light counter-clockwise
(<i>hkl</i>)	represents a crystal face or crystal plane.
{ <i>hkl</i> }	represents a crystallographic form comprising all the faces than can be derived from <i>hkl</i> by symmetry operations of the crystal.
*{001}	comprises (001), (010), (100), (00 $\bar{1}$), (0 $\bar{1}$ 0), ($\bar{1}$ 00).
*{111}	comprises (111), ($\bar{1}\bar{1}$ 1), ($\bar{1}$ 1 $\bar{1}$), (1 $\bar{1}\bar{1}$).
*{ $\bar{1}\bar{1}\bar{1}$ }	comprises ($\bar{1}\bar{1}\bar{1}$), (11 $\bar{1}$), ($\bar{1}$ 11), (111).
Trigonal-pyramid	is a molecular geometry with one atom at the apex and three atoms at the corners of a trigonal base

* For the case of NaClO₃ under space group P2₁3.

- σ is the supersaturation in the solution
- \mathbf{b} is the Burgers vector for a dislocation
- \mathbf{g} is the diffraction vector used in X-ray topography
- \mathbf{l} is the line direction of dislocations
- E_l is the line tension energy of a linear dislocation
- k is the “wavenumber” in EXAFS
- \vec{e} is the electric vector of the polarized X-ray beam

CHAPTER 1

Introduction

Summary:

This chapter introduces the background underpinning this research, followed by the motivation and purpose of the current study. The thesis layout will be presented and a route map illustrating clearly the work flow of this thesis is also provided.

1.1 Introduction

This chapter presents a brief description of the importance of habit modification in the area of crystallization and crystal growth, the reasons for the selection of the studied system, the objectives and the methodologies employed, followed by the layout of the thesis.

1.2 Research Background

Crystallization has long been playing a significant role in the chemical industries for the purposes of separation, purification, production, etc. Modern crystallization processes constantly need to meet the growing demands of the benefits of crystallization design to produce desirable crystals with favourable properties, such as good flowability, compaction characteristics, dissolution properties, etc. Crystal habit is one of the key factors affecting the processing properties, since even subtle changes in it can induce significant variation in the characteristics of the crystal. In order to modify and optimize the crystal habit to obtain more valuable advantages, impurities (also known as additives) are usually applied deliberately into the crystallization system during the process. The impurities can affect the growth rate of individual crystal faces by either blocking the movement of surface growth steps or disrupting the proper bonding network of the crystal (Clydesdale et al., 1994). However, the knowledge of structural aspects underpinning the crystal habit modification of many systems remains very limited, due to the lack of structural characterization of crystal growth mediated by impurities or other heterogeneous molecules. Consequently, structural research of crystal habit modification by impurity is not only necessary for facilitating the design and optimization of crystal habit in chemical industries, but also addresses the fundamental scientific request of understanding the complicated crystal surface chemistry during the impurity incorporation process.

$\text{NaClO}_3 / \text{Na}_2\text{S}_2\text{O}_6$ (host / impurity), as a representative habit modification system, has been chosen to be studied in this thesis. The ordinary habit of pure NaClO_3 crystals grown at moderate supersaturation exhibit the cubic $\{100\}$ faces, which dominate the habit, and twelve rhombic-dodecahedron faces of $\{110\}$ type and four tetrahedral faces of (111) , $(\bar{1}\bar{1}1)$, $(\bar{1}1\bar{1})$ and $(1\bar{1}\bar{1})$. (Hooper et al., 1983; Ristic et al., 1993).

Buckley (1930) employed 36 impurities to modify the habit of NaClO_3 , and concluded that dithionate ion ($\text{S}_2\text{O}_6^{2-}$) is the most effective in introducing the tetrahedral faces and eliminating the cubic faces. Most recently, based on habit modification observation and growth kinetics measurement, Ristic et al. (1993; 1994) and Wojciechowski (1995) presumed the incorporation mechanism of $\text{S}_2\text{O}_6^{2-}$ in NaClO_3 crystal¹ to be a SO_3 group of the $\text{S}_2\text{O}_6^{2-}$ ion substituting the ClO_3^- on the surfaces of $\{\bar{1}\bar{1}\bar{1}\}$ type and the other SO_3 being at an interstitial site and decreasing the velocity of the growing face (Figure 1.1). However, there is a lack of further characterization on this $\text{NaClO}_3/\text{Na}_2\text{S}_2\text{O}_6$ (host/impurity) system to study the doped crystal in terms of growth history, lattice distortion, local structure of impurity, etc. In addition, Ristic et al. (1993) observed for the first time, the growth of twinned NaClO_3 crystal which they interpreted as being due to an epitaxial relationship between the twin partners, induced by the $\text{S}_2\text{O}_6^{2-}$ impurity. Similarly, there hasn't been any further experimental progress to study this twinning phenomenon.

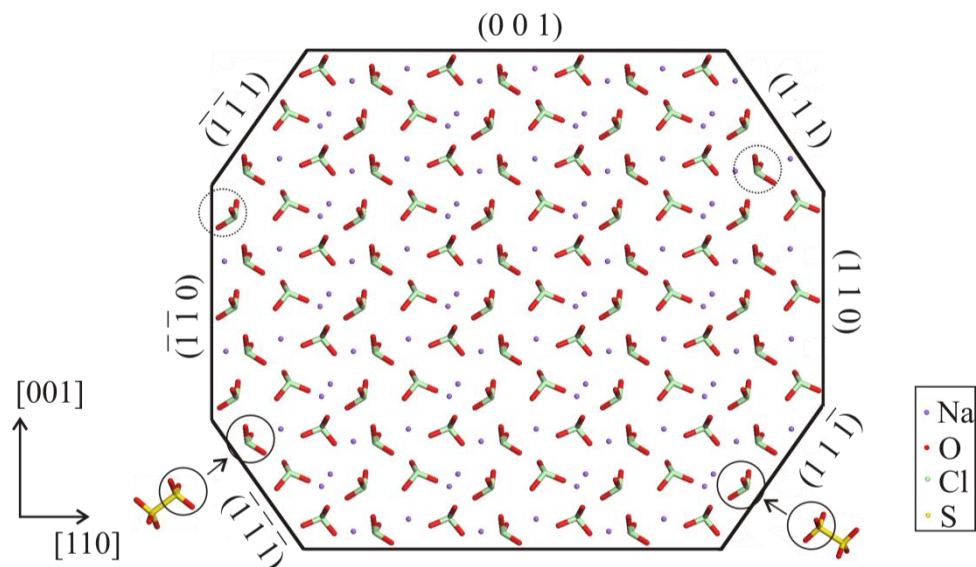


Figure 1.1 $(1\bar{1}0)$ projection of the structure of NaClO_3 . It shows facets (111) and $(\bar{1}\bar{1}\bar{1})$ of tetrahedron $\{111\}$ and facets $(\bar{1}\bar{1}\bar{1})$ and $(11\bar{1})$ of the opposite tetrahedron $\{\bar{1}\bar{1}\bar{1}\}$. The specific ClO_3^- on the $\{\bar{1}\bar{1}\bar{1}\}$ faces can be substituted (Ristic et al., 1993).

¹ Since the impurity $\text{Na}_2\text{S}_2\text{O}_6$ is also sodium salt as that of NaClO_3 , the impurity under discussion is thus only $\text{S}_2\text{O}_6^{2-}$.

1.3 Aims and Objectives of This Thesis

As described in the previous section, it is needed to perform experimental characterization on the habit modification system of $\text{NaClO}_3/\text{Na}_2\text{S}_2\text{O}_6$ (host/impurity), which contribute to our fundamental understanding on the complicated crystal surface chemistry during the impurity incorporation process and would fulfil our scientific interest on the complexities of this system. In addition, the effect of impurity on the crystallization kinetics of NaClO_3 is also of our interest. Thus, this thesis addresses the following research questions:

What is the structural mechanism for the action of sodium dithionate impurity on the crystal habit, defect structure, micro-crystallography and crystal kinetics of sodium chlorate?

The specific aims and objectives which address these questions are as follows:

- To grow NaClO_3 single crystals as a function of impurity concentrations and observe the habit modification process during crystal growth. To grow twinned crystals at relatively high impurity concentration and carefully observe the twinned habit.
- By characterizing and comparing the various types of defects between pure and doped crystals (including single and twinned) using X-ray topography to investigate their growth history and dislocation configuration. By determining the optical activity of the twin domains of the twinned crystal to approach the applicable twin law for the case.
- To determine the effects of $\text{Na}_2\text{S}_2\text{O}_6$ on the doped NaClO_3 crystals at micro-crystallographic level using X-ray multiple-wave diffraction, i.e. to probe the impurity-induced lattice distortion and local strain.
- To investigate the three-dimensional orientation and local structure of the $\text{S}_2\text{O}_6^{2-}$ ion within the $\{\bar{1}\bar{1}\bar{1}\}$ growth sectors of NaClO_3 crystal using X-ray absorption fine structure, to provide structural information for approaching the structural model of impurity incorporation. Also, to determine the impurity distribution in growth sectors of different types using XRF-mapping, for understanding the incorporation coefficient of the impurity at different faces.
- To approach the impurity incorporation mechanism, based on the results of molecular modelling and experiments, and correlate the model to the results from experimental characterizations. To discuss the effect of the impurity on

the growth mechanism of NaClO_3 , i.e. how the growth rate of $\{\bar{1}\bar{1}\bar{1}\}$ faces was inhibited.

- To characterize the meta-stable zone (MSZ) of NaClO_3 in aqueous solution as a function of impurity doping level and solution cooling rate using the turbidity detection, for the purpose of investigate the influence of $\text{S}_2\text{O}_6^{2-}$ impurity on the crystallization kinetics of NaClO_3 .

1.4 Layout of This Thesis

This thesis contains 10 chapters and a schematic route map representing the layout is shown in Figure 1.2. Chapter 1 describes briefly the background, the aims and objectives and the layout of this thesis. Chapters 2 and 3 review the literature related to the current work. Chapter 2 presents the fundamental knowledge of crystalline solids, the important theories in crystallization and crystal growth and the principles of the characterization methods used in this project. Chapter 3 compiles a literature review ranging from the habit modification of inorganic systems to the specific system of sodium chlorate (NaClO_3) by impurity sodium dithionate ($\text{Na}_2\text{S}_2\text{O}_6$). In Chapter 4 the information on the studied materials and the technical details of employed experimental methods are provided. Chapter 5 describes and discusses firstly the effects of $\text{Na}_2\text{S}_2\text{O}_6$ on the crystallization kinetics of NaClO_3 in aqueous solution as a function of impurity concentration and cooling rates, and secondly, but significantly, the crystal habit modification of NaClO_3 as a function of impurity concentration. The various types of defects in both pure and doped crystals are discussed in Chapter 6, where the growth history of the doped crystals was reconstructed to reveal the habit modification process. Also, the features of the twinned NaClO_3 crystal have been revealed by X-ray topography and optical activity measurement in Chapter 6, and the applicable twin law is determined. In Chapter 7, the micro-crystallographic information of the doped crystals is compared to that of a pure crystal, in terms of lattice distortion and local strain. Chapter 8 presents the determination the three-dimensional orientation and the local structure of the $\text{S}_2\text{O}_6^{2-}$ in the NaClO_3 crystal, in order to provide direct structural information for approaching the structural model of impurity incorporation. In Chapter 9, a comprehensive discussion based on both experimental and molecular modelling results is presented, aiming to establish a structural model of impurity incorporation. The habit-modifying

mechanism of NaClO₃ crystals by Na₂S₂O₆ impurity is also to be discussed. Chapter 10, as the final chapter, summarises the results and discussions of this thesis, and gives suggestions for future study after the current one.

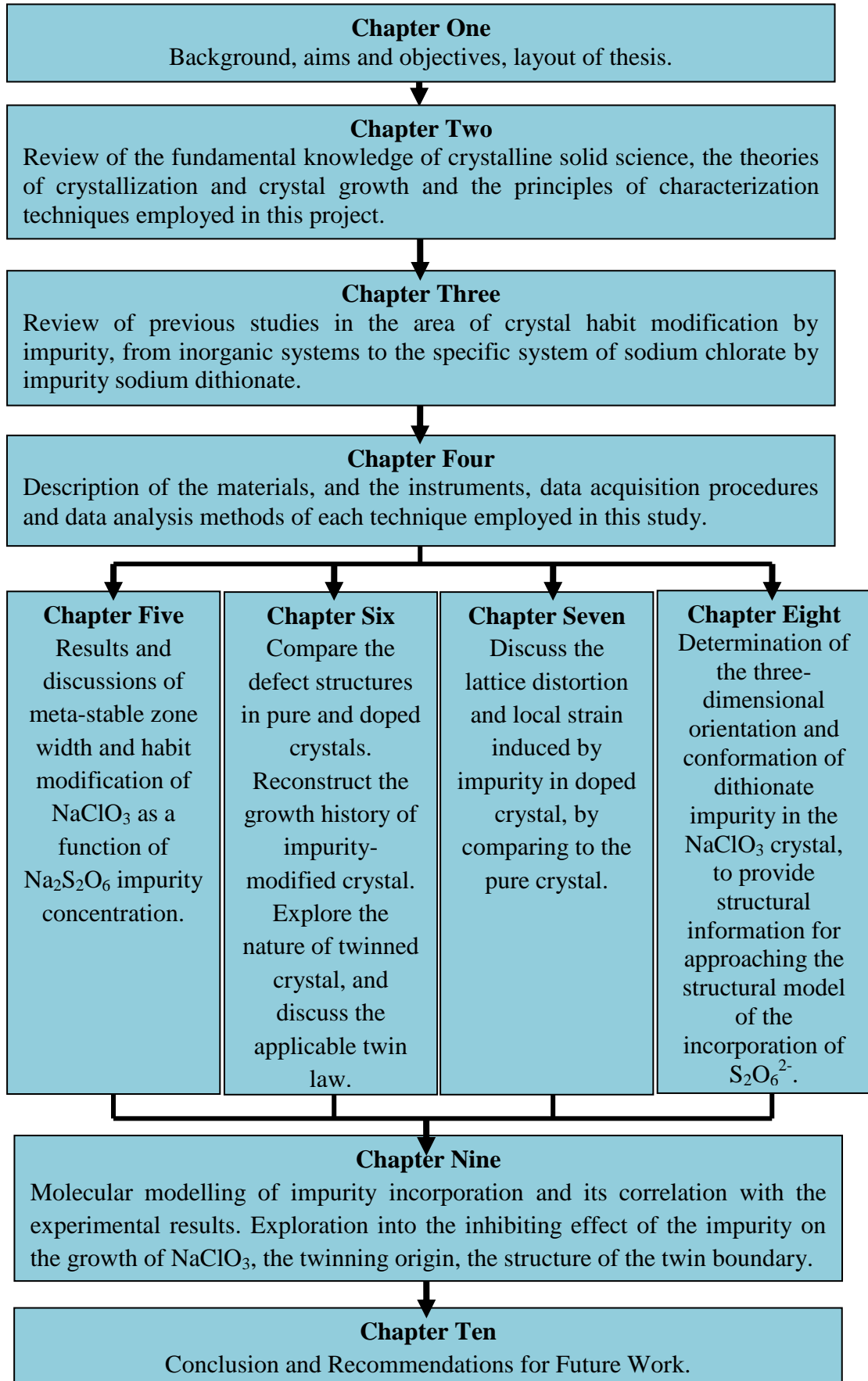


Figure 1.2 The route map illustrating the layout of this thesis.

CHAPTER 2

Crystal Science and Characterization of Crystallization and Crystal Growth

Summary:

This chapter summarizes the fundamental knowledge of crystalline state, the theories of crystallization and crystal growth and the principles of characterization techniques employed in this project.

2.1 Introduction

The aim of this chapter is to review the fundamentals of the crystalline state, crystallization and crystal growth, and the characterization methods used in this study. Firstly the fundamental concepts related to the area of crystallography are described, followed by a brief insight to isomorphism and polymorphism, crystal habit, crystal chemistry and crystal defects. Then, an overview is given on the concepts covering solubility, supersolubility and metastable zone. Next, the classification of the nucleation processes and other corresponding concepts are described. Following that, crystal growth theories are reviewed in detail. Finally, the principles underpinning the characterization methods employed in the current study are presented.

2.2 Fundamental of Crystalline State

2.2.1 Crystalline Solid

There are three general states of matter in our world – gas, liquid and solid – sorted with their different degrees of atomic or molecular mobility. Out of these three states, crystals fall into the category of solid. Being different from the other solid states, the molecules, atoms or ions in the crystals are always fixed in a position called “lattice”, and this causes a high degree of internal regularity which commonly results in definitely grown external crystal faces. Due to the unique internal crystal structure of a crystal, it always presents high symmetry determining many of its physical properties (Mullin, 1992). The following sections outline some fundamental principles used in describing crystalline solids.

2.2.2 Unit Cell

In the characterization of crystal structure, i.e. the atomic arrangement within a crystal, the most basic unit with all the necessary information is referred to as the “unit cell”. A unit cell is a small spatial box composed of one or more atoms, with a particular three-dimensional shape. The “lattice parameters” describes the lengths of sides (a , b , c) and the angles between sides (α , β , γ) of the unit cell (Figure 2.1). The atom

positions in the cell are described by their individual atomic positions (x, y, z) with respect to a defined zero origin commonly at a lattice point.

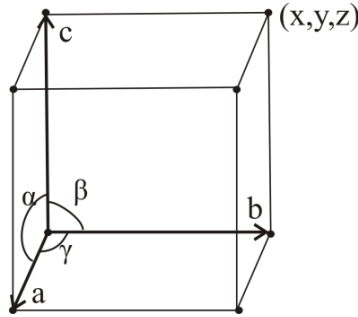


Figure 2.1 The three-dimensional unit cell, with three crystallographic axes, the lattice parameters (a, b, c) and (α, β, γ) .

2.2.3 Miller Indices

The notation system of Miller indices is widely used in crystallography and crystallization for indexing the planes and faces of crystals, in terms of the specific axial intercepts of each plane or face. Based on the definition of lattice vectors a, b and c in a crystal, this notation method utilizes the intercepts X, Y and Z of one particular plane on the axes x, y and z for illustration. The particular plane could be represented as (h, k, l) , where h, k and l are defined as follows:

$$h = \frac{a}{X} \quad k = \frac{b}{Y} \quad l = \frac{c}{Z} \quad (2.1)$$

A typical example of calculation of crystal faces is shown in Figure 2.2. The larger plane occupies intercepts of $X=2a, Y=b$ and $Z=c$, thus the calculation will be:

$$h = \frac{a}{X} = \frac{a}{2a} = \frac{1}{2} \quad k = \frac{b}{Y} = \frac{b}{b} = 1 \quad l = \frac{c}{Z} = \frac{c}{c} = 1 \quad (2.2)$$

Therefore, the plane is indexed as (122) since the indices usually use integers for convenience. Similarly, the smaller plane with intercepts $a, 1/2b, 1/2c$ can also be indexed as (122) . Furthermore, in Miller Indices there are two types of brackets used. Normally, the (122) indicates a single particular plane, whereas $\{122\}$ refers to one or more of the equivalent faces related to (122) by crystallographic symmetry.

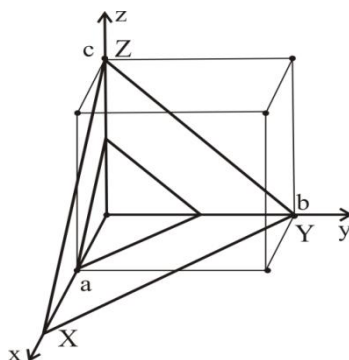


Figure 2.2 Intercepts of planes with defined crystallographic axes.

2.2.4 Crystal Symmetry

For particular crystal structures, the crystallographic unit could appear identical to itself after being operated with one or more alternative symmetry operations. As a result, a notation method to describe the symmetry of crystal in a convenient and efficient way has been defined. Three basic elements are used in symmetry operations, i.e. point, line and plane, by which we could define totally four classes of symmetric elements in crystallography including inversion centre, rotation axes, mirror plane and rotation-reflection axes. The four symmetric elements are shown in Table 2.1. In repeating lattices, there are two types of additional symmetry elements, i.e. screw axis and glide plane (Table 2.1).

Symmetric Element	Action	Notation
Inversion centre	Inverse along a point	$i, \bar{1}$
Rotation axis	Rotate by $360^\circ/n$ along an axis	1, 2, 3, 4, 6
Mirror plane	Reflect through a plane	m
Rotation-reflection axis	Rotate by $360^\circ/n$ along an axis and then Inverse along a point on the axis	$\bar{2}, \bar{3}, \bar{4}, \bar{6}$
Screw axis	Rotate $360^\circ/n$, followed by translation of r/n along that axis.	n_r
Glide plane	Reflect across plane, followed by translation of $1/2$ (usually) unit cell parallel to the plane along a, b, c, face diagonal (n), or body diagonal (d)	a, b, c, n, d

Table 2.1 Four classes of crystallographic symmetric elements.

For example, a simple cube is a highly symmetric shape as it possesses 23 elements of symmetry (1 centre, 9 planes and 13 axes). A cube unit could be operated with respect to its inversion centre, i.e. body centre (Figure 2.3), and it would appear identical to that before the operation. Any plane cutting the cube into two equivalent parts could be a mirror plane. Also, two types of symmetric axes exist in this structure. The axes of b and c in Figure 2.3 could simply act as 4-fold rotation axes and axis a is one of the 3-fold rotation axes, whilst the axes of b and c are both able to be the 4-fold rotation-reflection axes. It is worth noticing that, b and c in lower symmetric cubic structures such as $P2_13$ are only 2-fold screw axes.

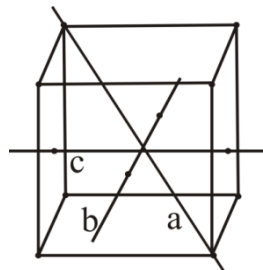


Figure 2.3 Schematic illustration of an example of symmetry operations for a simple cube unit. The line a is a typical 3-fold rotation axis, while b and c are typical 4-fold rotation axes in simple cubic structures.

2.2.5 Crystal Systems

The parameters of a unit cell could vary from one set to another, but actually there are only practically seven different types of shapes for the unit cell. They are defined to be seven crystal systems, and Table 2.2 shows the names of different systems as well as corresponding unit cell parameters.

Based on the concept of a crystal system, there could be different types of unit cells with various numbers of lattice points inside the lattice and the arrangement of lattice points. For example, some unit cells are primitive with lattice points at the face centres (F), body centres (I) or corners (P). In 1848, Bravais (Mullin 1992) published his idea of 14 possible types of lattice depending on geometrical considerations, which are listed in Table 2.2. Figure 2.4 illustrated the three typical types of Bravais lattices in the cubic system.

Crystal system	Edge lengths	Angles	Bravais lattice types
Cubic	$a=b=c$	$\alpha=\beta=\gamma=90^\circ$	Primitive
			Body-centred
			Face centred
Tetragonal	$a=b\neq c$	$\alpha=\beta=\gamma=90^\circ$	Primitive Body-centred
Hexagonal	$a=b\neq c$	$\alpha=\beta=90^\circ, \gamma=120^\circ$	Primitive
Orthorhombic/rhombic	$a\neq b\neq c$	$\alpha=\beta=\gamma=90^\circ$	Primitive
			Body-centred
			Face-centred
			Base-centred
Trigonal	$a=b=c$	$\alpha=\beta=\gamma\neq 90^\circ$	Primitive
Monoclinic	$a\neq b\neq c$	$\alpha=\gamma=90^\circ\neq\beta$	Primitive
			Base-centred
Triclinic	$a\neq b\neq c$	$\alpha\neq\beta\neq\gamma\neq 90^\circ$	Primitive

Table 2.2 General parameters of the seven crystal systems.

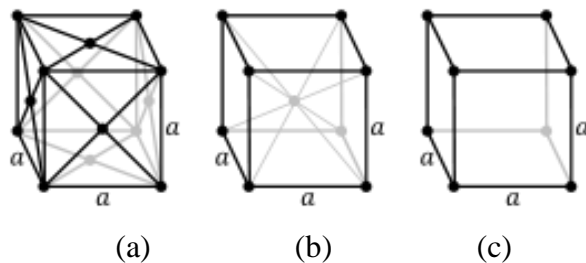


Figure 2.4 The schematic illustration of Bravais lattices - cubic types. (a) face-centred cubic; (b) body-centred cubic; (c) primitive cubic.

2.2.6 Isomorphism and Polymorphism

What cannot be avoided in crystallography is the topic of Isomorphs and Polymorphs. Isomorph is defined as two or more substances which will crystallize in nearly identical forms, with tiny differences in interfacial angles, e.g. sodium chlorate (NaClO_3) and sodium borate (NaBrO_3). The reason for this phenomenon might be the chemical similarity between them. And, under some circumstances the isomorphous substances can grow “one in another” to form “mixed crystals”. This kind of viewpoint provided significant understanding to the fact of sodium dithionate growing into the crystals of sodium chlorate as impurity. Polymorphism refers to the ability of a chemically identical substance to form more than one crystalline structure. The various kinds of crystalline forms presented by the same substance may result from the variation of external factors of crystallization cooling rate, crystallization pressure and change of solvent. Sulphur is a good example for explaining polymorph, since it will crystallize into orthorhombic crystals (α -S) from the solvent of carbon disulphide and monoclinic crystals (β -S) from the melt.

2.2.7 Crystal Habit

2.2.7.1 *Crystal habit of crystal grown from solution*

The topic of controlling crystal habit has been quite an interesting one among both the academic researchers for theoretical interest and the industrial practitioners for applicable demands. Crystal habit, also referred to as morphology of crystal, is a significant property among various properties of crystalline matter. It is worth noticing that, crystal morphology is normally used to depict the crystal forms of a crystal, whilst crystal habit is used to describe the final faces and their relative sizes. For example, the crystals shown in Figure 2.5a-c show the same crystal morphology which are all composed of the $\{100\}$ and $\{111\}$ forms, but their crystal habits are different which is reflected by the distinct sizes of the crystal faces.

Crystal habit influences many other properties of the crystal, e.g. flow and mixing properties, filtration property, surface chemical activity, etc. In this section, only the factors related to the habit of as-grown crystals from solution, which is the method

used in the current study, are of concern. The crystal habit of a crystal depends on the various growth rates of its faces. The faces with faster growth rates will disappear or never appear on the final habit, whilst the faces with slower growth rates could dominate the shape of a crystal. The growth rates of various facets are affected mainly by two categories of factors, i.e. internal factors and external factors. The former includes crystal structure and crystal defects, while the latter includes solution supersaturation, solvent property, solution composition, type of impurities and other growth conditions (e.g. growth temperature range, solution flow, ultrasound). Figure 2.5 shows examples of different crystal habits for the same crystal.

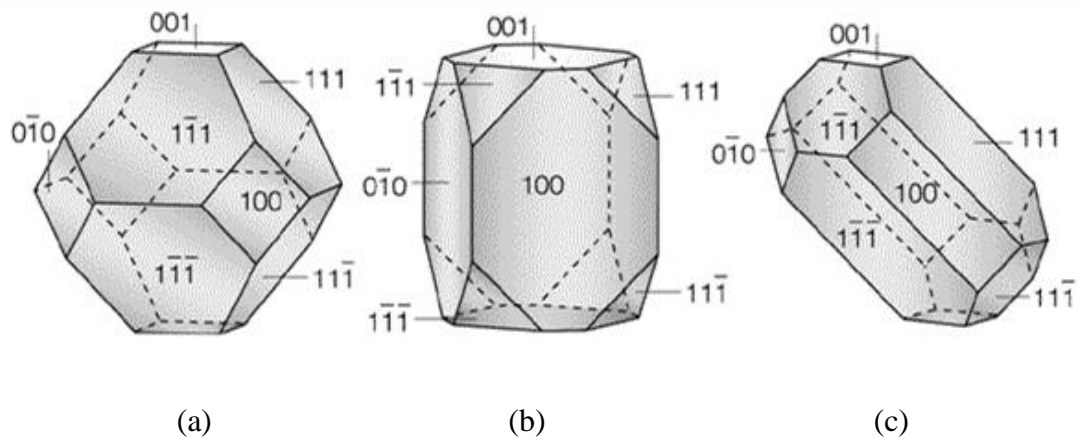


Figure 2.5 Several typical crystal habits of magnetite (Fe_3O_4). (a) Idealized cubooctahedra habit composed of $\{100\} + \{111\}$ forms. (b) Anisotropic habit composed of elongated $\{100\}$ and typical $\{111\}$. (c) Anisotropic habit composed of elongated $\{111\}$ and typical $\{100\}$. The latter two forms were derived from an anisotropic flux of ions surrounding the crystal or possibly anisotropic interactions between the magnetic growing units and the crystal surface (Mann et al., 1984; Mann and Frankel, 1989).

2.2.7.2 Theoretical crystal habit

a) Bravais–Friedel–Donnay–Harker theory

The earliest predictions on theoretical crystal habit were based upon only structural considerations, and the widely accepted theory of Bravais-Friedel-Donnay-Harker (BFDH) law (Donnay and Harkei, 1937; Donnay and Donnay, 1962; Prywer, 2004)

was established. According to BFDH law, the planes with larger lattice distance possess higher morphological importance (MI):

$$d_{hkl} > d_{h'k'l'} \longrightarrow MI(hkl) > MI(h'k'l') \quad (2.3)$$

thus, the size of crystal facets $\{hkl\}$ will appear relatively larger than that of $\{h'k'l'\}$ on the final crystal habit. An equivalent expression useful for linking the above relationship to experimental measurements can be:

$$R_{hkl} \propto \frac{1}{d_{hkl}} \quad (2.4)$$

where R_{hkl} is the relative growth rate normal to the planes $\{hkl\}$. Therefore, the theoretical BFDH habit of a crystal can be simply obtained as a drawn convex polyhedron, by defining the $\{hkl\}$ faces with respect to their individual d_{hkl} values. (Donnay and Harkei, 1937) This approach had been extended to deal with sub-layers (i.e. d_{hkl} / n), by considering the pseudo-symmetries² in some structures (Donnay and Donnay, 1962).

The rule determined in Equation 2.4 actually works well as it implies an energetic concept. During the depositing of a new plane onto the crystal surface, the released energy of planes with larger d-spacing is lower compared to those with smaller d-spacing, since the interaction between atomic layers reduces with increasing distance. Lower released energy corresponds to slower growth, hence a larger dominating surface. This is consistent with the BFDH rule, by which R_{hkl} is also smaller for planes with larger d-spacing, hence the plane appeared larger on the final crystal habit due to slower growth. Therefore, the BFDH rule $R_{hkl} \propto (1/d_{hkl})$ is popular and utilized in many cases, under the implied relationship between the growth rate R_{hkl} and the elementary representation of released energy during growth. Nevertheless, the BFDH law contains restrictions during application, because neither the lateral interactions of the growth units nor the fact that only the flat faces can grow by lateral mechanism are considered.

² Pseudo-symmetry refers to the operation that brings one component of the crystal space to a position very close to another. Such operation is highly close to a space group operation with limited deviation.

b) *The Hartman-Perdok theory*

Hartman and Perdok (Hartman and Perdok, 1955; Hartman, 1973) described the crystals as built up by strongly bonding the atoms or building blocks periodically to form straight edges parallel to important $[uvw]$ lattice orientations. The repeated straight rows containing atoms or building blocks present a close relationship with the periodicity of the crystal, thus the Hartman-Perdok theory is often referred to as periodic bond chains (PBCs). According to the PBCs theory, three types of typical faces are defined as follows:

- F-face : contain two or more PBCs
- S-face : contain one PBC
- K-face : contain no PBC

F-face, S-face and K-face are shown in Figure 2.6 by a simple structure with three PBC orientations respectively along three axes. It is not difficult to understand that the S and K faces would grow faster than the F faces, thus grown out and rarely observed on the final habit. The relatively slow growing F faces would then become predominant on the habit faces of a crystal. Based on the structural information of a crystal, it is possible to deduce the PBCs and predict the crystal morphology via computational methods for attachment energy. However, even among the F-faces there is competition, and only those with the lowest growth rates would be present on the final habit.

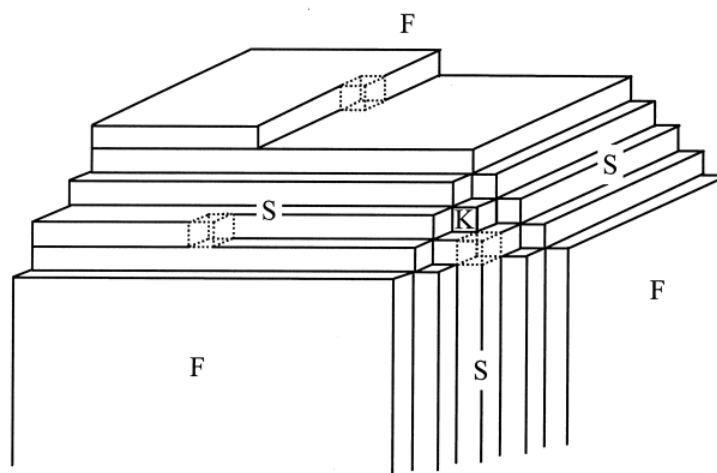


Figure 2.6 Schematic illustration for the surface structure according to the Hartman-Perdok theory for a cubic crystal. Three types of Kossel crystal surfaces are presented,

i.e. F (flat, parallel to at least two PBCs), S (stepped, parallel to one PBC) and K (kinked, not parallel to any PBCs). The dashed cubes are bonded to 3 other cubes. (after Hartman and Perdok, 1955)

The crystallization energy ($E_{\text{crystallization}}$, E_{cr}) occurred during the permanent bonding of a building block onto a crystal face can be expressed (Hartman, 1973, p379) as

$$E_{\text{cr}} = E_{\text{att}} + E_{\text{sl}} \quad (2.5)$$

where E_{att} represents the attachment energy which relates to the interaction between the building blocks and the surrounding crystal content, and is equal to the released bond energy during the attachment of the building blocks to the face concerned; E_{sl} represents the slice energy which refers to half of the energy released during the formation of an infinite slice. This relation has been adopted worldwide to predict the growth habit of crystals, by evaluating the kinetic meaning of attachment energy E_{att} . The Hartman-Perdok theory indicates that, the higher the E_{att} value, the higher the probability for building blocks to attach onto a crystal face. Therefore, the E_{att} becomes a reliable measure of the growth rate for a given growing face (hkl) (Hartman and Bennema, 1980), which can be expressed as

$$R_{\text{hkl}} \propto E_{\text{att}}^{\text{hkl}} \quad (2.6)$$

Thus, the Hartman-Perdok theory allows one to predict the growth habit of a crystal, by carefully choosing a brilliant model of building blocks. Authoritative reviews by Hartman (Hartman, 1973; 1987) should be further consulted, as the practical predictions by the above subjects are to some extent advanced and need to be explored seriously.

2.2.8 Crystal Chemistry

Crystalline solids may be generally specified into four types according to the different bonding types, i.e. ionic, molecular, covalent and metallic. The crystal involved in this study is of ionic composition. Ionic crystals consist of charged positive ions and negative ions bound together, mainly by electrostatic attraction between the ions. One ion should be enclosed by a number of the ions with opposite charge. The positive

charges compensate the negative charges inside the material, which makes it electrically neutral. Moreover, this kind of arrangement must occur on as small a scale as possible to keep neutrality, so the positive ions and negative ions are in the structure of alternative position. The force between two charged ions is defined by Coulomb's Law:

$$F = k \frac{q_1 q_2}{r^2} \quad (2.7)$$

where r is the separation distance and k is the proportionality constant. Thus, the interactive force is inversely proportional to the distance between two ions, and this makes it important to study the size and shape of the ions which have a critical effect on the inter-ionic distance. The exact arrangement of ions in lattice varies according to the size of the ions in the solid.

2.2.9 Crystal Defect

It is generally accepted that almost all crystal is imperfect, and grow with a variety of defects. Defects affect both the physical and chemical properties of crystals to a large extent, and there are mainly two types of defects, i.e. point defects and line defects.

A point defect refers to the structural fault that occurs in the lattice structure when the original atom arrangement is disrupted under unexpected condition, such as missing atom, atom in an irregular position or impurity atom incorporated in the bulk lattice.

Line defect is commonly known as a dislocation, and can be classified into two groups, edge dislocation and screw dislocation. An edge dislocation is caused by an extra plane of atoms existing between two regular atom planes (Figure 2.7a). A screw dislocation is formed by the displacement of atom planes in the crystal (Figure 2.7b). This kind of dislocation is of great importance in a classic growth mode where the dislocation contributes a lot by providing growth steps.

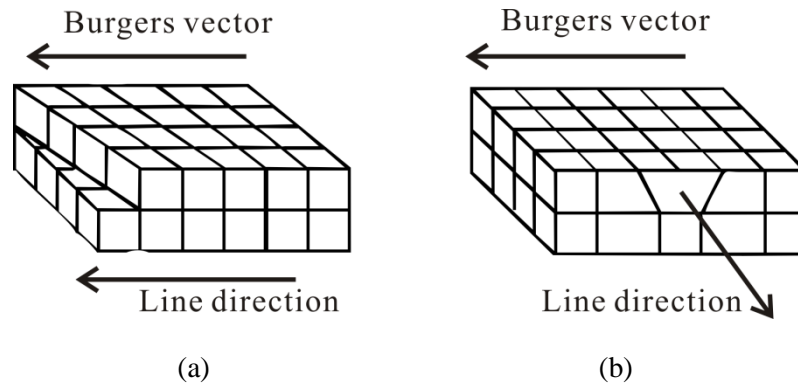


Figure 2.7 Schematic illustration of the directions of Burgers vector and dislocation line for screw dislocation (a) and edge dislocation (b).

2.3 Solubility and Supersaturation

2.3.1 Solubility

The generalized solution includes gas, liquid and solid solution, which are composed of two or more components to form a mixture at stable equilibrium. Since the crystal growth from aqueous solution is used in the current study, here the solution is referred to as the aqueous solution composed of solid solute dissolved in liquid solvent. Solubility is the measure of the equilibrium position between the solid form of a solute and the solution of the solute. In other words, it is used to measure the extent to which the solute dissolves in a specific solvent to form a homogeneous solution.

Different methods can be used for the expression of the solubility of ionic solutes, for example, 20g of NaClO_3 in 100g of H_2O , and equivalently 20g of NaClO_3 in 100g of solution. The dissolution of NaClO_3 in water at the equilibrium status can be expressed as $\text{NaClO}_3(\text{s}) \rightleftharpoons \text{Na}^+(\text{aq}) + \text{ClO}_3^-(\text{aq})$. Correspondingly, the equilibrium constant K_s which describes the dissolution behaviour of NaClO_3 in H_2O is equal to $[\text{Na}^+][\text{ClO}_3^-]$.

The solubility of a specific substance or even one specific phase of the substance depends on the intermolecular forces between solute and solvent and the entropy change during the dissolution. Therefore, all factors affecting this balance will be capable of changing the value of solubility, e.g. temperature and pressure. Either in laboratory or industrial processes, the outcome of single crystal growth or

crystallization depends severely on the equilibrium relationship of solute and solvent under varying conditions. Thus, solubility is essential data for chemical engineering.

2.3.2 Supersaturation and the Meta-stable Zone

Supersaturation illustrates the state in which the solution contains more dissolved solid than it ordinarily does at a specific temperature, which means the dissolving capacity of a solvent for a specific solute represents a higher value rather than the usual one. Such a state had been observed in very early investigations on crystal growth and crystallization, since the nucleation does not take place when the solution just becomes saturated from the unsaturated state.

The concepts of “supersaturation” and “supersolubility” were first introduced by Ostwald (1897) to define whether spontaneous nucleation would happen or not in super-cooled solutions. Later, the relationship between supersaturation and spontaneous crystallization was studied by Miers and Isaac (Miers and Isaac, 1906; Miers and Isaac, 1908), simultaneously they indicated the metastable zone on a solubility-supersolubility diagram after having done a large amount of experiments with different chemicals (Figure 2.8).

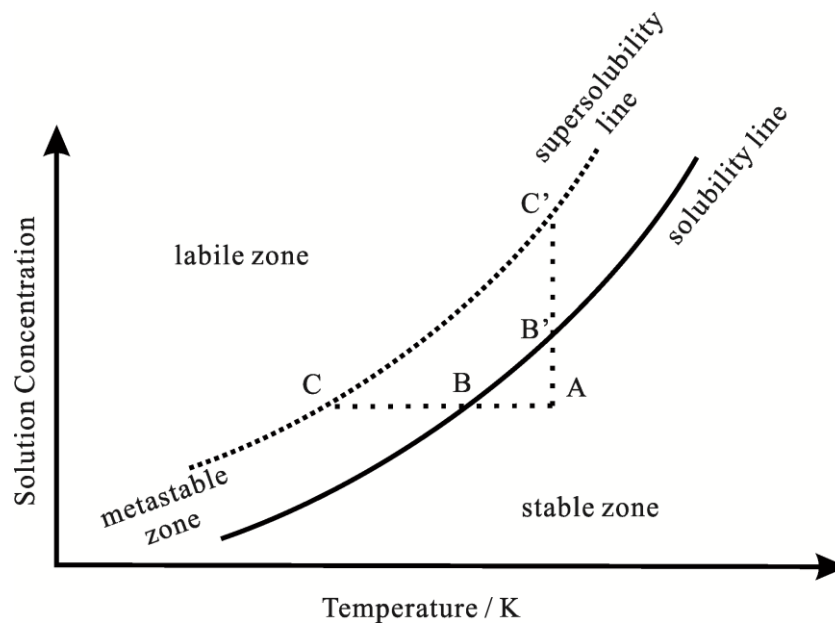


Figure 2.8 A typical solubility–supersolubility diagram. The metastable zone is illustrated as being between the solubility line and the supersolubility line. Path ABC and AB'C' indicated two different routes for obtaining supersolubility.

The dotted curve is the supersolubility curve, it presents the temperatures and concentrations under which spontaneous crystallization can occur, and the nearly parallel lower solid curve is the solubility curve. The two curves divide the diagram into three areas:

- The stable zone with unsaturated solution, in which not only nucleation is impossible, but also existing crystal will be dissolved.
- The meta-stable zone, located between the solubility and supersolubility curves, in which there is no chance for spontaneous crystallization to occur. However, the meta-stable zone is critical for single crystal growth, since crystal seeds will immediately begin to grow once they are placed in the solution, without homogeneous nucleation occurring.
- The labile zone, in which it is possible for spontaneous crystallization to occur.

Path ABC in Figure 2.8 indicated the solution is cooled down without any mass exchange with external environment. No crystallization occur until the temperature drops to C, and then crystallization could take place spontaneously in the solution or be induced by agitation, seeding or mechanical friction and collision. Also, supersaturated solution can be achieved by solvent evaporation. Path AB'C' represents the procedure of solvent evaporation under constant temperature. The effects of ABC and AB'C' are similar on most occasions, but the path ABC can have an extension into the labile zone under special circumstances, for example the solute is very soluble (e.g. sodium chlorate, sodium thiosulphate).

Considering the different demands of various applications and for less confusion relating to the basic units of concentration, supersolubility is expressed in a number of different ways. The common concepts corresponding to supersolubility are the concentration driving force (Δc), the supersaturation ratio (S), and the absolute supersaturation (S').

The expressions for these concepts are shown below:

$$\Delta c = c - c' \quad (2.8)$$

$$S = \frac{c}{c'} \quad (2.9)$$

$$S' = \frac{\Delta c}{c'} = S - 1 \quad (2.10)$$

Where c is the solution concentration, c' is the equilibrium saturation at the given temperature.

Experimental values of the supersolubility and also the width of meta-stable zone depend strongly on the actual experimental process. They can be affected by many external factors, including different cooling rates, reactor factors, speed of agitation and the presence of impurities (Nyvlt, 1971; Mullin, 1992).

From a more fundamental approach, the driving force for crystallization and crystal growth is the difference between the chemical potential of liquid phase (μ_l) and the solid phase (μ_s). Therefore, the driving force can be expressed as

$$S = \exp\left(\frac{\mu_l - \mu_s}{RT}\right) \quad (2.11)$$

where R is the gas constant and T is the absolute temperature.

2.3.3 Effect of Impurities on Solubility

Absolutely pure solution is the idealization which cannot be achieved in the laboratory at present, but for laboratory analysis the impurity in intended solution can sometimes be ignored. In industrial solutions especially, the impurity levels are inevitably high to some extent, which can cause a significant effect on the solubility of the solute.

In a binary solution, the appearance of a third component will lead to four conditions (Mullin, 1992):

- the impurity has no effect on the solution, but this rarely happens.
- the impurity chemically reacts with the original solution component or components, therefore introducing new species into the system.
- the impurity reduces the solubility of the solute in the solvent, e.g. alcohol added as impurity into the aqueous solution of sodium chlorate.
- the impurity enhances the solubility of the solute in the solvent.

In the research on protein precipitates by Bell et al. (1983), an empirical equation was established for the salting-out effect when adding an electrolyte impurity into the solution of a non-electrolyte:

$$\log \frac{c'}{c} = kC + \beta \quad (2.12)$$

where c' and c (mol L^{-1}) are the equilibrium saturation concentrations of the non-electrolyte solute in aqueous solution and salt-containing solution at salt concentration C (mol L^{-1}), respectively; k is the salting parameter and β the efficiency of the specific electrolyte at a particular temperature. This experience-based relationship is often utilized in predicting the precipitation of proteins both in laboratory and industrial scales by adding inorganic electrolytes into the aqueous solution.

Trace impurities are often deliberately added into crystallization systems in order to obtain the intended crystals with the desired habit, but simultaneously this sometimes leads to critical changes in the solubility of the product. Kubota et al. (1988) indicated that trace amount of chromium (III) (Cr^{3+}) triggers an obvious decrease in the solubility of potassium sulphate (K_2SO_4) in water when dissolving the solute in the solvent at a constant temperature. The decreasing extent of the K_2SO_4 solubility becomes larger along with increasing concentration (up to 150ppm) of Cr^{3+} . This was reasonably explained as the adsorbed Cr^{3+} on the K_2SO_4 crystal surface has suppressed the dissolving process. As a result, this measured “pseudosolubility” is affected by two competing processes, i.e. adsorption of Cr^{3+} and dissolution of K_2SO_4 . In the same publication, it was also reported that the experimentally observed solubility of K_2SO_4 become larger when cooling down an saturated solution from 50 °C to 40 °C in the presence of Cr^{3+} , compared to the solution without Cr^{3+} impurity. Therefore, it is reasonable to believe that sometimes the impurity in solution could suppress the solubility of the solute species and also may inhibit the recrystallization to induce larger “pseudosolubility”. Later, Kubota et al. (1994) reported the active species was not a single ion of Cr^{3+} but hydroxo-chromium(III) complex ions, which could be adsorbed onto the surface of K_2SO_4 crystal by forming hydrogen-bonding with the oxygen atoms of SO_4^{2-} .

Therefore, during practical solubility determinations, the advised measurement method for solubility is to approach from both the under-saturated condition and the over-saturated condition, in other words, determine the solubility line and supersolubility line simultaneously under the solubility of the system.

2.4 Nucleation

2.4.1 Introduction to Nucleation

Crystal growth in its broadest meaning is separated into two distinct processes. First in solution nucleation takes place, leading to formation of crystal nuclei. This is “nucleation”. Secondly the nuclei grow into macroscopic dimensions under supersaturation, which is “crystal growth” in a narrow sense. Therefore, before the review of crystal growth theories, in this section the basic theories of nucleation will be reviewed.

Nucleation sometimes happens spontaneously as the solute itself providing the nuclei, or most of the situations are nucleating on existing solid bodies as crystallization centres, such as dust from air or artificially added crystal seeds. External influences are always the factors to bring about nucleation in solution, e.g. agitation, friction, mechanical shock, spark discharges, and ultrasonic sound. Hunt and Jackson (Hunt and Jackson, 1966) found that the cavitation can cause very high pressure up to 105 bars which lowers the crystallization temperature of the solution, and is able to support some of the above nucleation conditions.

Mullin (Mullin, 1992) presented a simple scheme for nominating the different types of nucleation. “Primary” nucleation is used to describe the nucleation process taking place in a solution clear of any crystalline substance. “Secondary” nucleation is used when crystals are present in the solution being studied, and where nuclei are often induced in the vicinity of the existing crystals. This scheme by Mullin is shown in the figure below.

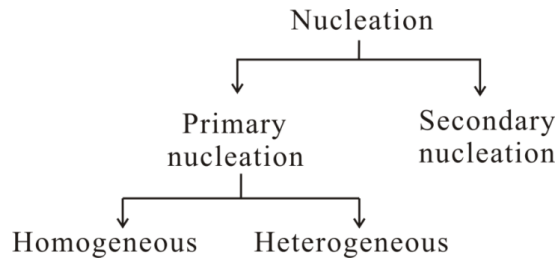


Figure 2.9 An illustration of nucleation classification.

2.4.2 Primary Nucleation

2.4.2.1 Homogeneous nucleation

Nucleation generally occurs with much more difficulty inside a uniform substance by the process of homogeneous nucleation rather than heterogeneous nucleation. Three steps take place during the process. Firstly, supersaturation (the driving force for nucleation) is critical, which can be formed by various methods, e.g. super cooling or evaporation of solvent. Secondly, the formed nuclei need to be sufficiently stable to resist dissolving. Finally all the constituent molecules have to orientate into a fixed lattice.

During the process of nucleation, there is a change in free energy (ΔG) between the liquid and the newly created solid phase. This change in free energy is balanced by the energy gain of creating a new volume and the energy cost due to creation of a new interface. When the overall change in free energy, ΔG is negative, nucleation is favoured (Mullin, 1992; Myerson, 2002). The classical nucleation theory, based on the treatment of condensation of a vapour to a liquid, originated from Volmer (1939) and other researchers. The energy difference associated with homogeneous nucleation can be expressed as below:

$$\Delta G = \Delta G_v + \Delta G_s = \frac{4}{3}\pi r^3 \Delta G_v + 4\pi r^2 \sigma \quad (2.13)$$

where ΔG_v is the volume excess free energy, ΔG_s is the surface excess free energy, ΔG_v is the volume excess free energy per unit volume and σ is the interfacial tension. The right-hand side of Equation 2.13 reveals that the excess free energy of formation possesses a maximum value (Figure 2.10), since the two terms are of opposite sign and relate to r respectively as cube and square.

A newly grown crystal seed in a supersaturated solution can either grow or re-dissolve depending on its size. The critical size r_{crit} , is defined as the minimum size of a stable nucleus. Nuclei of smaller size than this will re-dissolve into the solution, while the bigger ones will continue to grow. In the case of a spherical cluster, at the maximum value of ΔG the mathematic relationship can be expressed as $\frac{d\Delta G}{dr} = 0$, thus:

$$\frac{d\Delta G}{dr} = 8\pi r\gamma + 4\pi r^2 \Delta G_v = 0 \quad (2.14)$$

then a critical size r_{crit} can be obtained by resolving the above equation,

$$r_{crit} = \frac{-2\gamma}{\Delta G_v} \quad (2.15)$$

where ΔG_v is a negative quantity. From Equations 2.13 and 2.15 we have the critical energy ΔG_{crit} as

$$\Delta G_{crit} = \frac{16\pi\gamma^3}{3(\Delta G_v)^2} = \frac{4\pi\gamma r_{crit}^2}{3} \quad (2.16)$$

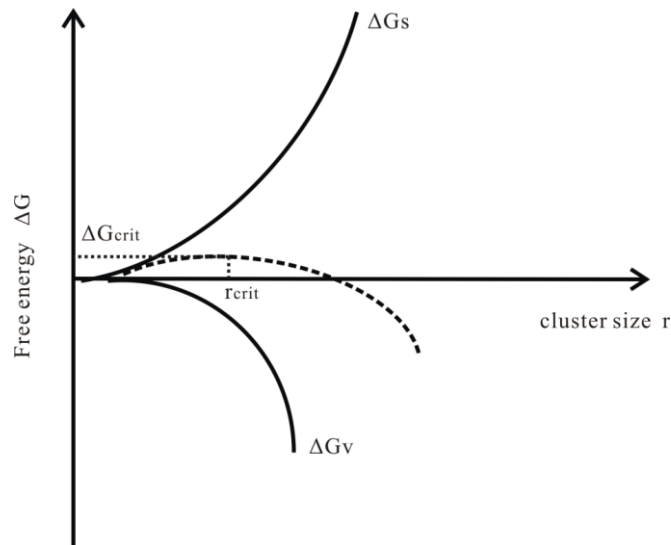


Figure 2.10 Free energy diagram relating to the “critical nucleus” in nucleation. The dashed line represents the summation of ΔG_v and ΔG_s , and it possesses a maximum value which corresponds to the critical size of the nucleus to be stable.

Although supersaturation is the driving force of nucleation, excessive supersaturation does not always aid nucleation, because it is also the driving force for crystal growth. In practice nearly every crystallization system has its own optimum temperature for

nucleation (Figure 2.11), and any situation except the optimum point will decrease the tendency to nucleate (Myerson, 2002).

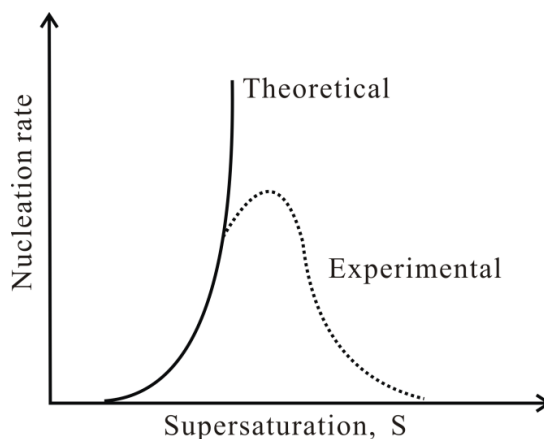


Figure 2.11 Effect of supersaturation on the nucleation rate. The theoretical curve indicates a monotonously increasing curve for the nucleation rate, but the real experimental curve reveals a function similar to Gaussian distribution.

2.4.2.2 *Heterogeneous nucleation*

Under most conditions, heterogeneous nucleation is the main type of nucleation in solutions, in the presence of inescapable solid or other kinds of impurities. Furthermore, one impurity acting as the accelerator in one system may play the role of inhibitor in another system.

Under typical laboratory conditions, aqueous solutions prepared in the normal way always contain various levels of exotic particles which can lead to heterogeneous nucleation. Actually, it is a fact that we can rarely prepare a solution 100 percent free of exotic impurity, what is mostly the perfect requirement in theory and unnecessary for most practical experiments. Besides, deliberate seeding is usually the control method for aiding single crystal growth, controlling product size and size distribution in chemical industries. To induce crystallization the used crystal seeds need not to be consistent with the crystallizing material, since an isomorphous material will also be able to induce crystallization in some cases, e.g. phosphates can often lead arsenate solutions to nucleation, and phenol is effective for m-cresol.(Mullin, 1992) Nevertheless, some other effective substances prompting nucleation of particular

systems are out of the above two conditions and need to be studied by considering other factors. (Liao and Ng, 1990)

Phase boundaries and external impurities will be the preferred places to form heterogeneous nuclei, since this type of nucleation requires lower free energy change than that associated with the formation of a critical nucleus under homogeneous condition. Free energy change under such heterogeneous conditions can be interpreted as:

$$\Delta G_{\text{heterogeneous}} = \Delta G_{\text{homogeneous}} \times f(\theta) \quad (2.17)$$

where θ refers to the contact angle between the crystalline deposit and the solid surface (Figure 2.12), thus $f(\theta)$ is less than unity.

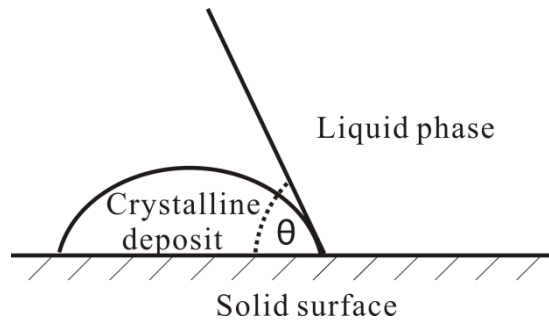


Figure 2.12 Schematic illustration of the angular relationship among the three phases. The contact angle θ between crystalline deposit and solid surface may vary along with the size of the deposit and the surface property of the deposit and the solid surface.

In 1939, Volmer (1939) explored the angular relationship among the solid, the liquid and the depositing compound, and expressed the term $f(\theta)$ as:

$$f(\theta) = \frac{(2 + \cos \theta)(1 - \cos \theta)^2}{4} \quad (2.18)$$

According to this equation, for complete non-affinity solids, $\theta = 180^\circ$, then $f(\theta) = 1$, i.e. the free energy of nucleation is the equivalent to that in homogeneous nucleation. For partial affinity, $0 < \theta < 180^\circ$, the factor $f(\theta)$ equals between 0 and 1, i.e. heterogeneous nucleation is easier to achieve than homogeneous under such situations.

If $\theta = 0^\circ$; it means the seeds are constituted by the same crystal which is going to produce and no nuclei need to form before crystal growth.

2.4.3 Secondary Nucleation

In the solutions under low supersaturation in which nucleation should not happen, existing crystals of the solute could cause an easy nucleation procedure. The crystallographers use secondary nucleation to distinguish this sort of nucleation from primary nucleation.

An early study on secondary nucleation was carried out by Ting and McCabe (1934), and reported that MgSO_4 solution nucleated in a more reproducible manner at relatively moderate supersaturation in the presence of MgSO_4 crystals. Similar investigation on the system of CuSO_4 was carried out by McCabe and Stevens (1951). Gyulai (1948) studied the phenomenon of secondary nucleation with the system of KBr , in which he mentioned that there are some integrated units on the crystal surfaces which can be stripped off by mechanical motion such as solution shearing and these kinds of particles were later proved to be able to act as the crystal seed leading to nucleation by Powers (Powers 1963). After that, many people paid attention to the mechanism of secondary nucleation, Strickland-Constable (1968) even raised several possible mechanisms for it. In his research (Strickland-Constable, 1979), found that the small crystals (which are more exactly recognized as fragments of the parent crystal) caused by collisions or hydrodynamic forces are in a disordered condition, and they are often rather difficult to grow. Another type of force which cannot be ignored is the crystal-agitator contacting force. Although just those crystals near the agitator blade can be affected by this force, it is believed that these kinds of forces are the prime reason for secondary nucleation. The efficiency of the rotator hardness as a function of nucleation rate was studied by Shah et al. (Shah et al., 1973), and the results indicated the harder the impeller is, the higher the nucleation rate.

The initial crystal seed size was one of the interesting topics around crystallization researcher. Mullin (1992) concluded several reasons for the nucleation efficiency related to crystal seed size. He described that the larger crystal seeds can produce

much more second seeds than smaller crystal seeds do, with the fact they get more chance to collide with impellers and will suffer more energy with bigger contact dimension. For the non-grown small crystals, it is because they are flowing within the turbulence eddies where they get no chance to contact with the impellers. The other reason for the crystals under 10 μm is these crystals are too small to grow at a fast rate and can only dissolve caused by their considerably disordered surfaces.

2.5 Crystal Growth

2.5.1 Introduction to Crystal Growth

In a supersaturated solution, once the nucleation stage took place, as discussed in the previous section, the process of crystal growth begins. Nuclei grow larger into macroscopic dimensions by the depositing solute molecules. This process is generally known as “crystal growth”. The process of crystal growth after nucleation dominantly controls the final crystal habit. Many growth mechanisms have been proposed either in an extended way to a deeper level for more complex problems or in a parallel way to explain unsolved problems. These mechanisms are comprehensively reviewed in this section under several headings.

Under most conditions, the process of crystal surface growth involves a typical route (see also Figure 2.13) shown below:

- (i) Bulk transport: solute ions or molecules arrive at the boundary layer surrounding the crystal surface.
- (ii) Diffusion from the boundary layer to the crystal surface caused by concentration gradient.
- (iii) Adsorption onto the surface and partial or total dissolution.
- (iv) Diffusion along the crystal surface to energetically favourable incorporation sites.
- (v) Attachment to surface step and partial or total dissolution.
- (vi) Diffusion along the surface step.
- (vii) Integration into the crystal at a kink or total dissolution.

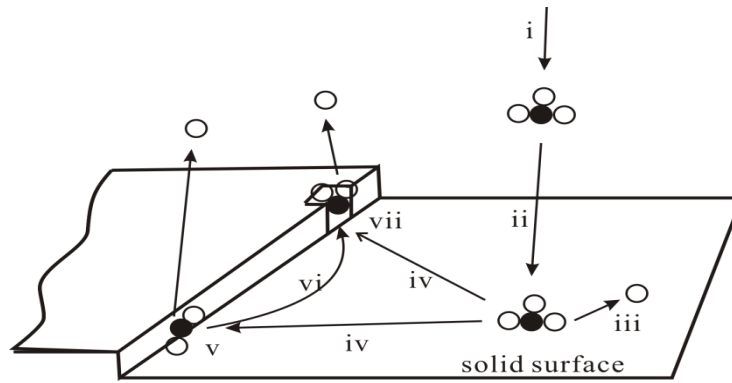


Figure 2.13 Schematic representation of stages involved in crystal growth: diffusion (i, ii, iii, iv, vi), attachment (v), integration (vii) and dissolution (iii, v, vii). (Elwell and Scheel, 1975)

2.5.2 Crystal Growth Theories

2.5.2.1 Surface energy theories

The surface energy theories started from Gibbs in 1878 (Gibbs, 1948) when he analogized the thermodynamical treatment from liquid droplet and reported that, the growth of crystals should always maintain a minimum total surface energy under given temperature and pressure. This simple analogy was later supported by Curie (1885), who proved this criterion by observing final equilibrium shapes of crystals from solution. Wulff (1901) further indicated that, the growth rate of crystal faces are corresponded to their individual surface energies. It is also suggested that the growth rates of different faces are related to the reticular density of different lattice planes, i.e. crystal face with greater reticular density possesses lower surface energy, thus will grow slower than others (Mullin, 1992). However, although the surface energy theories could, to some extent, explain the growth behaviour of crystals, their disadvantage such as not being applicable to the effect of supersaturation on growth rate, are preventing these theories from being widely utilized.

2.5.2.2 *Adsorption layer theories*

Adsorption layer theories have been widely accepted which are based on Volmer's (1939) original postulation that the crystal growth takes place by adsorbed layers of solute onto the growing surface. Many other studies (Kossel, 1934; Frank, 1949; Burton et al., 1951) further contributed to modification of Volmer's theory, by raising new ideas to solve more practical issues.

c) 2-D nucleation model

Volmer (1939) indicated that any crystallizing particles are two-dimensionally free to move on the surface of the crystal after arriving and losing some latent heat, but not immediately integrating into the crystal lattice. This rule is applicable to a large number of particles on the surface, and they can be considered to have built up an adsorbed layer between the crystal surface and the original solution. The thickness of the adsorbed layer is assumed to be about 1nm to 10nm.

Adsorbed molecules (or atoms) in the free layer will tend to migrate towards the most attractive position, i.e. where there are the maximum number of similar molecules, and link to other molecules at that location (Figure 2.14a). Ideally without interrupting factors, this adsorption-migration behaviour will continue, until a full surface plane is completed (Figure 2.14b). Before a new surface plane can be grown, it is necessary to construct another "attractive position". Thus, a monolayer nucleus of a reasonable size should form on the top of a previously grown plane (Figure 2.14c). The free energy change associated with the formation of the monolayer nucleus can be derived according to the manner used in homogeneous three-dimensional nucleation, although the energy here is essentially lower than that for three-dimensional nucleation.

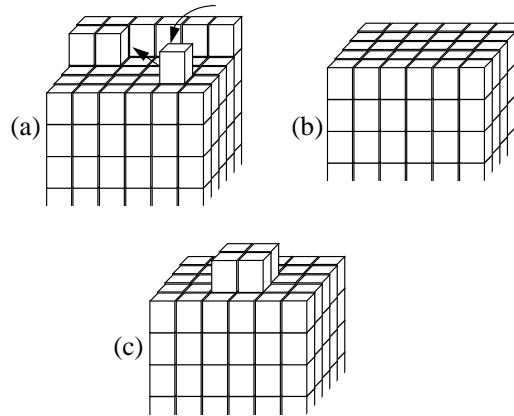


Figure 2.14 A mode of crystal growth without dislocations: (a) migration towards desired location, (b) completed layer and (c) surface nucleation.

d) *Kossel's model*

Kossel (Kossel 1934) raised a crystal surface model (Figure 2.15) by dividing the surface vacancies into several types. The growing layer on the surface is assumed to be a monatomic layer containing various types of positions which are suitable for atoms to integrate into or not. In addition, the newly adsorbed units on the crystal surface are free to move, but usually the preferable location is where the units could lose more degree of freedom. As a result, the kink sites are more preferred than step sites, while the surface sites are least admired. This growth manner makes the kink vacancy moving along the step and eventually the surface plane is completed. A new step should then be established probably by two-dimensional nucleation, inducing the growth of the next plane.

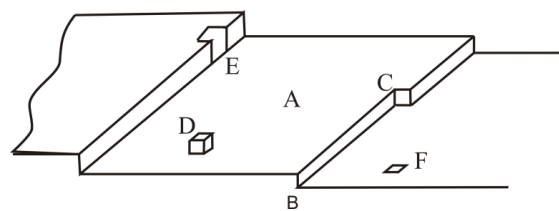


Figure 2.15 The schematic illustration of Kossel's Model of a growing crystal surface. (A) flat surface, (B) step between two faces, (C) kink site, (D) adsorbed unit, (E) edge vacancies, (F) surface vacancies.

e) *Spiral growth model*

Although Kossel's model explains well the formation of growing crystal surfaces, in practical application its limitations became apparent. The formation of a new step in Kossel's model largely depends on the surface nucleation rate, furthermore, related to the supersaturation. Therefore, under relatively low supersaturation, the driving force will be insufficient to create nucleus for a new step. However, Volmer and Schultz (1931) reported that the growth of iodine in vapour under 1 percent supersaturation was continuous with a fairly fast rate compared to predicted value.

Frank (1949) postulated the theory of spiral growth to improve Kossel's theory, which accounts for the fast growth under low supersaturation. Since there is rarely a perfect crystal without any dislocations during growth, he indicated that these existing screw dislocations have reduced the requirement of two-dimensional surface nucleation by providing favourable locations, like kink sites and step sites, for the solute molecules to integrate into (Figure 2.16). Once such a screw dislocation appeared, the crystal surface will grow continuously following an "upward spiral staircase" (Figure 2.16).

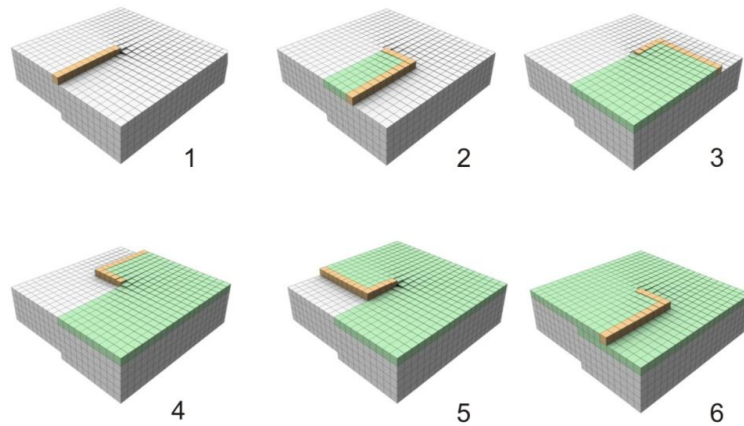


Figure 2.16 Schematic illustration of the development of crystal growth on a screw dislocation (Elwell and Scheel, 1975).

As the spiral step sites never vanish from the growing surfaces, the growth will continue at a theoretically maximum rate under given supersaturation. Burton, Cabrera and Frank (1951) developed an important kinetic theory (BCF theory), by which they were able to predict kink populations and estimate growth rate at given supersaturation. The BCF calculation can be expressed as

$$R = A\sigma^2 \tanh\left(\frac{B}{\Delta c}\right) \quad (2.19)$$

where R is the growth rate, A and B are variable constants depending on temperature and Δc is the supersaturation.

Besides qualitative analysis, it is worth noticing that the BCF theory was based on growth from vapour phase. When solving questions for crystal growth from solutions, it is difficult to resolve the relationship quantitatively due to many complex factors in the systems. For example, viscosity in solution is normally higher than that in vapour (ca. 10^{-3} Ns/m² \gg 10^{-5} Ns/m²), resulting in a much lower coefficient of volume diffusion (ca. 10^{-8} cm/s \ll 10^{-5} cm/s). In addition, the relationship between solute concentration and diffusion can be complicated, not to mention the mysterious surface diffusion in the adsorbed near-surface layer. Further reviews on understanding various surface-bulk diffusion conditions should refer to Bennema (1968; 1984) and Chernov (1984; 1993).

2.5.2.3 *Rough surface, continuous growth*

The growing crystal surfaces are possibly of a rough nature at molecular level, where growth units adsorbed on the surface are expected to incorporate into the growing surface with not much resistance. Since a large amount of growth units are easily adsorbed and incorporated into the surface, this rough surface growth model provides a faster growth rate compared to the adsorption layer growth models, e.g. 2-D nucleation model and spiral growth model.

The term of α factor was developed by Jackson (1975) to describe the nature of a crystal surface, which can be expressed as:

$$\alpha = \frac{\xi \Delta H}{RT} \quad (2.20)$$

where ξ is an anisotropy factor, ΔH is the enthalpy change upon crystal growth, R is the ideal gas constant and T is temperature. Thus, the α factor depends on the anisotropy factor and the entropy change. The former is mainly related to the number of neighbouring sites on the growing surface, and the latter mostly intrinsically depends on the growing species. Three types of growing surface nature, related respectively to three growth mechanisms, have been defined upon the value of α factor. If α is less than 2, the growing surface is expected to be rough at molecular

level and likely the growth is dominated by continuous growth mechanism. If α is larger than 5, the growing surface will be considered as molecularly flat, upon which the spiral growth around existing dislocations will contribute largely for the growth. If α is in between 2 and 5, the 2-D nucleation mechanism will likely dominate the growth. Nevertheless, there could exist a critical temperature for crystals consisting of a flat growing surface, above which a smooth surface will transit into rough nature (Onsager, 1944). This roughing temperature is closely related to the strength of intermolecular bonding.

2.5.2.4 *The diffusion theories*

Noyes and Whitney (1897) and Nernst (1904) developed the diffusion theory for interpreting crystal growth which are dominated by local diffusion, by assuming concentration gradient layers are formed near the growing surface and the growth process is reversed dissolution process. The corresponding expression is:

$$\frac{dx}{dt} = \frac{DS_s}{L}(C_2 - C_0) \quad (2.21)$$

where x (g/m^2) is the amount of depositing solute onto the crystal surface in time t (s), D (s^{-1}) is the diffusion coefficient of the solute, S_s (m^2) is the surface dimension of crystal, and L (m) is the thickness of the diffusion layer, C_0 (g/L) and C_2 (g/L) are the saturation concentration and real concentration of the corresponding solution.

However, the thickness of the diffusion layer greatly depends on the relative solid-liquid velocity which is solely linked with the agitation condition in the system. Although in stagnant aqueous solutions the above theory could work since layer thickness is nearly homogeneously distributed, Marc (1910) found that the layer thickness drops rapidly to virtually zero in vigorously stirred solution. Furthermore, the hypothesis of crystallization as reversed dissolution is not necessarily acceptable.

Miers (1904) explored the solution concentration in contact with the growing crystal, and found that the solution is supersaturated, not only saturated. Based on this finding, a further modification on diffusion theory was made by Berthoud (1912) and Valetton (1924), by dividing the growth process into two stages, i.e. diffusion of solute molecules from the solution to the solid surface and arrangement of molecules into a crystal lattice. These two steps can be presented as:

$$\frac{dx}{dt} = k_d S_s (C_i - C_0) \quad (2.22)$$

$$\text{and} \quad \frac{dx}{dt} = k_r S_s (C_2 - C_i) \quad (2.23)$$

where k_d is the coefficient of mass transfer during diffusion, k_r is a constant rate representing the process of arranging molecules into an oriented lattice, C_i is the intermediate solute concentration at the interface between the solution and the growing crystal.

However, in crystal growth, the diffusion theory still cannot be used easily, since accurate evaluation of involved parameters (e.g. k_d and k_r) remains obscure and the layer concentrations always vary at different points close to the crystal surface (Miers, 1927), normally the concentration is higher at the sharp corners of the external morphology than that at the centre of surfaces (Berg, 1938).

2.6 Characterization of Impurity Doped Single Crystal

2.6.1 Characterization of Defect Structure by X-Ray Topography

2.6.1.1 Introduction to X-ray topography

After the discovery of X-ray and X-ray diffraction imaging around 1900, the utilization of X-ray diffraction topography on crystal structure characterization has developed rapidly during the last century. It is an X-ray imaging technique based on Bragg diffraction and the aim of this kind of technique is to provide pictures of the distribution of defects within a bulk crystal. X-ray film papers are used to record the diffracted X-ray beam by the crystal, thus representing a two-dimensional spatial intensity map of reflected X-rays. Topographers could then observe the distribution of scattering power inside the crystal and the irregularities in a non-ideal crystal. Therefore, topography can be used for visualizing defect structure in many different crystalline materials and monitoring crystal quality, especially to observe the growth history when developing a new crystal growth system.

X-ray topography has already been successfully applied to many cases, in order to

study the dislocations as well as growth mechanisms by revealing the defects in a crystal. For example, this technique has been used to explore the directions of dislocation lines in ammonium hydrogen oxalate (Klapper et al., 1973), to reveal the dislocation configuration and crystal growth mechanism of KDP (Lai, 1998), to study the twinning phenomenon in KLiSO_4 by revealing growth sector boundaries and dislocations (Klapper et al., 1987), to explore the dislocation configuration in self-nucleated NaClO_3 crystals (Hooper et al., 1983), etc.

2.6.1.2 Basic principle and theory

The working process of diffraction topography could be demonstrated in an easy way as follows: an incident spatially extended X-ray beam is diffracted by the sample in a specific direction, and finally arrives at the film paper. There will be a strong diffracted beam from the crystalline material when the situation satisfies Bragg's Law shown below:

$$n\lambda = 2d \sin \theta \quad (2.24)$$

where n is an integer representing the order of diffraction, λ is the wavelength of incident X-ray beam, d is the interplanar space between atomic planes, and θ is the incident angle between the incident beam and the diffracting planes. Thus, when there are defects in the crystal leading to distortion of lattice spacing or lattice plane, the above Bragg relation is not applicable to both the perfect and distorted regions. Consequently, the recorded image (namely the *topograph*) from the topographic instrument can show this to the observer for further analysis.

The X-ray topography utilizes the contrasts on the recorded image to reveal the defects in a crystal. A homogeneous sample would yield a homogeneous intensity distribution in the recorded topograph. Intensity modulations (contrasts) arise from irregularities in the crystal lattice which could originate from various kinds of defects.

2.6.1.3 Absorption of X-rays

X-rays will be absorbed when going through the atomic positions in substances and meanwhile release photoelectrons which could be influential in determining the image type obtained in XRT. Thus, a term combination should be defined to express this, μt , where μ is the total linear X-ray absorption coefficient and t the sample thickness. Then μ is expressed as follows:

$$\mu = \frac{n}{V_C} \sum_i (\mu_a)_i \quad (2.25)$$

where n is the quantity of molecules per unit cell, and V_C is the volume of each unit cell and $(\mu_a)_i$ the atomic absorption coefficient of specific atomic site, i.e. this depends on the atom and the X-ray wavelength.

2.6.1.4 Topographic resolution

The topographic resolution achievable in topographic images can be limited by one or more of three factors: the resolution of the recording film, the experimental geometry and instrumental effects (Tanner, 1976).

f) Vertical Resolution

In the method of Lang's camera which was employed in this study, the diffraction planes are vertically parallel in the crystals, thus there is no diffraction in the vertical plane. The resolution δ recorded on the film can be expressed as:

$$\delta = LV / D \quad (2.26)$$

where L is the specimen-film distance, D is the source-specimen distance and V is the projected height of the source (Figure 2.17). In practical experiments, it is really difficult to set the distance between the specimen and the plate to below 1 cm, as a result when one substitutes a typical value, a resolution of the order of a few microns is obtained. Despite all that, the specimen-film distance should always be kept as small as possible to enhance vertical resolution.

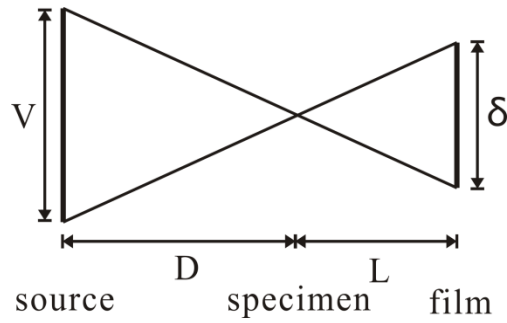


Figure 2.17 Schematic illustration of the criteria for vertical resolution. The beam source, specimen and film are arranged horizontally, with distance between them as indicated.

g) Horizontal Resolution

The divergence of the diffracted X-ray beam is not so important in effecting the resolution, since the value is very small in the horizontal direction. There are mainly three factors which may have serious influence on the resolution, including the instrumental vibration between specimen and film, simultaneous diffraction of both the $K\alpha$ lines, and the fundamental width of the dislocation image determined by the diffraction planes chosen.

First, due to the X-ray topography experiment by Lang's camera set up, it is vital to ensure the specimen and the film used for recording image are not moving towards each other. The necessary design to minimize mechanical vibration caused by the motor, which drives the specimen stage and the film holder for back and forth movement, is to utilize high quality motor and to adjust and grease the gears linking the rotation axis and the motor.

Second, the applied radiation from molybdenum X-ray tube inevitably possesses dual $K\alpha$ lines of $K\alpha_1$ and $K\alpha_2$ as well as spectral width for each line. The spectral width is generally small but still causes, to some extent, a loss of image resolution. Differentiation of Bragg's relation (Equation 2.24) indicates that the spread of Bragg angle $\Delta\theta_B$ is related to the spread of wavelength $\Delta\lambda$ as follows:

$$\Delta\theta_B = \tan\theta_B \frac{\Delta\lambda}{\lambda} \quad (2.27)$$

where θ_B is the Bragg angle for diffraction, λ is the wavelength of the X-ray beam. From this it can be seen that the spectral dispersion will result in approximately several microns shift of the image on the film. Similarly, the wavelength variation between the dual $K\alpha$ lines ($\Delta\lambda_{\alpha_1\alpha_2} \sim 4.3 \times 10^{-3}$) will introduce ~ 10 microns shift (Tanner, 1976). The contributions from these two factors are relatively small and would not be of much detriment to the results.

Third, since the topographic image is formed by lattice misorientation and the misorientation varies roughly against r^{-1} around a dislocation line, as a result the narrower the diffraction angle range is, the further from the dislocation line it will appear as misoriented. High order, weak reflections are related to narrow diffraction angle ranges, hence leading them to be of high sensitivity to lattice misorientation. As a result, the relatively higher order diffractions will produce wider dislocation images. Therefore, in order to obtain maximum spatial resolution, *strong low order reflections* are preferred. The half width of the reflection angle range $\Delta\theta_{1/2}$ can be expressed as:

$$\Delta\theta_{1/2} = 2dC\lambda|F|/\pi gV \cdot \cos\theta_B \quad (2.28)$$

where d is the interplanar distance, C is the polarisation factor of the beam, λ is the wavelength of X-ray, F is the structure factor of the reflecting plane, g is the diffraction vector of the specific plane, V is the volume of unit cell and θ_B is the Bragg angle. From Equation 2.28 it can be seen, the $\Delta\theta_{1/2}$ is proportional to wavelength. In experiments using Lang's camera, for obtaining optimum resolution, long wavelength (wide image width) is used together with low order strong reflections.

2.6.1.5 Contrast of topographs

Information from an X-ray topographic image is observed in the reorganization of topographic contrast. Under the experimental conditions using Lang's camera running on a laboratory X-ray source, the divergence of the beam is typically 100 seconds of arc, which is much wider than the diffraction range of a perfect inorganic crystal. As a result, when a uniform crystal is illuminated by a homogeneous X-ray beam, a large part of the beam penetrated straight through the crystal while a smaller part of the beam was diffracted by the crystal planes and arrived at the film. The topographic

image of this uniform crystal will show no contrast. However, it is typical that the distorted regions around defects (e.g. dislocations and imperfect growth sector boundaries) in the crystal are satisfying the Bragg law for certain parts of the penetrated beam and thus contribute to the intensity of diffracted beam arriving at the film. As a result, the image for the defective region will present as a darker area on the film. Therefore, characterization by X-ray topography relies heavily on the strains caused by all kinds of lattice distortion, and can be easily applied to reveal the presence of inclusions, growth sector boundaries and grown in dislocations for crystals (Tanner, 1976).

One of the concerns of this study is to identify the character of different dislocations in various growth sectors. There are three types of dislocations, i.e. pure screw dislocation, pure edge dislocation and mixed dislocation, with different characters. The characters of dislocations is represented by their Burgers vector \underline{b} and line direction \underline{l} , where \underline{b} represents the magnitude and direction of lattice distortion at a crystal lattice and line direction indicates the specific orientation of the dislocation line within a crystal (Hull and Bacon, 2001). Standard Burgers vector analysis for the determination of Burgers vector direction and character, has been readily established with the aid of *visibility rules* (Tanner, 1976). Invisibility on the topographic image occurs for screw dislocations when $\underline{g} \cdot \underline{b} = 0$, for edge dislocation when $\underline{g} \cdot \underline{b} = 0$ and also $\underline{g} \cdot \underline{b} \times \underline{l} = 0$ (where \underline{g} is the diffraction vector). Besides, the dislocations with mixed characters normally present contrast under either condition.

Pure screw dislocations (Figure 2.18a) possess Burgers vector \underline{b} parallel to the growth line direction \underline{l} of the dislocation. The distortion caused by screw dislocation is thus parallel to the line direction \underline{l} . Therefore, the lattice planes parallel to the Burgers vector \underline{b} are not distorted, and will not show contrast for the dislocation if these planes are used as diffraction planes. The diffraction vector \underline{g} of these planes is perpendicular to Burgers vector \underline{b} , which is consistent with the invisibility rule mentioned above for screw dislocation, i.e. $\underline{g} \cdot \underline{b} = 0$.

Pure edge dislocations (Figure 2.18b) possess Burgers vector \underline{b} perpendicular to the growth line direction \underline{l} , and the distortion happens in two directions including parallel to the Burgers vector and normal to the slip plane. Thus, the undistorted planes which will give no contrast to the edge dislocation are those perpendicular to the dislocation

line direction. Consequently, the more strict condition for edge dislocation to be invisible on a topograph is $\mathbf{g} \cdot \mathbf{b} = \mathbf{0}$ and also $\mathbf{g} \cdot \mathbf{b} \times \mathbf{l} = \mathbf{0}$, which defines the diffraction planes to be only in the direction perpendicular to the dislocation line.

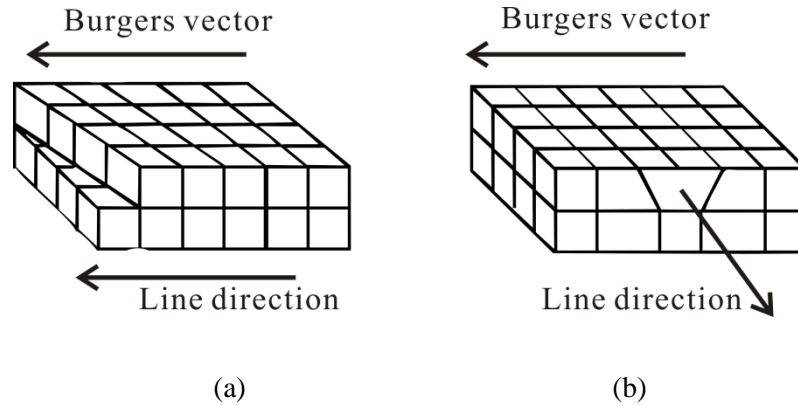


Figure 2.18 Schematic illustration of the directions of Burgers vector and dislocation line for screw dislocation (a) and edge dislocation (b).

2.6.2 Synchrotron X-Ray Radiation

Synchrotron radiation is generated by ultra-relativistic charged particles which are travelling at nearly the speed of light through magnetic fields in a designed storage ring. At synchrotron the radiation produces the entire electromagnetic spectrum, from radio waves, infra red light to X-ray and gamma rays.

As an extensively used technique, the synchrotron radiation provides high quality light applied to various characterization methods. The beams have better properties than common light sources:

- The spectrum of synchrotron radiation is continuous (i.e. *tuneable in energy/wavelength*) and has a wide range, from infra red light, visible light to hard X-ray. This enables different applications to be carried out at synchrotron stations using different radiation beams.
- High resolution according to *low beam divergence*, which enables the detection of lattice defects in crystalline material. For example, the values of vertical and horizontal divergence at Diamond Synchrotron are 0.001° and 0.006° , respectively.
- *High beam intensity* (also named flux) (about $10^3 - 10^6$ times of general X-ray light sources) which allows faster and better data collection in various of

applications and also makes it possible to detect low concentration elements such as the impurity used in this project

The main components of a typical synchrotron machine are shown below:

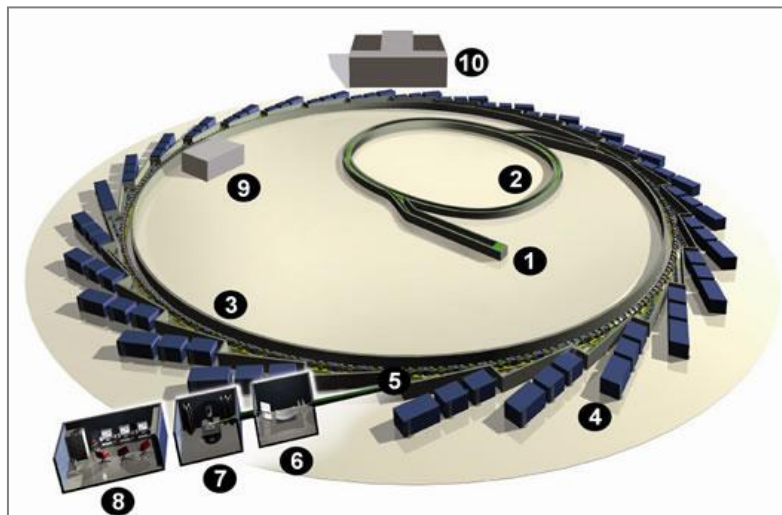


Figure 2.19 The brief structure of a synchrotron machine. 1: Injection system - the electron gun and the Linac; 2: Booster Synchrotron; 3: Storage Ring, consisting of a certain number of magnetic sections used for curving the electron beam; 4: beamline stations (composed of 5,6,7,8); 5: front ends, connected to the storage ring at a tangent; 6: optics hutch; 7: experimental hutch; 8: control cabin; 9: Radiofrequency (RF) Cavity; 10: main control office to the synchrotron. (Source: www.diamond.ac.uk)

2.6.3 Micro-crystallography by X-Ray Multiple-wave Diffraction

2.6.3.1 Introduction to X-Ray Multiple-wave Diffraction

X-Ray Multiple-wave Diffraction (XRMD) occurs when two or more sets of atomic planes in the crystal simultaneously satisfy the diffraction condition (Equation 2.24) to diffract the incident beam. The common Bragg diffraction is simply a two-beam case occurring on one set of planes, where only the incident beam and diffracted beam are concerned. Differing from that, the multiple-wave diffraction condition involves more beams simultaneously participating in the diffraction behaviour, requiring very strict conditions and thus is highly sensitive to small lattice distortions within the

crystal. It is commonly accepted that the lattice parameter can be measured by XRMD at an accuracy of 1×10^{-4} Å using the 3-beam case on germanium crystal and 5×10^{-5} Å using 4-beam cases on diamond crystal (Post, 1975; Lonsdale, 1947). XRMD has already been applied successfully to determine the lattice parameter change and crystal perfection for KDP crystals doped by various concentrations of Mn^{3+} ion, as well as to explore the impurity incorporation mechanism during the process (Lai et al., 2003; Remedios et al., 2010). This technique was also employed to investigate the changes in crystal lattices under an applied electric field of varying strength, by monitoring the diffraction peak positions in the Renninger Scan mode which was controlled to be solely related to lattice parameter (Avanci et al., 2000). In Se^+ ion implanted material of GaAs, XRMD acted as a method to discriminate mosaic and nearly perfect crystals by revealing the strain perpendicular and parallel to the surface (Morelhão and Cardoso, 1996; Hayashi et al., 1997).

2.6.3.2 Renninger mode

There are typically two modes used in practical measurement of X-ray multiple-wave diffraction (XRMD), i.e. the Renninger mode (Renninger, 1937) and pseudo-Kossel mode (Kossel, 1936). The former mode is applied in the current study thus will be reviewed here, while for the latter one readers could turn to other literatures.

In the Renninger mode of XRMD experiment, the crystal surface is first aligned for Bragg diffraction on the primary planes with reflection vector (h_p, k_p, l_p) and the intensity of the diffracted beam is monitored during the rotation (angle ϕ) around the primary reciprocal lattice vector (Figure 2.20). During the rotation of ϕ by maintaining the primary diffraction, other planes named secondary (h_s, k_s, l_s) and coupling (h_c, k_c, l_c) which are inclined with respect to the sample surface would both enter the diffraction condition. The diffraction geometry between these planes can be expressed as below (cf. Figure 2.20):

$$\vec{H}_p = \vec{H}_s + \vec{H}_c \quad (2.29)$$

Therefore, it is easy to see that the combination of secondary and coupling planes together could diffract the incident X-ray towards the same direction as that by the primary diffraction. As a result, the interaction between the primary reflection and the secondary reflection is established.

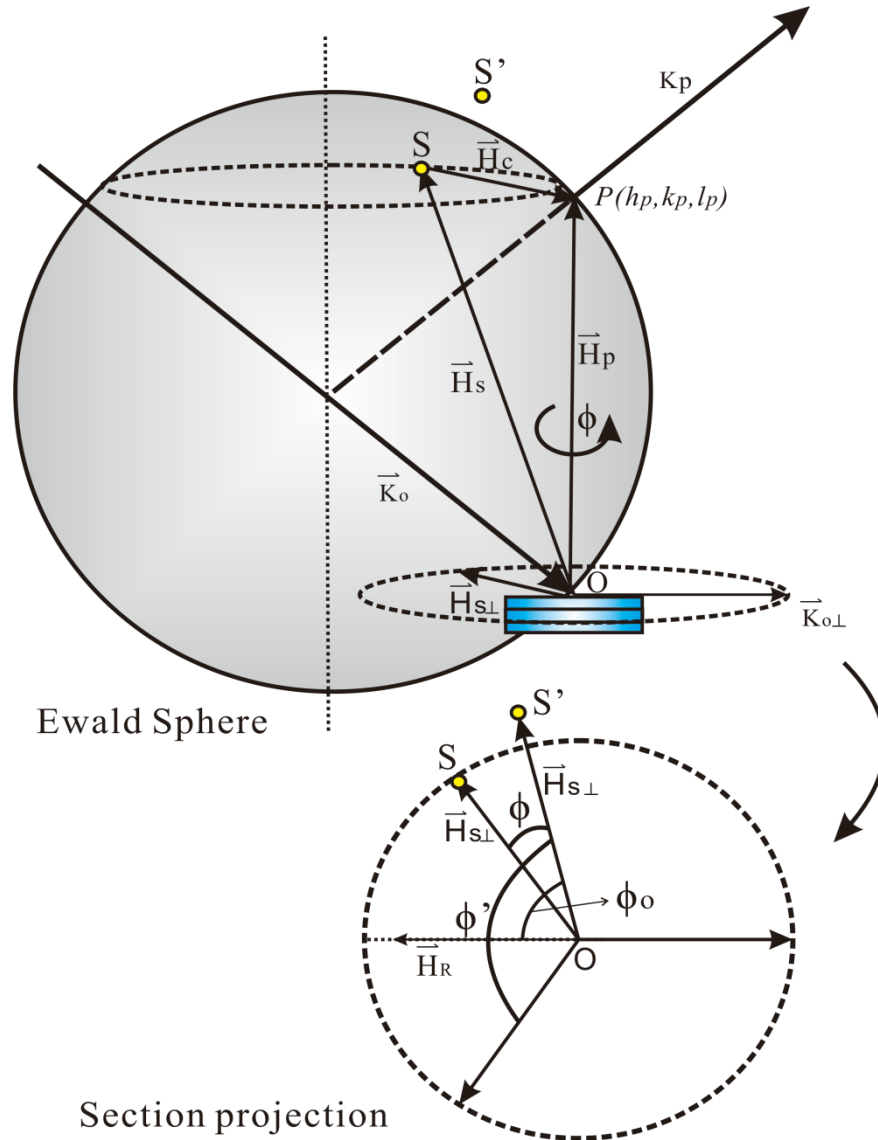


Figure 2.20 (a) Geometry of X-ray multiple-diffraction in reciprocal space using a three-beam case as example. (b) Section projection view for the indicated part. In the figures, \bar{H}_p is the reciprocal lattice vector of the primary plane, \bar{H}_s is the reciprocal lattice vector of the secondary plane, \bar{H}_c is the reciprocal lattice vector of the coupling plane, \bar{K}_o is the wavevector of the incident beam, \bar{H}_R is the reciprocal lattice vector of the primary plane.

In the pattern of *Intensity* versus ϕ , called Renninger Scan (RS) (Renninger, 1937), secondary peaks with positive (umweganregung) and negative (aufhellung) profiles can appear distributed according to the symmetry of the primary vector, representing the energy transfer from the secondary to (positive peak) or vice versa (negative peak) the primary reflection, and also considering the symmetry plane established by the ϕ rotation when the secondary reciprocal lattice points enter and leave the Ewald sphere (Figure 2.21). One can clearly observe in a RS these two types of symmetry mirrors whose position and intensity distributions are essential for most of the applications of this technique. When a peak in the RS represents an interaction of the incident, primary and only one secondary beam, it shows up as a three-beam peak which is named “three-beam case”, for example the peak indexed (202) in Figure 2.21 is actually representing the three-beam case of (000)(004)(202). Moreover, at the same peak position it can have two or more secondary beams interacting simultaneously, i.e. N-beam case (Figure 2.21).

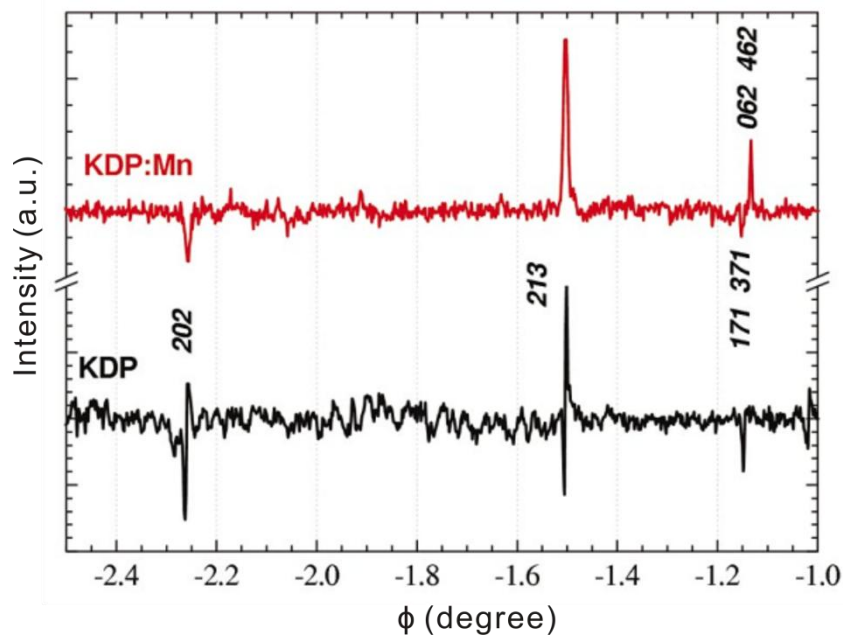


Figure 2.21 An example Renninger Scan pattern using 004 primary reflection, showing different peaks with their index numbers. The positive peaks are of umweganregung character and the negative ones are of aufhellung character. Those peaks indexed with one number are three-beam cases, and the peaks with index composed of two numbers are four-beam cases. (Lai et al., 2003)

2.6.3.3 Bragg surface diffraction (BSD)

A type of special three-beam case in X-ray multiple-wave diffraction named Bragg-surface diffraction (BSD) (Morelhão and Cardoso, 1993), occurs under adequate diffraction geometry, where the secondary diffracted beam propagates in the direction parallel to the crystal surface. A schematic illustration showing the multiple-wave diffraction for a BSD case inside a crystal is shown in Figure 2.22, where \vec{H}_p is the diffraction vector of the primary plane, \vec{H}_s is the diffraction vector of the secondary plane, and \vec{H}_c is the diffraction vector of the coupling plane. The BSD beams are quite sensitive to the surface properties, thus can reveal information on the sample surface which is useful for studying surface impurity incorporation effects (Lai et al., 2003), or even on the interface (layer/substrate), if such an interface is present, as in the semi-conductor epitaxial structures (Avanci et al., 1998). In short, the technique is feasible to provide significant information when successfully applied as a special high-resolution 3D probe for the study of crystal structure in the layers close to the sample surface.

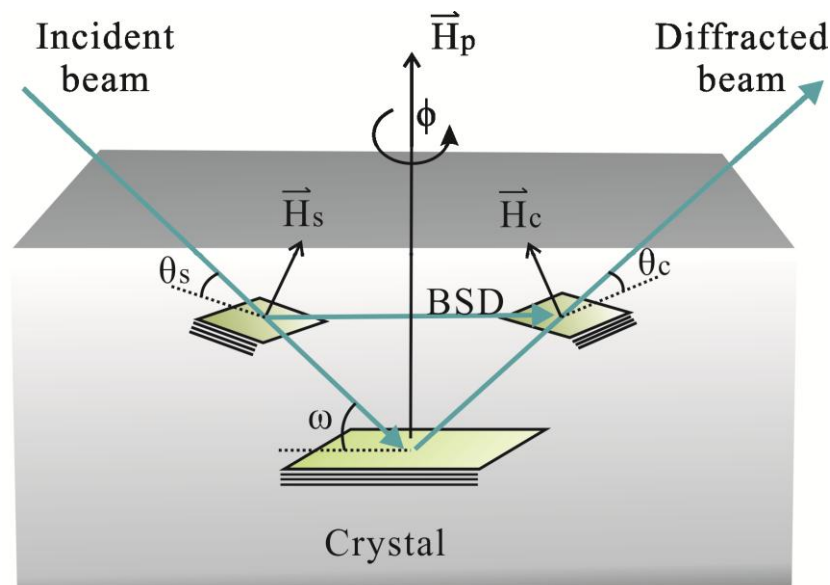


Figure 2.22 Schematic representation for the beam propagation paths of a typical three-beam case under X-ray multiple-wave diffraction in real crystal space.

2.6.3.4 Peak position

The angular positions of either positive peaks (intensive increase) or negative dips (intensity decrease) in a Renninger Scan pattern can most commonly be indexed by defining a reference-vector as zero point (Cole et al., 1962). As the diffraction geometry has been shown in Figure 2.20, it can be seen that during the rotation of ϕ , the secondary reciprocal lattice point S will enter and then leave the Ewald sphere. As a result, there are two ϕ positions for such a secondary plane to satisfy multiple-wave diffraction, at which point S is entering and leaving the sphere. These positions can be denoted by “IN” and “OUT”. In the projection pattern shown in Figure 2.20, the dotted line through O represents the incidence plane of the primary diffraction. The plane is symmetrically in the middle of the “IN” and “OUT” positions. There are two components of \overline{H}_S , i.e. $\overline{H}_{S\perp}$ and $\overline{H}_{S\parallel}$ which are normal and parallel to the primary diffraction vector \overline{H}_p , respectively. We suppose that, during the rotation of ϕ , initially the secondary plane was not on the Ewald sphere. The projection view of this initial position is S', with its corresponding component in the projection plane as $\overline{H}_{S'\perp}$. The reference unit vector \overline{H}_R is preferably defined as lying in the incidence plane of the primary diffraction and normal to \overline{H}_p . In order to bring the secondary plane from S' to S, the crystal will be rotated by an angle of ϕ degrees around \overline{H}_p . Therefore, from the geometry shown in Figure 2.20, the angle ϕ_0 between $\overline{H}_{S'\perp}$ and \overline{H}_R and β between $\overline{H}_{S\perp}$ and \overline{H}_R can be expressed as:

$$\phi_0 = \arccos(\overline{H}_{S'\perp}, \overline{H}_R) \quad (2.30)$$

$$\beta = \arccos(\overline{H}_{S\perp}, \overline{H}_R) \quad (2.31)$$

where the \overline{H}_R is:

$$\overline{H}_R = \frac{\overline{K}_o + \frac{\overline{H}_p}{2}}{\left| \overline{K}_o + \frac{\overline{H}_p}{2} \right|} \quad (2.32)$$

\bar{K}_o represents the wavevector of the incident beam. Thus, the ϕ angle for the “IN” and “OUT” positions is geometrically coincident to the reference vector, i.e.

$$\phi = \phi_0 \pm \beta \quad (2.33)$$

From Equations 2.30, 2.31 and 2.32, the peak position of a secondary reflection can be calculated as:

$$\cos(\beta) = \frac{1}{2} \frac{(H_S^2 - \vec{H}_S \cdot \vec{H}_P)}{\sqrt{\frac{1}{\lambda^2} - \frac{H_P^2}{4}} \sqrt{H_S^2 - H_{S\parallel}^2}} \quad (2.34)$$

The symmetric appearance of secondary peaks in the Renninger Scan (RS) pattern also depends on the crystallographic symmetry of the rotation axis. For example, the crystallographic rotation axes of two- and three-fold, are corresponding to four- and six-fold mirror symmetry in the RS pattern.

2.6.4 Determination of the Local Structure of the Impurity by X-ray

Absorption Fine Structure

X-ray absorption fine structure (XAFS) reveals the details of how X-rays are absorbed by the atoms of interest, by tuning the energy of illuminating X-rays near and above the selected core-level energies of the target atom species. The peaks and oscillations in the spectrum are closely related to the chemical and physical state of the target atom. As a result, XAFS is capable of identifying the formal oxidation state and coordination chemistry, probing electronic structure, bond length, angle, coordination numbers and species of neighbouring atoms. Because of its feasibility, XAFS is being widely applied in determining the chemical state and local atomic structure for selected atom species in crystalline or non-crystalline systems. Since XAFS is typically measured at one selected absorption edge of the target atom, it is often referred to as element-specific. Synchrotron XAFS has been applied to many cases for determining the local environment of different elements, for example, to study the chemical bonding of different sulphur compounds (Sekiyama et al., 1986), to explore and verify the electronic structure and molecular orientation of $S_2O_3^{2-}$ and

$S_2O_6^{2-}$ in the ionic crystals (Tyson et al., 1989), to determine the orientation of Mn-O and Mn-N bonds in complex compounds (Yano et al., 2007).

2.6.4.1 Brief principles

X-ray absorption fine structure (XAFS) concerns deriving fine structure from the X-ray absorption profile. The interaction between matter and X-rays (below 10keV) is mostly photo-ionization, in which X-ray photons are absorbed by an atom and excite an electron of the atom into a bound or quasi-bound state. The measured absorption coefficient within a certain energy region decreases as a oscillating curve (Figure 2.23), as the increasing energy of incident X-ray. The sharp jumps are referred to as absorption-edges and correspond to the individual threshold energies of related photoelectron transitions from core orbital to the lowest unoccupied orbital above the valence band. The available transitions are restricted by *dipole selection rules*, i.e. $\Delta L = \pm 1$, $\Delta J = 0$ or ± 1 , where ΔL and ΔJ are changed in total orbital angular momentum (L) and grand total angular momentum (J).

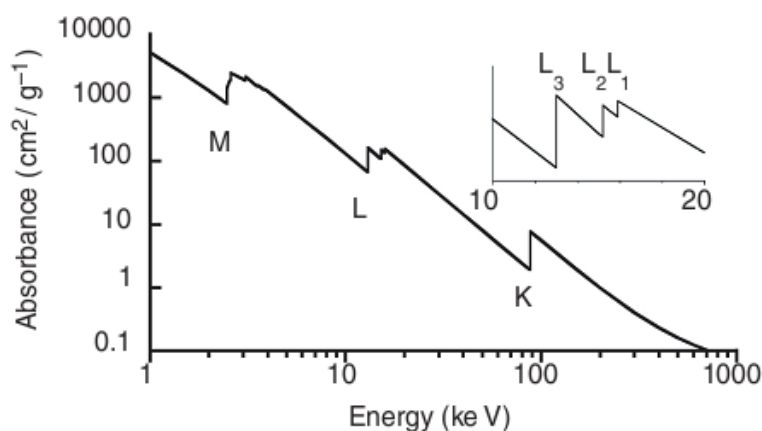


Figure 2.23 X-ray absorption spectrum for Pb, covering three edges which are K, L and M. The electron transitions at three edges are corresponding to excitations from the 1st, 2nd and 3rd shell, respectively. (Bunker, 2010)

A typical X-ray absorption spectrum could be divided into three regions according to different energy ranges which correspond to different physical mechanisms, i.e. Pre-edge, X-ray Absorption Near Edge Structure (XANES) and Extended X-ray Absorption Fine Structure (EXAFS). It is obscure to rigidly separate the XANES and EXAFS regions although efforts have been made and applicable for most cases

(Koningsberger and Prins, 1988). For certain times, XANES is also referred to as Near Edge X-ray Absorption Fine Structure (NEXAFS) in the study of low-Z molecules ($Z \leq 9$). Besides, the XAFS of low-Z species decay dramatically beyond the edge, leading to the practical difficulties of exploring information for light elements like sulphur (Bunker, 2010). Figure 2.24 shows the three energy regions as follows:

- Pre-edge is the region of up to ca. 20 eV below the absorption edge. For different absorbing atoms, none, one or more peaks may appear, representing the electronic transition from the core level into unfilled or half-filled bound state orbital which is generally controlled by dipolar selection rules. It reveals the oxidation state and local geometry of the absorbing atom.
- XANES is the part near the absorption edge, which follows the pre-edge region and ends at ca. 40 – 60 eV above the edge. It represents the ionization threshold by the edge position, as well as the oxidation state and local geometry of the absorbing atom which relate to the impact of multiple-scattering resonance.
- EXAFS is the region of typically 500 – 1000 eV above the absorption edge. It corresponds to the scattering of the ejected photoelectrons off neighbouring atoms. The EXAFS oscillations correspond to coordination number, bond distance and etc.

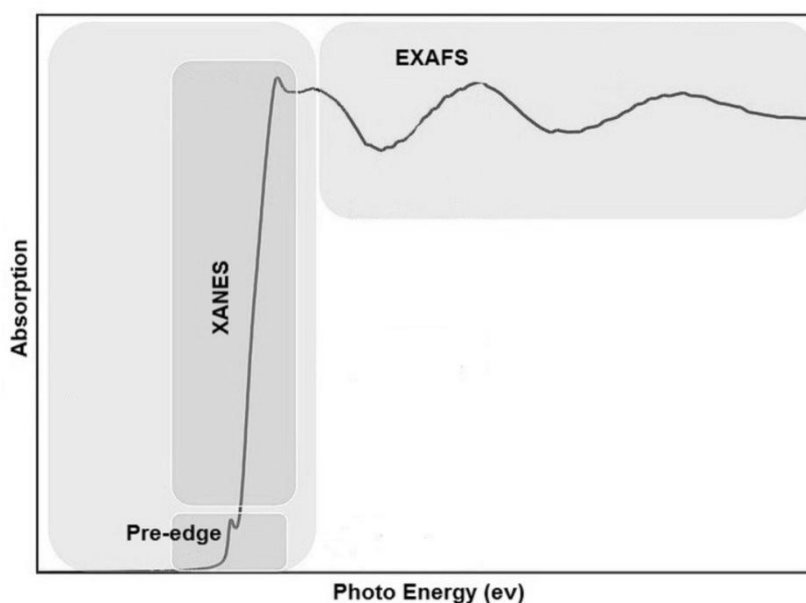


Figure 2.24 A typical X-ray absorption spectrum composed of three components, i.e. Pre-edge, XANES and EXAFS.

2.6.4.2 Basic theories

During the illumination by X-ray, matter could absorb the X-rays by photo-electric effect. This process happens only when the energy of the incident X-ray is greater than the binding energy of the electron in the quantum shell of an atom (Figure 2.25). The electron will absorb the energy of incident X-ray and get out from its quantum level, leaving a core hole behind. The possible excess energy of the incident X-ray could even help the electron to become a photo-electron and eject from the binding of the atom core.

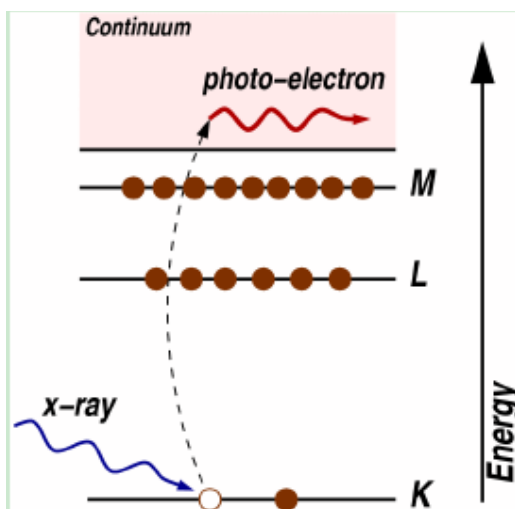


Figure 2.25 Illustration of the photoelectric effect in which the incident X-ray is absorbed by a core-level electron and the electron is excited out of its original level. (Newville, 2004)

During the energy scan by increasing incident X-ray energy, when the energy becomes equal to that of the binding energy of a core electron, a sharp 'jump' will appear in the absorption. This dramatic change corresponds to the excitation of this core level to the continuum, absorbing considerable beam energy. These absorption edge energies for various core-level shells of different atoms are well determined and tabulated (Thompson and Vaughan, 2009). Both K-edge and L-edge are applicable for XAFS measurements, and sometimes M-edge for considerable heavy elements. At the absorption edge and above, the absorbing atom is in an excited state with one core hole and one photo-electron. The atom at excited state typically does not last long and will decay within only a few femtoseconds (I.U., 10^{-15} second) of the absorption event.

There are two mechanisms for the excited atom to release the absorbed energy. The first is to release X-ray fluorescence (Figure 2.26), i.e. an electron from higher core-level drops into lower core-level ejecting X-ray of certain energy defined by the energy difference between the two core-levels. For example, the $K\alpha$ fluorescence line is released when an L shell electron drops into K shell. The second is to release energy through the Auger Effect, i.e. one electron drops into lower core-level releasing certain energy and, in the meantime, another electron absorbs the energy and gets into the continuum (sometimes emitted out of the sample). Each of the above two processes (two mechanisms) is feasible to measure the absorption coefficient μ during X-ray absorption fine structure study.

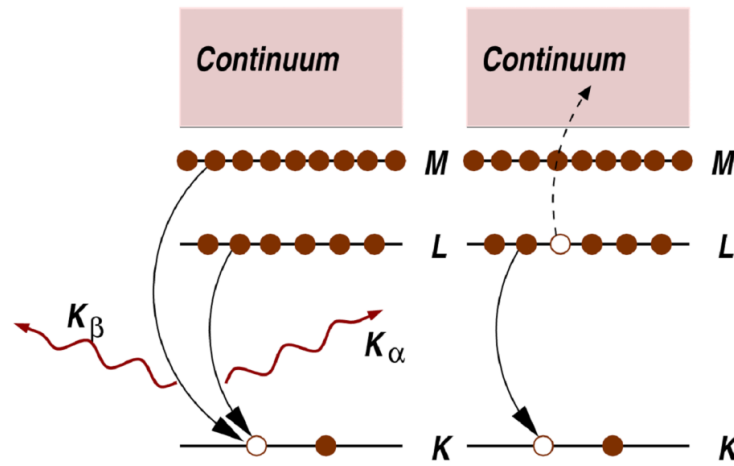


Figure 2.26 The two mechanisms for decay of the excited states: X-ray fluorescence (left) and the Auger effect (right). In both cases, the probability of emission (X-ray or electron) is directly proportional to the absorption probability. (Newville, 2004)

2.6.4.3 Available experimental geometries

Two measurement geometries are commonly utilized, i.e. transmission and fluorescence (or electron yield). Technical details of the experimental set-up is discussed in the methodology chapter for XAFS. For our concern from X-ray absorption fine structure measurement, the absorption coefficient $\mu(E)$ at different incident energy is described in two ways according to the above two geometries:

$$\text{Transmission} \quad \mu(E) = \log(I_0/I_t) \quad (2.35)$$

where I_0 is the incident intensity, I_f is the monitored intensity behind the sample.

$$\text{Fluorescence} \quad \mu(E) \propto I_f / I_0 \quad (2.36)$$

where I_0 is the incident intensity, I_f is the collected intensity of fluorescence line (or electron emission for Auger).

2.6.4.4 EXAFS theories

The practical analysis of XANES and EXAFS are commonly separate procedures. The quantitative calculation of XANES could not be done as well as that of EXAFS simultaneously, due to some difficulties in approximations and limits, although the computing of theoretical approaches for XANES has been improved during past decades. It is worth mentioning that, the EXAFS is rather a short-range order technique (typical probing a length scale below 5\AA) due to the rapid decrease in EXAFS signal from a scatter with the increase in the distance between absorber and scatter.

For EXAFS, one can describe the oscillations above the absorption edge by defining the fine-structure function $\chi(E)$ as below:

$$\chi(E) = \frac{\mu(E) - \mu_0(E)}{\Delta\mu_0(E)} \quad (2.37)$$

where $\mu(E)$ is the experimentally measured absorption coefficient, $\mu_0(E)$ is the background function, i.e. the absorption coefficient by an isolated atom, and $\Delta\mu_0$ is the coefficient difference measured at the threshold energy E_0 . However, more often the EXAFS oscillations are described by its nature, as introduced below.

When illuminating the material by X-ray within the energy range of EXAFS above absorption edge, photo-electron is emitted from the targeting atom shell, with the kinetic energy equal to the difference between the photo energy of incident X-ray and the inner-shell binding energy. Interference between the outgoing photo-electron wave and the backscattered wave from neighbouring atoms will occur. Furthermore, according to quantum theory this photoelectron can be considered as an outgoing spherical wave centred at the excited atom (Figure 2.27). Therefore, the X-ray energy

is usually converted into k (wave number of the photo-electron, unit \AA^{-1}) according to the equation below:

$$k = \sqrt{\frac{2m(E - E_0)}{\hbar^2}} \quad (2.38)$$

where E is the incident beam energy, E_0 is the energy of absorption edge and m is the electron mass. Since $k = 2\pi/\lambda$ it can be seen, with the increasing photon energy caused by the increasing energy of X-ray, the k of the photoelectron wave will increase resulting in a decrease of λ . This will lead to alternating constructive ($n\lambda=2r$, where n is the integer and r is the distance between absorber and backscatter) and destructive ($(n+0.5)\lambda=2r$) interference at the absorbing atom. If the backscattered wave reinforces the outgoing wave, the probability of absorbing the incident X-ray is enhanced. Moreover, the absorption is suppressed if the backscattered wave weakens the outgoing wave. Therefore, the probability of X-ray absorption will be affected, producing oscillations in the EXAFS.

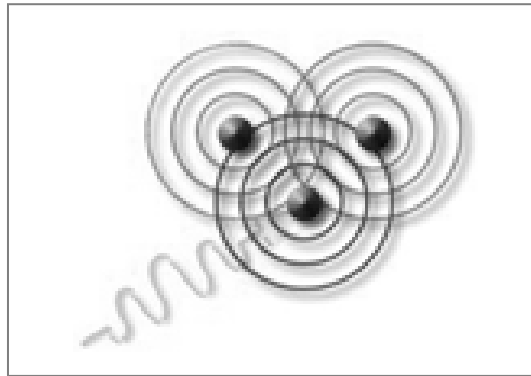


Figure 2.27 Interference of the photoelectron among atoms after its ejection from the core atom. (Koningsberger and Prins, 1988)

Sayers, Stern and Lytle formulated a simple and useful equation for χ , based on the context of single scattering approximation. The oscillations with various intensities in $\chi(k)$ depend on various types of neighbouring coordination shells, and could be represented from the EXAFS equation as below (Bunker, 2010).

$$\chi(k) = -\sum_j \frac{S_0^2 N_j f_j(k) e^{-2k^2 \sigma_j^2} e^{-2R_j/\lambda(k)}}{kR_j^2} \sin[2kR_j + 2\delta(k) + \varphi_j(k)] \quad (2.39)$$

where j refers to the j^{th} shell, S_0^2 is an amplitude reduction factor arising from many body effects, N_j is the number of atoms in the coordination shell, $f_j(k)$ is the scattering amplitude of the backscattering atom, σ_j^2 is the mean square displacement between the atoms which describes the disorder in the neighbouring distance (also referred to as the Debye-Waller factor), $\lambda(k)$ is the mean free path, R_j is the distance between the absorber and the backscattering atom, $\delta(k)$ is the phase-shift of the absorber, $\phi_j(k)$ is the phase-shift of the backscattering atom. The scattering properties of $f_j(k)$ and $\phi_j(k)$ of the backscattering atom are strictly dependent on the Z , thus, the EXAFS is sensitive to backscattering atom species. These terms can be divided into two catalogues for discussion as below.

a) Amplitude Terms

S_0^2 refers to a damping term, which solely depends on the absorbing atom and related 'many body effects'. Upon the ejection of a core electron, the remaining 'passive' atomic electrons in the excited state sense a different potential which is closely comparable to that of the atom of Z_{j+1} . As a result, the increased attraction of the nucleus can be considered as relaxing the other core electrons, by 'pulling' them to lower energy. However, these electrons can still be excited (multi-electron excitation) leaving the atom as "shake-up" if in bound state or "shake-off" if in continuum. The value of S_0^2 is closely related to the energy and wave function of the leaving photoelectron. The experiencing value is 0.7 – 0.8.

The occupancy number N in the coordination shell contributes linearly to the amplitude of the EXAFS.

The backscattering amplitude $f_j(k)$, is dependent upon the potential of the backscatter. As the atomic number of the backscatter increases, the amplitude generally increases for high k values. Generally, for relatively heavy atoms some periodic curves on the amplitude are usually observed with increasing k value; nevertheless, for light atoms the curves decreases monotonically according to increasing k . Effective values for $f_j(k)$ can be reasonably provided by computing programs like FEFF6.

σ_j^2 represents the "mean square displacement" between the absorber and backscatter due to thermal vibration. The value of σ_j^2 generally increases with distance, since the absorber and backscatter vibrate independently. Although this term is also referred to

as the “Debye-Waller factor”, it should be distinguished from that σ used in X-ray diffraction which illustrates the mean squared deviation of the atom position.

The amplitude reduction term $\exp(-2r_j/\lambda_j)$ adds exponential damping to the XAFS signal and accounts for the inelastic losses occurring in two possible ways. First, the ejected photo-electron can excite other physical processes such as Auger electrons, resulting in a loss of coherence of itself and consequently loses the possibility of contributing to EXAFS oscillation. Second, if the vacancy core hole has decayed before the time at which the photo-electron returns, it will be impossible for the interference to occur due to the mismatching coherence. This finite lifetime of the core hole limits the maximum neighbouring distance in EXAFS determination.

b) Phase Terms

In order to derive the distances and coordination numbers from EXAFS, it is of great importance to have accurate values for phase-shifts, since the overall effect of phase shift is shifting the effective emitting/scattering centre of the atom. The total phase term of sinusoid in Equation 2.39 is composed of three parts. $2kr_j$ results from the photoelectron path between the absorbing atom and the backscattering atom. $\delta(k)$ is the phase shift induced by the atomic potential when the photoelectron is ejected from the core shell. Since similar shift occurs when the photoelectron returns, the occurrence in the equation is $2\delta(k)$. The “ $\phi_j(k)$ ” is a function of k and depends on the backscatter species, which normally decreases monotonically with increasing energy.

2.6.4.5 Polarized EXAFS

The X-ray generated from synchrotron appears as linearly polarized if it is observed in the orbital plane of the storage ring. With this character, the EXAFS spectrum can be collected to determine the molecular orientation by probing the expected scatters around the core atom.

Under the particular condition in which polarized beam and orientated sample are used, the polarized EXAFS can present a maximum of three-fold enhancement in the amplitude of the EXAFS from a scatter, or conversely a minimum of 0 in the amplitude. The enhancement can be expressed as:

$$\chi(\text{polarized}) = 3(\chi(\text{isotropic}) \times \cos^2 \theta) \times n \quad (2.40)$$

where $\chi(\text{polarized})$ is the polarized EXAFS, $\chi(\text{isotropic})$ is the isotropic EXAFS such as the EXAFS measured from powder samples, θ is the angle between the electric vector of the X-ray beam and the absorber-scatterer vector, and n is the amount of equivalent scatters on the same shell. Here the $3\cos^2\theta$ is also referred to as the effective coordination number of a scatter ($N_{\text{effective}}$). Therefore, the orientated sample together with the polarized X-ray beam can be used potentially to determine the orientation of impurity molecular in the host sample in this study.

2.6.4.6 XANES theories and PDOS

The X-ray Absorption Near Edge Structure in an XAFS spectrum covers the energy range from the threshold (binding energy) to the starting point of EXAFS. There is generally no strict boundary between the two ranges, but as a commonly accepted rule, the upper limit of XANES ends at the energy where the electron wavelength is equal to the distance from the absorber to its nearest scatterer (Koningsberger and Prins, 1988).

The effect of measuring fluorescent photon during experiment is to sum up all possible final states of the photoelectrons. As a result, to qualitatively interpret the XANES spectrum it is useful to discuss the available final states corresponding to XANES. There are roughly three types of electron states in condensed systems, including core states, continuum states and unoccupied states. It is not difficult to understand the first two states, where core states describes the electron state of free atoms and continuum states represents the electrons with high energies such as the photoelectrons related in the scattering process of EXAFS. However, the unoccupied states covering the energy range from the Fermi level³ to the beginning of EXAFS, are the states where excited electrons populate within the XANES (Koningsberger

³ The Fermi Level is defined as the highest occupied molecular orbital in the valence band at 0 K, so that there are many states available to accept electrons.

and Prins, 1988). In addition, the low-lying continuum states can also accommodate electrons within the XANES region.

In condensed matter physics, the density of states (DOS) describes the amount of states per interval of energy within a particular energy level that are available to be occupied by electrons. The higher the DOS is at a specific energy level, the more states are available for electrons to populate. Besides, the partial density of states (PDOS) of a specific symmetry can solely be separated from the total DOS. Nevertheless, within the regime of XANES, the transition possibilities are directly related to the available states where the excited electrons can populate (Takahashi et al., 1999). As a result, the XANES will present a stronger peak within the energy range where there are more available unoccupied states (i.e. higher PDOS). Therefore, the XANES can be interpreted by calculating the PDOS of specific symmetry according to the dipole selection rules for particular systems.

2.7 Conclusions

This chapter has reviewed the fundamentals to the crystalline solid, crystallization and crystal growth, which underpin the most fundamental aspects of this study. The description started from the basic concepts in crystallography, defining the crystal and the structure and geometry of the crystal. The important definitions of isomorphism and polymorphism were classified. The habit, chemistry and defect of crystalline solids were introduced briefly. The basics of solutions and the nucleation theories were covered. Crystal growth theories were discussed in detail, which underpins a large part of this work. Furthermore, the relevant backgrounds and principles of the characterization methods for the features of single crystals as well as the crystallization process, have been well described and discussed.

CHAPTER 3

Crystal Habit Modification of Inorganic Systems and Sodium Chlorate

Summary:

A comprehensive review on the previous studies on crystal habit modification by impurity, from the wider range of inorganic systems to the specific system of sodium chlorate by impurity dithionate.

3.1 Introduction

This chapter reviews the previous studies focusing in the area of crystal habit modification. General review on the habit modification of crystals and the related mechanisms are first reviewed. A systematic review will be presented on the crystal habit of pure sodium chlorate (NaClO_3), covering the structures of different polymorphs, the crystal habit at different supersaturations, the topographic studies on dislocations, the kinetic studies on growth mechanisms and the investigation of strain in NaClO_3 crystals. Then, the habit modification studies of NaClO_3 by impurities will be reviewed, especially to discuss the impurity of $\text{S}_2\text{O}_6^{2-}$. Also, a number of X-ray absorption near edge structure (XANES) studies on various sulphur species have been reviewed, which will be used as reference to be compared to the XANES results in this study.

3.2 Habit Modification of Inorganic Systems and Related Mechanisms

Crystals of the same phase often exhibit various habits, influenced by a number of factors in different ways which can be divided into two categories, i.e. internal factors and external factors. The former include mainly the intrinsic crystal structure and crystal defects and the latter cover the ranges of solution supersaturation, growth temperature, solvent properties, impurities (or additives) and physical impacts including solution dynamics, magnetic and electric fields, microgravity, ultrasound, etc. Among all the factors the addition of impurity, or so-called modifier, is the most powerful and useful method by which, for certain systems, only a trace amount of impurity could change the crystal habit efficiently.

In early studies of crystal growth, when there were not many outstanding theoretical and experimental approaches for characterization, crystal habit was one of the mysterious subjects in both scientific and applied areas (Senarmont, 1854; Lehmann, 1891). During that time, the widely accepted mechanism was that the impurity could form micro-crystals by which the growth rate of the host crystals will be influenced. Before the utilization of X-ray diffraction techniques, the hypothesis along with this

mechanism is that the interplanar spacing of the impurity is comparable to that of the host crystal.

During the 1920s to 1950s, Buckley carried out a large number of experimental and theoretical studies on habit modification of crystals by impurity, concentrating particularly on the effect of inorganic and organic impurities on the growth of inorganic crystals (Deer, 1961). For instance, the {110} facets were enhanced on the original octahedron {111} habit of $\text{KAl}(\text{SO}_4)_2$ by adding KClO_3 , the (001) and $(00\bar{1})$ faces of K_2SO_4 crystals were enhanced by adding $\text{S}_2\text{O}_6^{2-}$ ion where its habit was {021} type, and the {001} become dominated on the habit of KClO_3 by adding MnO_4^{2-} (Buckley, 1930a; Buckley, 1932b; Buckley, 1932a). For the mechanisms of habit modification in aqueous solution, four aspects were concluded by Buckley (Buckley, 1949). First, different ions from different substances can recombine freely; second, the impurity itself maybe readily crystallized when given the opportunity (especially the particular acid dyes); third, two situations can occur for coloured impurities, i.e. incorporation in layers parallel to faces under which circumstance the whole crystal or most of it will be coloured, and inclusions in a specialized area such as from a point near the centre of the crystal to one surface but not other surfaces of the crystal; fourth, parallel-growth between crystal and impurity (e.g. KClO_3 and added impurity KMnO_4 (Buckley, 1932a)) can happen due to the almost identical lattices or the orientated inclusion of impurity on an ionic or molecular scale. The condition for parallel growth was also studied by Goldschmidt (Goldschmidt, 1929), where he indicated the corresponding inter-atomic space should not differ by more than about 10%.

The significant monograph of “Crystal Growth” by Buckley (Buckley, 1951) comprehensively reviewed the literature on crystal habit modification prior to that time. Since then, the research on the effects of impurity on crystal growth began to explore the adsorption mechanisms focusing on the microscopic level. The modern adsorption mechanism of impurity on crystals mainly focused on the development of surface adsorption mechanisms, mostly based on Kossel’s growth model. Dispersive studies on a wide range of aspects indicated different absorption sites for the impurity during crystal growth, but in total there are three recognized types of preferable adsorption sites for impurity incorporation, i.e. kink, steps, and ledge (Davey et al., 1974). The three possible locations for impurity adsorption are illustrated in Figure

3.1 based on the Kossel's Model. *Adsorption at kinks* will significantly reduce the number of active kinks on a surface, because of the incorporation of impurity into the host crystal lattice and prevent the kinks from integrating new solute (Chernov, 1984). At the same time, the importance of surface-solution diffusion is reduced by an increased distance between kinks due to the decreased number of them. Besides, the increasing distance between kinks may induce polygonization of growth steps (Davey, 1976). *Adsorption of impurity at steps* may severely induce a barrier to the diffusion of mobile growth units along the step and to their incorporation onto kinks or step sites (Sears, 1958). However, the step could continue to grow by squeezing through the impurity species at a reduced growth rate, which is related to the concentration of the impurity (Davey et al., 1974). Sears (Sears, 1958) and Burrill (Burrill, 1972) indicated *the adsorption on a ledge* is possibly happening when the surface diffusion dominates the growth process in a crystal system. The adsorption of the impurity will decrease the surface area and the flux of growth units to the kinks or step sites, leading to a reduction in step velocity. The kink site is assumed to be highly efficient in retarding the growth rate, followed by the step site which needs a greater quantity of impurity. The ledge sites are the least preferred location for impurity to be adsorbed.

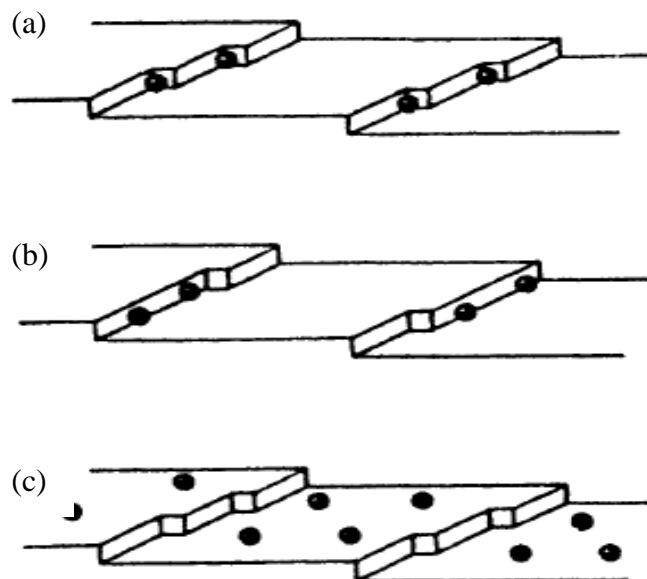


Figure 3.1 Locations of adsorbed impurity particles on the crystal face, Kossel model. (a) at kinks, (b) at steps, and (c) at ledges between steps. (Davey et al., 1974)

Since the 1980's, the recent interests in crystal habit modification have turned to the examination of the effects of "tailor-made" impurity (Lahav et al., 1985; Weissbuch et al., 1995) and design of such impurity for specific systems. The approach is made both by modern advanced experimental and computing modelling approaches, through the application of visualization techniques such as high-resolution optical microscopy and electron microscopy (Poornachary et al., 2007; Fiebig et al., 2007), molecular simulation packages such as HABIT95 (Clydesdale et al., 1996; Clydesdale et al., 2003), and the short range structures determination techniques of X-Ray Absorption Spectroscopy, X-Ray Multiple Diffraction, etc (Barrett et al., 1989; Cunningham et al., 1993; Lai et al., 2005; Remedios et al., 2010).

Heterogeneous impurities could modify the crystal habit by either affecting the properties of the solution or interrupting the solid state structure on the growing surface (Clydesdale et al., 1994). The latter case is of concern in the current study, which was induced by the incorporation of impurity onto the crystal growing surface. Clydesdale et al. (1994a; 1994b) assigned the impurities into two categories, i.e. "*disruptive tailor-made additives*" and "*blocking tailor-made additives*". The disruptive type additives are usually smaller in size but of high similarity compared to the structure of the host crystal molecule, e.g. benzoic acid as impurity in the growth of benzamide (Clydesdale et al., 1994). Thus this type of impurity can incorporate into specific surface sites and obstruct the proper bonding between the solid surface and the depositing material, hence causing a change in attachment energy for the subsequent growth layer which modifies the crystal habit. On the other side, the blocking type additives are generally larger in size than the host crystal molecule. These additives have one end group which has a structure similar to that of the host crystal, but another end group always exists which is structurally different and usually of larger size, e.g. biphenyl as impurity in the growth of naphthalene (Clydesdale et al., 1994). Due to the high similarity of one end group, the impurity can relatively easily incorporate onto the growing surface. The other larger end will act as a strong blocker preventing the depositing molecules in the solution from settling into their structurally ordered positions on the surface, thus reducing the growth rate of the specific crystal surfaces.

3.3 Previous Studies on the Crystal Growth of NaClO₃

3.3.1 The Different Structures of NaClO₃

Before to review the growth habit of sodium chlorate (NaClO₃), the different polymorphs of NaClO₃ as well as the corresponding structures will be described, since crystal structure is one of the key factors affecting the crystal habit.

NaClO₃ has been reported to be able to crystallize in several different phases (Meyer 1972). The most common also the most stable phase (phase I) crystallize in space group P2₁3 under room conditions (including the moderate temperature range of about 0~100 °C and the standard atmospheric pressure), and its structure was experimentally refined by Burke-Laing & Trueblood (1977) and Abrahams & Bernstein (1977) recently. The lattice parameters are $a=b=c= 6.5758 \text{ \AA}$, $\alpha=\beta=\gamma=90^\circ$; $Z=4$ (Abrahams and Bernstein, 1977). By cooling melted NaClO₃ to about 255 °C, Meyer and Gasperin (1973) found an unstable phase (phase III) of NaClO₃ in monoclinic form (P2₁/a) with $a=8.78 \text{ \AA}$, $b=5.17 \text{ \AA}$, $c=6.88 \text{ \AA}$, $\beta=110^\circ$; $Z=4$. Phase III can transform to the stable phase I when cooled to 230 °C. The phase III is likely to have been found also by Niinomi et al. (2013) in their study on droplet-evaporation induced nucleation at room conditions, where they reported an unstable unknown crystalline phase nucleated prior to the appearance of chiral NaClO₃ crystals. The unstable crystalline phase is achiral, and can easily transit into chiral spontaneous or by contacting with an existing chiral crystal. The structure of the unknown phase was reported as $a=8.42 \text{ \AA}$, $b=5.26 \text{ \AA}$, $c=6.70 \text{ \AA}$, $\beta=109.71^\circ$; monoclinic P2₁/a. Besides, a very unstable monoclinic phase (phase II) was obtained during the crystallization from solution by Meyer (1972), and the lattice parameters are $a=13.3 \text{ \AA}$, $b=10.8 \text{ \AA}$, $c=12.5 \text{ \AA}$, $\beta=100^\circ$; $Z=24$, monoclinic C2,Cm or C2/m. More specifically, Sowa (1995) carried out optical observation and powder X-ray diffraction to the NaClO₃ crystals in a specially designed cell under various pressures ranging from 0.0001 GPa ~ 3.81 GPa. He reported phase transitions from NaClO₃ i to NaClO₃ ii below 2GPa and from NaClO₃ ii to NaClO₃ iii below 4GPa. The structure of NaClO₃ i was determined to be space group P2₁3, but its lattice parameter ($a=b=c$) decreased from 6.5718 \AA at low pressure to 6.290 \AA at high pressure. Unfortunately, the structures of both NaClO₃ ii and NaClO₃ iii were not obtained.

To sum up, sodium chlorate (NaClO_3) can crystallize in many phases, most of which are unstable. But it is worth noting that, the crystalline material used in this study has been characterized by powder XRD and proved to be the stable phase I. Also, samples prepared from the as-grown single crystals were also examined by XRD, which were also of phase I. The reviewed works in next section were all based on crystal growth under normal temperature and pressure range at room conditions, in other words, the as-grown crystals under discussion are of phase I.

3.3.2 Habit of Pure NaClO_3 Crystal

To study the habit modification, it is of first importance to clearly understand the habit of the pure crystal without doping for comparison purpose. NaClO_3 crystals grown from aqueous solution at relatively high supersaturation exhibited the cubic form with six $\{001\}$ faces. With decreasing supersaturation, additional faces of $\{110\}$ and $\{111\}$ forms will appear. At very low supersaturation, the $\{120\}$ faces emerge occasionally (Bunn, 1961; Simon, 1983; Ristic et al., 1993). It was emphasized that in NaClO_3 crystals the opposite tetrahedral faces, i.e. $\{111\}$ and $\{\bar{1}\bar{1}\bar{1}\}$ ⁴, are *symmetrically non-equivalent*, which behave differently in terms of crystal growth and physical properties (Ristic, 1993; 1994). During growth from pure solution only the $\{111\}$ tetrahedral faces could form, with respect to the D- crystal structure (Abrahams and Bernstein, 1977; Ristic et al., 1994). The polar growth habit of pure sodium chlorate, comprising the $\{001\}$, $\{110\}$ and $\{111\}$ forms, has been predicted by Clydesdale et al. (1998) employing surface-specific attachment energy calculation based on the surface charges from ab initio calculation and interatomic potential parameters (Telfer et al., 1997). Contrary to the above literatures, Kern (1965, cited in Ristic, 1993) and Aoki (1979 cited in Ristic, 1993) proposed that the NaClO_3 crystal of cubic form emerges at low supersaturation and the tetrahedral faces only appear at relatively higher supersaturation. This was ascribed from the methods of using crystallographic structure to predict the macro-morphology employed by them (Ristic, 1993).

⁴ $\{111\}$ comprises (111) , $(\bar{1}\bar{1}1)$, $(\bar{1}1\bar{1})$, $(1\bar{1}\bar{1})$, whereas $\{\bar{1}\bar{1}\bar{1}\}$ comprises $(\bar{1}\bar{1}\bar{1})$, $(11\bar{1})$, $(\bar{1}11)$, $(1\bar{1}1)$.

The change of habit due to variation in supersaturation has been interpreted by Ristic et al. (1993), based on growth rate measurement for {001} and {110} faces under various supersaturation, whereas the simultaneous measurement for {111} was not possible. In their results, with the increase of supersaturation, the relative growth rate between {110} and {001} faces ($R_{110}:R_{001}$) increased. In principle, the maximum limit on relative growth rate between {110} and {001} is $R_{110} : R_{001} \approx 1.414$, beyond which value the {110} faces would vanish from the final habit. According to the measurement by Ristic et al. (1993), this value can be overtaken even below $S' \approx 0.2\%$, not to mention larger supersaturations. Nevertheless, such theoretical value for $R_{111} : R_{100}$ is about 1.732. Although the growth rate of {111} faces was not measured, Ristic et al. (1993) assumed that they would grow faster than {110}. Therefore, under high cooling rates, when the practical value overtaken the limit, the faces with faster growth velocity would vanish from the final habit. This explains the change of habit described above, mentioning the presence and absence of {110} and {111} faces. Furthermore, Ristic et al. (1994) measured the growth rate for $\{\bar{1}\bar{1}\bar{1}\}$ faces in the presence of 120ppm and 1200ppm of dithionate impurity. The growth rate is rather low compared to that of {001} or {110} faces (Ristic et al., 1993). Anyway, there is no data available for comparison between the $\{\bar{1}\bar{1}\bar{1}\}$ faces and the faces of other types.

3.3.3 Dislocations in Pure NaClO₃

A few X-ray topographic examinations of NaClO₃ were carried out to explore the dislocations in sodium chlorate crystals as well as their relationship to the growth mechanism (Mussard and Goldsztaub, 1972; Kito and Kato, 1974; Matsunaka et al., 1980; Hooper et al., 1983). Mussard and Goldsztaub (1972) reported that almost all the dislocations in NaClO₃ are perpendicular to the growth surface and are caused by relatively high supersaturation at some local sites on the growing surface. The dislocations have been connected to the faster growth rate of the growth sectors where they exist. Later, Kito and Kato (1974) assigned two types of dislocations in the NaClO₃ crystals grown from spontaneous nucleation. Type A originated from the nucleus and type B from impurity or inclusions during growth, while both of them are

perpendicular to the crystal surfaces of {001} type. Furthermore, Matsunaka et al. (1980) examined the dislocation in seven pieces of as-grown single crystals by seed under different supersaturation and demonstrated that the dislocations were always generated at the seed surface during its regeneration process and propagating perpendicular to growth surface. These line dislocations are distinguished into two types according to their path of propagating, i.e. straight propagating and curved propagating. The straight dislocation lines are reported to be present in all the crystals, while the curved ones seem to be happening in crystals grown under low supersaturation. Also, according to their observation of defect density from the topographs, it was concluded that the crystals grown under higher supersaturation were of a lower density of growth defects, compared to those grown under lower supersaturation. Besides, they stated that dislocations are not necessary as growth centres for the growth of NaClO₃ crystals at high supersaturation of ca. 3.8% to 6.5%.

After the three studies described above, Hooper et al. (1983) systematically explored the dislocation configurations in self-nucleated NaClO₃ crystals in detail, including crystals of habit {100} and the more complex habit with {100}, {110}, {120} and {111} facets. The preferred dislocation line directions have been computed with respect to different growth sectors. This calculation assisted the determination of the dislocation geometries in the self-nucleated crystals together with various diffraction vectors used for X-ray topography. Five catalogues of dislocations were classified, by distinguishing their origin and propagation route. The dominant dislocation lines in growth sectors of {100} type were attributed to be pure screw and pure edge dislocations with Burger's vector $\vec{b} = a \langle 100 \rangle$. The crystals with complex habit faces mentioned above were also investigated and concluded to be caused by the propagation of a large number of dislocations originated from the very defective nuclei.

Furthermore, Klapper (1980) reported the after-growth glide dislocation lines in NaClO₃, whose profiles were revealed to be rows of arcs with pinning points. This was assumed to be caused by internal defects surrounded by stresses or mechanical damage in the external surface.

3.3.4 The Growth Mechanisms of NaClO₃

The growth mechanism of pure NaClO₃ crystal has been studied by a number of publications. Bennema (1967) measured the growth rate of NaClO₃ in the relative supersaturation (Sr) range of 25×10^{-5} to 175×10^{-5} using weighing method, and concluded the growth mechanism to be spiral growth. Hosoya et al. (1978) reported the growth mechanism of NaClO₃ to be two-dimensional nucleation, based on their measurement of the growth rate of the (001) face as a function of supersaturation, in the Sr range of 3% ~ 5%. Matsunaka et al. (1980) measured the growth rate of {001} type face at different supersaturations. They stated that the growth mechanism is spiral growth or two-dimensional nucleation at supersaturation around 3%, and solely two-dimensional nucleation at supersaturation ranging from ca. 3.8% to 6.5%. Most recently, Ristic et al. (1993) concluded that the {001} faces grow by single spirals at Sr of 0.5% ~ 2% and by cooperating spirals at Sr of 2% ~ 3.7%. Another important point reported by Ristic et al. (1993) was that, the growth mechanism of the natural faces would not be influenced by the presence of S₂O₆²⁻ impurity at all the concentrations (i.e. 70ppm – 210ppm).

3.3.5 The Effect of Strain on the Growth of NaClO₃

Ristic et al. (1997) studied the influence of synchrotron radiation-induced strain on the growth and dissolution of NaClO₃ single crystals (0.8x0.8x0.1 cm³). Being placed in solution of very low supersaturation of 0.32%, the irradiated portion of the NaClO₃ crystal dissolved, but simultaneously the non-irradiated portion grew. They concluded that the elastic strain caused by irradiation affected the crystal growth in two ways. Firstly, it will increase surface-free energy, which can obstruct the generation of growth steps and slow down their propagation over the surface. Secondly, the chemical potential (μ_s) of the surface will increase, which can decrease the driving force for crystal growth ($\delta\mu = \mu_l - \mu_s$, where μ_l is the chemical potential of the liquid phase). Both the above effects will reduce the growth velocity of the crystal surface. In addition, examination of lattice strain on small NaClO₃ crystals has also been done by Ristic et al. (1988). It was concluded that the growth rate of NaClO₃ crystals depends on the degree of lattice strain. The most strained crystals grow slowest.

Moreover, the strong correlation between the increase of lattice strain and the reduction of crystal growth rate was also reported for the case of potash alum single crystals (Ristic et al., 1990; 1997).

In addition, the widely used etching technique which provides a direction measure of dislocation density also relies on a similar mechanism described above. Around the dislocations on the crystal surface the lattices are distorted. As a result of the stress caused by the distortion, the lattice compositions dissolve more easily at the dislocation sites than other areas. Thus, etch pits are formed (Dhanaraj et al., 2010).

3.4 Habit Modification of Sodium Chlorate by Impurities of RO_4^{2-} type and Sodium Dithionate

The first report on habit modification of sodium chlorate (NaClO_3) by impurities goes back to von Hauer (1877, cited in Buckley, 1930), who observed the enhancement of the tetrahedral face on these crystals grown from sulphate-doped solutions. Buckley (1930b) systematically studied the habit modification of NaClO_3 by employing 36 ionic species of RO_4^{2-} and related types (Table 3.1), where he indicated the dithionate ion $\text{S}_2\text{O}_6^{2-}$ to be the most powerful in enhancing the tetrahedral faces and suppressing the cubic faces (Table 3.1). Only 1:1000 ($\text{S}_2\text{O}_6^{2-} : \text{ClO}_3^-$) is needed to modify the cube into a tetrahedron. An observation study had been done by doping NaClO_3 with two of the top three impurities of strong habit-modifying power, i.e. borax ($\text{B}_4\text{O}_7^{2-}$) and thiosulphate ($\text{S}_2\text{O}_3^{2-}$) (Surender and Rao, 1993). They concluded that the impurity was affecting the growth steps on $\{100\}$ face where the steps were piled up and introduced the appearance of tetrahedral faces. They suspected that the impurity did not enter into the lattice.

Impurity	Impurity : host crystal (mole ration)
SeO_4^{2-}	3:1
ClO_4^-	2:1
$\text{Cr}_2\text{O}_7^{2-}$	1:1
CrO_4^{2-}	1:1
SO_4^{2-}	1:7
$\text{S}_2\text{O}_3^{2-}$	1:20
$\text{B}_4\text{O}_7^{2-}$	1:60
$\text{S}_2\text{O}_6^{2-}$	1:1000

Table 3.1 The critical concentrations for different impurity species to modify the habit of NaClO_3 from cube into total tetrahedral. (Buckley, 1930)

Most recently, Ristic et al. (1993; 1994) and Wojciechowski (1995) reported the habit modification and growth kinetics of NaClO_3 in the presence of $\text{S}_2\text{O}_6^{2-}$ impurity at varying concentrations. The presence of $\text{S}_2\text{O}_6^{2-}$ resulted in the rapid development of the $\{\bar{1}\bar{1}\bar{1}\}$ faces. These faces are opposite to those $\{111\}$ faces which appeared on the pure crystal. The critical concentration for $\text{S}_2\text{O}_6^{2-}$ to start changing the habit of NaClO_3 was reported to be approximately 70ppm (mole ratio, 1ppm=1/10⁶). The impurity-induced $\{\bar{1}\bar{1}\bar{1}\}$ faces enhanced rapidly with increasing impurity concentration, and above 210ppm the habit converted into a tetrahedron bounded by habit faces of $(\bar{1}\bar{1}\bar{1})$, $(11\bar{1})$, $(\bar{1}11)$ and $(1\bar{1}1)$. These tetrahedra show slightly rounded faces and edges, indicating a reduced perfection of these crystals. Ristic et al. (1993; 1994) proposed a structural model for this habit modification system based on structural viewpoint. The development of the $\{\bar{1}\bar{1}\bar{1}\}$ faces of NaClO_3 in the presence of $\text{S}_2\text{O}_6^{2-}$ was concluded to be the substitution of ClO_3^- by one SO_3 of the $\text{S}_2\text{O}_6^{2-}$ on these specific tetrahedral faces, while the other SO_3 of the $\text{S}_2\text{O}_6^{2-}$ protruding outside of growing surface and retarding the growth rate of these faces. However, there is no further experimental characterization to structurally explore the impurity incorporation mechanism. Besides, Ristic et al. (1993) also observed, for the first time, growth twins of sodium chlorate which they interpreted as being due to an epitaxial relationship between the twin partners, induced by the $(\text{SO}_3)_2^{2-}$ ions. However, again, there has not been any further experimental approach to characterize the twinning origin or to determine the applicable twinning law.

3.5 Position of Sulphur K-edge and Profile of the XANES

This study employed the technique of X-ray Absorption Fine Structure (XAFS) to explore the chemical environment of the impurity by scanning the K-edge spectrum of sulphur, thus, here the related literature will be reviewed. The X-Ray Absorption Near Edge Structure (XANES) scientifically represents a fingerprint of each oxidation state for various elements, which is equivalent in the respect of Standard X-ray Powder Diffraction Pattern. Sulphur XANES on many species has widely been explored, in terms of simple inorganic and organic molecules and also complex minerals and mixtures (Queen et al., 2013; Fleet, 2005; Li et al., 1995). The sulphur K-edge represents dipole allowed transition of S 1s to unoccupied antibonding orbitals at the low end of the conduction band. The shifting of the absorption-edge position in sulphur K-edge XANES generally reveals the oxidation state of sulphur in both inorganic and organic species. Since the scope of the current study is to explore the effect of sulphur-containing impurity $S_2O_6^{2-}$ on the crystal habit of $NaClO_3$, hereinafter a review on peak positions of sulphur K-edge XAFS on a series of ionic species is necessary, including sulfide S^{2-} , disulfide S_2^{2-} , elemental S^0 , sulphite SO_3^{2-} , sulphate SO_4^{2-} , thiosulphate $S_2O_3^{2-}$ and dithionate $S_2O_6^{2-}$ (Table 3.2). It can be seen that the K-edge position for S species is generally shifting to the higher side with increasing oxidation number. The energy varies from 2469.0 eV in iron sulphide (-2 oxidation state) to 2482.1 eV in potassium sulphate (+6 oxidation state) (Tauson et al., 2012; Filipponi et al. 1993), covering a difference of about 13.1 eV. However, Li et al. (1995) reported that in various metallic sulphides the S^{2-} shows quite dispersive values from 2469.4 eV to 2473.4 eV, which can be explained as the band gap opened up due to the direct bonding between metal cation and sulphur anion (Fleet, 2005). It has also been noticed here that, the values of different compounds published by Sekiyama et al. are about 2 eV lower than average values from other literature.

Ion	Formal charge	Compound	Edge peak (eV)	Reference
S ²⁻	-2	FeS	2469.0	(Tauson et al., 2012)
		CoS	2469.9	(Bonnin-Mosbah et al., 2002)
		FeS	2469.9	(Crabb et al., 1992)
		Cu ₂ S	2470.1	(Li et al., 1995)
		^a 20 various sulphides	2469.4 to 2473.4	(Li et al., 1995)
S ₂ ²⁻	-1	FeS ₂	2471.0	(Tauson et al., 2012)
		FeS ₂	2471.2	(Li et al., 1995)
		FeS ₂	2471.6	(Bonnin-Mosbah et al., 2002)
		FeS ₂	2472.1	(Sugiura, 1981)
S ⁰	0	S	2471.5	(Tauson et al., 2012)
		S	2471.7	(Filipponi et al., 1993)
		S	2472.0	(Li et al., 1995)
		S	2472.0	(Fleet, 2005)
SO ₃ ²⁻	+4	Na ₂ SO ₃	2475.5	(Sekiyama et al., 1986)
		Na ₂ SO ₃	2477.3	(Tauson et al., 2012)
		Na ₂ SO ₃	2477.4	(Li et al., 1995)
		Na ₂ SO ₃	2477.8	(Fleet, 2005)
		Na ₂ SO ₃	2478.2	(Filipponi et al., 1993)
SO ₄ ²⁻	+6	Na ₂ SO ₄	2479.9	(Sekiyama et al., 1986)
		CaSO ₄	2481.3	(Li et al., 1995)
		^b 8 other sulphates	2481.2 to 2481.7	
		Na ₂ SO ₄	2481.7	
		Na ₂ SO ₄	2481.9	(Fleet, 2005)
		K ₂ SO ₄	2481.4	(Tauson et al., 2012)
S ₂ O ₃ ²⁻	-2 & +6	Na ₂ S ₂ O ₃	2482.1	(Filipponi et al., 1993)
			2469.2 (S -2)	(Sekiyama et al., 1986)
	-1 & +5	Na ₂ S ₂ O ₃	2476.4 (S +6)	
			2470.8 (S -1)	(Li et al., 1995)
			2479.3 (S +5)	
-2 & +6	Na ₂ S ₂ O ₃	2471.4 (S -2)	(Fleet, 2005)	
		2480.2 (S +6)		
S ₂ O ₆ ²⁻	+5	Na ₂ S ₂ O ₆	2476.5	(Sekiyama et al., 1986)
		Na ₂ S ₂ O ₆	2480.9	(Filipponi et al., 1993)

Table 3.2 Peak positions of K-edge XANES. * ^a and ^b indicate more available data on sulphide and sulphate compounds.

Since the dependence of XANES on the oxidation state might represent specific features in some particular cases, during the analysis of XANES the overall profile including the peak positions and the shape of spectrum is more often used (Fleet, 2005). A series of sulphur XANES have been reviewed by the author from different literatures and reproduced to present the usual profile of different sulphur anions (Figure 3.2).

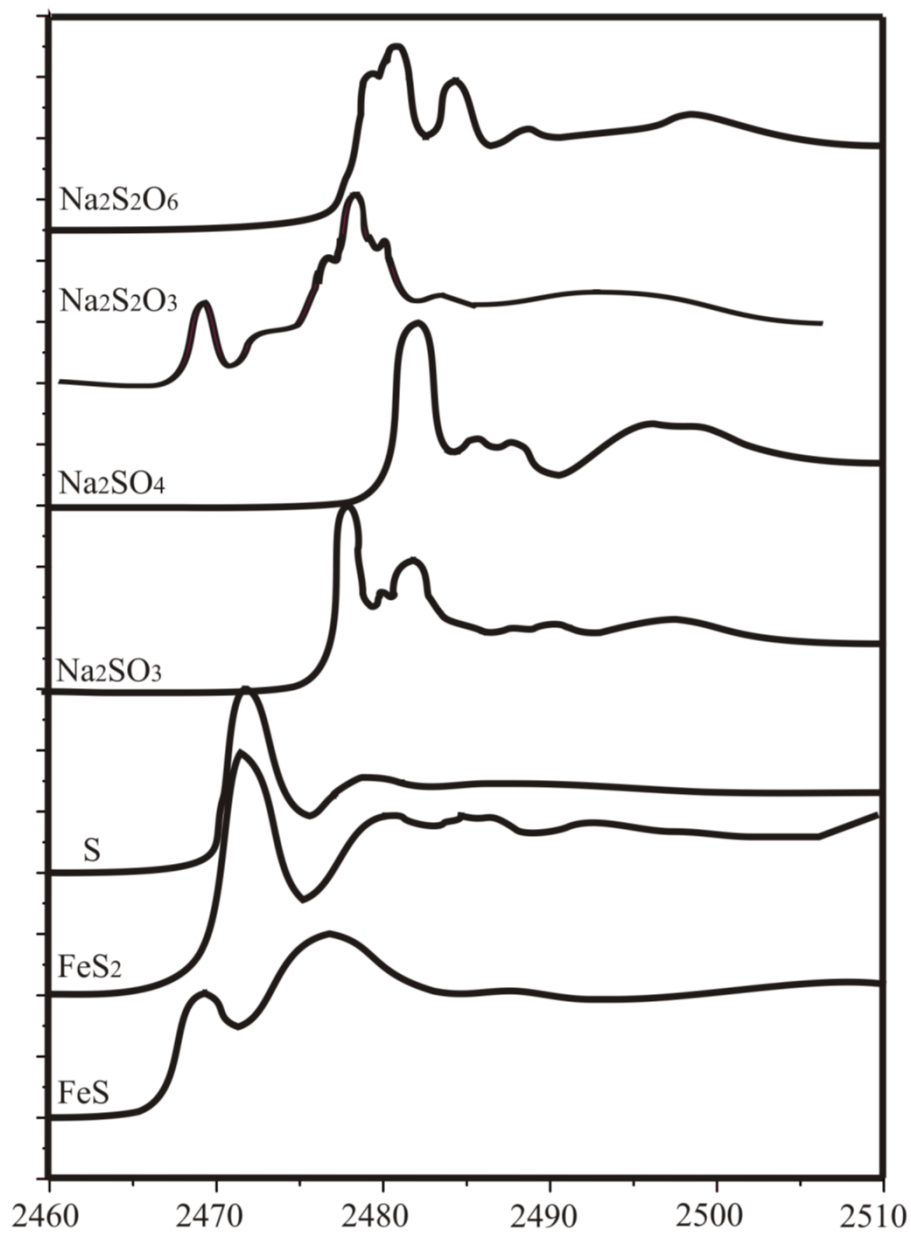


Figure 3.2 Sulphur K-edge XANES of different reference compounds. Each spectrum has been normalized with respect to the pre-edge and most intensive peak. (Crabb et al., 1992; Bonnin-Mosbah et al., 2002; Filippini et al., 1993; Sekiyama et al., 1986)

3.6 Conclusions

This chapter summarized previous studies on the habit modification of crystals and some other related studies, from the wider scale of inorganic systems to the specific case of NaClO_3 doped with $\text{Na}_2\text{S}_2\text{O}_6$. The review on the habit modification of crystals was described approximately in chronological order. The development in the field of the incorporation mechanism and the habit-modifying mechanism of the impurities was presented. Studies of pure NaClO_3 were reviewed prior to the description of its habit modification by impurity. The different structures (different phases), the habit under different growth conditions, the dislocation configuration and the growth mechanism of NaClO_3 were reviewed and summarized. Also, the significant effect of artificially-induced strain on the growth of NaClO_3 was reviewed. All the knowledge based on the literatures of pure NaClO_3 is necessary for underpinning the study of its habit modification by impurity. The previous studies on the habit modification of NaClO_3 have been reviewed. For the $\text{NaClO}_3/\text{Na}_2\text{S}_2\text{O}_6$ (host/impurity) system, although Ristic et al. (1993; 1994) and Wojciechowski (1995) proposed an incorporation mechanism based on habit modification observation and growth kinetics measurement, we can conclude that it is necessary to carry out further exploration into the growth history, defect configuration, micro-crystallography (e.g. lattice distortion) and local structure of the impurity, in order to understand the structural mechanism for the action of $\text{Na}_2\text{S}_2\text{O}_6$ impurity in the habit modification of NaClO_3 crystal. Nevertheless, twinned NaClO_3 crystal hasn't been characterized other than the report of its existence (Ristic, 1993). X-ray absorption near edge structure (XANES) studies on a variety of sulphur species have also been reviewed, which will be needed for comparison purpose during the analysis of XANES data later in this thesis.

CHAPTER 4

Materials and Methodology

Summary:

Description of the information of the materials used in the current study, and the instruments, data acquisition procedures and data analysis methods for each technique employed in this study.

4.1 Introduction

This chapter details the materials and methods used for studying the habit modification of sodium chlorate (NaClO_3) by dithionate impurity $\text{S}_2\text{O}_6^{2-}$. The details of the materials including NaClO_3 and $\text{Na}_2\text{S}_2\text{O}_6$ are described in the materials section. The methodology section describes all the techniques employed in the current study. The experimental work was designed to characterize the incorporation of $\text{S}_2\text{O}_6^{2-}$ impurity in NaClO_3 crystals, by exploring the crystallization kinetics (meta-stable zone width), defect configuration, lattice distortion and local structure of $\text{S}_2\text{O}_6^{2-}$. The molecular modelling methods were adopted to explore the crystallographic nature and surface chemistry of the system and establish the structural model for the habit modification process.

4.2 Materials

Sodium chlorate (NaClO_3) exists as a white crystalline powder with a relative formula mass of 106.44, and was purchased from Sigma Aldrich in the purity grade of ReagentPlus (>99%, part no. 244147). NaClO_3 crystallizes in the space group $P2_13$, with four molecules in one unit cell being arranged in a special order (Abrahams and Bernstein, 1977). As a result, although the molecules of NaClO_3 are absolutely achiral, they crystallize in two enantiomers of crystalline forms due to the crystallographic arrangement, i.e. D- enantiomer and L- enantiomer (Viedma, 2005)⁵. The D- crystal rotates plane polarized light clockwise, while the L- crystal rotates plane polarized light counterclockwise. The absolute configuration for the crystal structure of NaClO_3 had been determined with respect to its optical activity, i.e. D- and L- (Ramachandran and Chandrasekaran, 1957). The structure applied in the current study for molecular modelling, was derived from the structure file with identification number icsd-1301 from Inorganic Crystal Structure Database (ICSD). The lattice parameters are $a=b=c=6.57584 \text{ \AA}$, $\alpha=\beta=\gamma=90^\circ$. The structure is of D- optical activity.

Sodium dithionate dihydrate ($\text{Na}_2\text{S}_2\text{O}_6 \cdot 2\text{H}_2\text{O}$) as white crystalline powder with a molecular weight of 242.14, was purchased from Chemsworth in the purity grade of

⁵ D- and L- correspond to dextrorotary and levorotatory, respectively.

99%. $\text{Na}_2\text{S}_2\text{O}_6$ crystallizes in the centrosymmetric space group Pnma, with four molecules in one unit cell (Kirfel et al., 1980). Its structural data was numbered icsd-26326 in ICSD. The lattice parameters are $a=6.407 \text{ \AA}$, $b=10.751 \text{ \AA}$, $c=10.665 \text{ \AA}$, $\alpha=\beta=\gamma=90^\circ$.

4.3 Meta-stable Zone Width

4.3.1 Instrument

The AUTOMATE system (manufactured by H.E.L.) is an automatically controlled reactor system composed of four independent 50mL reactors with an individual speed-tuneable stirrer, temperature probe, and turbidity probe. It was employed to monitor the crystallization process in order to measure meta-stable zone width (MSZW).

The turbidity probe could provide accurate detection of crystallization and dissolution onset points as a function of temperature. The temperature control system relies on a Julabo Refrigerated Circulators with a temperature working range of $-50 \text{ }^\circ\text{C}$ to $+200 \text{ }^\circ\text{C}$, connected to the double-layer glass jackets under each reactor. The Winiso software provided by HEL can control the whole instrument automatically by following a experimental plan which can be set up by the user. Figure 4.1 shows the main AUTOMATE instrument used to measure the MSZW.

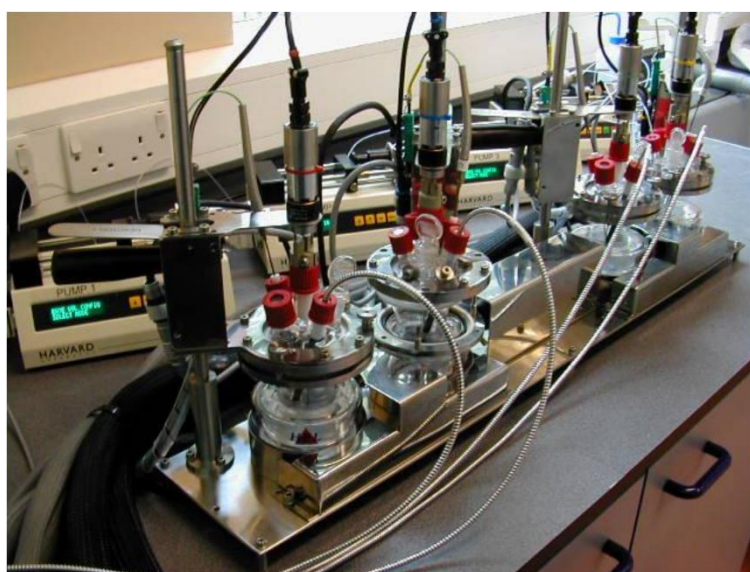


Figure 4.1 The main components of the AUTOMATE units.

4.3.2 Experiment

In the MSZ experiments, the needed amount of the impurity sodium dithionate is typically very small and difficult to be measured with a balance. Thus, prior to the MSZ experiments, the $\text{Na}_2\text{S}_2\text{O}_6$ solid was dissolved into a certain amount of water to prepare a solution, which is easier to be measured in the experiments. During each MSZ measurement, 46.00g of sodium chlorate (NaClO_3) was first placed in the glass reactor. Then, the impurity $\text{Na}_2\text{S}_2\text{O}_6$ was added as a calculated volume (V_{impurity}) of solution at the appropriate concentration. Lastly, distilled water was added as $(40 - V_{\text{impurity}})$ mL. After that, the reactor was sealed using the screw on the glass top of the reactor. The temperature profile was edited using the WINISO software installed on the PC. The experiment was then ready to run.

The temperature profile was normally set as below. First, the reactor was heated to 60 °C which was above the saturation temperature and kept at a constant temperature for over 30mins to make sure all the crystalline material was fully dissolved. Second, the solution was slowly cooled down at a fixed cooling rate to the low temperature at which crystallization can occur, this temperature varies between different experiments with different concentration of impurity with different cooling rates. Finally, the vessel was heated up again to re-dissolve the crystals, in order to obtain the dissolution temperature. Under each experimental condition, the above procedure was repeated 3 times to avoid measurement errors.

The MSZW was measured as a function of impurity concentration, under three different cooling rates of 0.25, 0.5 and 1.0 °C/min, respectively. The impurity concentrations were 0, 40, 70, 100, 130, 160, 190, 220, 250, 280, 310 ppm.

4.4 Crystal Growth

4.4.1 Apparatus of Crystal Growth

The ideal solution status for single-crystal growth in the laboratory is that which is controlled in the meta-stable zone, so that self-nucleation will not happen but the inserted crystal seed can grow. There are two ways to approach such conditions, i.e. by decreasing the solution temperature from a higher value to the level between the solubility line and the supersolubility line (Figure 2.8) of a system, or by increasing the solution concentration through continuous evaporation. The first approach can be reliably implemented and is better for quantitative study since the temperature can be simply monitored. Thus, this study grew single crystals by inserting seed crystal and decreasing solution temperature.

The apparatus for single crystal growth is composed of three units, each can work independently. Every unit is essentially built up by two main components, i.e. the flask as the container of growth solution and the water bath for temperature control. The flask is of 600mL capacity, covered by a fixed lid with a double-layer rotational tube sealed by water. The internal tube is fixed to the lid, and the external tube is tied with a polymer o-ring to the impeller which stirs the growth solution and the crystal seed. Hence, this lid can prevent the solvent of growth solution from evaporating. The impeller is driven by a variable speed motor (maximum 60rpm), and possesses an opening for the wire suspending the seed. To maintain the desired constant temperature for the solution in the flask, water bath heating employed an infra-red light as heater which provided diffuse heating ability rather than an immersion heating source. The temperature is controlled by a contact-thermometer filled by mercury connected to a relay box followed by the infra-red light. During crystal growth, the infra-red light provides discrete heating to compensate the water temperature to maintain a constant value. The water bath utilized a fast stirrer mounted on a 360rpm motor, to ensure good heat transfer within the bath for uniform temperature distribution.

A conductivity meter was initially equipped on the crystal growth rig. However, the probe head made of metal caused unwanted crystallization during the growth of single crystal. As a result, the solution concentration was not monitored online during the

crystal growth. Similarly, an attempt to monitor the rate of increase in the physical dimensions of the growing crystal, by mounting a ruler outside the growth flask, failed because of distortions caused by refraction at the glass wall of the crystallization vessel.

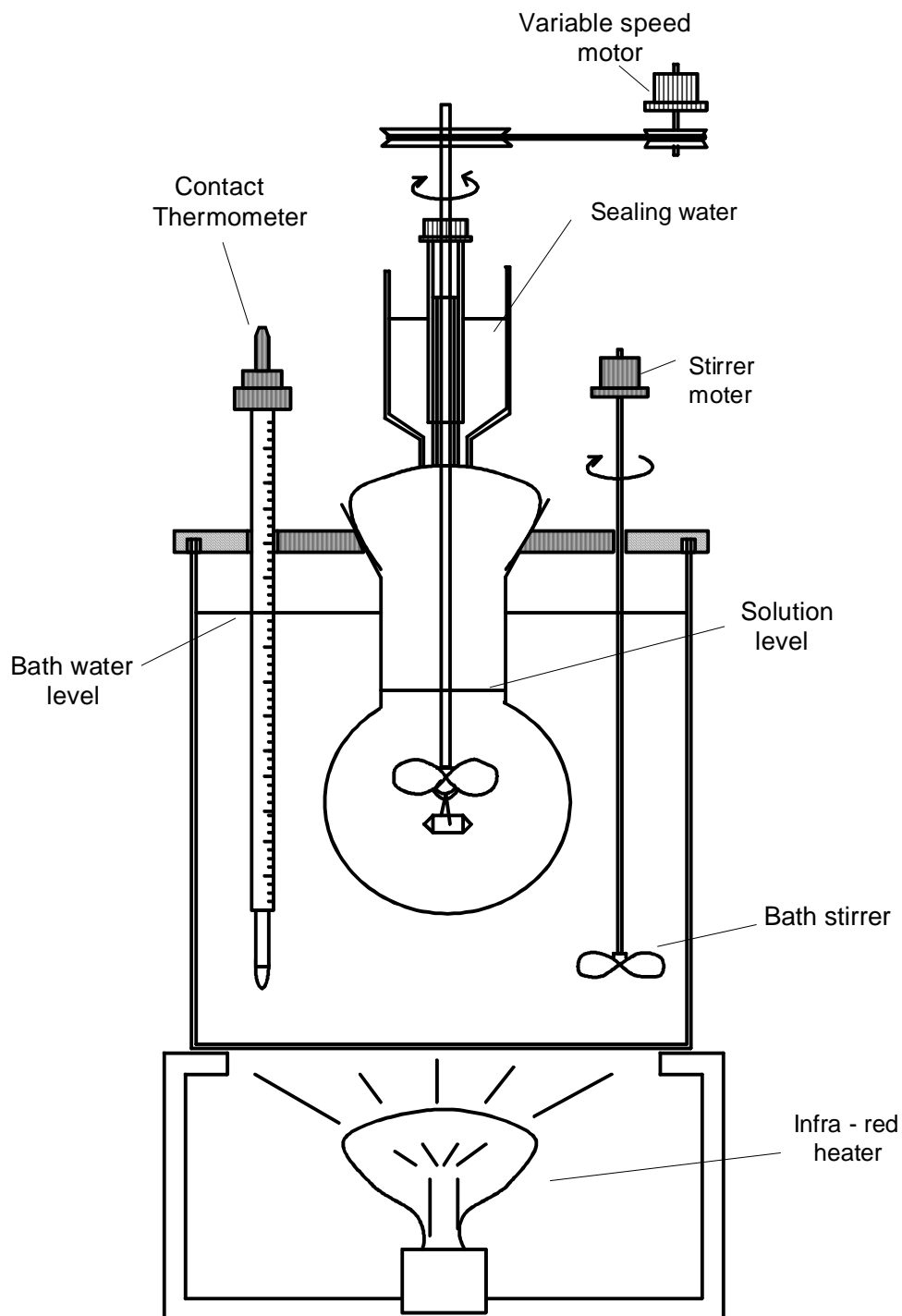


Figure 4.2 Schematic illustration of the apparatus for crystal growth.

4.4.2 Seed Preparation By Evaporation

Seeds of pure sodium chlorate (NaClO_3) crystal were used to grow large single crystals in the current study. The seed crystals were prepared by the evaporation of NaClO_3 solution following the method below. 262.8g sodium chlorate was dissolved in 300mL distilled water (i.e. solubility at 10 °C) in a conical flask, by heating to ca. 25 °C (room temperature 13~17 °C) and using magnetic stirring. The clear solution was vacuum filtered through a pre-heated sintered glass funnel into a pre-heated filter flask, and then divided into 3 evaporation dishes (radius x height is 95 x 55 mm) (Figure 4.3a). These solutions under local room temperature are under saturated. Parafilm was used to seal the evaporation dishes, but 3, 6 and 9 holes of about 2mm diameter on the parafilm of different dishes were punched, to allow the slow evaporation of water at different rates. Within 7 to 14 days, crystals would normally grow to the desired size of several millimetres in three dimensions. The crystals presenting faces of only {001} type (Figure 4.3b) were selected as seed. The selected seeds were picked up and dried by wiping with a soft tissue. Since the perfection of seed crystal would severely affect the quality of as-grown single crystal, the seed crystals were examined under optical microscopy, and only those with least optical defects were stored for use.

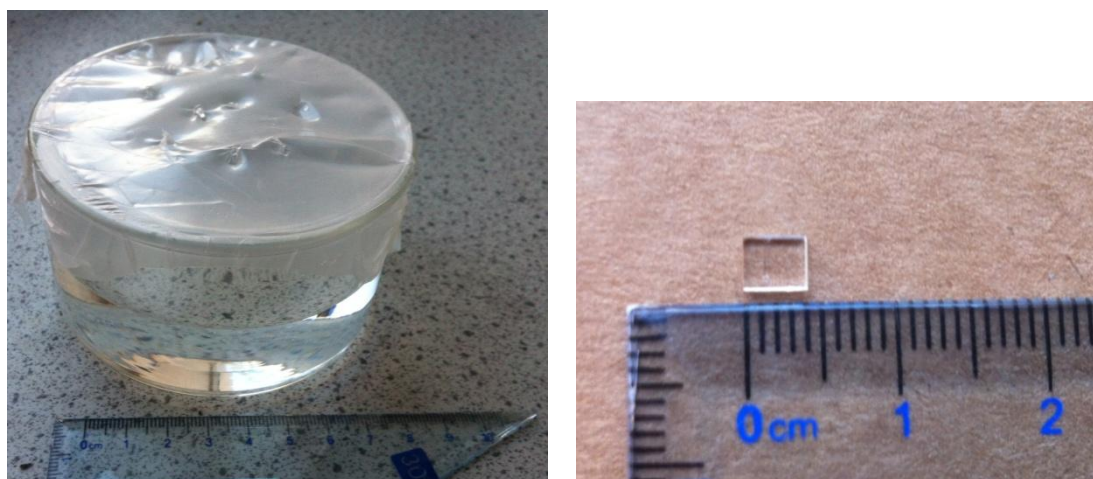


Figure 4.3 (a) Photo of the apparatus for seed preparation by evaporation. (b) The crystal seed used for single crystal growth. The seed presents only {001} faces.

4.4.3 Growth Solution Preparation

In order to study the habit modification of dithionate ($S_2O_6^{2-}$) as a function of impurity concentration, the solutions of sodium chlorate were prepared by doping with various concentrations of $S_2O_6^{2-}$. Besides the different impurity quantities, the other properties of the growth solutions are basically the same.

Growth solution composition is prepared by mixing 480g $NaClO_3$ and 400mL H_2O in a conical flask. This was the solubility of $NaClO_3$ at 45.5 °C. Impurity for doped solutions is added to the above mixture as a soluble crystalline solid of sodium dithionate dehydrate ($Na_2S_2O_6 \cdot 2H_2O$), by a calculated mole ratio ($S_2O_6^{2-} : ClO_3^-$) starting from 40ppm ($4 \times 10^{-5} : 1$) to 1000ppm, respectively. The mixture is sealed by parafilm to prevent water loss and stirred intensively for fast dissolution at about 60 °C on a hot plate with a magnetic stirrer for several hours until the solution became clear for at least one hour.

The visibly clear solution inevitably contains undesirable impurities, such as dust from the air. Therefore, the solution is vacuum filtered through a pre-heated sintered glass funnel into a pre-heated filter flask. The loss of solution temperature during filtration is not sufficient to cause crystallization, since the solution temperature was deliberately heated to 60 °C and the filter flask was pre-heated. At last, the solution is directly transferred into the growth flask. The water bath was prepared in advance and maintained at 45.5 °C before the filtration, and the solution was left for at least 12 hours to reach temperature equilibrium between the solution and the water bath.

To ensure the solution is saturated, a piece of test crystal is suspended into the solution. If it dissolves or grows, the solution temperature would be adjusted accordingly to approach the equilibrium point. When a good equilibrium temperature (T_{equi}) was recorded, the test crystal was removed and the solution temperature was typically increased by 3 °C to remove possible nuclei in the solution introduced during the above test. After maintaining this higher temperature for at least 3~4 hours, the solution temperature was adjusted back to a temperature ($T_{equi}+0.5$ °C) which is 0.5 °C higher than the recorded equilibrium temperature.

4.4.4 Seeding and Growth

A pin hole was drilled through the middle of the seed crystal using a 0.25mm metric twist drill mounted on a hand driven pin vice. The drill was frequently soaked in distilled water during the drilling, in order to dissolve the material for quick drilling and minimise the mechanical damage. The seed was then tied by a nylon thread to the bottom of the glass impeller which was taken out of the growth flask. Before putting the impeller back into the growth flask, the seed was rinsed quickly in distilled water and dried by soft tissue to remove any crystal powder on the seed surface from the drilling operation.

The seed crystal was positioned about 2 cm above the growth solution level when putting the impeller back into the flask. There was a waiting time of 15 minutes before immersing the seed into the growth solution, which allowed the seed to approach the solution temperature in order to prevent the seed from possible damage caused by thermal shock. The seed crystal was then slowly immersed into the growth solution, at the same time the water bath temperature was adjusted by decreasing 1.0 °C (i.e. to $T_{\text{equi}}-0.5$ °C). Therefore, the seed crystal would slightly dissolve due to the temperature being higher than T_{equi} at the beginning, and then started to grow after the growth solution reached the bath temperature.

By lowering the water bath temperature by 0.5 °C⁶ every 12 hours, the seed crystal had been growing larger. The crystal growth was completed when the crystal reached the desired size. Each growth circle for a large single crystal could take 2~3 weeks. Crystal was picked up and quickly dried by soft tissue, and wrapped with several layers of soft tissues to let the crystal slowly cool down to room temperature.

⁶ The temperature modulation of 0.5 °C every 12 hours corresponds to the cooling rate of 1.0 °C/day. For other cooling rates of 0.125 °C/day and 0.5 °C/day, the corresponding modulation was 0.0625 °C/day and 0.25 °C/day, respectively.

4.5 ICP-OES

In order to determine the effective segregation coefficient of dithionate ions ($S_2O_6^{2-}$) in the doped sodium chlorate ($NaClO_3$) as-grown crystals, in the current study the quantitative determination for $S_2O_6^{2-}$ in bulk crystals grown from various doping concentrations were performed by the elemental analysis method of inductively coupled plasma optical emission spectrometry (ICP-OES) where sulphur concentration is measured. ICP-OES measures the light emitted from thermally excited sample ions which is with element specific characteristic wavelength. This intensity of the light is separated and measured in a spectrometer, and converted to an elemental concentration by comparison with elemental standards. This study employed third party service provider Butterworth-Laboratories for such ICP-OES measurements.

The measurement was done with confidence since the sulphur concentrations in the specimens were far above the detection limit of the instrument which is ~ 1 ppb (10^{-3} ppm). Powder specimens were prepared from grinding crystal plate cut from the growth sector of $\{ \bar{1} \bar{1} \bar{1} \}$ type of doped crystals. Sulphur concentration was measured and then converted into the concentration of $S_2O_6^{2-}$ ion.

4.6 Powder X-Ray Diffraction (PXRD)

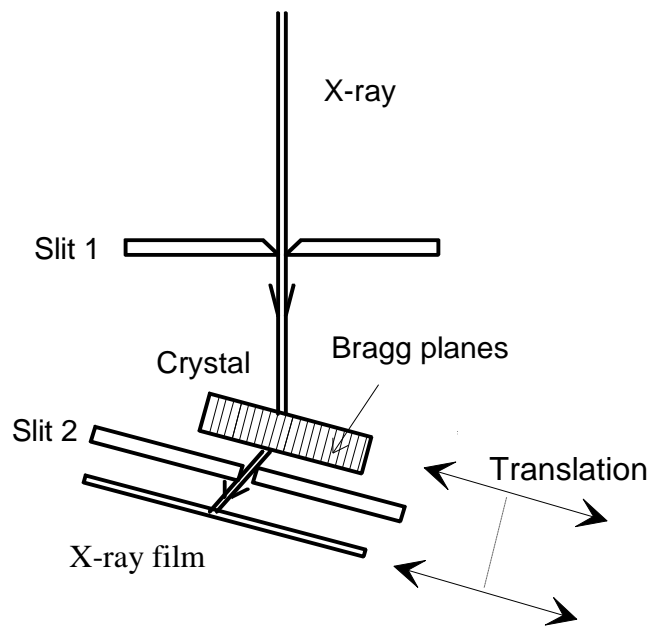
The powder obtained by grinding crystal pieces cut from pure and doped single crystals (include 70ppm, 130ppm, 160ppm, 190ppm and 220ppm) was examined by PXRD using Philips PanAlytical Diffractometer. X-ray generated from a copper tube running at 40 kV x 40 mA was employed, and a 0.5mm slit was inserted between the X-ray source and the sample. The 2θ was scanned from 5° to 80° with step size 0.017° for all samples. In addition, a rotating spinner was used at the sample stage. The powder diffractograms were analyzed by Rietveld Refinement in PanAlytical Highscore Plus, referring to the crystal structure data ICSD-1301 (Abrahams and Bernstein, 1977).

4.7 X-Ray Topography

4.7.1 Experiment Setup

X-ray topography with its various techniques is a highly powerful non-destructive method for the visualization and characterization of defects in single crystals. In the present study the transmission method by Lang (1959) with a conventional molybdenum X-ray tube has been applied. A review particularly devoted to the topography of twinned crystals has been presented by Klapper et al. (1987).

The topographic camera employed here is composed of three main components, i.e. a Mo X-ray source providing a proper beam line followed by the collimator and slits, a sample stage, a film holder to upload the X-ray film and a solid X-ray detector at the end. The experimental arrangement is schematically shown in Figure 4.4a and the photograph of the instrument employed is shown in Figure 4.4b:



(a)

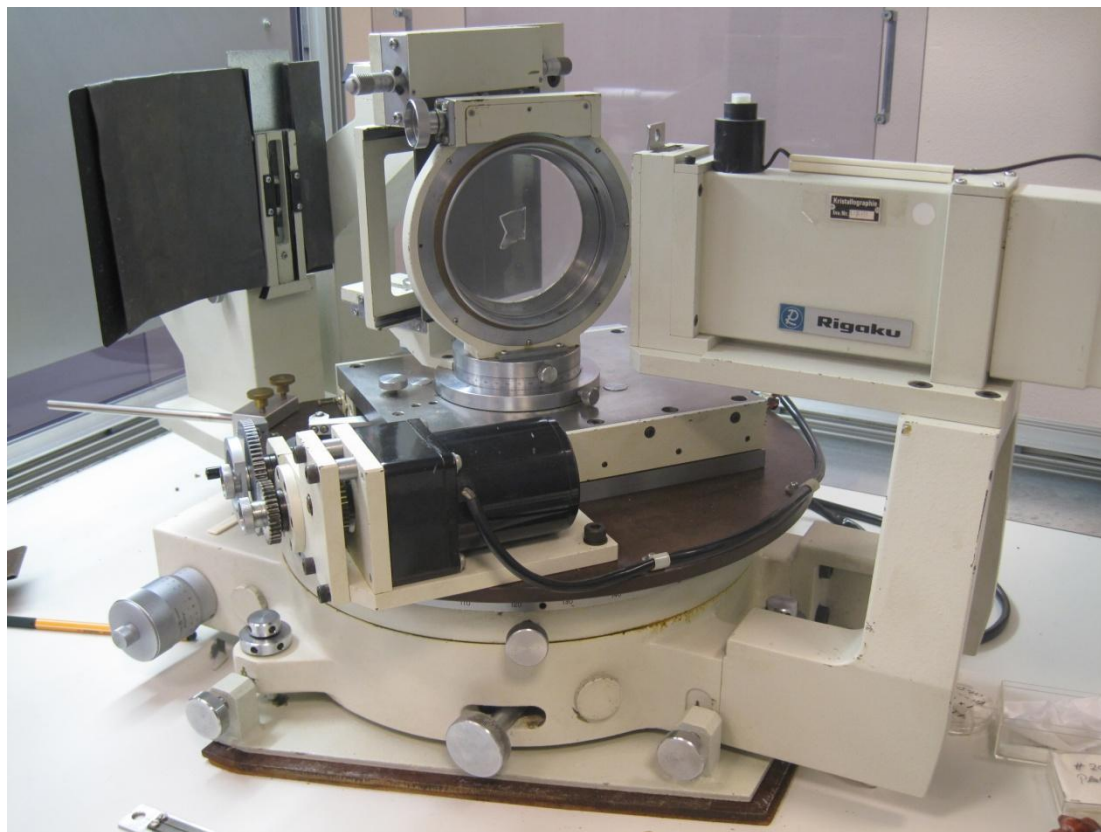


Figure 4.4 Schematic representation and photograph of the employed Lang's Camera for x-ray topography. (a) Schematic representation of Lang's camera. (b) Photograph of the employed Lang's Camera (the X-ray tube was located on the right hand side is not included in the photo).

4.7.2 Sample Preparation and Recording the Topograph

The sample plates were cut parallel to (010) or ($\bar{1}\bar{1}0$) according to the convenience for observation of dislocation lines. A tungsten wire solvent saw, with water as solvent, was used to cut crystals to prepare crystal plates for topography. The plates were wet polished, quickly rinsed and dried with fine tissues. The final thickness of the crystal plates was about 1.5 ± 0.1 mm.

To characterize dislocation high spatial resolution is desirable for better observation. Reflections of strong and low order are most suitable. In the current study, the reflections of 002, $\bar{1}\bar{1}\bar{1}$ and 120 have been selected for use.

To take a topograph, the positions of the crystal plate and film was first well aligned according to the chosen reflection plane (see the procedure described in Appendix I). The X-rays generated from the Mo X-ray tube are collimated by Slit1 (Figure 4.3) to obtain a narrow beam with small divergence to achieve a clear image of the dislocations. The incident beam is diffracted by the chosen set of crystallographic planes and through Slit2 the transmitted beam will be stopped while only the diffracted beam arrives at the X-ray film. The crystal and the X-ray film will both be traversed under the X-ray beam to get the image of the entire crystal. Each run took approximately 5 – 10 hours, depending on the traversing distance.

At the end of each exposure to the X-ray, the film used for recording the topographic image was removed from the holder in a dark room. It was then processed through development, washing, fixing, washing and drying. At last, the film was digitalized by electronic scanner (EPSON V750 Pro).

4.8 Polarized-light Microscopy

A simple arrangement with a light source, two polarizers and a high-resolution camera was used. The crystal plates were placed between the polarizers which were first adjusted to the crossed position (Figure 4.5). Sodium chlorate shows a rather high dispersion of the specific rotation with wavelength. Thus twin domains of opposite optical rotation appear in white light by different colours and are thus easily recognised. Since in a cubic crystal, free of birefringence, the optical rotation power is independent of the direction of the light beam (isotropy), this holds for any orientation of the crystal plates. The optical activity of the crystal is identified by rotating the analyser clockwise from the crossed position while observing the colour change. The change of colour in the order of blue, violet and yellow indicates the crystal to be dextrorotary (D-), while the opposite order indicates levorotary (L-) (Bunn 1961, p.90).

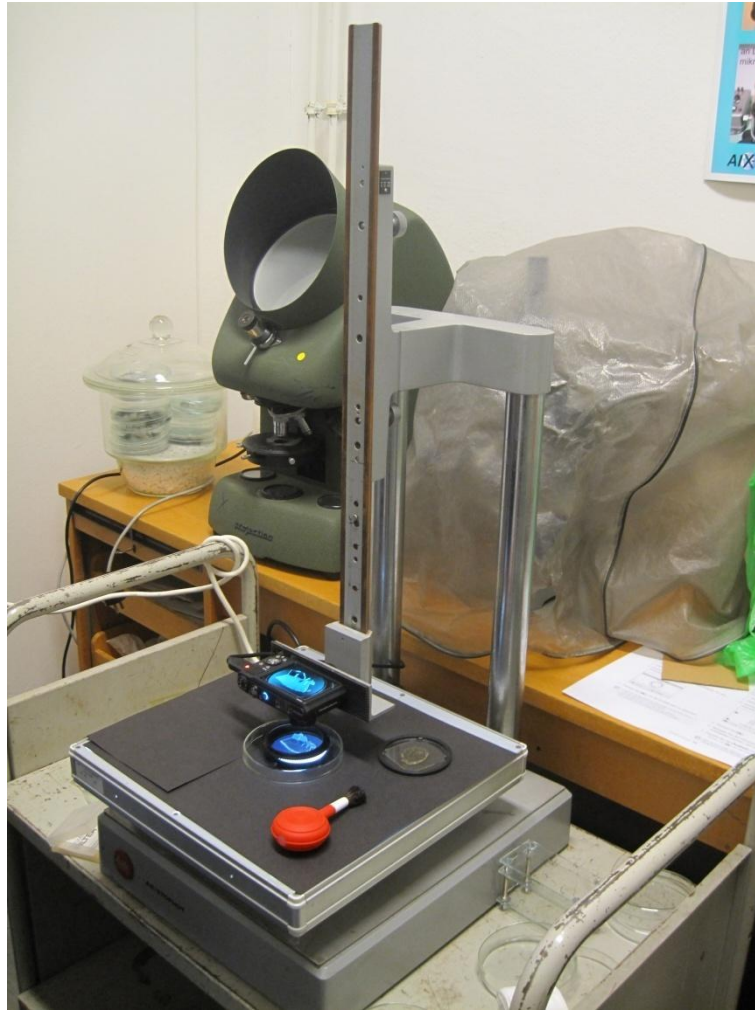


Figure 4.5 The instrumental set up of polarized optics for determining the optical activity of a single crystal plate.

4.9 X-Ray Multiple-wave Diffraction

4.9.1 Experiment Setup

The high-resolution X-Ray Multiple-wave Diffraction (XRMD) measurements of sodium chlorate (NaClO_3) crystals were carried out at beamline XRD1 at the Brazillian Synchrotron Radiation Facility (LNLS) in Campinas, Brazil (Figure 4.6). The synchrotron possesses a storage ring maintaining energy at 1.37 GeV with a beam current of 250mA.

The incident X-ray beam used in this study was of wavelength $\lambda=1.5498\text{\AA}$, as defined using a silicon (111) monochromator. The Huber multi-axis diffractometer as set up on the beamline composed of a three-axis goniometer (2θ , ω , and ϕ) and a χ rotatable table was the main operational instrument for XRMD measurements (Figure 4.7). There is a goniometer head mount on the top of the three-axis goniometer which can provide crystal tilt in the ω direction and its normal direction as well as movement (Δx , Δy) parallel to the rotation plane of ϕ . A Cyberstar scintillation detector rotates independently as 2θ during the measurements. The minimum step size of both ω and ϕ was 0.0005° . The axis of χ rotation is collinear with the direction of the incident beam, thus the beam polarization can be varied by rotation of the χ table. Here, the angle $\chi=0^\circ$ corresponds to orientation of the synchrotron storage ring plane, and $\chi=90^\circ$ corresponds to the normal to direction. In the current thesis, all measurements were done under the condition $\chi=90^\circ$. All the motors' movements were operated by a station computer with controlling and data acquisition software.

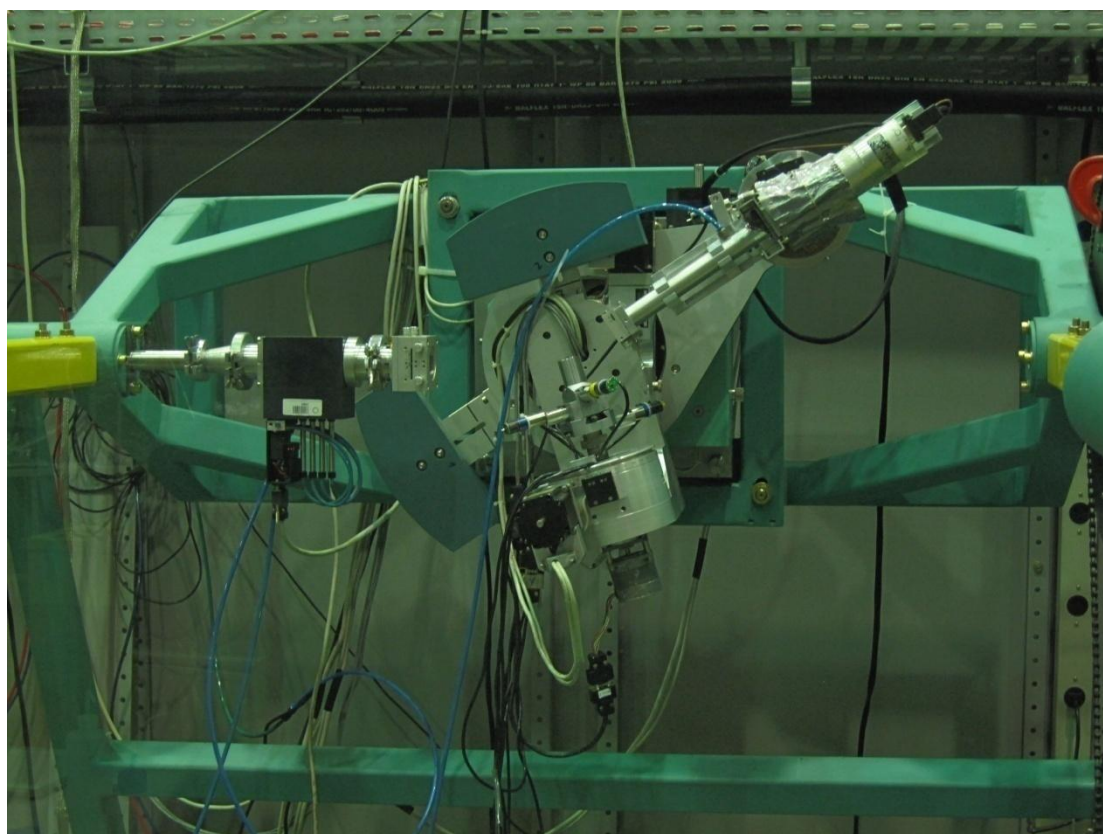


Figure 4.6 The instrumental set-up at beamline XRD1 at the Brazillian Synchrotron Radiation Facility (LNLS). The incident X-ray beam produced from the storage ring comes from the left-hand side.

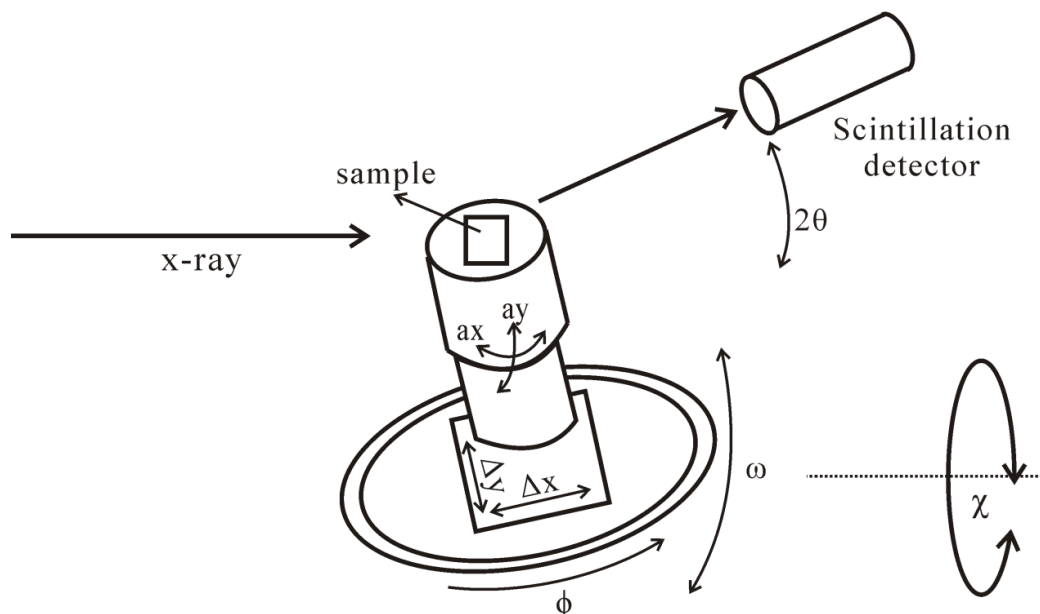


Figure 4.7 Schematic illustration of the beamline set-up for measuring XRMD at XRD1, LNLS.

4.9.2 Renninger Scan and $\omega:\phi$ Mapping

The samples used for XRMD measurements were cut parallel to (001) planes from various sodium chlorate (NaClO_3) single crystals of different dithionate doping concentration, using the solvent saw (section 4.7.2). The doping concentrations of measured crystals included pure, 70ppm, 130ppm, 160ppm, 190ppm and 220ppm. Crystal plate of thickness of approximately 5 mm was mounted to the sample stage by rubber cement (Marabu Fixo Gum).

Before recording the scans, the crystal must essentially be aligned to maintain a very good parallel relationship between the (001) planes and the rotation plane of ϕ . See Appendix II for the detailed alignment method.

In order to obtain most positive peaks (“umweganregung”, section 2.6.3.2) in the Renninger Scan (RS) mode, the primary reflection of XRMD was preferably selected as (004) reflection, due to its low reflectivity (i.e. low structure factor). (004) RS was performed by rotating ϕ in the angular range of $\phi = -25 \sim 105^\circ$; with step size $\phi = 0.002^\circ$. In addition, the $\omega:\phi$ maps for (120) three-beam BSD (Bragg surface diffraction) case were also taken by using (004) as primary reflection, by scan ω from

28.24 °~ 28.38 °(step size 0.002 °) at each rotation of ϕ by step size 0.002 °from 23.56 ° ~ 23.82 °.

Besides, for the purpose of discriminating the different effects of the proposed affected planes of $(1\bar{1}1)$ and $(\bar{1}11)$ and unaffected planes of (111) and $(\bar{1}\bar{1}\bar{1})$, (002) reflection was also employed. This was because the above secondary reflections can be BSD cases (schematic illustration in Figure 4.8) under the primary reflection (002) , which are sensitive to the surface strain of the sample. Step size for scanning was $\phi = 0.0006^\circ$. The penetration depth for a BSD scan is approximately 100 ~ 300Å (Chang, 2004).

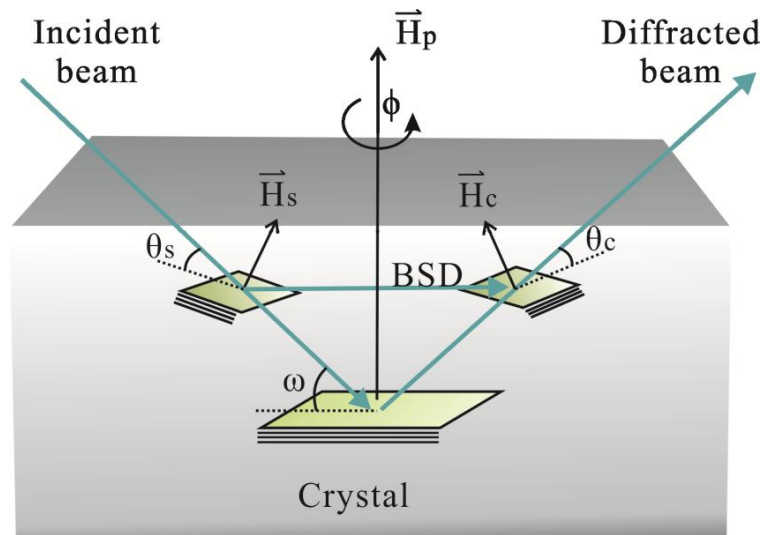


Figure 4.8 Schematic representation for the beam propagation paths of a typical three-beam case under X-ray multiple-wave diffraction condition in real crystal space. \vec{H}_p is the diffraction vector of the primary diffraction plane, \vec{H}_s is the diffraction vector of the secondary diffraction plane, \vec{H}_c is the diffraction vector of the coupling diffraction plane. ω , θ_s and θ_c corresponds to the incident angles of the primary diffraction, secondary diffraction and couple diffraction, respectively. ϕ is the rotation axis normal to the primary diffraction planes.

4.9.3 Data Analysis

In the scientific program Origin, the (002) Renninger Scans and (004) Renninger Scans were first both normalized against the same background intensity of 2850 (a.u.). Each scan was then subtracted by a baseline which passes through the background line.

The program UMWEG (Rossmanith, 2003), capable of calculating the multiple-wave diffraction pattern as intensity versus ϕ angle, was used to index the RS peaks and simulate an RS pattern for fitting the experimental data. The calculation using the UMWEG program solely requires an input file written in ASCII, which can be done by Notepad in Windows. The key items in the input file include lattice parameter, wavelength of incident beam, range of ϕ scan (default rotation direction: Huber-HasyLab-4 circle), number of steps per degree, space group number, number of atoms in the asymmetric unit and atom positions.

During the simulation for the $\{111\}$ and $\{\bar{1}\bar{1}\bar{1}\}$ peaks in 002 Renninger Scans, the lattice parameter was used as input file. For scans of different crystals, the lattice parameter was varying. All the lattice parameters were recorded and tabulated.

The original data of $\omega:\phi$ maps scanned for the BSD case (120), was normalized against the highest peak intensity of all the maps in program Origin (reference intensity was 4225 a.u.). By setting ϕ as the x axis, ω as the y axis and the detector signal as the z axis⁷, the whole datasheet was converted into matrix. Then the matrix was plotted as a contour plot to form the map.

For mosaic spread, the rocking curves of 120 BSD reflection were derived from the original data of $\omega:\phi$ maps, and plotted as a function of the angle of ω (for $\eta_{\text{perpendicular}}$) and ϕ (for $\eta_{\text{in-plane}}$). The scans of rocking curves were then normalized against the same background intensity of 2850. Then, in Origin package, the diffraction peak on the rocking curve was fitted by Gaussian function. The fit results can give peak width as FWHM (full width at half maximum) and the corresponding error. Following the calculation equation below:

⁷ Data in “detector signal” was converted to $\log_{10}(\text{detector signal})+1$, in order to obtain smooth variation and avoid “0” when converting to matrix.

$$\eta_{perp.} = \frac{FWHM(\omega)}{2.355} \quad (4.1)$$

$$\eta_{in-plane} = \frac{FWHM(\phi)}{2.355} \quad (4.2)$$

where $\eta_{in-plane}$ is the mosaic spread in the plane of the primary reflection, $\eta_{perp.}$ is the mosaic spread in the plane normal to that, and the constant 2.355 is derived from the relationship between the angular distribution of the mosaic blocks and the actual deviation from the Bragg angle (Freund et al., 1996).

4.10 X-Ray Absorption Fine Structure

4.10.1 Experiment Setup

The X-Ray Absorption Fine Structure (XAFS) measurements of sodium chlorate (NaClO_3) crystals were carried out at the synchrotron beamline I18 (Figure 4.9) of Diamond Light Source, Oxfordshire, UK. Diamond synchrotron possesses a storage ring maintaining energy at 3 GeV with nearly constant currents of 300mA. Scanning of beam energy can be performed by a Si (111) monochromator. Beam slit before the illuminated sample was about 0.1mm V by 0.2mm H. A nice 4-element Si Drift detector (Vortex ME-4) was employed at beamline I18 to measure the fluorescent X-ray. Beam energy was calibrated by beamline scientists prior to the measurements. The beam flux at sample was approximately 4×10^{12} ph/s at 10 keV.

A two-axis sample stage capable of providing rotation of θ and ω was used (Figure 4.10 and 4.11). The rotation planes of θ and ω were perpendicular to each other, while that of θ is parallel to the orbital plane. The sample stage, fluorescence detector and ion chamber for monitoring I_0 are all covered by the protective environment filled with helium gas (Figure 4.10).



Figure 4.9 The instrumental set-up at beamline I18 of Diamond Light Source. The incident X-ray beam produced from the storage ring comes from the upper right side in the photo.



Figure 4.10 Photograph of the sample environment filled with helium gas. The propagation path of the X-ray was fully covered by helium gas, to reduce the scattering and absorption of soft fluorescent X-ray by air.

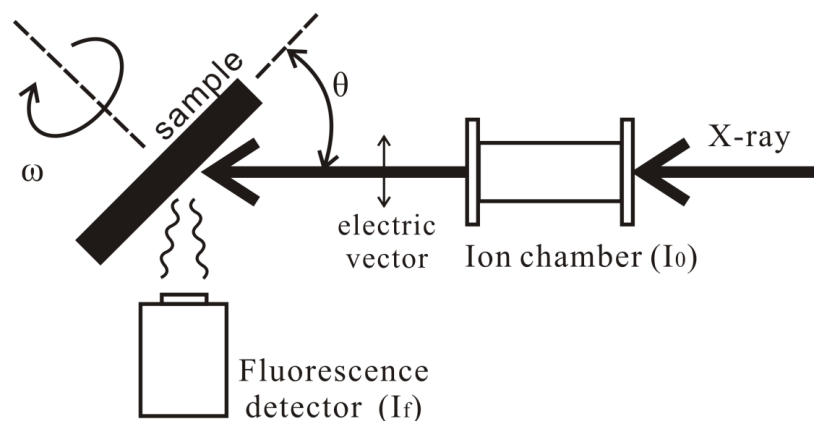


Figure 4.11 Schematic illustration of the beamline set-up for measuring XAFS at Diamond I18.

4.10.2 Sample and Data Acquisition

h) Sample and experimental geometry

A $(\bar{1}10)$ crystal plate was cut from 190ppm $S_2O_6^{2-}$ -doped $NaClO_3$ crystal for EXAFS measurements and X-Ray Fluorescence (XRF) mapping. In such a cutting direction the sulphur-sulphur bond is assumed to align perpendicular to one of the edges (Figure 4.12), based upon the speculated structural model for the incorporation of $S_2O_6^{2-}$ in $NaClO_3$ crystal by Ristic (1993; 1994). Besides, the XANES spectra were measured at various orientations on the $(\bar{1}\bar{1}\bar{1})$ surface of 800ppm doped crystal.

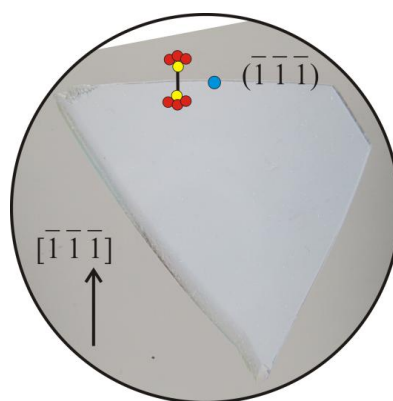


Figure 4.12 The $(\bar{1}10)$ crystal plate was cut from 190ppm $S_2O_6^{2-}$ -doped $NaClO_3$ crystal for polarized EXAFS. The blue spot indicates the sampling position on the plate. The $S_2O_6^{2-}$ is illustrated schematically in the figure on the $(\bar{1}\bar{1}\bar{1})$ face.

Polarized EXAFS spectra were collected on the edge of the $(\bar{1}\bar{1}\bar{1})$ sector (thus the sampling spot is close to the $\{\bar{1}\bar{1}\bar{1}\}$ surface) in the 190ppm $(\bar{1}\bar{1}0)$ plate at two orientations – one maximizing the EXAFS from second shell sulphur by fixing the electric field vector \vec{e} of X-ray beam parallel to the sulphur-sulphur bond of $S_2O_6^{2-}$, the other minimizing that EXAFS by fixing the \vec{e} perpendicular to sulphur-sulphur bond (Figure 4.13). The XRF mapping was also collected on the same sample.

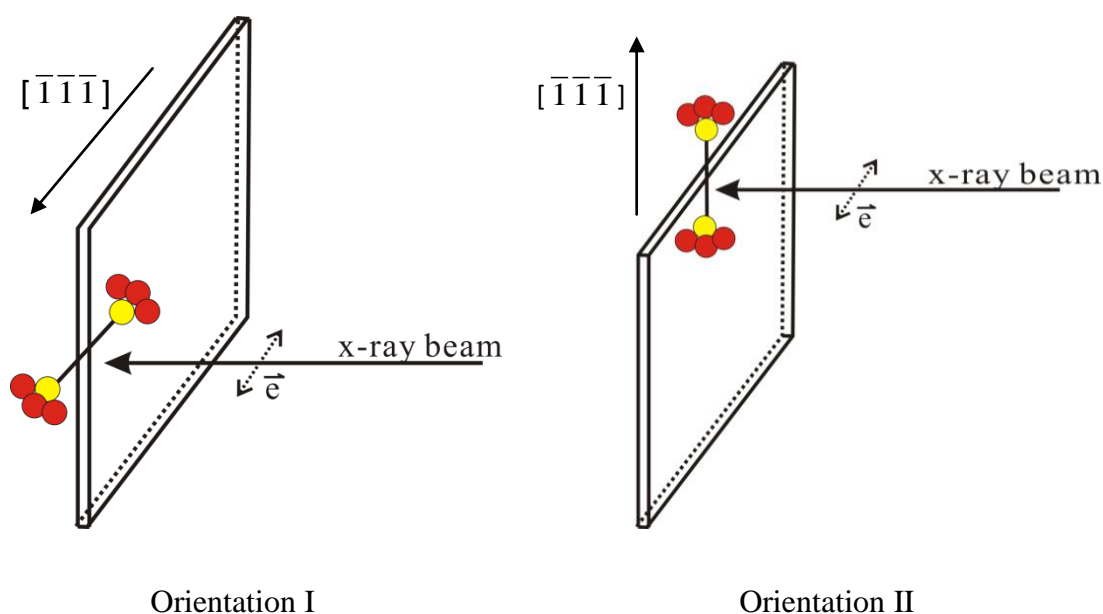


Figure 4.13 The crystal was first aligned to make the sulphur-sulphur bond (along $[111]$ axis) parallel to the electric field vector \vec{e} of beam (orientation I), in order to enhance the EXAFS signal from second shell atom sulphur (first shell atom is oxygen). Then the plate was rotated 90° along its normal direction to make the sulphur-sulphur bond perpendicular to the electric field vector (orientation II).

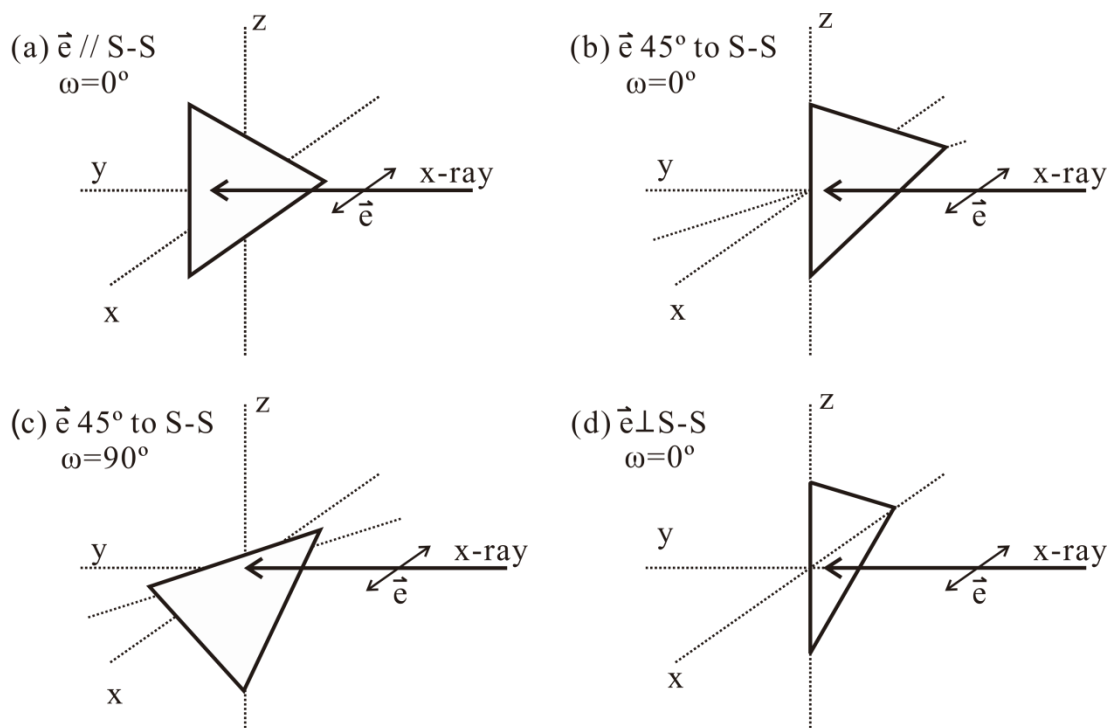


Figure 4.14 The geometries used for XANES measurement on a 800ppm sample. The triangle represents the tetrahedral surface on which the XANES was measured. XANES spectra on 800ppm $\text{S}_2\text{O}_6^{2-}$ -doped NaClO_3 crystal were collected at 4 orientations, in order to precisely determine the molecular orientation of the impurity on the $(\bar{1}\bar{1}\bar{1})$ surface by experimentally probing its electronic structure. The geometries used in the experiment are shown in Figure 4.14.

The practical position of the experimental X-ray spot are roughly shown in the figures. ω was the angle rotated along the S-S axis (i.e. $[\bar{1}\bar{1}\bar{1}]$ crystal axis). The zero position of ω is shown in (a) and 90° is shown in (c), where the clockwise rotation was defined as “+” and anticlockwise “-” if observing along the X-ray incident direction.

i) Scan parameters

The EXAFS and XANES spectra were measured using the same scan parameters at the sulphur K-edge with the pre-edge region from 2400.0 to 2466.0 eV at a step size of 5 eV, the edge region from 2466.0 to 2487.25 eV at a step size of 0.25 eV, and the post-edge region from 2487.25 to 2815.85 eV.⁸ The counting times for signal at each

⁸ The k-edge of Cl at 2822 eV, is closely following the S k-edge and limiting the collection of k-edge EXAFS for S.

step were set to 0.5 second at the pre-edge, 1 second at the edge region and 6 seconds at the post-edge region.

The XRF map was collected with a fixed incident energy of 2700.00 eV. The beam slit before the sample was about 0.1mm V by 0.2mm H. The scans were carried out across a specific area of the sample, during which the step sizes in the x and y directions were both 0.5 mm. The fluorescence signal at each spot was collected for 1.0 s. The energy-window was set to sulphur K α at around 2307 eV, so that only the specific fluorescence photons were recorded.

4.10.3 Data Analysis

j) EXAFS analysis

The program Demeter (latest version 0.9.17) (Ravel and Newville, 2005) based on FEFF and IFEFFIT, was used to process and analyze the EXAFS. The two graphical user interface (GUI) packages integrated in Demeter, i.e. Athena and Artemis, were employed jointly.

EXAFS raw data was first *imported* into Athena and converted to $\mu(E)$ according to Equation 2.36 ($\mu(E) \propto I_f / I_0$) under the fluorescence mode. Since the experimental measurements were repeated 4 times at each orientation, the scans were *merged* and *averaged*. During the measurements the EXAFS data was collected as long as it can, however, it terminated at the appearance of the chlorine edge which is one of the main compositions of the crystal. As a result, EXAFS data after 2770.00 eV was *truncated* (abandoned).

Next, the data was *normalized* in Athena by defining the three parameters of “ E_0 ”, “pre-edge range” and “normalization range”. “ E_0 ” was initially set to the energy of first peak on the first derivative of $\mu(E)$. “Pre-edge range” and “normalization range” were used to define two regions of data, i.e. pre-edge region and post-edge region. After the two ranges had been set, a line is regressed to the data in the pre-edge region and a polynomial for the post-edge region, where the latter can be varied by adjusting the “normalization order” parameter. The normalization constant (also named “edge step”), $\mu_0(E_0)$, was automatically evaluated as the vertical difference between the extrapolation of the pre-edge and post-edge lines at the E_0 . Once the above steps were

done, then the pre-edge portion was subtracted and brought down to near $y=0$ line, and the post-edge portion after “ E_0 ” was subtracted and flattened to near the $y=1$ line. By defining the “Rbkg” parameter the internal algorithm “Autobk” in Athena would produce a piece-wise spline as a background line to remove the low frequency Fourier components from the data $\mu(E)$. At the same time, $\chi(k)$, the difference between the experimental $\mu(E)$ and the background spline were normalized and converted from energy into photoelectron wavenumber. Then, the $\mu(E)$ can be Fourier transformed into R-space in Athena, for the purpose of checking the quality of background subtraction. At this stage, the data can be saved as a project file (*.prj).

Artemis was used for fitting the EXAFS, based on the theoretical EXAFS paths (including amplitudes and phases) calculated by FEFF 6 (Rehr et al., 1992). The input file for FEFF was created by importing a structural model (which is shown together with the results in a later chapter) into the program ATOM and designating the sulphur atom as the core atom. At the same time, the EXAFS data saved as an Athena project file was imported into Artemis. Artemis was then used to perform least-squares fitting of the theoretical EXAFS to the experimental data. There are many variable parameters during the fitting, but to perform a fitting the amount of variable parameter should not exceed N_{idp} (independent number, $\approx 2\Delta k\Delta R/\pi$). During the fitting procedure, the parameters of “ ΔE_0 ” (shift of edge position E_0) and “ S_0^2 ” (amplitude reduction factor) were refined while being uniformly applied to all scattering paths. The “ ΔR ” (variation of absorber-scatterer distance) and “ σ^2 ” (mean square displacement) were unique for each path and were refined for all scattering paths. The coordination number “N” was refined as well, in order to approach the effective coordination numbers of different scatterers under the experimental conditions using the polarized beam and orientated sample. The EXAFS fittings were performed well for first shell and second shell, but the third shell was not fitted with confidence due to high noise and limited k range.

k) XANES analysis

The XANES spectra were also *merged, truncated and normalized* according to the method described above, using the same package Demeter. However, in order to well interpret the XANES, here it needs to quote the partial density of states (PDOS) and unoccupied molecular orbital of $S_2O_6^{2-}$ ion which were calculated by Dr.

Che Seabourne (Lan et al., 2014) using the CASTEP pseudopotential DFT code (Pickard, 1997; Clark et al., 2005; Gao et al., 2008; Gao et al., 2009). The calculation was carried out in the ground electronic state. The basis set size was controlled by the choice of kinetic energy cut-off value, which was set at 725 eV. The system was sampled in reciprocal space using a Monkhorst-Pack grid of k points separated by 0.067\AA^{-1} (Monkhorst and Pack, 1976; Lan et al., 2014). The PDOS from Seabourne's calculation was used to compare with the experimental XANES. With the current author's efforts, the unoccupied orbitals were selected according to the appropriate energy windows after the comparison between PDOS and experimental XANES. Then, the slices crossing the volume of the specific unoccupied orbitals have been created by considering the real rotation of $\text{S}_2\text{O}_6^{2-}$ on the $(\bar{1}\bar{1}\bar{1})$ surface of NaClO_3 crystal. According to the proposed structural model by Ristic et al. (1993; 1994) of $\text{S}_2\text{O}_6^{2-}$ impurity on $(\bar{1}\bar{1}\bar{1})$ surface of NaClO_3 crystal, one SO_3 group of $\text{S}_2\text{O}_6^{2-}$ should retain the same orientation as that of the substituted ClO_3^- (cf. Figure 8.2 for more information). The orientations of ClO_3^- at different ω positions (section 4.10.2) used in the XANES measurement of 800ppm sample (cf. Figure 4.14) are shown below:

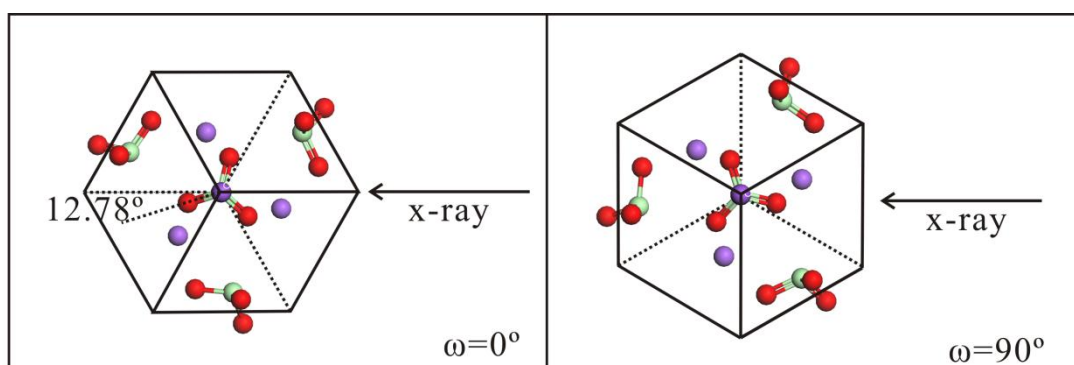


Figure 4.15 The molecular orientation of ClO_3 on $(\bar{1}\bar{1}\bar{1})$ surface of NaClO_3 crystal. The ClO_3 at the centre of the two figures is the one substituted by impurity.

l) XRF-Map analysis

The XRF maps were reconstructed using the package PyMCA (Solé et al., 2007). After importing the raw data into PyMCA, the data of sulphur $\text{K}\alpha$ emission against mapping positions in x and y can be exported as a colour RGB map.

4.11 Molecular Modelling

In this study, the atomic charge calculations were performed for both ClO_3^- and $\text{S}_2\text{O}_6^{2-}$ ions by program MOPAC2009. The calculations used the semi-empirical method PM6 (Stewart, 2007), and the spin states of Singlet as default. The input for atom coordination number was XYZ, for which the values were derived from the crystal structures deposited in the Inorganic Crystal Structure Database (ICSD) under reference code icrd-1301 (Abrahams and Bernstein, 1977) and icrd-26326 (Kirkel et al., 1980).

The structural model for the impurity incorporation was explored using the visualization program Material Studio (MS). The cif format files containing the structures, derived as described above, were imported into MS to observe and discuss their structure, chemistry of specific surfaces, etc.

4.12 Conclusions

This chapter detailed the chemicals NaClO_3 and $\text{Na}_2\text{S}_2\text{O}_6 \cdot 2\text{H}_2\text{O}$ which were used in this study, as well as their crystallographic information. It also described all the experimental and computational methods employed in this study. The study of the meta-stable zone width using turbidity detection and the growth of single crystals using the temperature-controlled crystal growth unit were detailed. Instrumental details, data acquisition process and data analysis methods for the determination of crystal defects by X-ray topography, crystal lattice distortion by X-ray multiple-wave diffraction and local environment of $\text{S}_2\text{O}_6^{2-}$ by X-ray absorption fine structure were discussed in depth. The computational methods adopted to explore the crystallographic and chemical texture and of the system and set-up rational molecular model for the habit modification process were also described. In addition, the operation of other methods which assisted in the study, such as ICP-OES, PXRD and optical microscope, have also been summarized in this chapter.

CHAPTER 5

Crystallization Kinetics, Crystal Growth and Habit Modification of NaClO₃

Summary:

Results and discussion about the effect of Na₂S₂O₆ on the meta-stable zone width and crystal habit of NaClO₃.

5.1 Introduction

This chapter aims to explore the influence of impurity sodium dithionate ($\text{Na}_2\text{S}_2\text{O}_6$) on the metastable zone width of sodium chlorate (NaClO_3) in aqueous solution, and, more importantly, to describe the habit modification of NaClO_3 single crystals grown from aqueous solutions doped with $\text{Na}_2\text{S}_2\text{O}_6$. The metastable zone width of NaClO_3 in aqueous solution was determined as a function of impurity concentration, at three different cooling rates. Pure single crystals were grown at different cooling rates to observe the influence of cooling rate on the crystal habit, in order to fully understand the habit of the pure crystal which is necessary for the comparison with doped crystals. Doped single crystals were grown with different impurity concentrations, ranging from 40ppm to 1500ppm in mole ratio¹, to observe the habit modification of NaClO_3 in the presence of various impurity concentrations. Twinned crystals formed in solutions doped with relatively high impurity concentration. In order to observe the morphology transition process between the opposite faces of $\{111\}$ and $\{\bar{1}\bar{1}\bar{1}\}$, pure seed with $\{111\}$ faces were seeded in doped solution to grow, and doped seed with $\{\bar{1}\bar{1}\bar{1}\}$ faces was seeded in pure solution to grow. In order to study the segregation coefficient of the impurity in NaClO_3 crystal, the impurity concentration was measured in different sectors of 40ppm doped crystal, and as a function of doping concentration in different crystals, respectively.

It is significant to emphasize that NaClO_3 crystallizes in space group $P2_13$ which is noncentrosymmetric, thus, the $\{111\}$ facets and their geometrically opposite $\{\bar{1}\bar{1}\bar{1}\}$ facets are crystallographically non-equivalent. The Miller indices of these faces in the current study followed the definition in the previous study by Ristic et al. (1994), in which the coordinates of a D- structure were considered. Thus, the pure tetrahedral faces were referred to as $\{111\}$ and the doped tetrahedral faces were $\{\bar{1}\bar{1}\bar{1}\}$ type.

¹ In this thesis, mole ratio is applied rather than weight ratio, since it well reveals the habit-modifying power of the impurity in the sense of quantity. For example, by 40ppm doped crystal the habit-modifying power of 40 $\text{S}_2\text{O}_6^{2-}$ ions on 10^6 ClO_3^- ions can be estimated by the characterizations in this thesis.

5.2 Effect of Impurity on The Metastable Zone Width

To the author's best knowledge, no characterization on the metastable zone width (MSZW) of NaClO_3 in aqueous solution has been reported before, not to mention the effect of $\text{S}_2\text{O}_6^{2-}$ impurity on the MSZW. So that there is no previous data can be used as comparison. In order to assess the effect of $\text{S}_2\text{O}_6^{2-}$ impurity on the MSZW of NaClO_3 in aqueous solution, the MSZW was measured as a function of impurity concentration, at three different cooling rates of 0.25, 0.5 and 1.0 $^\circ\text{C}/\text{min}$, respectively. The impurity concentrations used were 0, 40, 70, 100, 130, 160, 190, 220, 250, 280 and 310ppm.

Figure 5.1 shows three different curves according to the three cooling rates applied. The first point on each curve represents the MSZW measured for the pure NaClO_3 solution. By comparing the first point of each curve to the other points on the same curve, it can be seen that the MSZW of the pure solution is smaller than that of the doped solutions. Thus, the results indicate that the presence of $\text{S}_2\text{O}_6^{2-}$ impurity has increased the metastable zone width of NaClO_3 in aqueous solution.

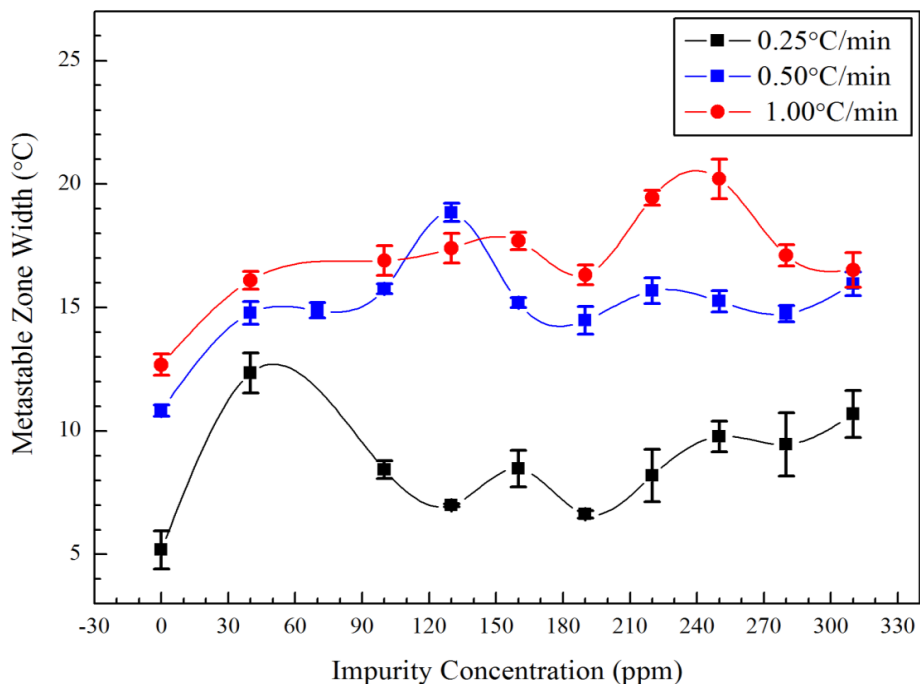


Figure 5.1 The variation of metastable zone width of NaClO_3 in the presence of $\text{S}_2\text{O}_6^{2-}$ impurity. Three curves in different colours correspond to the three cooling rates used in the MSZW measurement. Error bars on the curves indicates the uncertainty of the measurement. The three lines were produced in order to guide the reader for better visualization.

On the MSZW curve at cooling rate of 0.25 °C/min, there is an obvious large peak at impurity concentration of approximately 40ppm (Figure 5.1). By searching through the other two curves of 0.50 °C/min and 1.00 °C/min, there are also such large peak on each of them at about 130ppm and 250ppm, respectively. After the apparent peak in the curves of 0.25 °C/min and 0.50 °C/min (Figure 5.1), the MSZW dropped to a level similar to that before the peak, and continued to increase in a very slow trend with the increase of doping concentration. The appearance of such peaks has been reported for the system of Cu²⁺ and Mg²⁺ doped KCl by Titiz-Sargut and Ulrich (2002), however, the mechanism was reported as unclear. Therefore, it can be concluded here that, there exists an *optimal impurity concentration* in enhancing the MSZW of NaClO₃, after which concentration the enhancing effect keeps growing slowly with the increase of doping concentration.

Through comparing the three curves (Figure 5.1), it is manifest that the cooling rate also affected the MSZW of NaClO₃. That is, the higher the cooling rate is, the larger the MSZW is. Furthermore, the optimal impurity concentration for enhancing the MSZW increased with the increase of cooling rate. At higher cooling rate, the optimal impurity concentration shifted towards a higher doping concentration. This implies that the enhancing effect of the impurity on the MSZW is reduced with the increase of cooling rate.

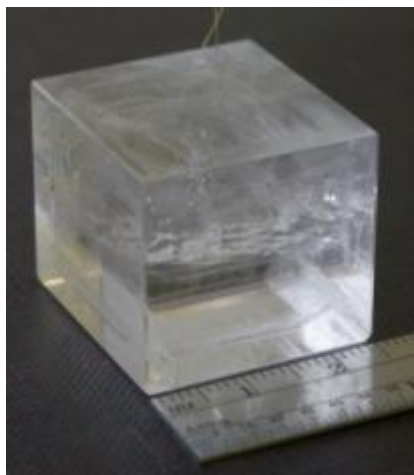
5.3 Habit of Pure NaClO₃ Crystal

Before the exploration into the habit modification of NaClO₃ by S₂O₆²⁻ impurity, for comparison purposes it is necessary to grow pure NaClO₃ single crystals prior to the growth of doped crystals, and fully explore the habit of pure crystal under the current experimental conditions, e.g. the size of the growth vessel, the stirring speed in the solution, etc. Thus, pure single crystals were grown at three cooling rates, i.e. 1.0 °C/day, 0.5 °C/day and 0.125 °C/day.

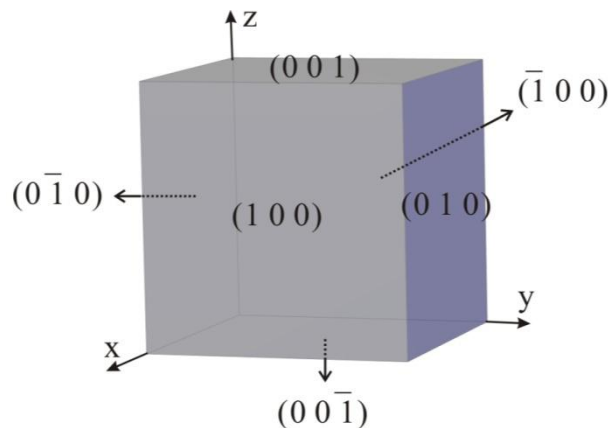
At the relatively high cooling rate of 1.0 °C/day, the crystal habit was found to be dominated by cubic faces of {001} type (Figure 5.2 and 5.3). When the cooling rate was 0.5 °C/day, the habit was dominated by six {001} faces as well as 12 {110} faces

(Figure 5.4). At the low cooling rate of $0.125\text{ }^{\circ}\text{C}/\text{day}$, the tetrahedral faces of $\{111\}$ type (which includes (111) , $(\bar{1}\bar{1}1)$, $(\bar{1}1\bar{1})$ and $(1\bar{1}\bar{1})$) appeared on the final habit, besides the $\{001\}$ and $\{110\}$ faces (Figure 5.5). To sum up, $\{001\}$ faces dominated the habit at high cooling rate, while the $\{110\}$ faces appeared at a moderate cooling rate and the $\{111\}$ faces only emerged at a very low cooling rate.

In addition, in the particular case shown in Figure 5.3, 5 faces of $\{110\}$ type appeared on the edges of the cube at the cooling rate of $1.0\text{ }^{\circ}\text{C}/\text{day}$. However, $\{110\}$ faces are likely to be present on the habit only at lower cooling rates as described above. The appearance of these faces is ascribed to the reduction of effective supersaturation at the growing surface of the seeded crystal, due to the parasitic crystals formed on the bottom of growth solution. Nevertheless, it is worth noticing that not all of the twelve symmetric $\{110\}$ faces appeared. It is also interesting to see that the height of this crystal is smaller than its width, implying that its growth in the $[001]$ or $[00\bar{1}]$ direction was suppressed. These observations will be discussed by combining the topographic results in the next chapter (cf. section 6.3.2).



(a)



(b)

Figure 5.2 (a) Pure NaClO_3 crystal grown from aqueous solution without impurity at the cooling rate of $1.0\text{ }^{\circ}\text{C}/\text{day}$. Habit faces are of $\{001\}$ type. (b) Schematic illustration for the crystal shown in (a).

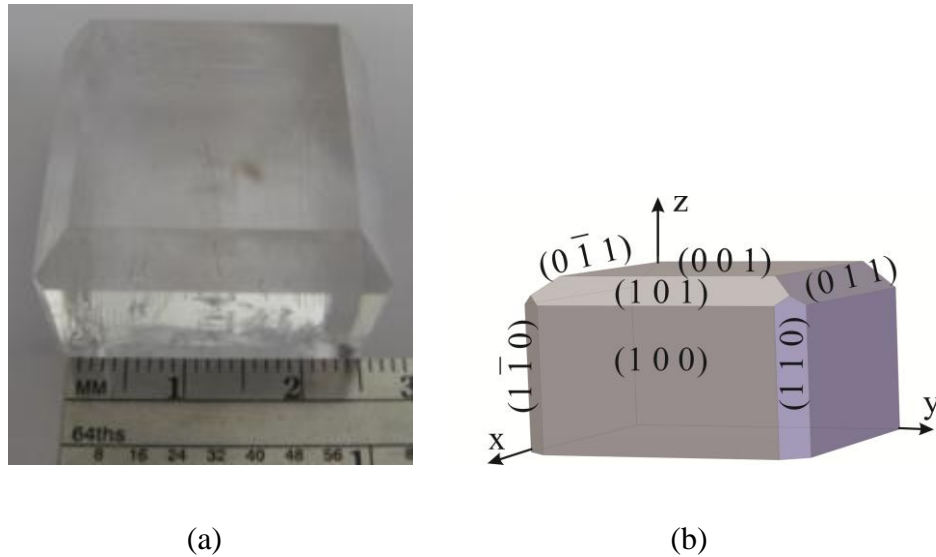


Figure 5.3 (a) Pure NaClO_3 crystal grown from aqueous solution without impurity at the cooling rate of $1.0\text{ }^\circ\text{C/day}$. Parasitic crystals formed in the solution at the bottom of the flask. Habit faces are six $\{001\}$ faces and five $\{110\}$ faces. (b) Schematic illustration for the crystal shown in (a).

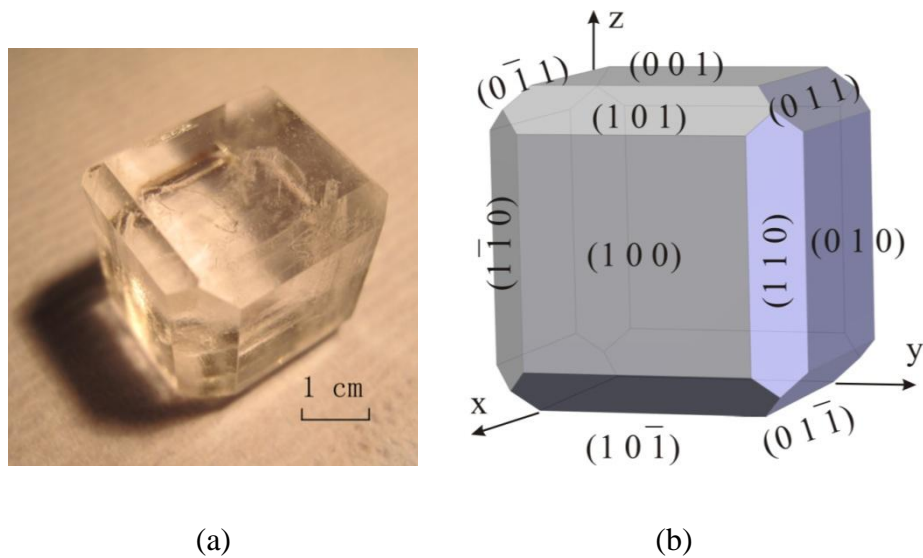


Figure 5.4 (a) Pure NaClO_3 crystal grown from aqueous solution without impurity at the cooling rate of $0.5\text{ }^\circ\text{C/day}$. Habit faces are of $\{001\}$ and $\{110\}$ types. (b) Schematic illustration for the crystal shown in (a).

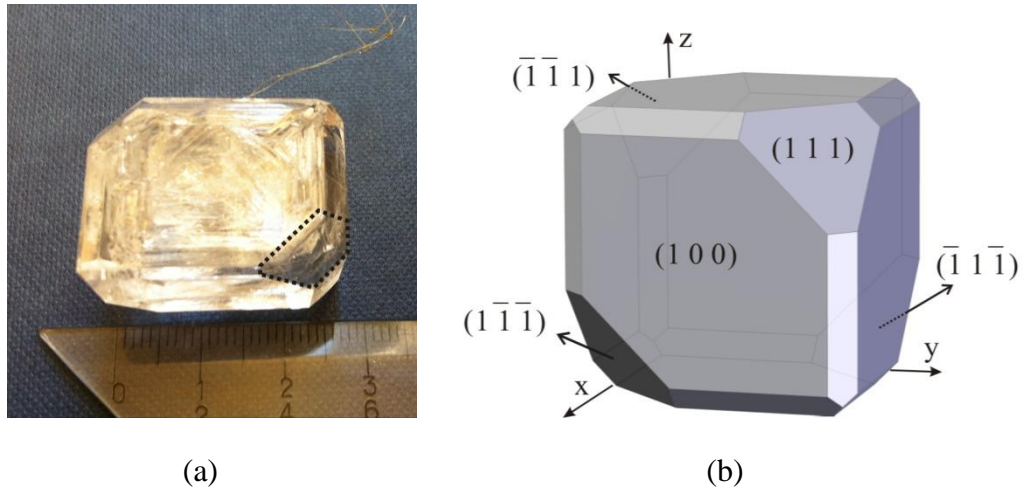


Figure 5.5 (a) Pure NaClO_3 crystal grown from aqueous solution without impurity at the cooling rate of $0.125\text{ }^\circ\text{C/day}$. The (111) face of the crystal is highlighted by tracing with dotted lines since the contrast of the photo is low due to large volumes of inclusions in the crystal. (b) Schematic illustration for the crystal shown in (a).

5.4 Habit Modification of NaClO_3 by The $\text{S}_2\text{O}_6^{2-}$ Impurity

In order to investigate the influence of impurity concentration on the habit modification of NaClO_3 , doped single crystals were grown under different concentrations of $\text{S}_2\text{O}_6^{2-}$, ranging from 40ppm to 1500ppm (mole ratio, $1\text{ppm}=1/10^6$), at the same cooling rate of $1.00\text{ }^\circ\text{C/day}$. The crystals grown at relatively low doping concentration (e.g. 40ppm) present both impurity-induced $\{\bar{1}\bar{1}\bar{1}\}$ faces as well as original $\{001\}$ and $\{110\}$ faces (Figure 5.6a), whereas the crystals grown at relatively higher doping concentrations (i.e. from 70ppm and above) are dominated by impurity-induced $\{\bar{1}\bar{1}\bar{1}\}$ faces (Figure 5.8). Besides, the twinned crystal only formed at very high doping concentrations (Figure 5.11). To clearly describe the habit modification of NaClO_3 , the single crystals and the twinned crystals will be presented separately.

5.4.1 Habit Modification of NaClO_3 at Moderate $\text{S}_2\text{O}_6^{2-}$ Concentration

Doped crystal grown at 40ppm (mole ratio) impurity concentration presents 6 $\{001\}$ faces, 12 $\{110\}$ faces, and 4 symmetric faces of $\{\bar{1}\bar{1}\bar{1}\}$ type (Figure 5.6a). The boundaries between the surfaces of $\{\bar{1}\bar{1}\bar{1}\}$ and $\{001\}$, $\{\bar{1}\bar{1}\bar{1}\}$ and $\{110\}$ showed curved edges instead of straight ones, while the boundaries between $\{001\}$ and $\{110\}$

were the normal straight edges (Figure 5.7). This implies that the unstable growth rate of the $\{\bar{1}\bar{1}\bar{1}\}$ face varied at different regions across its surface.

The final habit of doped crystals grown from solutions doped by 70ppm to 1000ppm $S_2O_6^{2-}$ are typically dominated by large tetrahedral faces of $\{\bar{1}\bar{1}\bar{1}\}$ type, and sometimes $\{001\}$ faces can appear as small flat surfaces at the edges of the tetrahedron (Figure 5.8).

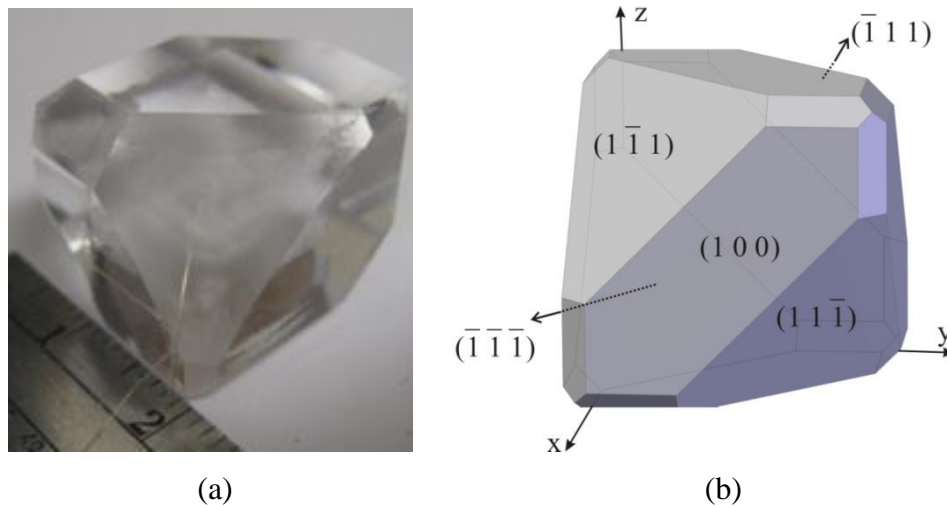


Figure 5.6 (a) NaClO₃ crystal grown from aqueous solution doped with 40ppm $S_2O_6^{2-}$ at the cooling rate of 1.0 °C/day. Predominant habit faces are of $\{\bar{1}\bar{1}\bar{1}\}$, $\{001\}$ and $\{110\}$ types. (b) Schematic illustration for the crystal shown in (a).

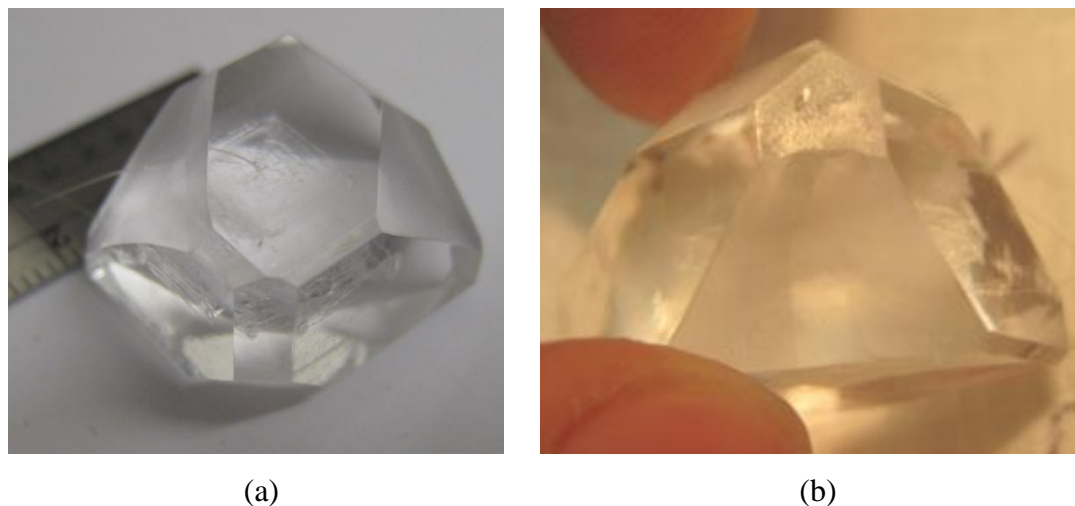


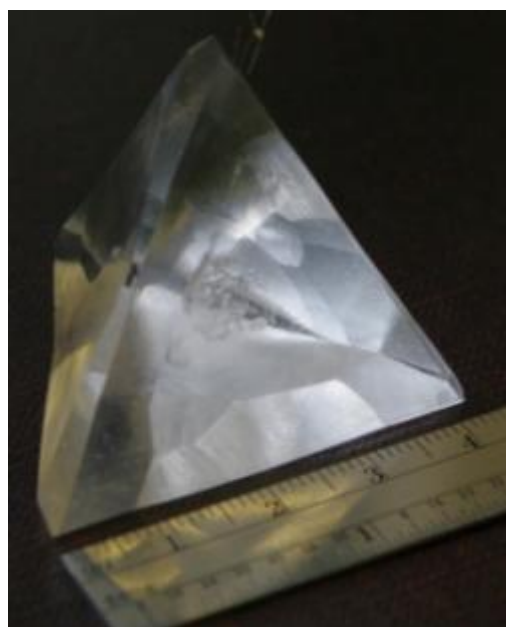
Figure 5.7 The same NaClO₃ crystal doped with 40ppm $S_2O_6^{2-}$ as shown in Figure 5.6, for the purpose of showing the curved edges between $\{\bar{1}\bar{1}\bar{1}\}$ and $\{001\}$ in (a) and that between $\{\bar{1}\bar{1}\bar{1}\}$ and $\{110\}$ faces in (b).



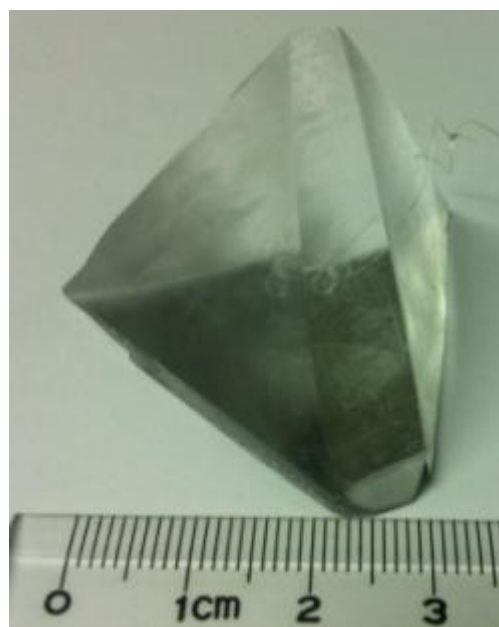
(a) 70ppm



(b) 130ppm

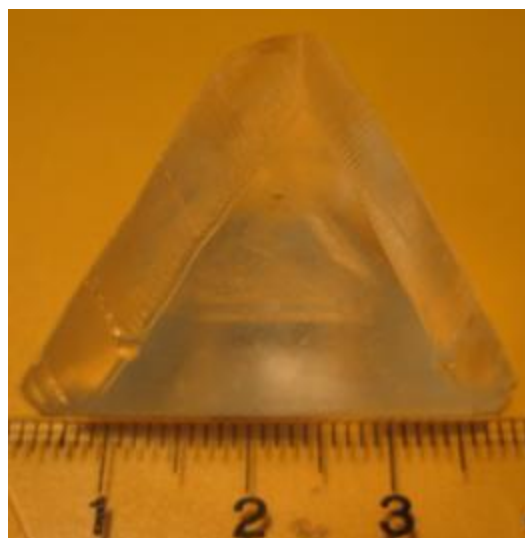


(c) 160ppm

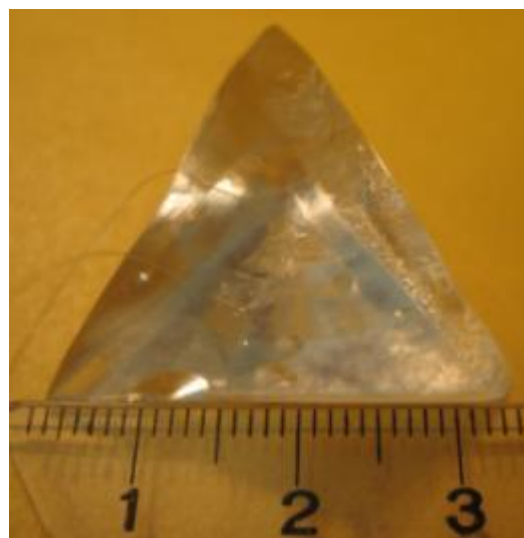


(d) 190ppm

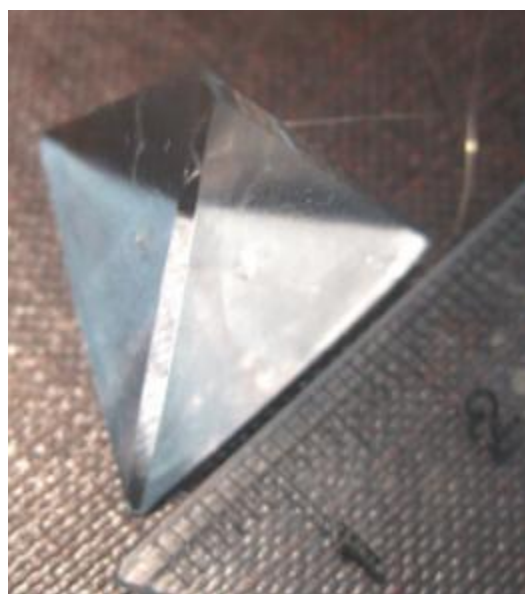
Figure 5.8 (a-d) NaClO_3 crystals grown from aqueous solutions doped with 130ppm – 220ppm $\text{S}_2\text{O}_6^{2-}$ impurity. (a) Crystal grown from 70ppm doped solution. The three facets on the tetrahedral edges were defined by cutting prior to the photographing. (b) Crystal grown from 130ppm doped solution. Six $\{001\}$ faces presented on the edges with considerable size. (c) Crystal grown from 160ppm $\text{S}_2\text{O}_6^{2-}$ doped solution. It presented two narrow faces of $\{001\}$ type. (d) Crystal grown from 190ppm $\text{S}_2\text{O}_6^{2-}$ doped solution. Four $\{001\}$ faces presented, one of which was of a relatively larger size.



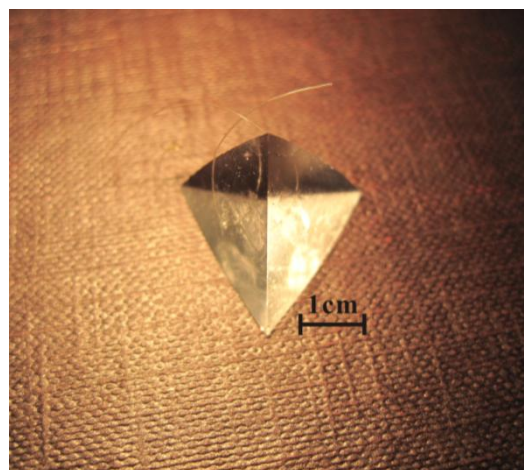
(e) 220ppm



(f) 340ppm



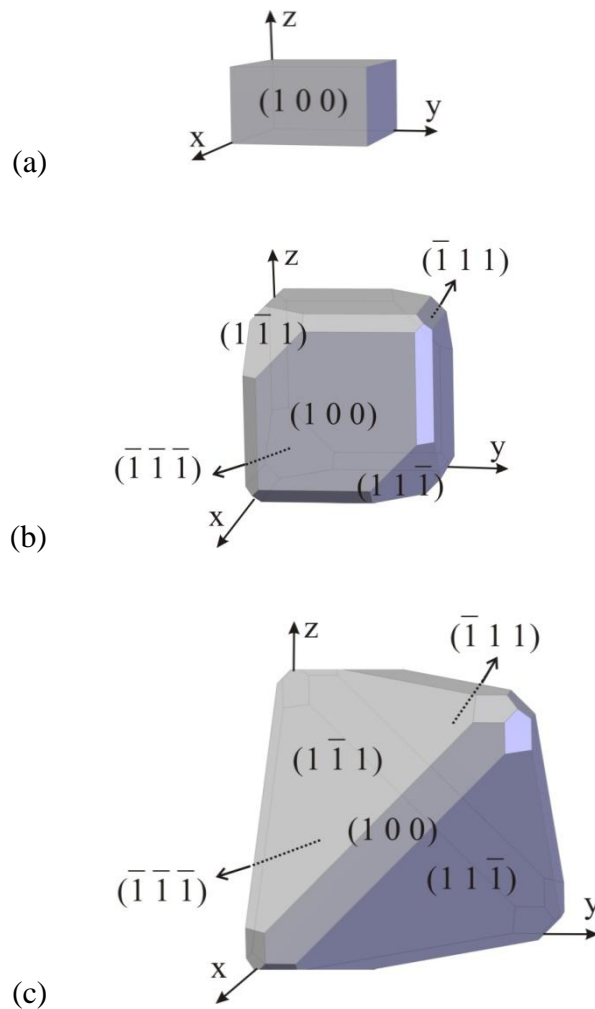
(g) 460ppm



(h) 1000ppm

Figure 5.8 (e-h) NaClO_3 crystals grown from aqueous solutions doped with 220ppm – 1000ppm $\text{S}_2\text{O}_6^{2-}$ impurity. (e) Crystal grown from 220ppm doped solution. The two facets on the tetrahedral edges were defined by cutting prior to the photographing. (f) Crystal grown from 340ppm doped solution. Four $\{001\}$ faces presented on the tetrahedral edges. One $\{001\}$ face of considerable size contained many inclusions (left side in figure). (g) Crystal grown from 460ppm doped solution. It is significant that the $\{001\}$ faces are quite regular, with a straight border at the sector boundaries to their neighbouring sectors. (h) Crystal grown from 1000ppm doped solution. No visible $\{001\}$ faces appeared on the final habit.

The growth of these doped crystals (i.e. 70ppm to 1000ppm) had similar process (Figure 5.9). In the first 6 to 48 hours, the crystal regenerates its morphology from the rounded shape of slightly dissolved seed. The regenerated morphology was usually composed of the faces of $\{001\}$, $\{110\}$ and $\{\bar{1}\bar{1}\bar{1}\}$ types. However, in the later days, $\{001\}$ and $\{110\}$ faces were continuously becoming smaller and finally grown out. At the same time, the $\{\bar{1}\bar{1}\bar{1}\}$ faces grew larger and finally dominate the final crystal habit. Occasionally, small $\{001\}$ faces can persist at the edge of the tetrahedron without being squeezed out. Once the tetrahedron has formed, the crystal would continue growing by keeping the tetrahedral morphology during further growth. The individual steps during the morphology change are shown in Figure 5.9.



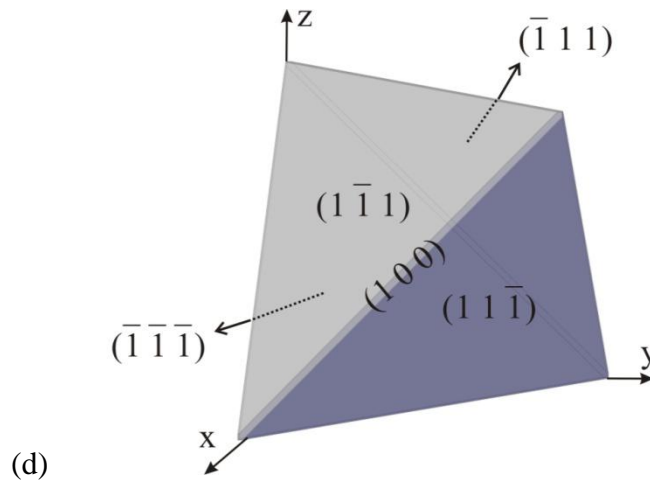


Figure 5.9 Schematic illustration for a typical process of crystal morphology changing from the cubic seed (a) to the tetrahedron (d). Seeds prepared from evaporation were usually of a half cube, due to the contacting limit at the bottom of the evaporating dish.

It is worth noticing that, the higher impurity concentration had a stronger effect in enhancing the $\{\bar{1}\bar{1}\bar{1}\}$ faces. That is, during the morphology changing from cubic to tetrahedral shape described above, the time used for $\{\bar{1}\bar{1}\bar{1}\}$ faces to dominate the morphology decreased as the impurity concentration increased.

In addition, the $\{001\}$ faces could either all appear on the edges of a tetrahedron or individually appear at random. Besides, they emerged either as smoothly flat faces covering the whole edge (Figure 5.8d), or as small facets covering part of the edge (Figure 5.11a). It was also noticed that, in some cases, the $\{\bar{1}\bar{1}\bar{1}\}$ faces of doped crystals were concave, causing the middle of the surface to be lower than the vicinal areas (Figure 5.8c).

5.4.2 Twinned NaClO_3 Crystal Formed at High $\text{S}_2\text{O}_6^{2-}$ Concentration

Ordinarily, large single NaClO_3 crystals were, without twinning, grown in moderately $\text{S}_2\text{O}_6^{2-}$ -doped solutions as described in last section. However, twinned crystals, were occasionally formed in the solution doped with high $\text{S}_2\text{O}_6^{2-}$ concentrations of 800ppm (Figure 5.10), 1000ppm (Figure 5.11a and b) and 1500ppm (Figure 5.11c).

Two types of twinning had been observed. In the first case, after some period of the crystal growth, on a growing surface of the existing tetrahedral single crystal developed from the seed, a new twin domain was formed on the surface (Figure 5.10). The newly developed tetrahedron has its base sitting on the basal surface of the existing tetrahedral crystal, and the two tetrahedra were in a relative position twisted by 60° along the 3-fold axis of $[\bar{1}\bar{1}\bar{1}]$. In the second case, more often, large twinned crystals emerged at the bottom of the growth flask, rather than from the seeded single crystals. They appeared to be two oppositely intergrown tetrahedra, occasionally with a small lens-shaped (001) facet on the curve [110] edge on the top of one domain (Figure 5.11a). This macro habit corresponds to the observation by Ristic et al. (1993). Due to the contact with the bottom of the vessel, only the top half of the twinned crystal was grown, whereas the growth of the lower half was inhibited. The recovered ideal morphology is shown in Figure 5.11d.

Each twin domain of the above cases is in the shape of tetrahedron with four apexes. It can be observed that the apexes of the two domains are in opposite direction within the same twinned crystal (Figure 5.10 and 5.11). This indicates that the twin domains are of opposite morphological polarity.

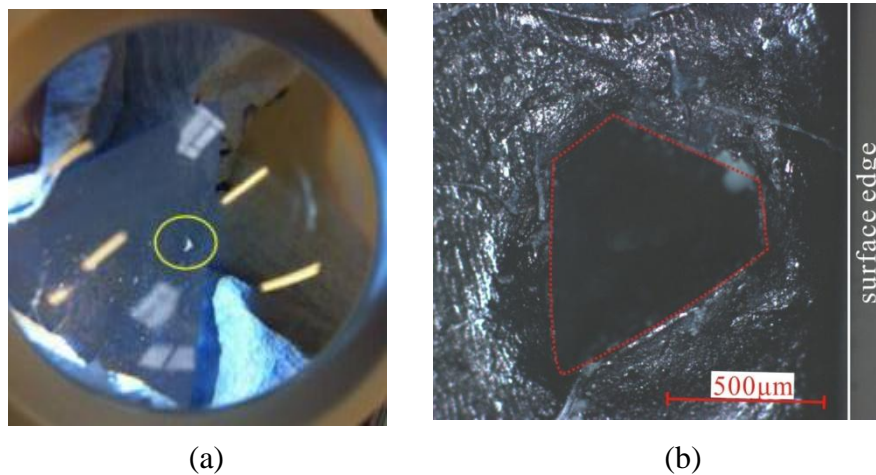
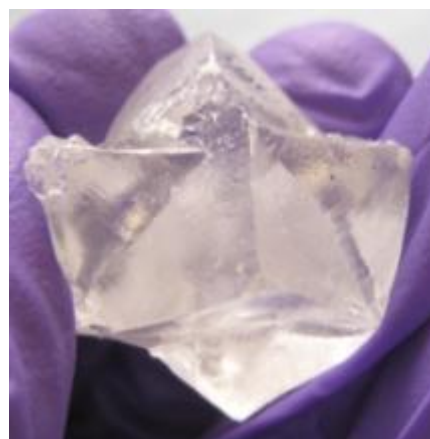


Figure 5.10 Photograph of the twinning case of NaClO_3 formed in the solution doped by 800ppm $\text{S}_2\text{O}_6^{2-}$. (a) View from larger scale showing one tetrahedral face of the larger domain, under an optical magnifier. The smaller domain which formed on the surface of the larger domain is circled in yellow. (b) Magnified view of the second twin domain sitting on the surface of the large domain. The second twin domain has been highlighted by the dotted red line.



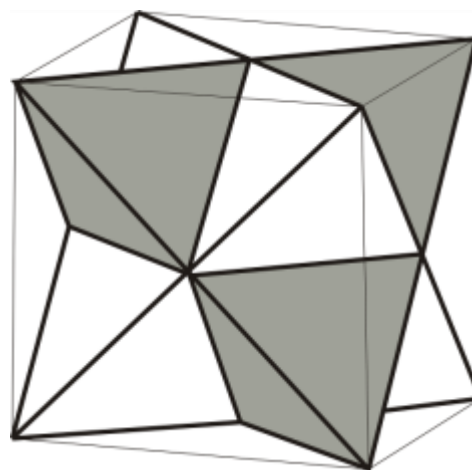
(a)



(b)



(c)



(d)

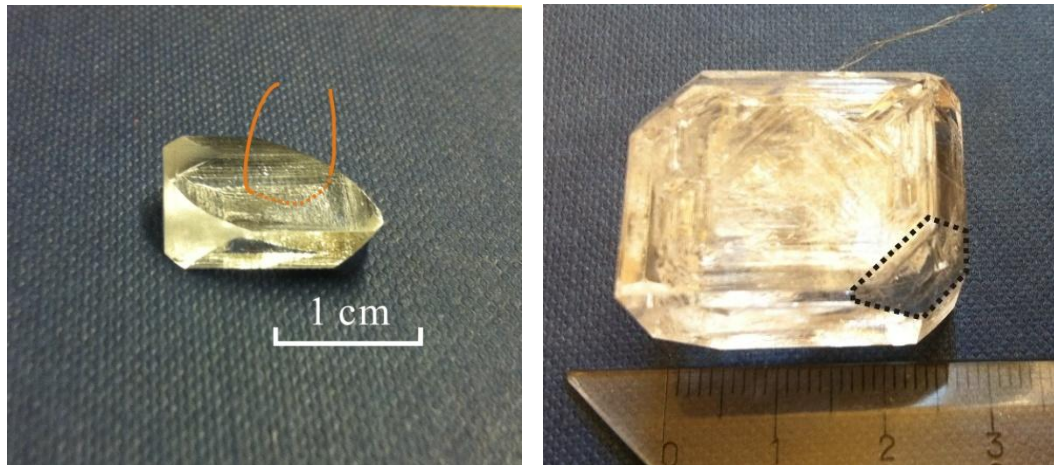
Figure 5.11 Photographs of the twinned NaClO_3 crystals grown at the bottom of the growth vessel. All twinned crystals show two intergrown opposite tetrahedra with slightly rounded faces and edges. (a) Twin crystal formed in 1000ppm doped solution. On one (110) edge a lens-shaped (001) facet is visible. (b) Another twin crystal formed in 1000ppm doped solution. (c) Twin crystal formed in 1500ppm doped solution. (d) Ideal morphology of the twinned crystal.

5.5 Transition Between Pure {111} and Doped $\{\bar{1}\bar{1}\bar{1}\}$

In order to experimentally confirm that the tetrahedral habit faces of {111} on the pure NaClO₃ crystal are geometrically opposite to the tetrahedral habit faces of $\{\bar{1}\bar{1}\bar{1}\}$ on the doped NaClO₃ crystal, two sets of crystal growth were carried out as follows.

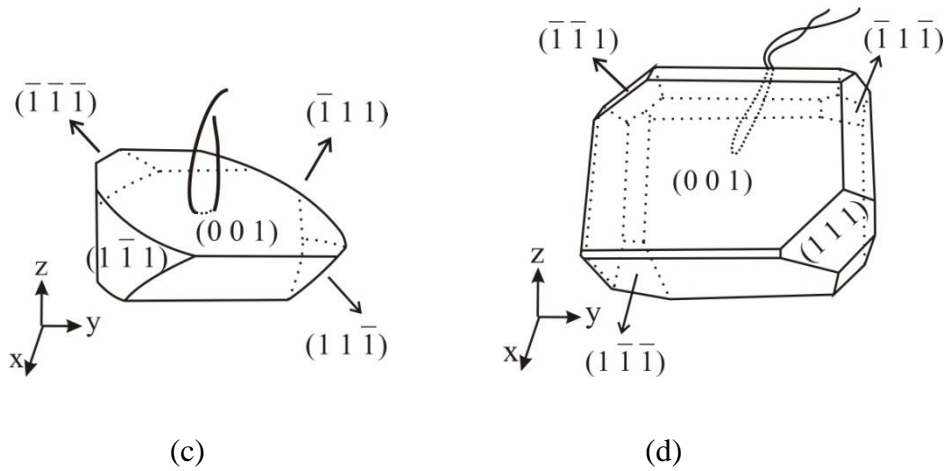
In the first case, the S₂O₆²⁻-doped seed with four $\{\bar{1}\bar{1}\bar{1}\}$ faces (Figure 5.12a) was placed in pure NaClO₃ aqueous solution to grow. During the growth, the $\{\bar{1}\bar{1}\bar{1}\}$ faces were growing at a fast growth rate and had quickly grown out. At the same time, the {111} faces slowly appeared at four corners of the cube which were geometrically opposite to the $\{\bar{1}\bar{1}\bar{1}\}$ faces (Figure 5.12b). The directions of the tetrahedral faces were judged with respect to the direction of the nylon thread used to suspend the seed. As a result, the {111} faces appeared on the final habit of the as-grown crystal (Figure 5.12b). Therefore, the tetrahedral {111} faces presented on the pure crystal are geometrically opposite to those tetrahedral $\{\bar{1}\bar{1}\bar{1}\}$ faces induced by S₂O₆²⁻ impurity.

In the second case, the pure seed with four {111} faces (Figure 5.13a) was placed in 160ppm S₂O₆²⁻-doped aqueous solution to grow. It was observed that the {111} faces grew out rapidly, while at the opposite corners of the cube the flat faces of $\{\bar{1}\bar{1}\bar{1}\}$ type appeared. Thus, this confirms that the tetrahedral $\{\bar{1}\bar{1}\bar{1}\}$ facets induced by the impurity are geometrically opposite to those tetrahedral {111} facets presented on the pure crystals.



(a)

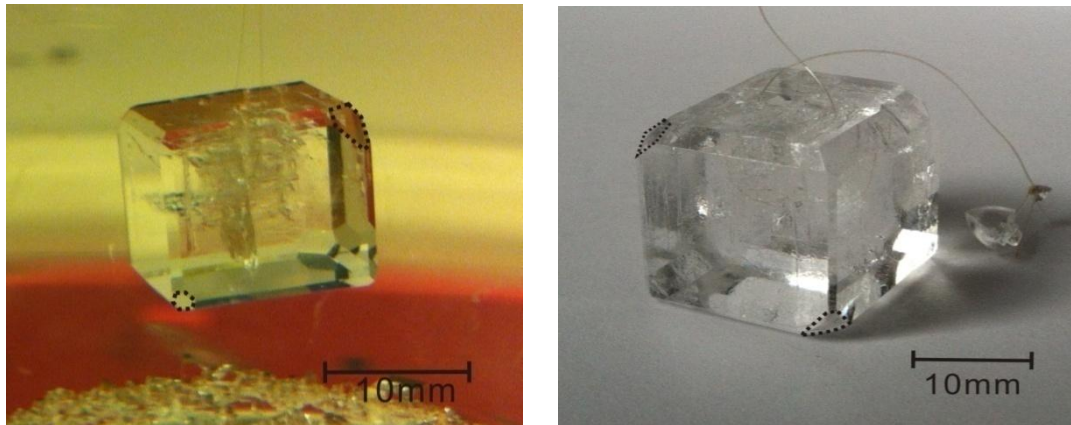
(b)



(c)

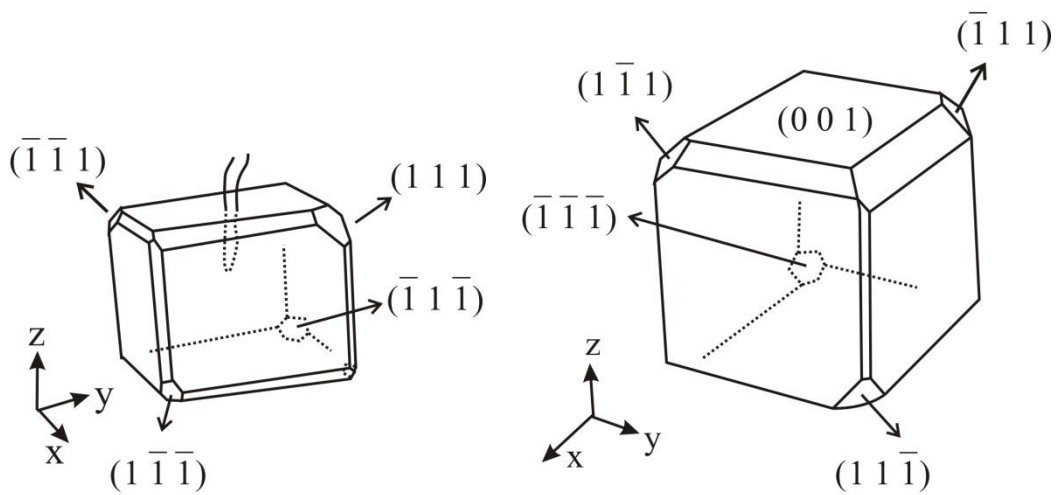
(d)

Figure 5.12 (a) Doped seed with $\{\bar{1}\bar{1}\bar{1}\}$ faces prepared by evaporating 160ppm doped solution. The thread has been drawn onto the photograph as a coloured line for illustration. The position and direction of the drawn thread is identical to that used in the experiment. (b) The as-grown pure crystal with $\{111\}$ faces, grown from the $S_2O_6^{2-}$ -doped seed. (c) Sketch of the doped seed in (a). (d) Sketch of the as-grown pure crystal in (b).



(a)

(b)



(c)

(d)

Figure 5.13 (a) Pure seed with $\{111\}$ faces prepared by evaporating NaClO_3 aqueous solution. (b) The as-grown doped crystal with $\{\bar{1}\bar{1}\bar{1}\}$ faces grown from 160ppm doped solution. (c) Sketch of the pure seed in (a). (d) Sketch of the as-grown doped crystal in (b).

5.6 Segregation Coefficient

The segregation coefficient² of the $S_2O_6^{2-}$ impurity in $NaClO_3$ crystal was assessed by measuring the sulphur concentration in the $NaClO_3$ crystal, using Inductively Coupled Plasma Optical Emission Spectrometry (ICP-OES). On one hand, the sulphur concentration was measured as a function of doping concentration, by sampling in the $\{\bar{1}\bar{1}\bar{1}\}$ sectors of various crystals doped with different impurity concentrations. On the other hand, the measurement was also performed to explore the coefficient in different growth sectors, by sampling in the (001), (110) and $(\bar{1}\bar{1}\bar{1})$ growth sectors of the 40ppm doped crystal. Sulphur concentrations were then converted into the concentrations of $S_2O_6^{2-}$ and summarized in Table 5.1 and 5.2.

The results in Table 5.1 indicate that, the $S_2O_6^{2-}$ concentrations in the bulk crystals were generally higher than that in the growth solutions for all the doping levels, by about 18.6 ~ 27 percent. The curve in Figure 5.14 is produced from the calculated segregation coefficient in Table 5.1. Although the fluctuation in the curve is not strong, a peak can be seen at 160ppm. This feature is very similar to that observed in the MSZW measurement as a function of impurity concentration (cf. section 5.2). There is likely to be an optimal impurity concentration under certain cooling rate where the segregation is maximum. However, the reason behind this is unclear.

Impurity conc. solution (ppm)	Sampling growth sector	Crystal conc. (ppm)	Segregation Coefficient ($S_{\text{bulk}}/S_{\text{solu.}}$)
40	$(\bar{1}\bar{1}\bar{1})$	49.4	1.235
100	$(\bar{1}\bar{1}\bar{1})$	125.2	1.252
160	$(\bar{1}\bar{1}\bar{1})$	203.2	1.270
220	$(\bar{1}\bar{1}\bar{1})$	261.0	1.186
340	$(\bar{1}\bar{1}\bar{1})$	411.2	1.209
1000	$(\bar{1}\bar{1}\bar{1})$	1203.0	1.203

Table 5.1 Segregation coefficient of $S_2O_6^{2-}$ in crystals grown from aqueous solution doped with various impurity concentrations. All crystals were grown at 1.0 °C/day.

² Segregation coefficient can be defined to be the ratio of the impurity concentration in the host crystal to that in the solution.

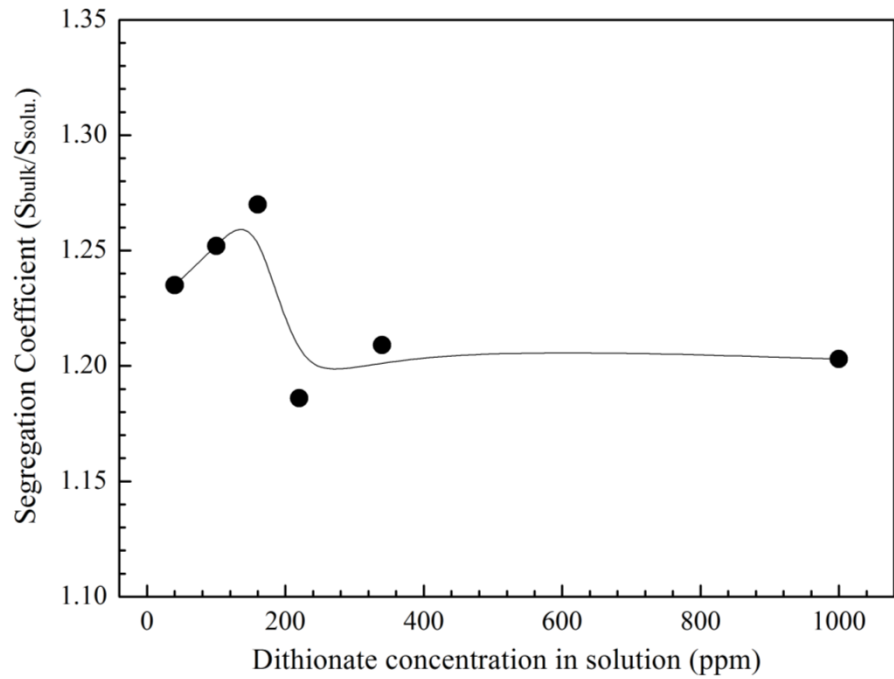


Figure 5.14 Segregation coefficient of $S_2O_6^{2-}$ in crystals grown from aqueous solution doped with various impurity concentrations. The data points were derived from Table 5.1. They were fitted with a spline line (black solid line in the figure).

From Table 5.2 it can be seen that, the impurity concentrations in different growth sectors of a single crystal are different. The $(\bar{1}\bar{1}\bar{1})$ sector apparently is of the most capability for impurity adsorption. The (110) and (001) sectors are more or less at the same level, with segregation coefficient to be less than half of that in the $(\bar{1}\bar{1}\bar{1})$ sector.

Solution concentration (ppm, mole ratio)	Sampling growth sector	Crystal concentration (ppm, mole ratio)	Segregation Coefficient (S _{bulk} /S _{solution})
40	$(\bar{1}\bar{1}\bar{1})$	49.0	1.225
40	(110)	20.1	0.503
40	(001)	22.2	0.555

Table 5.2 Segregation coefficient of $S_2O_6^{2-}$ in different growth sectors of 40ppm doped crystal.

5.7 Discussions

The results of the metastable zone width (MSZW) measurements are quite clear. It was observed that the impurity can enhance the MSZW of NaClO_3 in aqueous solution, which can possibly be attributed to a suppressive effect on the nucleation process by the impurity. Also, high cooling rate presents the same effect of enhancing the MSZW, i.e. the higher the cooling rate is, the wider the MSZW is. However, it was also found that the high cooling rate can reduce the enhancing effect of the impurity. Besides, at each cooling rate, an optimal impurity concentration for enhancing the MSZW was observed.

By comparing the habit of pure NaClO_3 crystals grown under various cooling rates, it can be seen that the final habit was dominated by faces of $\{001\}$ type under relatively high cooling rate of $1.0\text{ }^\circ\text{C/day}$, whereas the $\{110\}$ faces presented at moderate cooling rate of $0.5\text{ }^\circ\text{C/day}$. Moreover, the tetrahedral faces of $\{111\}$ type only presented on the final crystal habit at the relatively low cooling rate of $0.125\text{ }^\circ\text{C/day}$. Since the internal growth factors, such as the crystal structure and the dislocations participated in the growth (cf. section 6.3), can be considered as almost identical for these crystals based on the same growth conditions, the change of habit can be attributed to the variation of cooling rate. Therefore, under high supersaturation the crystal habit is composed of solely $\{001\}$ faces, and $\{110\}$ and $\{111\}$ faces can appear with decreased cooling rate hence low supersaturation. The observed change of habit due to the variation in supersaturation in the current study is consistent with that reported by Simon (1983) and Ristic et al. (1993). In addition, the habit modification due to varied supersaturation has been interpreted by Ristic et al. (1993), based on growth rate measurement for different faces under various supersaturation (reviewed in section 3.3.2).

The different final habits of the doped NaClO_3 crystals at various doping concentrations are summarized in Table 5.3. The representative single-crystals selected for study were grown under approximately identical conditions, except the different doping concentrations ranged from 40ppm to 1000ppm. Within this concentration range, the single-crystals present all the possible habits of NaClO_3 in the presence of $\text{S}_2\text{O}_6^{2-}$. It was noticed that under low impurity doping levels (i.e. 40ppm), the as-grown crystal possesses final habit faces of $\{\bar{1}\bar{1}\bar{1}\}$, $\{001\}$ and $\{110\}$ types with analogous size. From the doping concentration 70ppm up to 1000ppm, the final habits of the as-grown crystals were tetrahedron dominated by $\{\bar{1}\bar{1}\bar{1}\}$ faces.

This clearly shows that the impurity plays an important role in inducing the $\{\bar{1}\bar{1}\bar{1}\}$ faces, starting from a trace amount of 40ppm in the growth solution (Table 5.3). Also, the size of the faces of other types will be decreased with the increasing doping concentration. The observed habits of NaClO_3 crystals modified by $\text{S}_2\text{O}_6^{2-}$ impurity agree with those reported before, by Buckley (1930), Ristic et al. (1993; 1994) and Wojciechowski (1995). For general conclusion, from this host/impurity system it can be seen that the habit-modifying impurity usually incorporate into the host on certain crystal surfaces and affect the crystal habit.

Impurity concentration	Final habit faces
pure	{001}, {110}, {111}
40ppm	{001}, {110}, $\{\bar{1}\bar{1}\bar{1}\}$
70 ~ 1000ppm	$\{\bar{1}\bar{1}\bar{1}\}$, small {001} [*]
above 1000ppm	$\{\bar{1}\bar{1}\bar{1}\}$, small {001} [*] ; occasional twinned crystal

* The appearance of {001} faces is at a low probability, and not all the symmetry faces will appear.

Table 5.3 Type of final habit faces of NaClO_3 crystals grown from solutions doped with different impurity concentrations.

The twinned crystals can form occasionally in the growth solution at the doping concentration of 800ppm and above. The habit of twinned crystal presents two tetrahedra with opposite morphological polarity. The opposite morphological polarity between twin domains is one of the critical evidence to judge the twinning law of this system. Further discussion will be presented together with the optical activity measurement in the next chapter.

It is also of great significance to have proved that the {111} on pure crystal and the $\{\bar{1}\bar{1}\bar{1}\}$ on doped crystal are geometrically opposite. Also, the different sensitivity of these faces to the dithionate impurity implies that these opposite faces are of different nature. This was expected, since the crystal structure of NaClO_3 is non-centrosymmetric which can result in different surface structures between the opposite faces of {111} and $\{\bar{1}\bar{1}\bar{1}\}$. Further explorations into the surface structure of these faces will reveal the intrinsic reason for their different behaviour during impurity incorporation process. This will be presented in the molecular modelling chapter.

The segregation coefficient ($S_{\text{bulk}}/S_{\text{solution}}$) was determined to be around 1.18 ~ 1.27 among crystals grown from different doping concentrations. Besides, the reason for

why the maximum coefficient appeared at 160ppm remains unknown. It is worth noticing that, the coefficient measured in (001) and (110) sectors were much lower than that in $(\bar{1}\bar{1}\bar{1})$ sector, implying that the impurity prefers to incorporate into the $(\bar{1}\bar{1}\bar{1})$ sector. This assists in understanding the strong inhibiting effect of impurity on the growth rate of $\{\bar{1}\bar{1}\bar{1}\}$ faces.

5.8 Conclusion

The MSZW of NaClO_3 in aqueous solution was determined, and it was found that both the presence of $\text{S}_2\text{O}_6^{2-}$ and the high cooling rates can enhance the MSZW of NaClO_3 , respectively. However, the high cooling rate can weaken the enhancing effect of the impurity. An optimal impurity concentration for enhancing the MSZW was observed, the reason for which is still unknown.

The habit of pure crystal grown at the cooling rate of 1.0 °C/day was solely composed of {001} faces. The {110} and {111} faces can appear at lower cooling rates of 0.5 °C/day and 0.125 °C/day, respectively. These observed changes agree with that reported by Simon (1983) and Ristic et al. (1993). The $\text{S}_2\text{O}_6^{2-}$ started to induce $\{\bar{1}\bar{1}\bar{1}\}$ tetrahedral faces from a minimum concentration of 40ppm. Under low impurity doping concentration the {001} and {110} faces could survive on the final habit, but they were severely suppressed and grew out when the impurity concentration was increased, i.e. including and beyond 70ppm. Sometimes {001} faces can appear as small flat surfaces at the edges of the tetrahedron. The $\{\bar{1}\bar{1}\bar{1}\}$ tetrahedral faces on doped crystals are geometrically opposite to those {111} faces on pure crystals.

With relatively high impurity concentration over 800ppm in the growth solution, twinned crystal was formed at a low probability. The twinning phenomenon was observed as either a small tetrahedral crystal in the morphologically opposite direction on the existing large face of $\{\bar{1}\bar{1}\bar{1}\}$ type or two large inter-grown tetrahedral crystals.

The segregation coefficient results revealed that the impurity concentration in $(\bar{1}\bar{1}\bar{1})$ sector is more than twice of that in (001) and (110) sectors. The segregation coefficient in $(\bar{1}\bar{1}\bar{1})$ sector was fluctuating around 1.2 among different crystals of different doping concentrations. An optimal impurity concentration appeared at 160ppm, the reason for which is still unclear. -

CHAPTER 6

Defect Structure, Growth History and Optical Activities of NaClO₃ in the Presence of S₂O₆²⁻

Summary:

Results and discussion on the defect configuration of both pure and doped sodium chlorate crystals. The nature of the impurity-induced twinned crystal is also explored.

6.1 Introduction

This chapter aims to explore the crystal growth history during the habit modification of NaClO_3 crystals by $\text{S}_2\text{O}_6^{2-}$ impurity, as well as the nature of the twinned crystal, using X-ray topography and Polarized light microscopy. The basic characteristics of various types of defects will be described firstly, and then detailed characterization for dislocation lines in both pure and doped crystals will be carried out. The growth history of typical doped crystals will be discussed in terms of relative growth rate determination, in order to reveal the habit change process during the crystal growth affected by impurity. The growth history and optical activity of the twinned crystal will be discussed, aiming at determining the applicable twinning law for the current case.

6.2 Growth Defects

6.2.1 Growth Sectors and Growth Sector Boundaries

Bulk crystals, developed with planar habit faces, normally consist of different volumes which are related to individual growth faces in discrete directions. These volumes are referred to as *growth sectors*. According to Wulff's theory (Wulff, 1901), the final habit of a crystal usually exhibits only the faces with relatively slower growth rates. Nomination for growth sector is generally identical to its corresponding crystal face, defined by the growth direction of the face. The boundary between growth sectors is referred to as the *growth sector boundary*. Figure 6.1 shows the typical growth sectors and growth sector boundaries of the pure and doped NaClO_3 crystals.

In the topograph of a pure crystal plate (Figure 6.2), there is no visible topographic contrast at any growth sectors boundaries. This is ascribed to the high perfection of the crystal which has resulted in no strain (or very small and undetectable strain) between the growth sectors. Since there's no strain at the boundaries, there is no topographic contrast. However, two types of growth sectors, i.e. $\{001\}$ and $\{101\}$, can be theoretically deduced from the habit faces indicated by the external shape of the plate. The deduced boundaries are shown in Figure 6.2b using dotted straight lines.

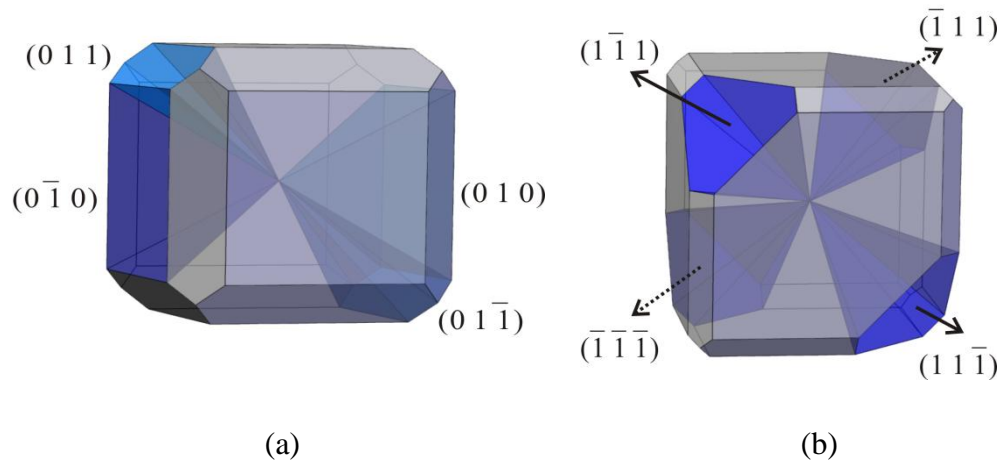


Figure 6.1 Schematic illustration of the typical growth sectors and growth sector boundaries of the pure and doped NaClO_3 crystals. (a) Pure crystal presenting the habit faces of $\{100\}$ and $\{110\}$ types. Four different growth sectors are highlighted, including (010) , $(0\bar{1}0)$, (011) and $(01\bar{1})$, to enhance the visual effect of their volume and the boundaries between them. (b) Doped crystal presenting the habit faces of $\{100\}$, $\{110\}$ and $\{\bar{1}\bar{1}\bar{1}\}$ types. The four $\{\bar{1}\bar{1}\bar{1}\}$ growth sectors are highlighted.

However, in the doped crystals, the growth sector boundaries can be observed by topographic contrasts in two ways, i.e. from either direct contrast of the boundary itself or different contrast between the neighbouring sectors. In the first case, the slightly faulty boundary can present higher contrast than the vicinal area, due to the increased local impurity incorporation at the boundary where neighbouring faces meet as expected (Chernov, 1984). The topograph of the 40ppm doped crystal (Figure 6.3a) shows clearly such contrasts between the $(\bar{1}\bar{1}0)$ and $(\bar{1}\bar{1}\bar{1})$ sectors as well as the (110) and $(11\bar{1})$ sectors. It is worth noticing that, the above boundaries appeared as double contrast bands. This implies that the boundaries are inclined to the experiment plate normal. An inclined boundary will intersect with the two surfaces of the crystal plate at two different lines shifted against each other in the plane of the plate. The two lines were imaged at different positions on the topograph. Thus, the growth sector boundary was presented as the double band on the topographic image. This can be confirmed by observing the morphology of this crystal (Figure 5.7). Second, in the latter case, although some boundaries have no contrast of their own, they can still be recognized when the contrasts of neighbouring sectors are different. For example, the boundary between $(\bar{1}\bar{1}\bar{1})$ and $(00\bar{1})$ in 40ppm doped crystal (Figure 6.3) can be

judged by the suddenly changed contrast in the two sectors. Besides, the growth striations (cf. section 6.2.2), which appeared intensively in only the doped crystals, have largely facilitated the identification of different growth sectors as well as their boundaries in the current study. For example, the growth sector boundary between $(\bar{1}\bar{1}\bar{1})$ and $(\bar{1}\bar{1}1)$ in 160ppm doped crystal (Figure 6.4), can be judged by the sharp bending of striations in the neighbouring growth sectors.

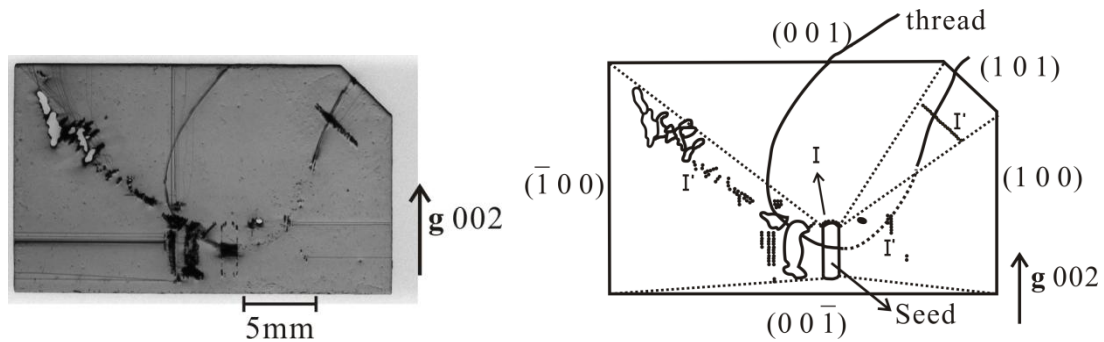


Figure 6.2 (a) Topograph of the (010) plate of pure crystal. Reflection 002, film D7. It shows no contrast at the boundaries between different growth sectors. Small black dots: surface damages. (b) Sketch of the topograph in (a) in which I and I' represent solvent inclusions.

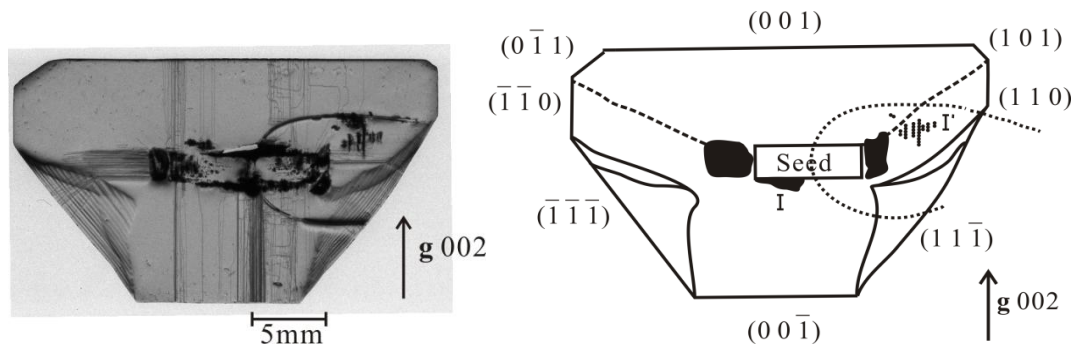


Figure 6.3 (a) Topograph of the $(\bar{1}10)$ plate of 40ppm $S_2O_6^{2-}$ -doped $NaClO_3$ crystal. Reflection 002, film D7. Crystal external outline is well revealed, corresponding to a couple of habit faces. The growth sector boundaries between $(00\bar{1})$ sector and $(\bar{1}\bar{1}\bar{1})$ as well as $(11\bar{1})$ sector can be distinguished by observing the relatively higher topographic contrast than vicinal area at the interface where they meet. The boundaries between the $\{001\}$ sectors and the $\{110\}$ sectors are nearly invisible, except a very faint line between (001) and $(\bar{1}\bar{1}0)$. (b) Sketch for the topograph in (a), in which I and I' represent solvent inclusions.

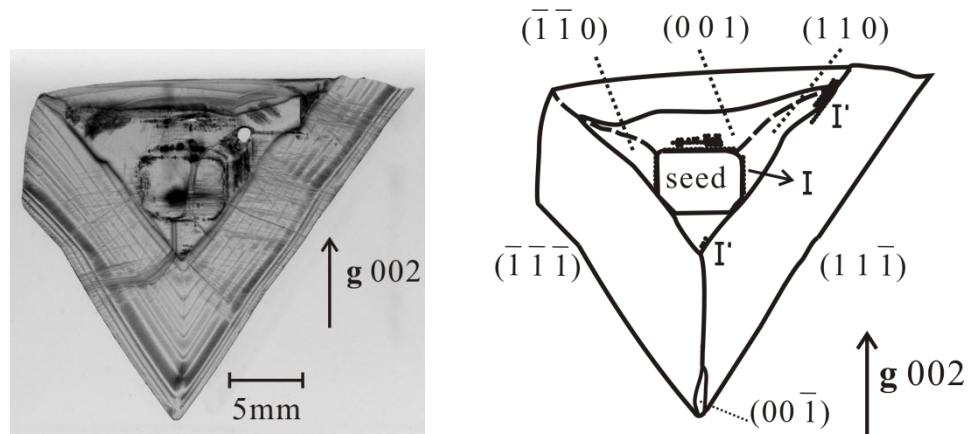


Figure 6.4 (a) Topograph of $(\bar{1}10)$ plate of 160ppm $S_2O_6^{2-}$ -doped $NaClO_3$ crystal. Reflection 002, film D4. (b) Sketch for the topograph in (a), in which the I and I' represent solvent inclusions.

6.2.2 Growth Striations

On the topograph of doped crystals, the striations as roughly parallel black lines in the $\{\bar{1}\bar{1}\bar{1}\}$ type sectors (Figure 6.3 and 6.4) are referred to as *growth striations*. Growth striations are conventionally accepted as being caused by non-uniform impurity incorporation into the growing front (Klapper, 2010). During the growth of doped crystals, the water bath temperature was adjusted by $-0.5\text{ }^\circ\text{C}$ at a time twice a day. As a result, the growth solution temperature fluctuated every time the water bath temperature was changed. The variation in the supersaturation caused by these temperature fluctuations induced variation in the crystal growth rate and, accordingly, the adsorption and incorporation of impurity (Sangwal 1996). This resulted in inhomogeneous layers parallel to the growing front. Consequently, any slight variation of lattice parameter existing among these inhomogeneous layers would lead to visible topographic contrast in the topographs (Chernov, 1984; Smolsky et al., 1999). Since the inhomogeneous layers were formed at the continuously growing front, the induced striations usually lie parallel to the growth faces (Figure 6.3 and 6.4). In addition, since no impurity was present during the growth of the pure crystal, no growth striations were observed in the pure crystal (Figure 6.2).

Nevertheless, from the topographs of doped crystals shown in Figure 6.3 and 6.4 it can be seen that the striations exist only in growth sectors of $\{\bar{1}\bar{1}\bar{1}\}$ type. In the

growth sectors of {001} and {110} types, no striations can be observed. Given this striking difference, it is concluded that the preferred incorporation locations for $S_2O_6^{2-}$ impurity are the growth faces of $\{\bar{1}\bar{1}\bar{1}\}$ type rather than the others including the {001} and {110} types. The reason for this can be explained as the different surface natures of different faces may facilitate or impede impurity incorporation. This will be further inspected using molecular modelling in later chapters.

6.2.3 Inclusions

Large volumes of defects have been observed in both the pure and doped crystals, which are referred to as inclusions. The inclusions mainly exist at the seed-crystal interface³ (marked as I in Figure 6.5 and 6.6) and within different growth sectors (marked as I' in Figure 6.5 and 6.6). The inclusions in the current study are attributed to solvent inclusions rather than foreign particles or impurity precipitations.

During the re-generation process⁴ of the seed in the early crystal growth stage, the rounded surface of the slightly dissolved seed favours the entrapment of solvent, which normally leads to more or less an inclusion spongy zone around the seed (Figure 6.5 and 6.6). It is worth mentioning that, these inclusions can be largely reduced by slowly decreasing solution temperature at this stage but is much more time consuming.

Inclusions in growth sectors are normally ascribed to the fluctuation of growth conditions. This inevitably happens during crystal growth, such as variation of local supersaturation due to different growth rate across the crystal surface, vortex caused by solution flow, vibration of stirrer, etc. All these situations might cause temporary instability of the growing face, resulting in inhomogeneous elevations and depressions. Elevated growth layers will possibly grow and spread over the depressed lower layers, thus a volume of solvent will be trapped in the closed space between the lower layer and the upper layer. Besides the inclusions formed as a point, it is also common to see

³ The seed-crystal interface refers to the interface between the seed and newly grown region.

⁴ The slightly dissolved seed has a rounded shape and will regenerate its morphology in the early crystal growth stage.

a group of inclusions formed like a plane parallel to the growth face, for example, the inclusions marked as I' in sector (101) and sector (100) in Figure 6.5b. These inclusions aligned well in a line parallel to their growth faces, indicating that they were formed on the whole growing front at some point during growth. As a result, these inclusions can represent the size of that face at certain time points during growth.

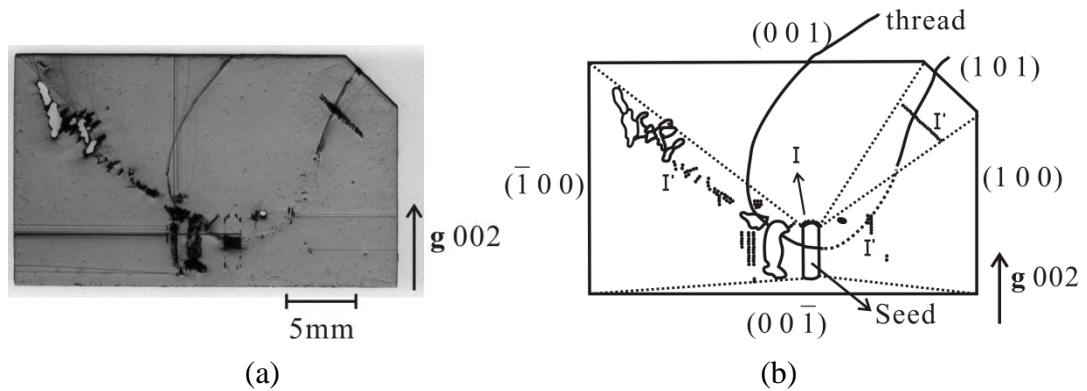


Figure 6.5 (a) Topograph of (010) plate of pure NaClO₃ crystal. Reflection 002, film D7. (b) Sketch for the topograph in (a), in which I and I' represent solvent inclusions.

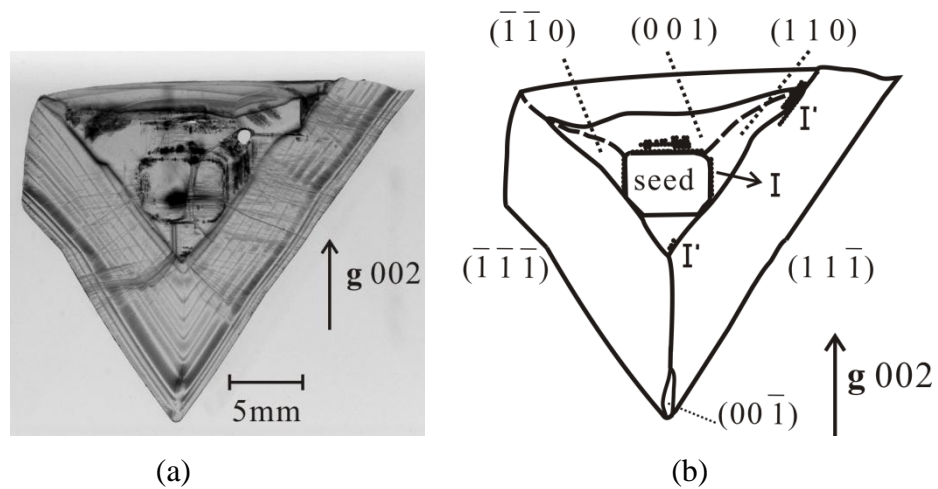


Figure 6.6 (a) Topograph of (110) plate of 160ppm S₂O₆²⁻-doped NaClO₃ crystal. Reflection 002, film D4. (b) Sketch for the topograph in (a), in which I and I' represent solvent inclusions.

6.2.4 Dislocations

The dislocations observed in the NaClO_3 crystals presented mainly three different profiles, including straight lines (e.g. mark S in Figure 6.7), irregularly bow-shaped lines (e.g. mark P in Figure 6.7), and curved lines (e.g. mark C in Figure 6.7). The straight lines were referred to as grown-in dislocations which will be characterized in later sections, and the other two types were post-growth dislocations.

By observing the sources of the dislocation lines in both pure and doped crystal (Figure 6.5 and 6.6), it can be seen that most dislocations revealed by the topographs were generated at the inclusions, either at the seed crystal interfaces or within different growth sectors (Figure 6.6). Another dislocations source was the dislocations contained in the seed (Figure 6.6). However, none of the dislocations in the pure crystal were observed to be generated from the inclusions at the seed-crystal interface (Figure 6.5). This might be attributed to the slower modulation of solution temperature during the re-generation process of the seed, which reduced the chance of producing dislocations at the inclusions.

The observed post-growth dislocation lines, including the bow-shaped and curved lines, were produced from the movement of grown-in dislocation lines after the crystal growth. In the former case, the dislocation line was generally composed of bow-shaped segments and in the latter case it was commonly composed of several irregular curved segments. The origin for such relaxation movements is attributed to the thermal stress caused by temperature gradients during crystal growth in the solution of varying temperature or during the cooling of the crystal after growth (Klapper, 2000).

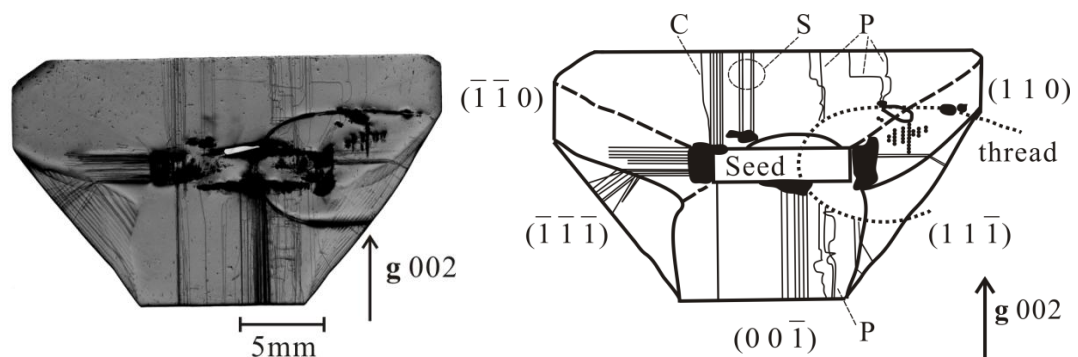


Figure 6.7 (a) Topograph of $(\bar{1}\bar{1}0)$ plate of 40ppm $\text{S}_2\text{O}_6^{2-}$ -doped NaClO_3 crystal. Reflection 002, film D4. (b) Sketch for the topograph in (a). C: curved dislocation line, S: straight dislocation line, P: bow-shaped dislocation line.

6.2.5 Discussion on the Defects

Growth sector boundaries of pure NaClO_3 crystals showed no contrast on their topograph, revealing high perfection at the boundaries. However, topographs of $\text{S}_2\text{O}_6^{2-}$ doped crystals showed clear growth sector boundaries between the $\{\bar{1}\bar{1}\bar{1}\}$ sectors and their neighbouring sectors, either by the contrast of the boundary itself or different contrasts of the neighbouring sectors. The growth sector boundaries reflect the growth history of crystals, which will be discussed later in this chapter.

Growth striations appeared in only the doped crystals rather than the pure ones. The striations were ascribed from the non-uniform impurity incorporation into the growing front caused by the temperature fluctuation in the growth solution during crystal growth. Nevertheless, the striations appeared in growth sectors of only the $\{\bar{1}\bar{1}\bar{1}\}$ type, but neither the $\{001\}$ sectors nor $\{110\}$ sectors. Thus, the $\{\bar{1}\bar{1}\bar{1}\}$ faces are the favourable faces for impurity incorporation.

Inclusions have been observed both at the seed interface and within the growth sectors. It was noticed that inclusions are important sources for generating dislocations in the crystals.

The dislocation lines presented in the seeded crystals are of three types, including straight line, curved line and irregular line composed of bow-shaped segments. Three sources for dislocations have been identified, i.e. extended from the dislocations in the seed, generated at the interface of the seed during the regeneration process, and induced by inclusions during crystal growth. The density of dislocation lines in the as-grown crystals mainly depends on three aspects including the quality of the seed, the cooling rate used in the regeneration process of the seed, and the density of inclusions which is closely connected with the stability of growth conditions.

6.3 Dislocation Characterization

A grown-in dislocation line of a certain type generally possesses a specific angle against the growth direction of the face. In each growth sector, grown-in dislocations normally propagate along several preferred directions. The preferred directions of dislocation lines in various sectors of NaClO_3 have already been reported by Hooper et al. (1983). Thus, the character of the grown-in dislocations, e.g. pure screw, pure edge or mixed, can be identified by comparing the angles of the dislocation lines in the topograph to that in the calculation.

The grown-in dislocation lines in various growth sectors of both the pure and doped crystals will be characterized in this section in order to evaluate the growth mechanism of the NaClO_3 crystals and to find out whether the characters of the dislocations were affected by the impurity. Some other features of particular defects are also discussed. In addition, the crystal grown at 40ppm doping concentration will be discussed separately from the crystals grown at relatively high impurity concentration (i.e. from 70ppm and above), because the former crystal is composed of both impurity-modified $\{\bar{1}\bar{1}\bar{1}\}$ faces and original $\{001\}$ and $\{110\}$ faces whereas the latter ones presents only impurity-modified $\{\bar{1}\bar{1}\bar{1}\}$ faces.

6.3.1 Theoretical Burgers Vectors and Preferred Dislocation Line Directions

The energy of linear dislocations is related to its line tension energy E_l , which is expressed as (Hooper et al., 1983):

$$E_l = ck|\mathbf{b}|^2 \quad (6.1)$$

where c is a constant related to crystal structure, k is the energy factor which depends on the elastic properties of the crystal, $|\mathbf{b}|$ is the modulus of a specific Burgers vector (\mathbf{b} is Burgers vector). Growth dislocations in crystals normally propagate along preferred directions in specific growth sectors.

In principle, the preferred dislocation line directions in a crystal are those directions along which the elastic energy (strain energy) per unit length, i.e. $E_l / \cos \alpha$ where α

is the angle between the line direction (\mathbf{l}) and the growth direction (\mathbf{n}), is a minimum. Hooper et al. (1983) evaluated the value of minimized k with respect to the angle α , for the dislocations with Burgers vectors of $\langle 001 \rangle$ and $\langle 110 \rangle$ types in various growth sectors for NaClO_3 . The details of the preferred dislocation lines are shown in Table 6.1.

Type	\mathbf{n}	$M(\mathbf{n})$	\mathbf{b}	\mathbf{l}	character	$S(\mathbf{l})$	$\alpha(\mathbf{l}, \mathbf{n})$ /°	E_1 /eV nm ⁻¹
1a	(001)	6	[001]	[001]	screw	100.0	0.0	40.7
1b	(001)	6	[010]	[001]	edge	0.0	0.0	68.6
1c	(001)	6	[011]	[015]	mixed	70.7	11.0	104.3
1d	(001)	6	[110]	[001]	edge	0.0	0.0	137.3
2a	(110)	12	[100]	[310]	mixed	94.6	26.0	44.8
2b	(110)	12	[001]	[110]	edge	0.0	0.0	67.8
2c	(110)	12	[110]	[110]	screw	100.0	0.0	99.9
2d	(110)	12	[101]	[531]	mixed	72.0	17.1	114.5
2e	(110)	12	$[\bar{1}10]$	[110]	edge	0.0	0.0	127.1
3a	$(\bar{1}\bar{1}\bar{1})$	8	$[00\bar{1}]$	$[\bar{1}\bar{1}\bar{3}]$	mixed	89.9	28.7	47.8
3b	$(\bar{1}\bar{1}\bar{1})$	8	$[\bar{1}\bar{1}0]$	$[\bar{9}\bar{9}\bar{5}]$	mixed	93.4	14.3	105.9
3c	$(\bar{1}\bar{1}\bar{1})$	8	$[1\bar{1}0]$	$[\bar{1}\bar{1}\bar{1}]$	edge	0.0	0.0	128.6

Table 6.1 Calculation of the preferred dislocation lines with their related crystallographic details $S(\mathbf{l})$ is the portion of screw character in a mixed dislocation, $M(\mathbf{n})$ is the multiplicities of a particular growth sector. For different symmetrically equivalent growth sectors the values of \mathbf{b} and \mathbf{l} might vary accordingly. (Hooper et al., 1983).

6.3.2 Dislocation Lines in Pure NaClO₃ Crystal

The pure crystal plate for X-ray topography characterization was cut parallel to its (010) plane along the a axis. The recorded topograph is shown in Figure 6.8a, and its growth sectors shown in the sketch (Figure 6.8b) were theoretically deduced according to the shape of the plate. It can be seen, dislocations are mainly originated from inclusions. It should be noted that the topograph in Figure 6.8a was taken by 002 reflection, hence some dislocations were invisible according to the visibility rules (cf. Chapter 2.6.1.5). Invisibility occurs for screw dislocations when $\mathbf{g} \cdot \mathbf{b} = 0$, for edge dislocation when $\mathbf{g} \cdot \mathbf{b} = 0$ and also $\mathbf{g} \cdot \mathbf{b} \times \mathbf{l} = 0$ (where \mathbf{g} is diffraction vector, \mathbf{b} is Burger's vector, \mathbf{l} is dislocation line direction). The dislocations with mixed characters normally present contrast under either condition.

Most of the dislocations in the growth sectors of (100), (001) and ($\bar{1}00$) are straight lines, with their line directions \mathbf{l} aligned parallel to the growth directions \mathbf{n} , i.e. $\alpha(\mathbf{l}, \mathbf{n})=0^\circ$. With this angular information and the visibility rules under the 002 reflection, these dislocations were assigned according to the reference calculation (Table 6.1). For example, by judging the $\alpha(\mathbf{l}, \mathbf{n})=0^\circ$ of the dislocation lines in (100) and (001) sectors (Figure 6.8), they can be either pure screw 1a or pure edge 1b. But according to visibility rules, a pure screw dislocation in the (100) sector is invisible under 002 reflection, where $\mathbf{g} \cdot \mathbf{b} = [002] [100]=0$. Nevertheless, in the (001) sector, the pure edge dislocation is invisible due to $\mathbf{g} \cdot \mathbf{b} = [002] [010]=0$ and $\mathbf{g} \cdot \mathbf{b} \times \mathbf{l} = [002] [010] \times [001]=0$. Thus, the visible dislocations in (100) sector are 1b type of pure edge character, and those in (001) sector are 1a type of pure screw character. All the results after assignment are tabulated in Table 6.2. The measured angular values are consistent with the calculated values.

In addition, a number of dislocation lines with irregular curvature have been observed in sector (001) (marked 1a* in Figure 6.8b). These irregularly curved dislocation lines are due to the post-growth movement of grown-in dislocations (cf. section 6.2.4).

It is also interesting to see that the development of the ($00\bar{1}$) growth sector is extremely small compared to the other three {001} sectors (Figure 6.8a), which can be attributed to be its high perfection and lack of screw or mixed dislocations as

growth centres. This feature manifestly implies that the growth mechanism of $\{001\}$ faces under the current growth conditions is by spiral growth at screw dislocations.

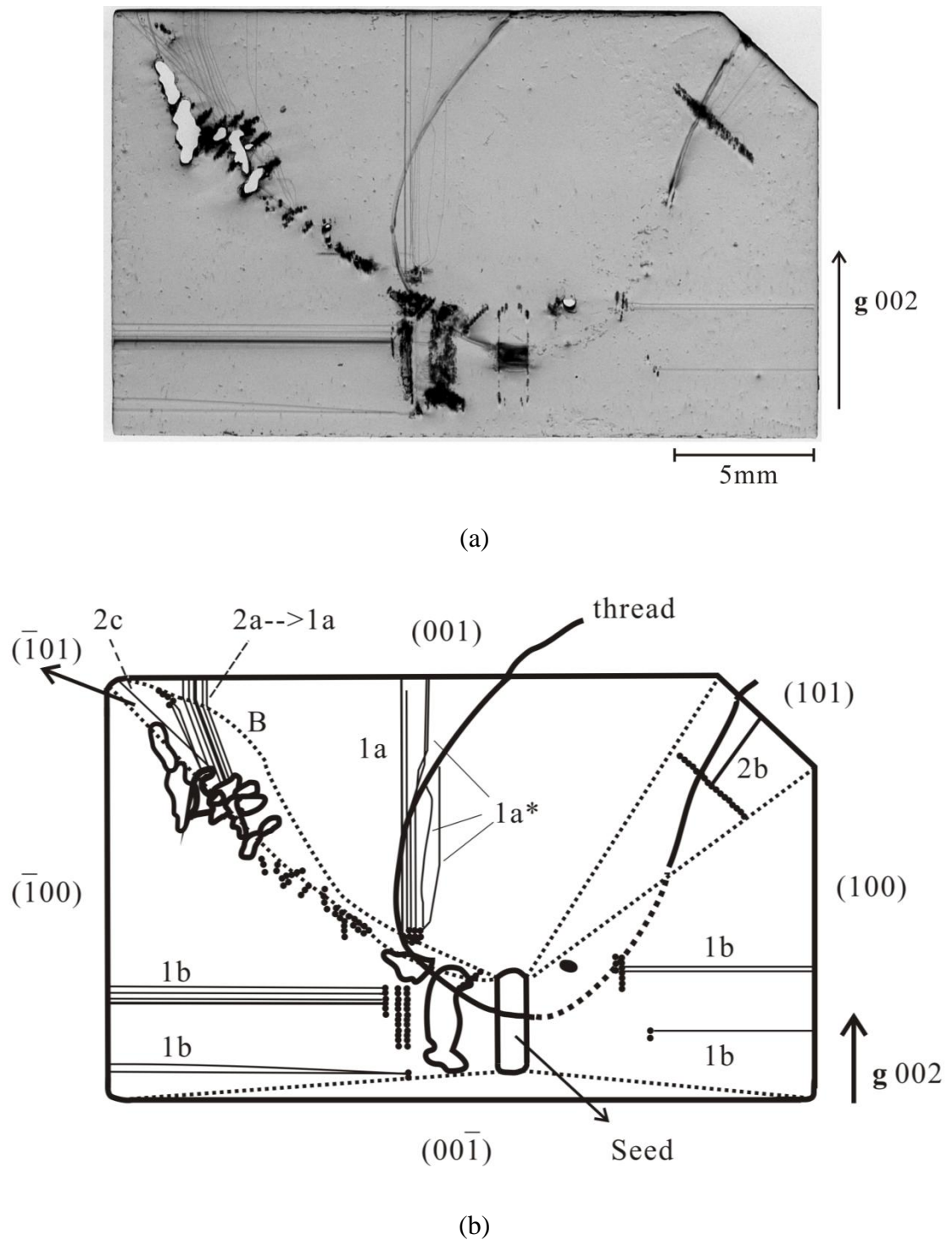


Figure 6.8 (a) Topograph of the (010) plate of pure NaClO_3 crystal. Reflection 002, film D4. (b) Sketch for the topograph in (a).

	(100) sector			$(\bar{1}00)$ sector		
b	$\alpha(\text{obs.})$	type	$\alpha(\text{calc.})$	$\alpha(\text{obs.})$	type	$\alpha(\text{calc.})$
[010]	$0 \pm 0.5^\circ$	1b,edge	0.0°			
[010]				$0 \pm 0.5^\circ$	1b,edge	0.0°

	(001) sector		
b	$\alpha(\text{obs.})$	type	$\alpha(\text{calc.})$
[001]	$0 \pm 0.5^\circ$	1a,screw	0.0°

Table 6.2 The observed dislocation lines in the {001} type growth sectors of pure NaClO₃ crystal and their characterizations. Reflection 002.

One very clear dislocation line can be observed in the growth sector (101), see Figure 6.8a. According to the calculated values, the measured angle of $\alpha=0 \pm 2^\circ$ makes this dislocation line to possibly be a dislocation of 2b, 2c or 2e type. However, the growth sector boundaries between sectors (101) and (001) or (101) and (100) have not shown variation of slope after the appearance of this dislocation line (Figure 6.8a). This implies that the relative growth rates between (101) and (001) or (101) and (100) had not changed. Therefore, this dislocation line did not provide active growth sites and thus should be attributed to be of pure edge type, i.e. 2b or 2e. Since the 2b type is by far lower in line tension energy than the 2e type, it is more reasonable to assign this dislocation line as 2b type (Table 6.3).

Very interestingly, at the top-left corner of the topograph it can be seen (Figure 6.8a), along roughly the $[\bar{1}01]$ direction there are bunches of dislocation lines. These lines can be separated into two categories by their line profile and orientation, i.e. the bend line which was composed of two segments lying respectively at 19.0° and 0° to the [001] direction, and the straight line lying at 45.0° to the [001] direction. For the bent lines, the first segment, before the bending point, is consistent with the 2a type dislocation line in growth sector $(\bar{1}01)$, which aligns with an α angle of 26° to $[\bar{1}01]$ direction (19.0° against [001] direction). Also, the second segment after the bending point, lying with an α angle of 0° to [001] direction, is consistent with the 1a type dislocation line in growth sector (001). The two segments lead to the assignment of $2a \rightarrow 1a$ for these dislocation lines, during whose propagation the dislocation type

changed from mixed to pure screw. Thus, this bunch of bent dislocation lines implies that a growth sector ($\bar{1}01$) of considerable size existed, and the dislocation lines originating in it had crossed the boundary and continued propagating in sector (001). By connecting the bending points among these dislocation lines, a curved boundary is recovered (dotted line marked B in Figure 6.8b). However, there is hardly any sign of the ($\bar{1}01$) face in the final habit shown by the plate. The curvature of the boundary and the disappearance of ($\bar{1}01$) face will be explored below.

The dislocation line with straight profile mentioned above makes an angle of 0.0° with the $[\bar{1}01]$ direction (45.0° with $[001]$ direction) (Figure 6.8a), which could possibly be of type 2b, 2c or 2e. In addition, the curved boundary (marked B in Figure 6.8b) is turning towards sector ($\bar{1}01$) during growth, which implies a faster growth of sector ($\bar{1}01$) compared to its neighbouring sector (001). Fast growth rates of the crystal faces rely on the presence of persistent growing sites, such as pure screw dislocations or mix dislocations. Thus, the straight dislocation line is determined to be 2c pure screw (but not 2b or 2e) (Figure 6.8b), which is able to support spiral growth for the rapid growth of sector ($\bar{1}01$). Furthermore, the fast growth of ($\bar{1}01$) face resulted in a smaller facet size, which cannot be observed in the final habit.

b	(101) sector			$(\bar{1}01)$ sector		
	$\alpha(\text{obs.})$	type	$\alpha(\text{calc.})$	$\alpha(\text{obs.})$	type	$\alpha(\text{calc.})$
[010]	$0 \pm 2^\circ$	2b,edge	0.0°			
[001]				$26 \pm 2^\circ$	2a,mixed (part of 2a \rightarrow 1a)	26.0°
$[\bar{1}01]$				$0 \pm 2^\circ$	2c,screw	0.0°

Table 6.3 The observed dislocation lines in $\{101\}$ type growth sectors of pure NaClO_3 crystal and their characterizations. Reflection 002.

6.3.3 Dislocations in 40ppm $\text{S}_2\text{O}_6^{2-}$ -doped NaClO_3 Crystal

The plate of $(\bar{1}10)$ cut from 40ppm doped crystal was systematically explored using three reflections, i.e. 002, 012 and $11\bar{1}$. The contrast of some dislocation lines varied according to the applied reflection vector \mathbf{g} , which necessarily assists the assignment of Burgers vector by considering visibility rules. The visibility rules have been stated in the last section.

6.3.3.1 Reflection 002

In the topograph by 002 reflection (Figure 6.9a), it can be seen that most dislocations originated from the seed-crystal interface. The dislocation lines in different growth sectors will be dealt with separately below.

First, in the symmetric sectors of (001) and $(00\bar{1})$, a number of straight dislocation lines lie closely at 0° with respect to the growth directions of the sectors (Figure 6.9). Since dislocation lines of 1b and 1d (pure edge types) will be invisible when using reflection 002 due to $\mathbf{g} \cdot \mathbf{b} = 0$ and $\mathbf{g} \cdot \mathbf{b} \times \mathbf{l} = 0$, these visible dislocation lines are designated to type 1a of pure screw character (Table 6.4). In addition, there are a large number of post-growth dislocation lines (cf. section 6.2.4) presenting in these sectors, for which the assignment of dislocation type is not applicable.

Second, it can be seen that most of the dislocation lines in symmetric sectors of $(11\bar{1})$ and $(\bar{1}\bar{1}\bar{1})$ are extended from the sectors of (110) and $(\bar{1}\bar{1}0)$ (Figure 6.9a and b), except that the several lines in sector $(11\bar{1})$ were extended from $(00\bar{1})$. The two different types of dislocation lines with α angles of $24.1(\pm 3)^\circ \sim 25.0(\pm 3)^\circ$ and $0(\pm 3)^\circ$ to the growth directions can be assigned to 3a(28.7°) and 3c(0.0°), by comparing to the calculation in Table 6.1.

Third, in the symmetric sectors of (110) and $(\bar{1}\bar{1}0)$, all the dislocation lines are propagating parallel to the growth directions of the sectors (i.e. $\alpha(\mathbf{n}, \mathbf{l}) = 0^\circ$) (Figure 6.9a). A large number of these dislocation lines have crossed the growth sector boundaries and continued propagating in sectors of $(11\bar{1})$ and $(\bar{1}\bar{1}\bar{1})$, whose segment in the $(11\bar{1})$ and $(\bar{1}\bar{1}\bar{1})$ sectors were previously assigned to be 3a and 3c with Burgers vector of [001] and $[1\bar{1}0]$, respectively. When the dislocation lines crossed the sector boundaries, they normally should retain the same Burgers vector. Thus, the

dislocation lines in sectors (110) and $(\bar{1}\bar{1}0)$ discussed are attributed to 2b and 2e types. For the remaining dislocations in sector $(\bar{1}\bar{1}0)$, they are preferred to be assigned as 2b rather than 2e, due to the much lower E_1 (thus more possibility to appear) of 2b than that of 2e. In addition, the termination of these lines within the growth sector was probably due to a slight miscut angle of the plate.

It is noticed that, the $(\bar{1}\bar{1}\bar{1})$ sector emerged at a certain point during the crystal growth (Figure 6.9a), before which it did not exist before. This implies an intensive incorporation of the $S_2O_6^{2-}$ impurity at the specific growth sectors of $\{\bar{1}\bar{1}\bar{1}\}$ type, which has greatly inhibited the growth rate of these sectors.

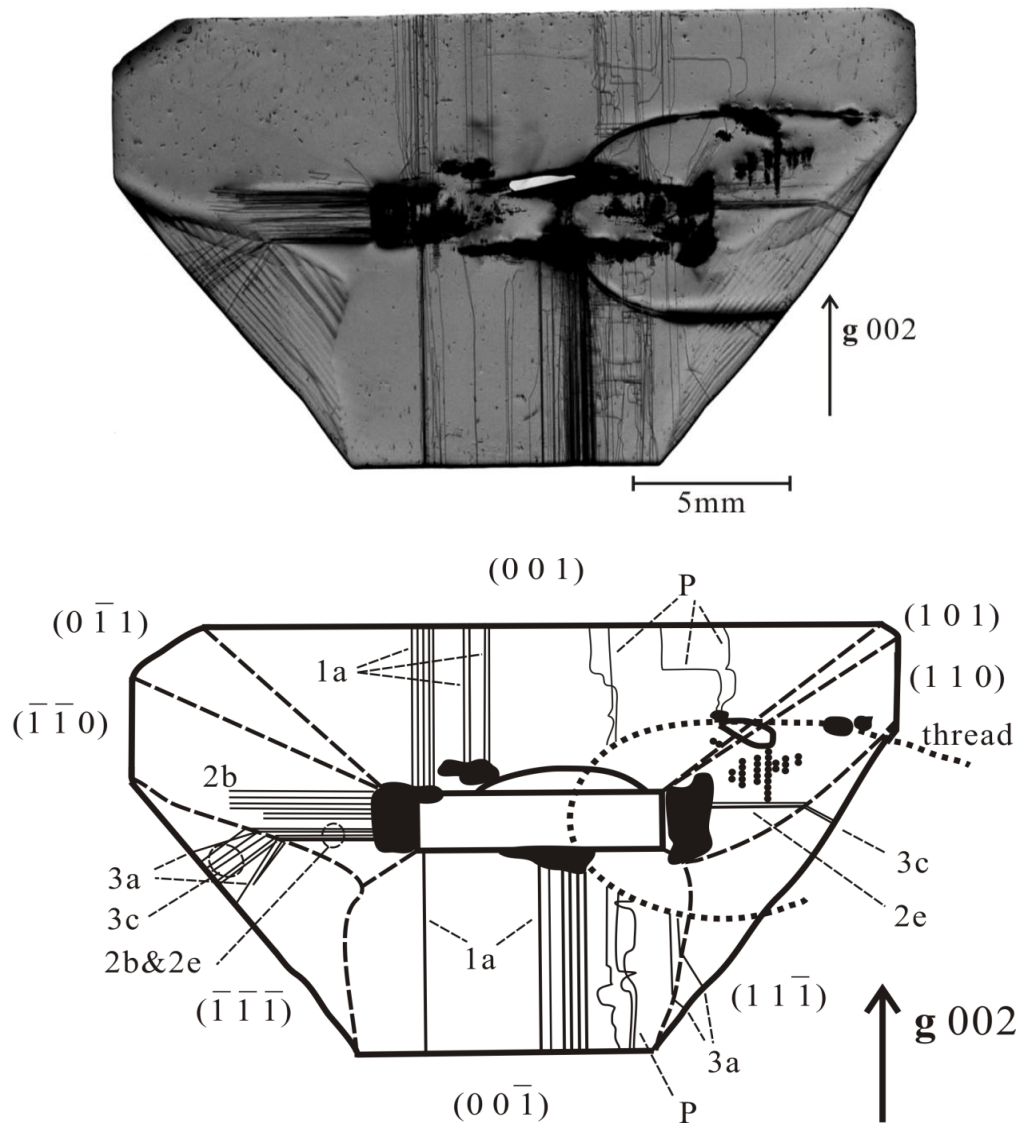


Figure 6.9 (a) Topograph of the $(\bar{1}\bar{1}0)$ plate of 40ppm $S_2O_6^{2-}$ -doped $NaClO_3$ crystal. Reflection 002, film D4. (b) Sketch for the topograph in (a). The growth sector

boundaries with no contrast on the topograph were deduce from the outer shape of the plate and are drawn with dashed line, while some ; dotted line: the thread used for hanging crystal seed during growth.

	(001) sector			$(00\bar{1})$ sector		
b	$\alpha(\text{obs.})$	type	$\alpha(\text{calc.})$	$\alpha(\text{obs.})$	type	$\alpha(\text{calc.})$
[001]	$0 \pm 0.5^\circ$	1a,screw	0.0°			
$[00\bar{1}]$				$0 \pm 0.5^\circ$	1a,screw	0.0°

	(110) sector			$(\bar{1}\bar{1}0)$ sector		
b	$\alpha(\text{obs.})$	type	$\alpha(\text{calc.})$	$\alpha(\text{obs.})$	type	$\alpha(\text{calc.})$
$[\bar{1}10]$	$0 \pm 0.5^\circ$	2e,edge	0.0°			
[001]				$0 \pm 0.5^\circ$	2b,edge	0.0°
$[1\bar{1}0]$				$0 \pm 0.5^\circ$	2e,edge	0.0°

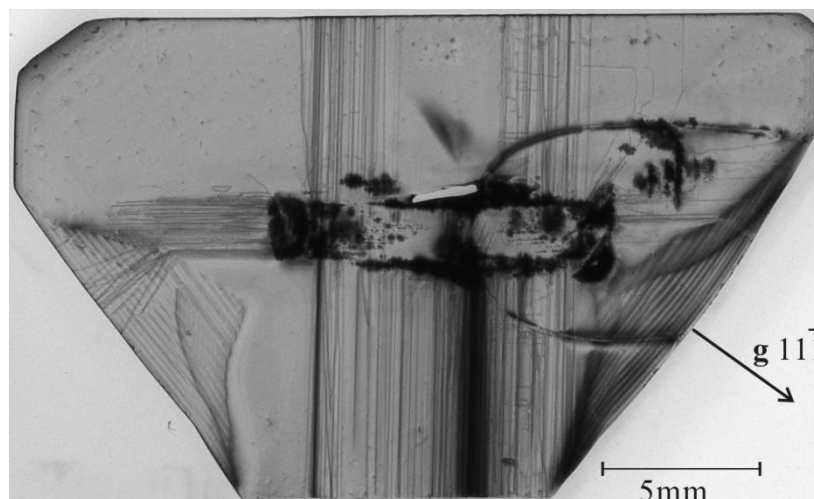
	$(11\bar{1})$ sector			$(\bar{1}\bar{1}\bar{1})$ sector		
b	$\alpha(\text{obs.})$	type	$\alpha(\text{calc.})$	$\alpha(\text{obs.})$	type	$\alpha(\text{calc.})$
$[00\bar{1}]$	$25.0 \pm 3^\circ$	3a,mixed	28.7°			
$[\bar{1}10]$	$0 \pm 3^\circ$	3c,edge	0.0°			
[001]				$24.1 \pm 3^\circ$	3a,mixed	28.7°
$[1\bar{1}0]$				$0 \pm 3^\circ$	3c,edge	0.0°

Table 6.4 The observed dislocation lines in the $(\bar{1}10)$ plate of 40ppm $\text{S}_2\text{O}_6^{2-}$ -doped NaClO_3 crystal and their characterizations. Reflection 002.

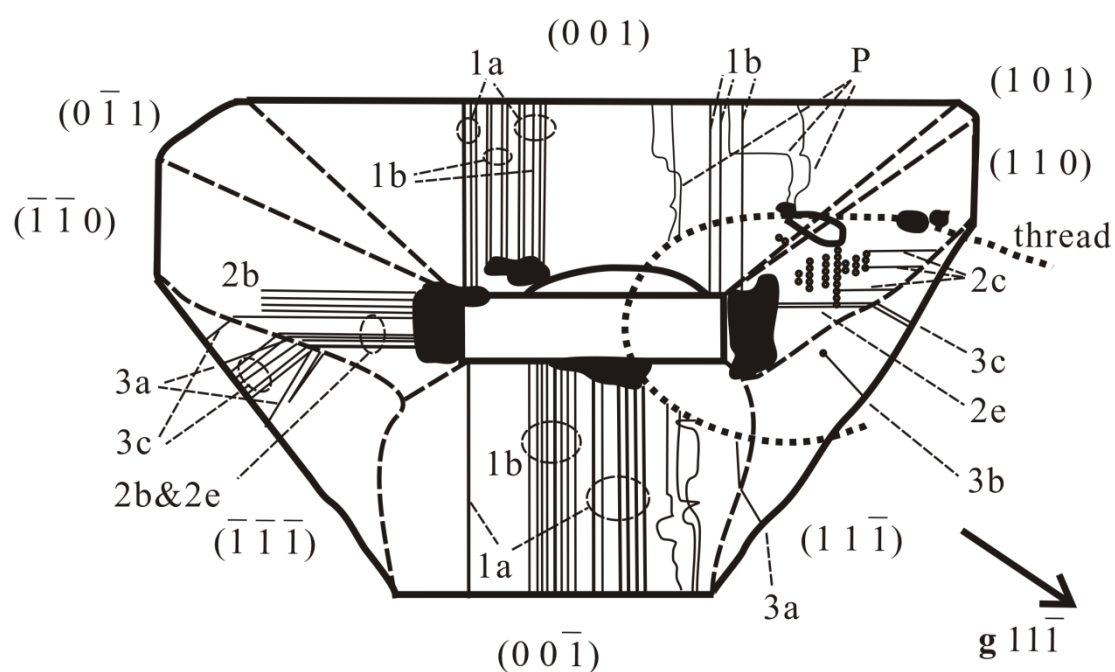
6.3.3.2 Reflection $11\bar{1}$

As shown in Figure 6.10a, the topograph of plate ($\bar{1}10$) taken by reflection $11\bar{1}$ presents different features compared to that taken by reflection 002 (Figure 6.9). While most dislocation lines in the 002 topograph are retained in the $11\bar{1}$ topograph, more dislocation lines emerged in this topograph. But, the large amount of dislocation lines have caused overlapping among lines resulting in reduced resolution in some regions. The assignment for the retained dislocation lines from 002 topograph will not be repeated.

In the growth sectors of (001) and ($00\bar{1}$) (Figure 6.10), some dislocation lines with an α angle of 0° can be newly identified which were not revealed by the 002 topograph, thus they are of pure edge type according to the visibility rules. These lines can be assigned as 1b or 1d according to Table 6.1, but 1b is more likely due to lower line energy. In the (110) sector, several dislocation lines originating from the inclusions (Figure 6.10) were seen for the first time. They lie with an α angle of 0° and were invisible under 002 reflection (Figure 6.9), according to Table 6.1 these should be assigned as 2c dislocation of pure screw character. A well contrasted dislocation line with α angle of $11.8(\pm 3)^\circ$ is newly observed in the growth sector of ($11\bar{1}$) (Figure 6.10). According to the calculated values of α in this sector (Table 6.1), this dislocation is assigned as 3b type. All dislocation lines and their characterizations are summarized in Table 6.5.



(a)



(b)

Figure 6.10 (a) $(\bar{1}10)$ plate of of 40ppm $S_2O_6^{2-}$ -doped $NaClO_3$ crystal. Reflection $11\bar{1}$, film D4. (b) Sketch for the topograph in (a). Dashed lines: growth sector boundaries; dotted line: the thread used for hanging crystal seed.

b	(001) sector			(00 $\bar{1}$) sector		
	α (obs.)	type	α (calc.)	α (obs.)	type	α (calc.)
[001]	$0 \pm 0.5^\circ$	1a,screw	0.0°			
[010]	$0 \pm 0.5^\circ$	1b,edge	0.0°			
[00 $\bar{1}$]				$0 \pm 0.5^\circ$	1a,screw	0.0°
[0 $\bar{1}$ 0]				$0 \pm 0.5^\circ$	1b,edge	0.0°

b	(110) sector			$(\bar{1}\bar{1}0)$ sector		
	α (obs.)	type	α (calc.)	α (obs.)	type	α (calc.)
[$\bar{1}\bar{1}$ 0]	$0 \pm 0.5^\circ$	2c,screw	0.0°			
[$\bar{1}\bar{1}$ 0]	$0 \pm 0.5^\circ$	2e,edge	0.0°			
[00 $\bar{1}$]				$0 \pm 0.5^\circ$	2b,edge	0.0°
[1 $\bar{1}$ 0]				$0 \pm 0.5^\circ$	2e,edge	0.0°

b	(11 $\bar{1}$) sector			$(\bar{1}\bar{1}\bar{1})$ sector		
	α (obs.)	type	α (calc.)	α (obs.)	type	α (calc.)
[001]	$24.1 \pm 3^\circ$	3a,mixed	28.7°			
[110]	$11.8 \pm 3^\circ$	3b,mixed	14.3°			
[$\bar{1}\bar{1}$ 0]	$0 \pm 2^\circ$	3c,edge	0.0°			
[00 $\bar{1}$]				$23.0 \pm 3^\circ$	3a,mixed	28.7°
[1 $\bar{1}$ 0]				$0 \pm 2^\circ$	3c,edge	0.0°

Table 6.5 The observed dislocation lines in the plate ($\bar{1}\bar{1}0$) of 40ppm $S_2O_6^{2-}$ -doped $NaClO_3$ crystal and their characterizations, as well as the calculated values. Reflection $11\bar{1}$.

6.3.3.3 Reflection 012

The 012 topograph (Figure 6.11a) shows very good spatial resolution for the dislocation lines, due to the strong reflection of 012 planes. The overall features of the defects revealed by this topograph are quite similar to those of the $11\bar{1}$ topograph, except to some extent the α angles have slightly changed (with deviation within 1.5°) due to the different reflection for X-ray topography. Thus, the assignment for the regular dislocation lines of straight profile will be similar to that used for the $11\bar{1}$ topograph and will not be repeated here. The results of assignments for the 012 topograph are tabulated in Table 6.6.

However, a striking difference can be found when comparing the 012 topograph to the 002 and $11\bar{1}$ topographs. That is, the bow-shaped dislocation lines (i.e. post-growth dislocation lines) are invisible on only the 012 topograph. But, the reason for this phenomenon is unclear.

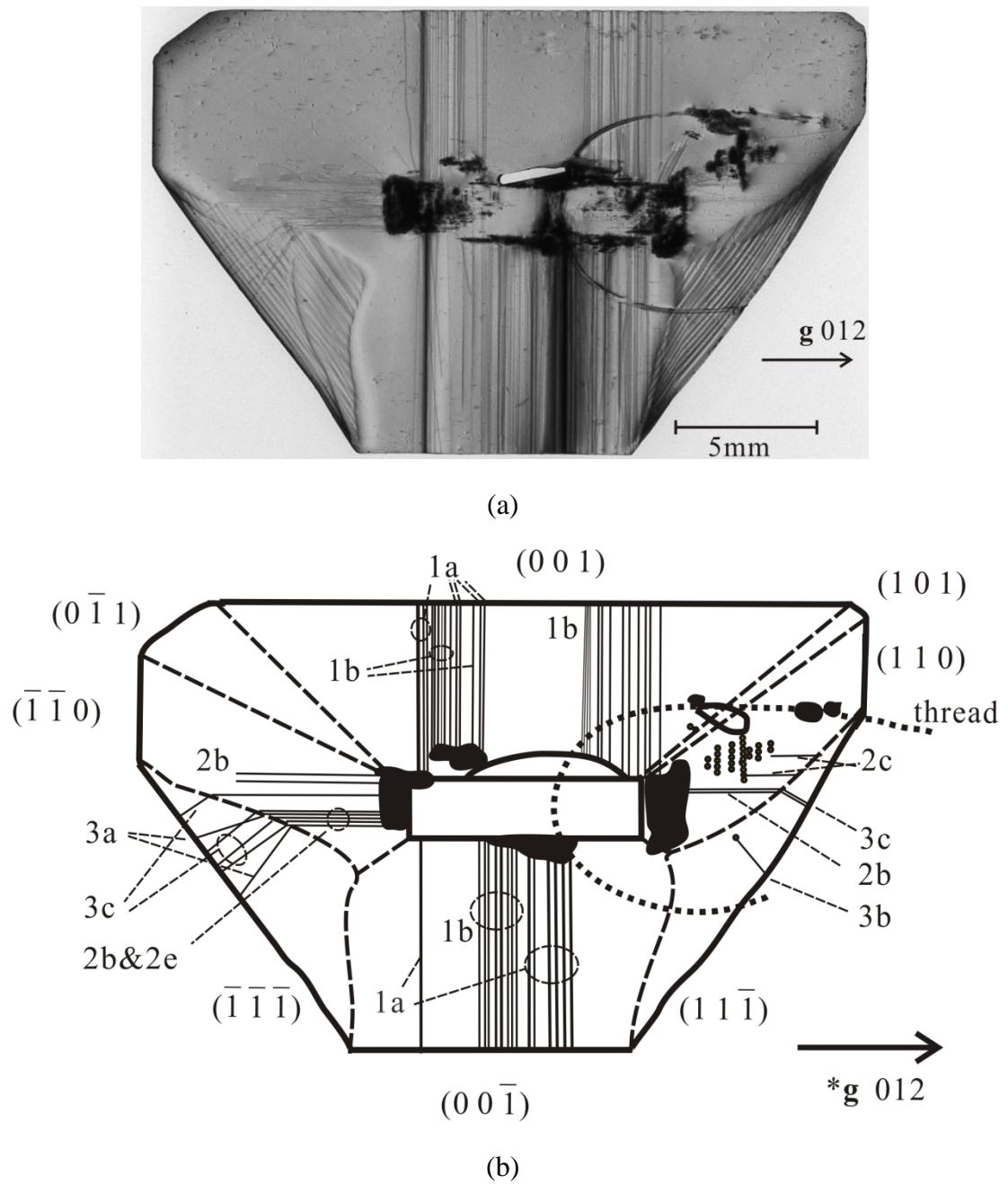


Figure 6.11 (a) $(\bar{1}10)$ plate of 40ppm $S_2O_6^{2-}$ -doped $NaClO_3$ crystal. Reflection 012, film D4. (b) Sketch of the topograph in (a). Dashed lines: growth sector boundaries deduced from the outer shape of the plate; dotted line: the thread used for hanging crystal seed during growth; *: the reflection plane is inclined to the plate.

b	(001) sector			$(00\bar{1})$ sector		
	$\alpha(\text{obs.})$	type	$\alpha(\text{calc.})$	$\alpha(\text{obs.})$	type	$\alpha(\text{calc.})$
[001]	$0 \pm 0.5^\circ$	1a,screw	0.0°			
[010]	$0 \pm 0.5^\circ$	1b,edge	0.0°			
$[00\bar{1}]$				$0 \pm 0.5^\circ$	1a,screw	0.0°
$[0\bar{1}0]$				$0 \pm 0.5^\circ$	1b,edge	0.0°

b	(110) sector			$(\bar{1}\bar{1}0)$ sector		
	$\alpha(\text{obs.})$	type	$\alpha(\text{calc.})$	$\alpha(\text{obs.})$	type	$\alpha(\text{calc.})$
[001]	$0 \pm 0.5^\circ$	2b,edge	0.0°			
[110]	$0 \pm 0.5^\circ$	2c,screw	0.0°			
$[00\bar{1}]$				$0 \pm 0.5^\circ$	2b,edge	0.0°
$[1\bar{1}0]$				$0 \pm 0.5^\circ$	2e,edge	0.0°

b	$(11\bar{1})$ sector			$(\bar{1}\bar{1}\bar{1})$ sector		
	$\alpha(\text{obs.})$	type	$\alpha(\text{calc.})$	$\alpha(\text{obs.})$	type	$\alpha(\text{calc.})$
[110]	$13.3 \pm 3^\circ$	3b,mixed	14.3°			
$[\bar{1}\bar{1}0]$	$0 \pm 2^\circ$	3c,edge	0.0°			
$[00\bar{1}]$				$21.9 \pm 3^\circ$	3a,mixed	28.7°
$[1\bar{1}0]$				$0 \pm 3^\circ$	3c,edge	0.0°

Table 6.6 The observed dislocation lines in the plate $(\bar{1}\bar{1}0)$ of 40ppm $\text{S}_2\text{O}_6^{2-}$ -doped NaClO_3 crystal and their characterizations. Reflection 012.

6.3.4 Dislocation Lines in 160ppm $\text{S}_2\text{O}_6^{2-}$ -doped Crystal

Since the 160ppm doped crystal possesses habit faces of tetrahedral $\{\bar{1}\bar{1}\bar{1}\}$ and squeezed small $\{001\}$ facets on the edge of the tetrahedron, it can represent the typical features of crystals doped by relatively higher impurity concentration (i.e. 70ppm and above). In this section, the $(\bar{1}\bar{1}0)$ plate of 160ppm doped crystal will be used for dislocation characterization using 002 and $11\bar{1}$ reflections.

6.3.4.1 Reflection 002

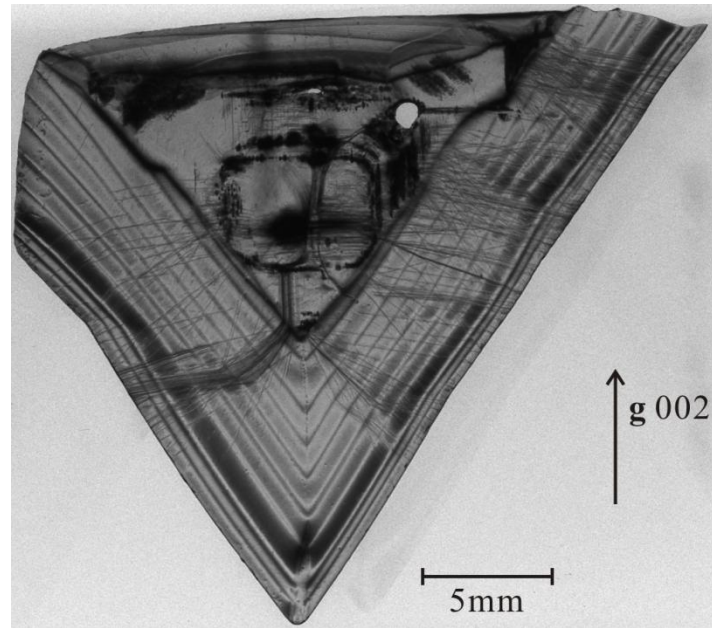
From this 002 topograph (Figure 6.12a) it can be seen that the seed possesses a large amount of dislocation lines, especially in the directions of $[110]$ and $[\bar{1}\bar{1}0]$, some of which were extended into the as-grown crystal. Also, a large quantity of dislocation lines were generated from the inclusions in the growth sectors and at the growth sector boundaries. In addition, for this 002 topograph the dislocation lines in sectors of (110) and $(\bar{1}\bar{1}0)$ will not be discussed due to the low resolution.

In the (001) and $(00\bar{1})$ sectors, there are dislocation lines with an α angle of $0(\pm 0.5)^\circ$ pointing to directions of $[001]$ and $[00\bar{1}]$, respectively (Figure 6.12a). According to the calculations in Table 6.1 and the invisibility law $\mathbf{g} \cdot \mathbf{b} = 0$ under reflection 002, these dislocation lines are assigned as 1a type of pure screw character with Burgers vector of $[001]$ or $[00\bar{1}]$, respectively. Most 1a type dislocation lines with Burgers vector $[00\bar{1}]$ have entered $(\bar{1}\bar{1}\bar{1})$ sector and continued propagation along $[\bar{1}\bar{1}\bar{1}]$ direction. The dislocations should retain a Burgers vector of $[00\bar{1}]$ during crossing of the growth sector boundary. But, according to Table 6.1 the dislocation lines along $[\bar{1}\bar{1}\bar{1}]$ direction are 3c type with Burgers vector of $[1\bar{1}0]$. Furthermore, in the $(\bar{1}\bar{1}\bar{1})$ sector these dislocation lines changed to 3a type dislocation (α angle of $0(\pm 0.5)^\circ$) with Burgers vector of $[00\bar{1}]$. Therefore, it is likely that the dislocation lines have retained the Burgers vector of $[00\bar{1}]$ while crossing the boundary. But their segments along the $[\bar{1}\bar{1}\bar{1}]$ direction should be assigned as 3c* rather than 3c due to the Burgers vector of $[00\bar{1}]$, which finally transformed to 3a type. The 3c* type possessing a Burgers vector of $[00\bar{1}]$ was not reported in the calculation of preferred low energy dislocations by Hooper et al. (1983). Thus, both the transformation $3c^* \rightarrow 3a$ and the

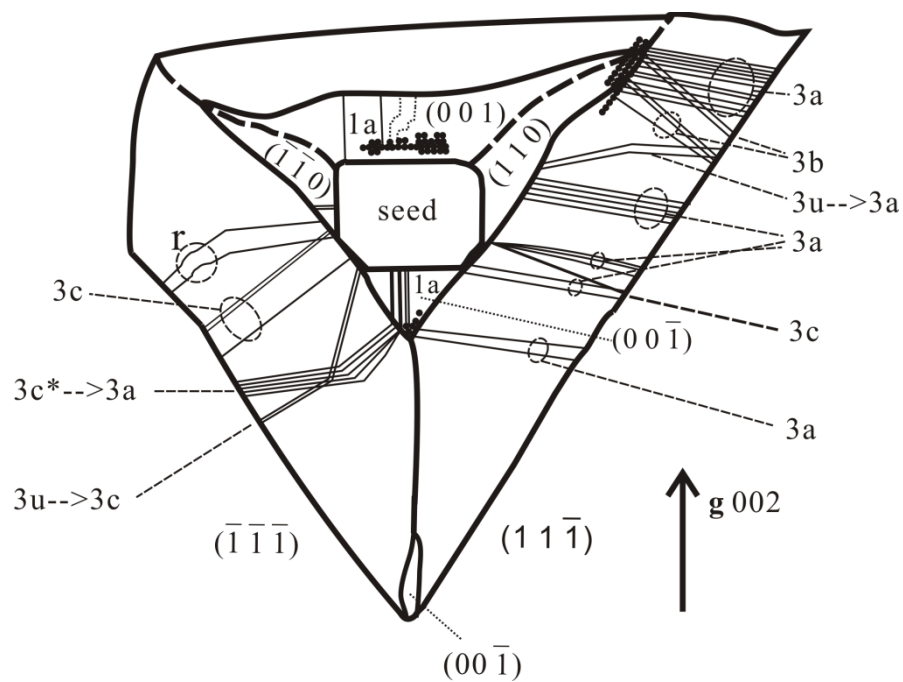
absence in the calculation of preferred low energy dislocations imply that $3c^*$ type dislocation is an intermediate type with relatively high energy.

In the growth sectors of $(11\bar{1})$ and $(\bar{1}\bar{1}\bar{1})$, conventional dislocation lines with straight profiles have been assigned to be of type 3a, 3b and 3c, by judging the α angles while considering the visibility law. The results are tabulated in Table 6.7.

More complicated, a type of dislocation lines lies with an α angle of approximately 36.5° (3u in Figure 6.12b) and is observed in both the sectors of $(11\bar{1})$ and $(\bar{1}\bar{1}\bar{1})$, but no consistent dislocation lines from the calculation (Table 6.1) can be found. Their straight profile indicates that they are not post-growth dislocation lines. This type of dislocation line is defined as 3u type in the current study (Figure 6.12b), with unknown Burgers vector. Furthermore, it is observed that the two cases of these 3u dislocation lines have finally changed into conventional dislocation types ($3u \rightarrow 3a$ and $3u \rightarrow 3c$) during further growth, respectively. Since dislocation lines always tend to transform only from higher energy type to lower energy type, this change of line direction implies that the 3u type dislocation possesses higher line tension energy than both 3a and 3c. Thus, 3u type dislocation is an intermediate type dislocation with relatively high energy.



(a)



(b)

Figure 6.12 (a) Topograph of $(\bar{1}10)$ plate of 160ppm $S_2O_6^{2-}$ -doped $NaClO_3$ crystal. The upper and left margins of 160ppm plate $(\bar{1}10)$ are not integral due to previously artificial cutting of the crystal. Reflection 002, film D7. (b) Sketch for the topograph in (a). P indicates post-growth relaxed dislocation lines; r indicates partially curved dislocation lines; 3c* indicates the irregular dislocation line in line direction 3c but with a Burgers vector different from the calculated preferred value.

b	(001) sector			(00 $\bar{1}$) sector		
	α (obs.)	type	α (calc.)	α (obs.)	type	α (calc.)
[001]	$0 \pm 0.5^\circ$	1a,screw	0.0°			
[00 $\bar{1}$]				$0 \pm 0.5^\circ$	1a,screw	0.0°

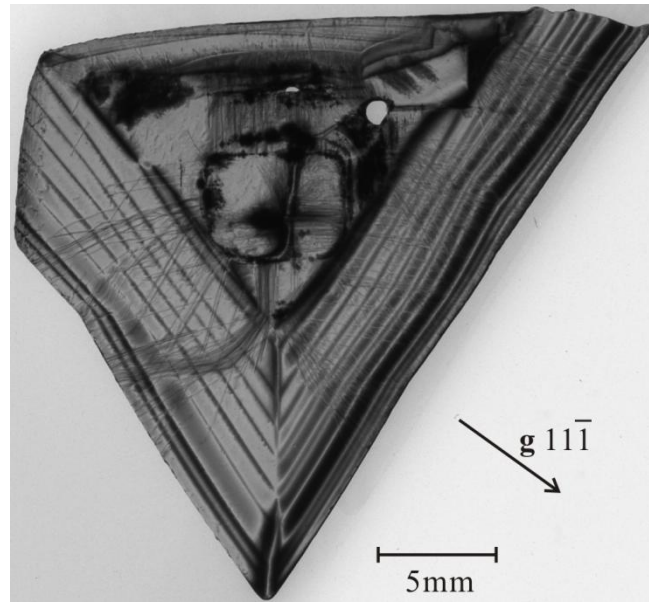
b	(11 $\bar{1}$) sector			$(\bar{1}\bar{1}\bar{1})$ sector		
	α (obs.)	type	α (calc.)	α (obs.)	type	α (calc.)
[001]	$26.6 \pm 3^\circ$	3a,mixed	28.7°			
[110]	$12.1 \pm 3^\circ$	3b,mixed	14.3°			
[$\bar{1}$ 10]	$2 \pm 3^\circ$	3c,edge	0.0°			
N/A	$36.5 \rightarrow 29.1$ $(\pm 3)^\circ$	$3u \rightarrow 3a, N/A$	N/A			
[1 $\bar{1}$ 0]				$0 \pm 3^\circ$	3c,edge	0.0°
[00 $\bar{1}$]				$0 \rightarrow 26.8$ $(\pm 3)^\circ$	$3c^* \rightarrow 3a,$ N/A	$0.0 \rightarrow 28.7^\circ$
N/A				$36.5 \rightarrow 0$ $(\pm 3)^\circ$	$3u \rightarrow 3c,$ N/A	N/A

Table 6.7 The observed dislocation lines in the plate ($\bar{1}\bar{1}0$) of 160ppm $S_2O_6^{2-}$ -doped $NaClO_3$ crystal and their characterizations. Reflection 002.

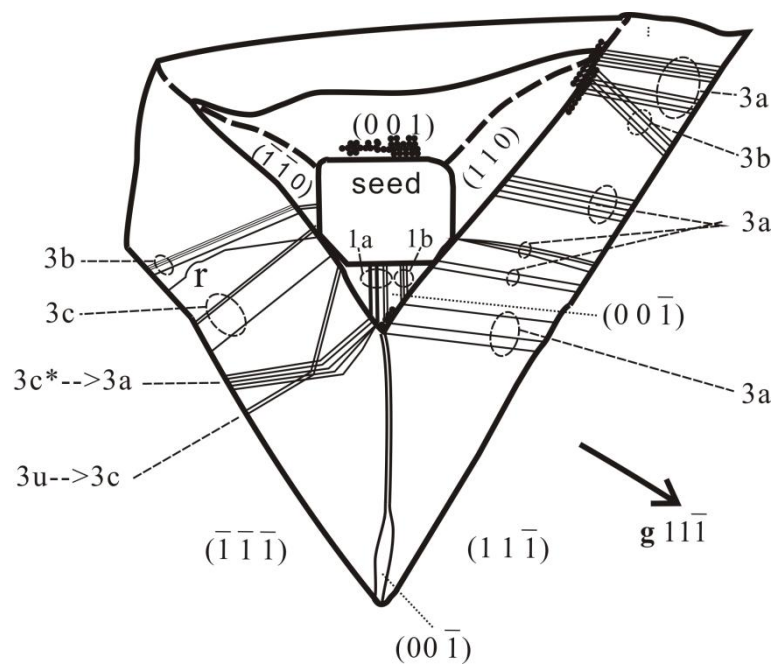
6.3.4.2 Reflection $11\bar{1}$

The $11\bar{1}$ reflection revealed a large number of dislocation lines in the (001) sector. However, the density of dislocation lines is too high to distinguish individual lines, which results in impossibility for dislocation assignment. In the $(00\bar{1})$ sector, besides the 1a type dislocation lines assigned in the 002 topograph, there now appeared several dislocation lines with α angle of 0° which should be assigned as 1b type of pure edge character.

In $(11\bar{1})$ and $(\bar{1}\bar{1}\bar{1})$ sectors, the dislocation lines are almost identical with that revealed by the 002 topograph, except the 3c type dislocation in sector $(11\bar{1})$ is out of contrast due to $\mathbf{g} \cdot \mathbf{b} = 0$ and $\mathbf{g} \cdot \mathbf{b} \times \mathbf{l} = 0$ where $\mathbf{g} = (11\bar{1})$, $\mathbf{b} = [1\bar{1}0]$ and $\mathbf{l} = [11\bar{1}]$. The assignment for general dislocations is similar to that used in the 002 topograph, and the results are tabulated in Table 6.8.



(a)



(b)

Figure 6.13 (a) Topograph of $(\bar{1}10)$ plate of 160ppm $S_2O_6^{2-}$ -doped $NaClO_3$ crystal. Reflection $11\bar{1}$, film D7. (b) Sketch of the topograph in (a). P indicates post-growth relaxed dislocation lines; r indicates partially curved dislocation lines; 3c* indicates the irregular dislocation line in line direction 3c but with a Burgers vector different from the calculated preferred value.

	(00 $\bar{1}$) sector					
b	α (obs.)	type	α (calc.)			
[00 $\bar{1}$]	0.0 \pm 0.5 $^{\circ}$	1a,screw	0.0 $^{\circ}$			
[0 $\bar{1}$ 0]	0.0 \pm 0.5 $^{\circ}$	1b,edge	0.0 $^{\circ}$			

	(11 $\bar{1}$) sector			$(\bar{1}\bar{1}\bar{1})$ sector		
b	α (obs.)	type	α (calc.)	α (obs.)	type	α (calc.)
[001]	23.3 \pm 3 $^{\circ}$	3a,mixed	28.7 $^{\circ}$			
[110]	11.4 \pm 3 $^{\circ}$	3b,mixed	14.3 $^{\circ}$			
[$\bar{1}\bar{1}$ 0]				12.7 \pm 3 $^{\circ}$	3b,mixed	14.3 $^{\circ}$
[1 $\bar{1}$ 0]				0.0 \pm 3 $^{\circ}$	3c,edge	0.0 $^{\circ}$
N/A				0.0 \rightarrow 31.4 (\pm 3) $^{\circ}$	3c* \rightarrow 3a, N/A	0.0 \rightarrow 28.7 $^{\circ}$
N/A				35.0 \rightarrow 0.0(\pm 3) $^{\circ}$	3u \rightarrow 3c, N/A	N/A

Table 6.8 The observed dislocation lines in the plate (11 $\bar{1}$) of 160ppm S₂O₆²⁻-doped NaClO₃ crystal and their characterizations. Reflection 11 $\bar{1}$.

6.4 Growth History of Impurity Affected Crystal

6.4.1 Introduction

The orientation of a growth sector boundary depends on the relative growth rates of neighbouring sectors. Under ideal growth conditions when the relative growth rates are constant, the sector boundaries in a crystal are straight; however, during actual crystal growth the boundary lines are often found to be curved due to the fluctuation of relative growth rate caused by the change of growth velocity of growth sectors. The growth history of the doped crystal can be reconstructed by exploring the growth sector boundaries and calculating the relative growth rate between the crystal faces of {001}, {110} and $\{\bar{1}\bar{1}\bar{1}\}$ types. This will help to understand the habit modification

process of the NaClO_3 crystal in the presence of $\text{S}_2\text{O}_6^{2-}$ impurity. The relationship between relative growth rate and growth sector boundary is illustrated in Figure 6.14 (Klapper, 2010). The mathematical relation is:

$$\frac{v_1}{v_2} = \frac{\cos \beta_1}{\cos \beta_2} \quad (6.2)$$

where v_1 and v_2 are the growth velocities of individual faces, v_1/v_2 represents the relative growth rate, β_1 and β_2 are the angles between the growing directions of individual sectors and the growth-sector boundary. Theoretically, there is an upper limit on the relative growth rate between $(\bar{1}\bar{1}\bar{1})$ and $(00\bar{1})$, beyond which value the $(\bar{1}\bar{1}\bar{1})$ face would vanish from the morphology. This limit is $R_{111} : R_{100} \approx 1.732$, at which the boundary will be propagating along the $[\bar{1}\bar{1}\bar{1}]$ direction and the size of $(\bar{1}\bar{1}\bar{1})$ face will be constant. Similarly the lower limit is $R_{\bar{1}\bar{1}\bar{1}} : R_{00\bar{1}} \approx 0.578$, below which value the $(00\bar{1})$ will disappear.

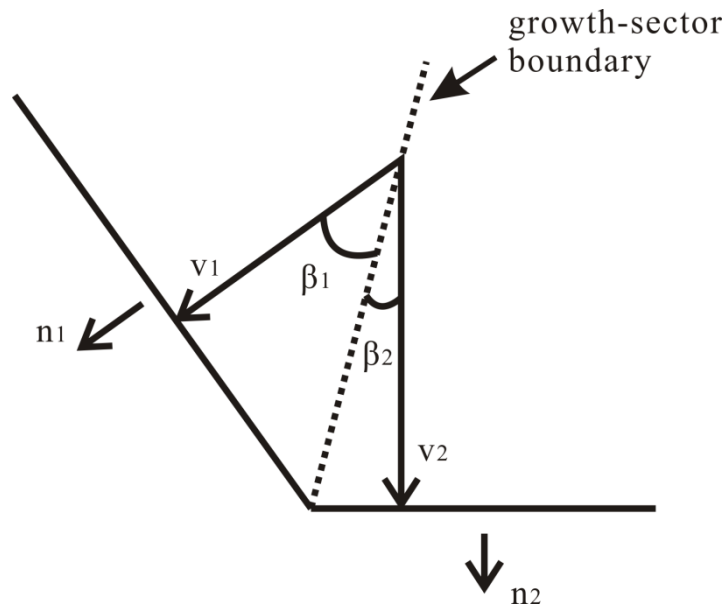


Figure 6.14 Illustration of the relation between growth velocities of v_1 and v_2 of the $(\bar{1}\bar{1}\bar{1})$ and $(00\bar{1})$ sectors. n_1 and n_2 are the growing direction of the two sectors. β_1 and β_2 represent the angle between the growth sector boundary and the growth directions of the two sectors.

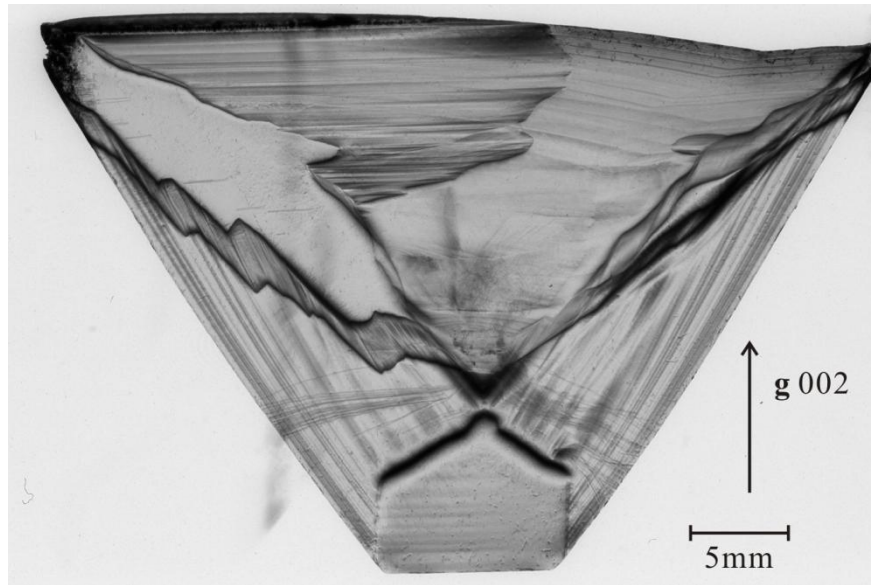
6.4.2 190ppm Doped Crystal as Representative Case

Since 190ppm $S_2O_6^{2-}$ -doped $NaClO_3$ crystal (Figure 6.15a) possesses good shaped sector boundaries and growth sectors of reasonable sizes, its topograph was considered as the suitable representative for exploring the growth history of the doped crystals.

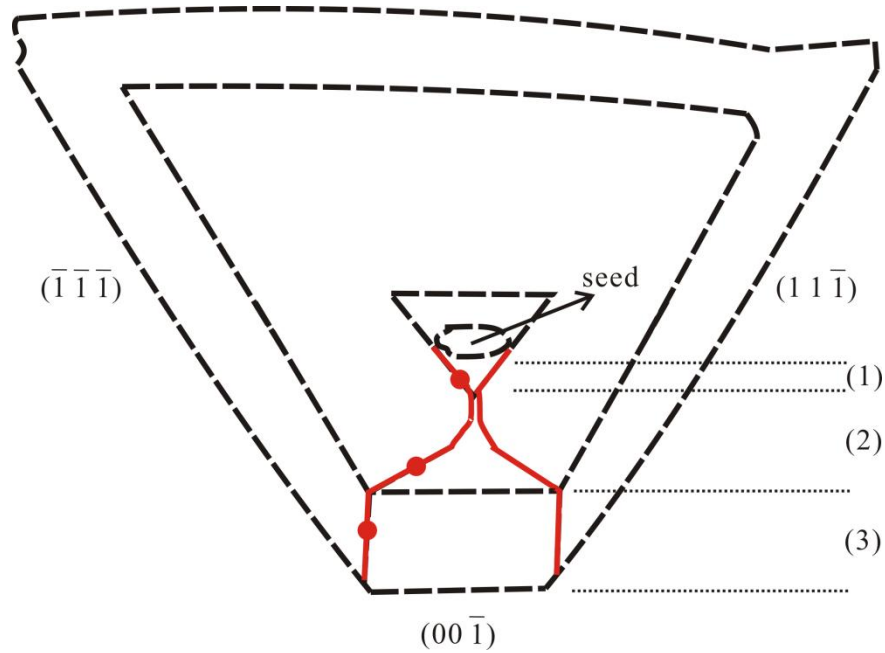
It can be seen that the growth sector boundaries between the $(00\bar{1})$ sector and its two neighbouring sectors of $(11\bar{1})$ and $(\bar{1}\bar{1}\bar{1})$ present a polyline profile composed of mainly three segments in different directions (Figure 6.15). This feature implies that the crystal growth was composed of 3 distinct stages (Figure 6.15b). One from the two boundaries was used for the measurement of β angles, since the two boundaries are almost identical. The angular values was measured at the three points on the boundary between the $(\bar{1}\bar{1}\bar{1})$ and $(00\bar{1})$ sectors (Figure 6.15b), and were tabulated in Table 6.9.

Stage	β_1	β_2
1	89°	35.3°
2	2°	56.7°
3	51.5°	3.2°

Table 6.9 The β angles measured at the three sampling points on the growth sector boundary shown in Figure 6.15a. β_1 and β_2 represent the angle between growth sector boundary and the growth directions of the $(\bar{1}\bar{1}\bar{1})$ and $(00\bar{1})$ sectors, respectively.



(a)



(b)

Figure 6.15 (a) Topograph of $(\bar{1}\bar{1}0)$ plate of 190ppm $\text{S}_2\text{O}_6^{2-}$ -doped NaClO_3 crystal. Reflection 002, film D4. (b) Sketch for the topograph in (a). Dashed lines represent the shape of the crystal at different stages during the growth, the red line followed the boundary between $(00\bar{1})$ sector and its two neighbouring sectors of $(11\bar{1})$ and $(\bar{1}\bar{1}\bar{1})$. The three spots on the red line are the sampling points for the calculation of relative growth rate.

During stage 1, after seeding in, within a short period, the boundaries between the central sector $(00\bar{1})$ and its two neighbouring sectors of $(11\bar{1})$ and $(\bar{1}\bar{1}\bar{1})$ are converging towards a point. The relative growth rate for stage 1 calculated with the corresponding values in Table 6.9 was :

$$\frac{v_{(1)-1}}{v_{(1)-2}} = \frac{\cos 89^\circ}{\cos 35.3^\circ} = 0.021$$

where $v_{(1)-1}$ represents the growth rate of $(\bar{1}\bar{1}\bar{1})$ sector and $v_{(1)-2}$ represents that of $(00\bar{1})$ sector during stage 1. In principle, the calculated small value of 0.021 can be attributed to a decelerated growth velocity of the $(\bar{1}\bar{1}\bar{1})$ sector or an accelerated growth velocity of the $(00\bar{1})$ sector. However, there is no favourable condition for accelerating the growth velocity of the $(00\bar{1})$ sector in the current experiment. So that, the only possibility is that the growth of the $(\bar{1}\bar{1}\bar{1})$ sector nearly stopped during stage 1, due to the strong inhibiting effect of the $S_2O_6^{2-}$ impurity. Thus, the two $\{\bar{1}\bar{1}\bar{1}\}$ sectors were expanding in size since its growth almost stopped, while the $(00\bar{1})$ sector is growing faster than $\{\bar{1}\bar{1}\bar{1}\}$ sectors and becoming tapered (Figure 6.15). In addition, during stage 1 the solution supersaturation has accumulated due to the continuous cooling rate and the slow growth of the small crystal.

During stage 2, the size of $(00\bar{1})$ sector began to expand rapidly while that of the $(\bar{1}\bar{1}\bar{1})$ sector seems unchanged. The relative growth rate for stage 2 calculated with the corresponding values in Table 6.9 was :

$$\frac{v_{(2)-1}}{v_{(2)-2}} = \frac{\cos 2^\circ}{\cos 56.7^\circ} = 1.82$$

where $v_{(2)-1}$ represents the growth rate of $(\bar{1}\bar{1}\bar{1})$ sector and $v_{(2)-2}$ represents that of $(00\bar{1})$ sector. The value is slightly beyond the maximum limit of 1.732, revealing that the growth velocity of $(\bar{1}\bar{1}\bar{1})$ sector is much larger than that of $(00\bar{1})$ sector, compared to the results during stage 1. This can possibly be resulted from accelerated growth velocity of $\{\bar{1}\bar{1}\bar{1}\}$ sectors or decelerated growth velocity of $(00\bar{1})$ sector.

During stage 2, on one hand, a large number of dislocations from $(00\bar{1})$ sector have penetrated the growth sector boundaries and entered the $\{\bar{1}\bar{1}\bar{1}\}$ type sectors (as 3a screw or 3b mixed character), which can accelerate the growth rate of $\{\bar{1}\bar{1}\bar{1}\}$ sectors by spiral growth. On the other hand, the supersaturation was relatively high due to the accumulation during stage 1. Thus, those dislocations of mixed character as active growing sites can largely accelerate the growth of $\{\bar{1}\bar{1}\bar{1}\}$ sectors under relatively high supersaturation. At the same time, due to the loss of dislocation lines as active growth sites, the growth velocity of $(00\bar{1})$ sector was greatly decelerated. Therefore, the relative growth rate ($v_{(2)-1} : v_{(2)-2}$) has largely raised, which is ascribed from the accelerated growth velocity of $\{\bar{1}\bar{1}\bar{1}\}$ sectors and the simultaneously decelerated growth velocity of $(00\bar{1})$ sector. This explained the enhancement of $\{001\}$ sectors during stage 2.

During stage 3, the size of $(00\bar{1})$ sector stayed more or less as a constant. The relative growth rate for stage 3 calculated with the corresponding values in Table 6.9 was :

$$\frac{v_{(3)-1}}{v_{(3)-2}} = \frac{\cos 51.5^\circ}{\cos 3.2^\circ} = 0.623$$

where $v_{(3)-1}$ represents the growth rate of $(\bar{1}\bar{1}\bar{1})$ sector and $v_{(3)-2}$ represents that of $(00\bar{1})$ sector. The value is slightly above the low limit of 0.578, indicating a stabilized competition between $(\bar{1}\bar{1}\bar{1})$ sectors and $(00\bar{1})$ sectors. The lower growth velocity of $(\bar{1}\bar{1}\bar{1})$ sectors in stage 3 compared to that during stage 2, is due to the stabilized supersaturation under which condition it has reached the competition balance among dislocation density, impurity concentration and supersaturation. The competition relation presented in stage 3 will result in coexistence of $(00\bar{1})$ and $(\bar{1}\bar{1}\bar{1})$ sectors during further growth.

The above 3-stage competition between the $(00\bar{1})$ sector and the $\{\bar{1}\bar{1}\bar{1}\}$ sectors can also be clearly represented by the topograph of $(\bar{1}10)$ plate of 460ppm doped crystal (Figure 6.16). The seed position is clearly depicted by the thin spongy area at the

regeneration interface and in stage 1 the shrinking of $(00\bar{1})$ sector is distinctly revealed by the pyramid shape towards a narrow neck. Following that, a very short period (stage 2) during which the $(00\bar{1})$ sector expanded a little can be observed. The expansion is not so big compared to that in 190ppm plate (Figure 6.15), which may be attributed to a smaller accumulated supersaturation during stage 1. It can be seen that the growth of $(00\bar{1})$ in stage 3 is quite smooth, and the boundaries between the $(00\bar{1})$ and $\{\bar{1}\bar{1}\bar{1}\}$ sectors are clearly contrasted.

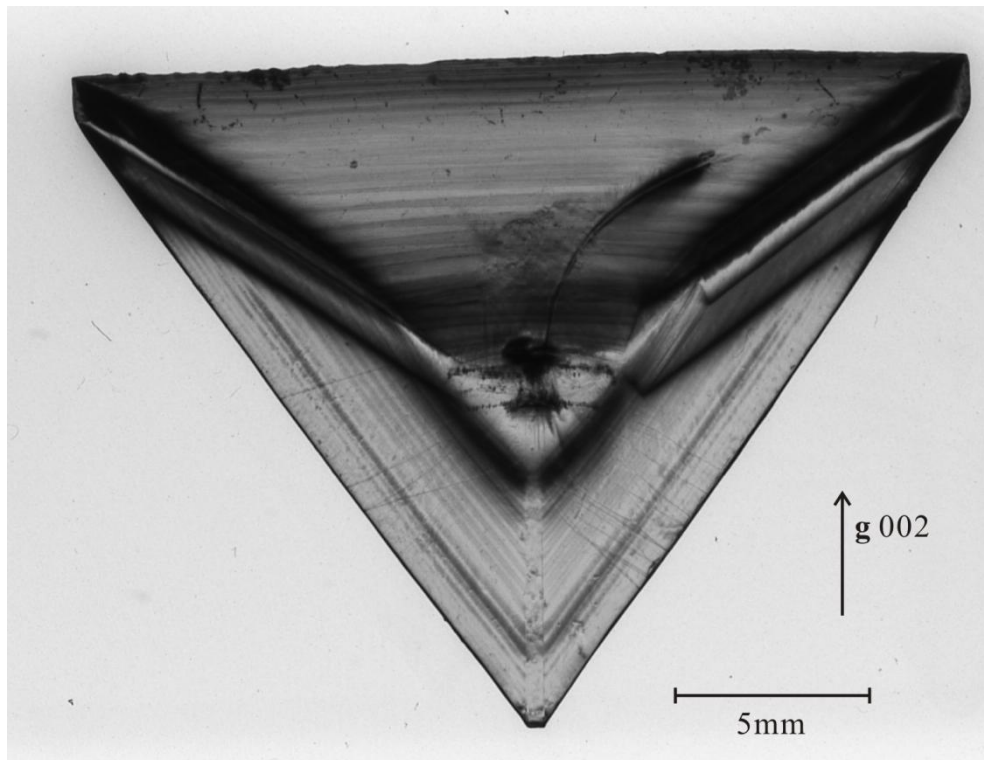


Figure 6.16 (a) Topograph of $(\bar{1}\bar{1}0)$ plate of 460ppm $S_2O_6^{2-}$ -doped $NaClO_3$ crystal. Reflection 002, film D4.

To sum up, the growth of $S_2O_6^{2-}$ -doped $NaClO_3$ crystals was composed of 3 distinct stages as discussed above. Among different stages the competition between the neighbouring growth sectors of $\{\bar{1}\bar{1}\bar{1}\}$ type and $\{001\}$ type varied, due to the immigration of dislocations, the variation of supersaturation, etc.

6.5 Characterization of the Twinned Crystal

6.5.1 Optical Activity of The Twin Domains

Two crystal plates, prepared by cutting the twinned crystal shown in Figure 5.11a, were used for optical activity determination and X-ray topography. The first plate (i.e. plate I) was cut parallel to (110) plane, through the curved lens-shaped [110] edge and the centre of the twinned crystal. This enables to trace the growth history from the nucleation region (i.e. the centre of the twinned crystal) to the crystal final outline shape. The second plate (plate II) was cut from one of the remaining halves, normal to plate I and through its apex edge as well as the centre of the twinned crystal. Each plate contains both of the twinning crystal domains.

Figure 6.17 and 6.18 show the photographs of plates I and II under polarized light, with the analyser rotated by approximately 20° clockwise and anticlockwise respectively from the crossed position. The different optical activities of the twin domains are clear revealed by the different colours they exhibit. In addition, one domain was determined to be levorotary (L-) and the other dextrorotary (D-)⁵. The two domains are therefore referred as D- domain and L- domain respectively in the later discussion.

The twinned crystals exhibited re-entrant edges which are the outcrops of the twin boundaries at the crystal surface (Figure 6.17 and 6.18). The twin boundaries are formed by the path of the re-entrant edge during the growth and thus have the character of a growth-sector boundary. They are roughly aligned along {100} plane which is the twin reflection plane referring to the twin law. The twin boundaries and the twin domains converge into one point (white solid circle in Figure 6.17 and 6.18) which is the origin of twinning. Such a twinning is considered to be initiated at the nucleation stage. In Figure 6.17a, a small part of the D- domain is observed within the large L- domain. This is due to the thickness of the plate containing a small volume portion of the D- domain crystal grown in the direction normal to the plate cut.

⁵ Method used for optical activity determination was described in methodology chapter.

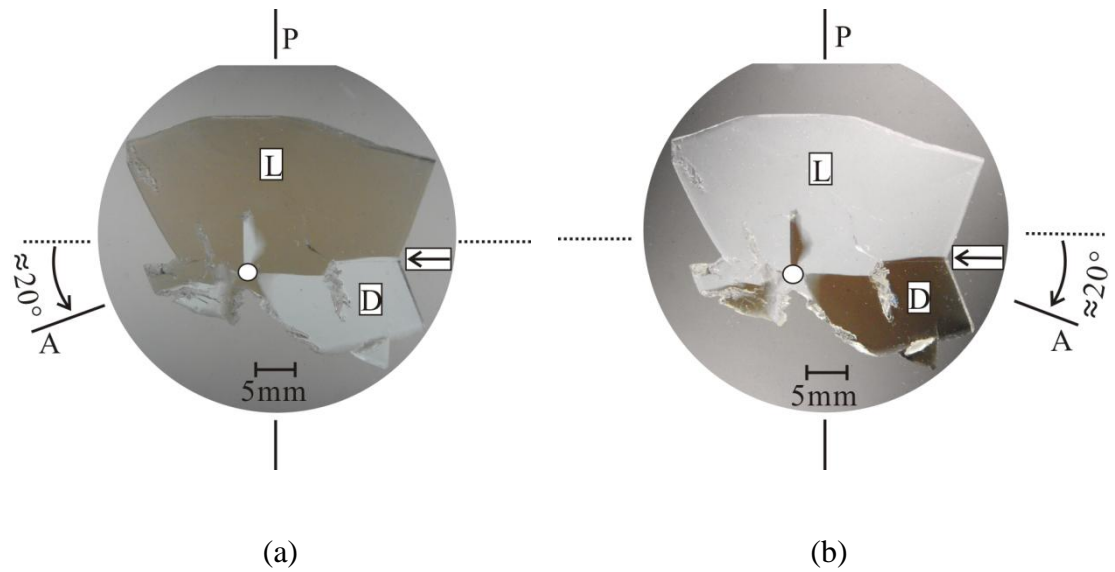


Figure 6.17 Photograph of plate I (i.e. (110) plate) in polarized white light. (a) Analyser A rotated anticlockwise by about 20° from the crossed-polarizer position (dotted line). (b) Analyser A rotated clockwise by roughly the same angle with respect to the crossed-polarizer position (dotted line). White solid circle: self-nucleation site of the twinned crystal; Arrow: re-entrant edge; P: position of polarizer; A: position of analyser; L: L- domain; D: D- domain.

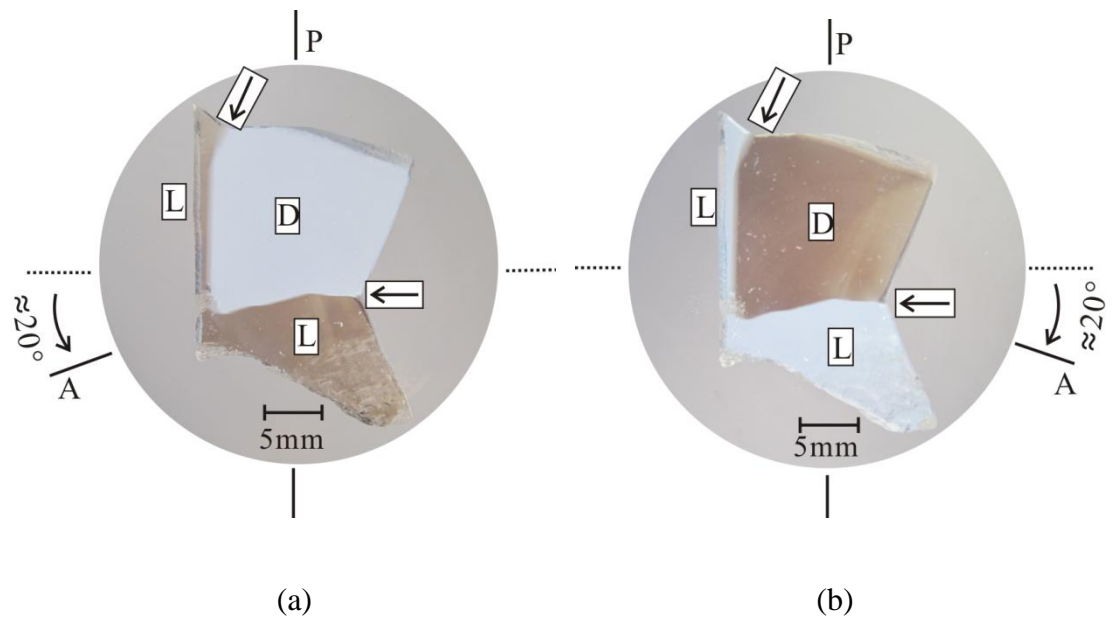


Figure 6.18 Photograph of plate II (i.e. $(1\bar{1}0)$ plate) in polarized white light. All the data and labels are analogous to Figure 6.17.

The allocation of Miller indices for such an enantiomorphous twinning system, based on the crystallographic structure associated with the chiralities of the two domains, is essential. For the crystal structure of the D- domain, Ristic et al. (1993) assigned the $\{\bar{1}\bar{1}\bar{1}\}$ indices to the tetrahedral faces on the habit modified crystal. In this case, the 3-fold axis of one of the four ClO_3^- ions on a growing face is aligned normal to the face with the Cl sitting on the apex of the ClO_3 trigonal pyramid pointing outwards from the face. In the twinning system, the faces of $\{111\}$ type in the L- domain present the opposite orientations of ClO_3^- ions (see Figure 6.19b) to that of $\{\bar{1}\bar{1}\bar{1}\}$ faces of the D- domain (Figure 6.19a), so that one indexed direction refers to two sets of lattice planes with the different structures from the two domains respectively (Figure 6.19c and d). Therefore, the Miller indexing is, in particular for the sodium chlorate twinning crystal system, defined with a subscript of the domain to which the plane belongs. For example, $(111)_L$ refers to the (111) plane or face in the L-domain, whereas $(111)_D$ refers to the (111) plane or face in the D-domain.

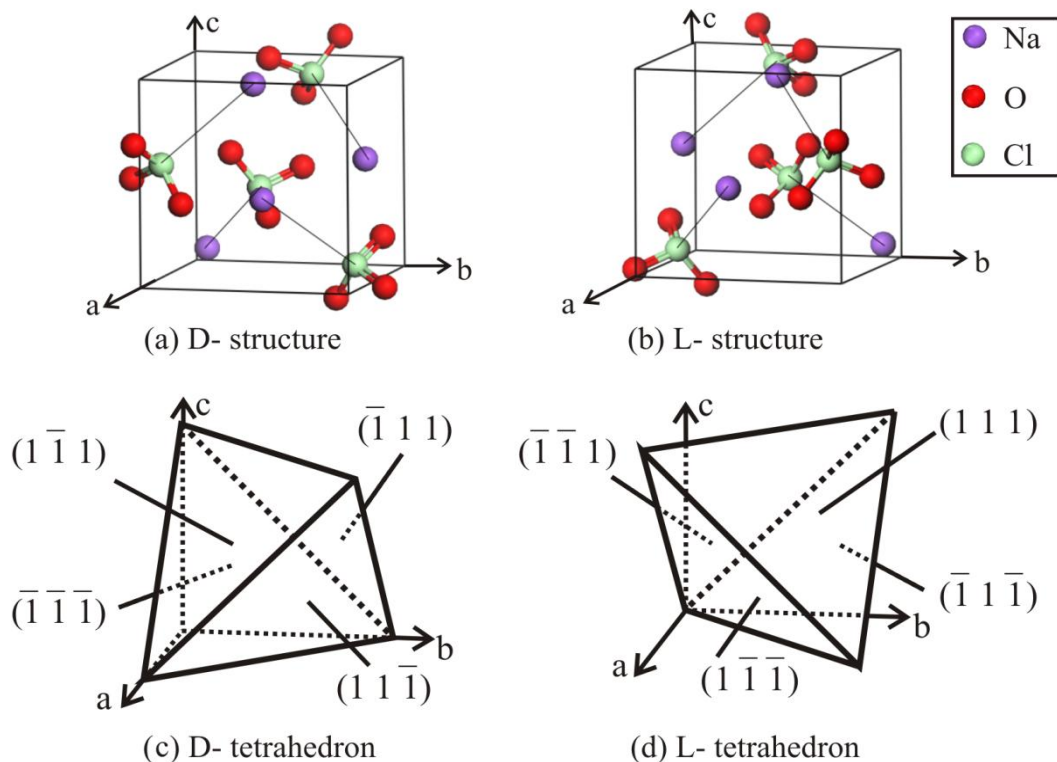


Figure 6.19 (a) The D- structure of NaClO_3 . (b) The L- structure of NaClO_3 . (c) The Miller indices for habit faces of doped NaClO_3 of D- structure. (d) The Miller indices for habit faces of doped NaClO_3 of L- structure.

6.5.2 Topograph of Twinned Crystal

Figure 6.20 and 6.21 show the topographs of plates I and II (cf. Figure 6.17 and 6.18) of 002 reflection, together with sketches of their defects and growth sectors. The presence of twinning is recognized only by the re-entrant edges and the contrast of the associated twin boundaries. Compared to the crystals grown from pure solutions (Figure 6.8), the dithionate-doped crystals are considerably disturbed, which is shown in the topographs that the growth sectors are clearly observed by pronounced striations and growth-sector boundaries. The striations are more or less wavy, indicating the non-planarity of the tetrahedral growth faces in each crystal domain. The sector boundaries are exhibited with the strong contrast between $(001)_L$ and $\{111\}_L$ type sectors and along the track lines where the growth striations change directions, having provided that growth striations are parallel to the growing faces respectively. An interesting feature revealed in Figure 6.20a is that, the small (001) growth sector, corresponding to the lens-shaped (001) facet shown in Figure 5.11a, embedded between two tetrahedral sectors. The associated sector boundaries are inclined with respect to the plate surface and therefore appear to be broad bands of strong contrast, indicating different perfection and slightly different lattice parameters of the $\{111\}_L$ type and the $(001)_L$ sector. The irregular shape of the (001) sector exhibits its 'growth history', starting from the region of nucleation (grey circle) to the end of crystal growth. After the development to a wide (001) sector from the growth origin, its facet had almost vanished by a very fast growth for some period, and then became wide by slowing down its growth rate.

It is interesting that dislocations are not observed in all the growth sectors of the twinned crystal. Only a few dislocation lines are recognized in the $(\bar{1}\bar{1}1)$ sector of D-domain and the $(\bar{1}\bar{1}\bar{1})$ sector of L-domain (e.g. Figure 6.20a), and the (111) sector of D-domain (e.g. Figure 6.21a). These dislocations originate from highly imperfect regions (e.g. row C of inclusions in Figure 6.20a). The curved contrast line in Figure 6.20a, shown as dashed line and labelled S in Figure 6.20b, is a crack in the crystal plate. The hatched regions at the bottom parts of Figure 6.20b and 6.21b are, rather than be shown in the topographs (Figure 6.20a and 6.21a), strongly disturbed with pronounced mosaic character. They partially are out of X-ray diffraction position due to strong misorientation.

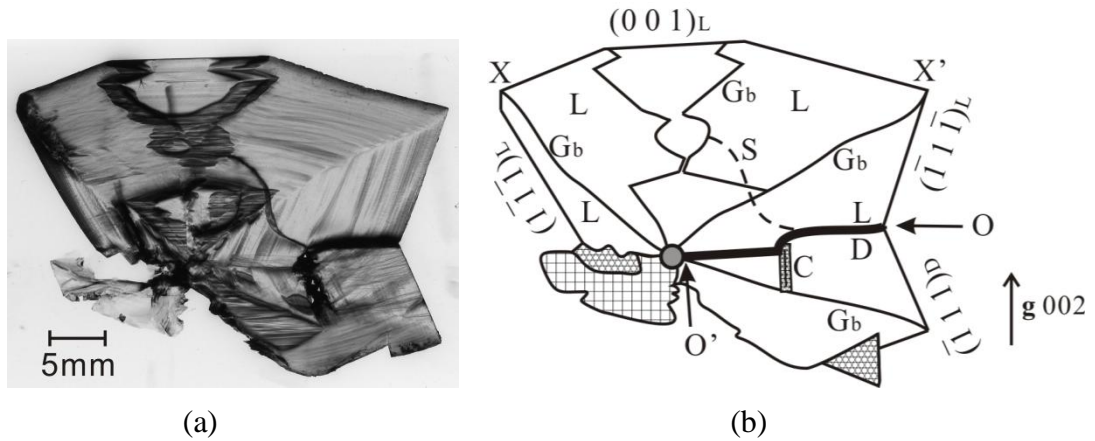


Figure 6.20 (a) X-ray topograph of (110) plate I, reflection 002, Mo-K α radiation. (b) Schematic illustration of growth sectors with their indices and twin domains. The upper margin X-X' of the plate corresponds to the rounded tetrahedral edge with the lens-shaped (001) facet shown in Figure 5.11a. Thick line O-O': growth twin boundary; Gb: growth-sector boundaries between growth sectors; grey solid circle: nucleation region of the twinned crystal; C: row of liquid inclusions, the origin of dislocations; S: crack in the plate, merging into the twin boundary O-O'; dark region at bottom left and bottom right: strongly disturbed part of crystal, partially out of reflection position; **g**: diffraction vector 002.

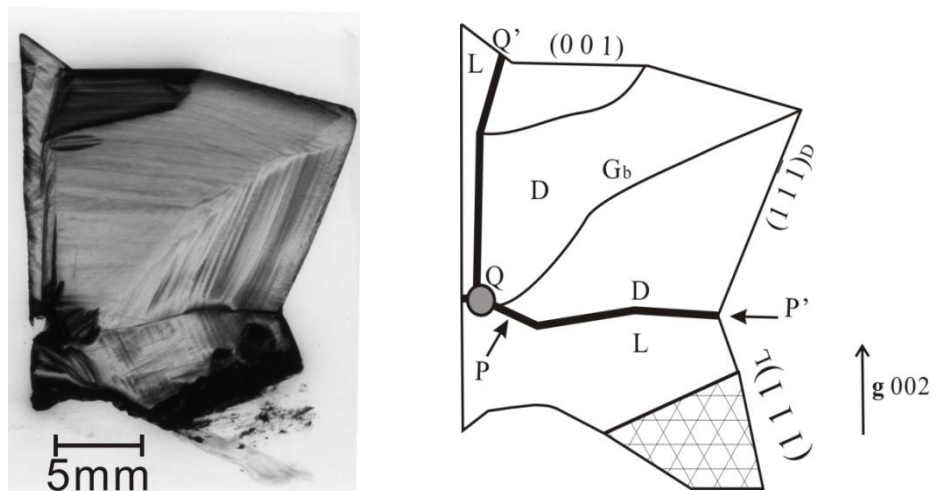


Figure 6.21 (a) X-ray Topograph of (110) plate II, reflection 002, Mo-K α radiation. (b) Schematic illustration of growth sectors with their indices and twin domains. Thick lines P-P' and Q-Q': twin boundaries; grey solid circle: nucleation region of the twinned crystal; Gb: growth -sector boundaries; hatched region at bottom right: strongly disturbed part of crystal; **g**: diffraction vector 002.

6.6 Discussion

The observed grown-in dislocations in various growth sectors were satisfactorily consistent with the calculation at the preferred line directions of dislocations (Hooper et al., 1983). The sources for the dislocation lines in $\{001\}$ and $\{110\}$ type sectors are the dislocations contained in the crystal seed and generated from the inclusions, whereas the dislocation lines in the $\{\bar{1}\bar{1}\bar{1}\}$ sectors of doped crystals were extended from the dislocation lines in $\{001\}$ sectors or $\{110\}$ sectors or generated from the inclusions during crystal growth.

Dislocation lines in the $\{001\}$ sectors of both pure and doped NaClO_3 crystals were found to be types of 1a pure screw and 1b pure edge, propagating normally to the growth faces. This result is consistent with the previously reported results on seeded pure NaClO_3 crystals by Matsunaka et al. (Matsunaka et al., 1980), and also the study of self-nucleated pure NaClO_3 crystals (Hooper et al., 1983).

Dislocation lines in the $\{110\}$ sectors of pure NaClO_3 crystals were assigned to be types of 2a mixed, 2b pure edge and 2c pure screw, while that in doped crystals was assigned to be types of 2b pure edge, 2c pure screw and 2e pure edge. The reason for the absence of 2e in pure crystal and 2a in doped crystal are unclear, but might be attributed to the limited crystal volume of the plate under observation. The $\{110\}$ sectors in both pure and doped crystals, which contained dislocation lines were found to be relatively defective, either possessing a spongy area or containing planar inclusions. Besides, it was observed that the $\{110\}$ sectors can only develop into a face of reasonable size when the sector is defective (Figure 6.8), whereas in some directions of $\langle 110 \rangle$ type there were no inclusions or dislocation lines and no crystal face observed in the final habit.

In the $\{\bar{1}\bar{1}\bar{1}\}$ sectors, some dislocation lines were of regular straight profile and assigned as types of 3a mixed, 3b mixed and 3c pure edge. At the same time, two types of dislocation lines, i.e. 3c* and 3u, were observed in the doped crystal. These dislocation lines were intermediate types with relatively high energy, and transformed to other dislocation lines during crystal growth. The existence of 3c* and 3u dislocation lines in doped crystal might have benefited from the impurity incorporation, which possibly helped them to be temporarily stabilized.

The development of the $(00\bar{1})$ growth sector in pure crystal was quite small compared to other three $\{001\}$ sectors (Figure 6.8a), which was attributed to its high perfection and lack of screw or mixed dislocations as growth centres. This feature manifestly indicates that the growth mechanism of $\{001\}$ faces was by spiral growth at screw dislocation sites.

During the observation described in Section 6.4, the growth of $\{\bar{1}\bar{1}\bar{1}\}$ faces was found to be inhibited and almost stopped until a number of dislocation lines had entered into these sectors. This phenomenon simply indicates that the $\{\bar{1}\bar{1}\bar{1}\}$ faces were growing by the mechanism of spiral growth relying on screw dislocations.

The 3-stage process of habit changing clearly reconstructed the crystal growth history of doped NaClO_3 crystal. It is found that the tetrahedral habit was related to the inhibiting effect of impurity on the growth of $\{\bar{1}\bar{1}\bar{1}\}$ faces. The effect caused by impurity is investigated by molecular modelling in later chapters.

The morphology of the growth twins exhibited two intergrown opposite tetrahedra (Figure 5.11a). Taking into account the symmetry of point group 23 of the single crystal, the following two different twin laws have to be considered:

- (i) Due to the symmetry 23, the operation of a 90 or 270 rotation around one of the three cubic axes $\langle 100 \rangle$ would have the same effect as rotation along a two-fold axis around one of the six diagonal directions $\langle 110 \rangle$. Any of these equivalent operations transforms a tetrahedron into its opposite one, whereby the threefold axes $\langle 111 \rangle$ are inverted, but the chiral handedness is preserved.
- (ii) In point group 23, the operation of a reflection plane of $\{100\}$ type normal to one of the three cubic two-fold axes $\langle 100 \rangle$ would have the same effect as the inversion $\bar{1}$. All these operations transform a tetrahedron into its opposite one, whereby the threefold axes $\langle 111 \rangle$ are inverted *and* the chiral handedness is changed.

The optical characterization of the twin domains shows that the twin operation had reversed the optical rotation sense (cf. section 6.5.1), i.e. it changed the handedness of

the domains. This, together with the observed morphology of opposite polarity between the domains, confirms that the twin law (ii) is applicable for this case, thus the growth twins of NaClO_3 are $m\{100\}$ as well as $\bar{1}$ inversion twins. In literature this kind of twins is called ‘ $\Sigma 1$ twinning’ (indicating the full coincidence of the lattices of the twin partners) (Hahn and Klapper, 2003). In addition, to the author’s best knowledge, this study is the first time to explore the twinned crystals which were induced by deliberately added impurity. It is speculated that, the twinning can also occur in other host/impurity systems when the impurity is properly chosen.

Generally, the pure crystal used for topographic study was a good representative since its habit faces contain both $\{001\}$ and $\{110\}$ type but not only the former type. The crystal grown at 40ppm doping concentration was a good representative for crystals grown under low doping concentration, composing both impurity-modified $\{\bar{1}\bar{1}\bar{1}\}$ faces and original $\{001\}$ and $\{110\}$ faces. The 160ppm crystal can represent the crystals doped by relatively high impurity concentrations (i.e. from 70ppm to 1000ppm) which usually were dominated by impurity-modified $\{\bar{1}\bar{1}\bar{1}\}$ faces whilst sometimes $\{001\}$ faces can appear. The representative twinned crystal used for characterization was of considerable size, and presented well developed faces on both domains.

6.7 Conclusions

In this chapter, the defect configurations of pure and doped NaClO_3 crystals have been characterized. Dislocation lines of three types of profiles have been observed, including straight line, curved line and irregular line composed of bow-shaped segments. The dislocations in the as-grown crystals are from three sources, i.e. extension of the dislocations in the seed, being generated at the inclusions around the interface of the seed, and induced by inclusions in the growth sectors. Detailed characterization was performed for the grown-in dislocation lines of straight profile in the $\{001\}$, $\{110\}$ and $\{\bar{1}\bar{1}\bar{1}\}$ growth sectors for both pure and $\text{S}_2\text{O}_6^{2-}$ -doped NaClO_3 crystals. The results showed satisfactory consistency with the theoretical calculations by Hooper et al. (1983), except that two extra intermediate types of dislocation lines with relatively high energy were observed in the $\{\bar{1}\bar{1}\bar{1}\}$ growth sectors of doped

crystals. The discussions on the growth mechanism of $\{001\}$ and $\{\bar{1}\bar{1}\bar{1}\}$ faces have concluded that they are of spiral growth relying on screw dislocation or screw component of mixed dislocation. This agrees with the studies by Bennema (1967), Matsunaka et al. (1980) and Ristic et al. (1993).

Growth striations were observed only in the $\{\bar{1}\bar{1}\bar{1}\}$ type sectors of doped crystals rather than the sectors of other types or of the pure crystal. This clearly indicated the incorporation of $S_2O_6^{2-}$ impurity only occurs at the surfaces of $\{\bar{1}\bar{1}\bar{1}\}$ type. The growth history of $S_2O_6^{2-}$ -doped $NaClO_3$ crystal has been interpreted by calculating the relative growth rate between the $(00\bar{1})$ sector and $\{\bar{1}\bar{1}\bar{1}\}$ sectors, revealing the habit modification process from cube to tetrahedron. The growth velocities of the $\{\bar{1}\bar{1}\bar{1}\}$ faces were inhibited by the impurity.

For the twinned crystal, the optical activities of the two twin domains were found to be opposite, i.e. one is dextro- (D-) and the other one levo- (L-). Through validation by X-ray topography, these two domains were confirmed to be opposite in morphological polarity. Based on these two facts it was concluded that this twinning case follows the twin law $m\{100\}$ (or equivalently the inversion $\bar{1}$). The twin boundary showed the feature of a growth boundary, whose structure will be discussed later in this thesis with the aid of molecular modelling technique.

CHAPTER 7

Determination of Lattice Distortion Induced by the Impurity Incorporation

Summary:

The characterization of lattice distortions at various lattice planes within both the pure and dithionate-doped sodium chlorate crystals, to determine the effect of impurity incorporation on the crystal lattices.

7.1 Introduction

This chapter explores the lattice distortions caused by the incorporation of dithionate ($S_2O_6^{2-}$) impurity in the crystal lattice of sodium chlorate ($NaClO_3$) by applying X-Ray Multiple-wave Diffraction. 002 Renninger Scans covering a large angular scale were performed on five doped crystals of different doping concentrations as well as a representative pure crystal, in order to explore the effect of impurity incorporation on the crystal lattice planes. Since the $\{\bar{1}\bar{1}\bar{1}\}$ faces were observed to be affected by the $S_2O_6^{2-}$ impurity while the $\{111\}$ faces were not (Chapter 5), the 004 Renninger Scans were taken for certain planes of $\{\bar{1}\bar{1}\bar{1}\}$ and $\{111\}$ types by setting them to the Bragg Surface Diffraction (BSD) condition, to discover the effect of impurity incorporation on the lattice parameters of these planes. The crystal quality was determined in terms of a $\omega:\phi$ mapping and the mosaic spread calculated from that.

7.2 Lattice Planes Disturbed by Impurity Incorporation

In order to explore the impact of the incorporation of $S_2O_6^{2-}$ ions into the $NaClO_3$ crystal structure, a series of Renninger Scans (RSs), as a function of impurity concentration, were performed on different samples using the (004) reflection¹ as the primary reflection under XRMD conditions². A comparison between the RS of pure and doped crystals, around the $\phi = 0^\circ$ symmetry mirror, using the (004) primary reflection, is shown in Figure 7.1. The indexing of the peaks was made using the UMVEG programme (Rossmannith, 2003). When the crystal was rotated around the axis normal to the (001) surface (i.e. the (004) reflection planes), symmetry mirrors are established according to the symmetry of the primary vector. Besides these mirrors, one additional mirror is also established when the secondary reciprocal lattice points.

¹ The diffraction plane is usually referred to as reflection plane in XRMD.

² The principles of XRMD were illustrated in Figure 2.22 in section 2.6.3.3.

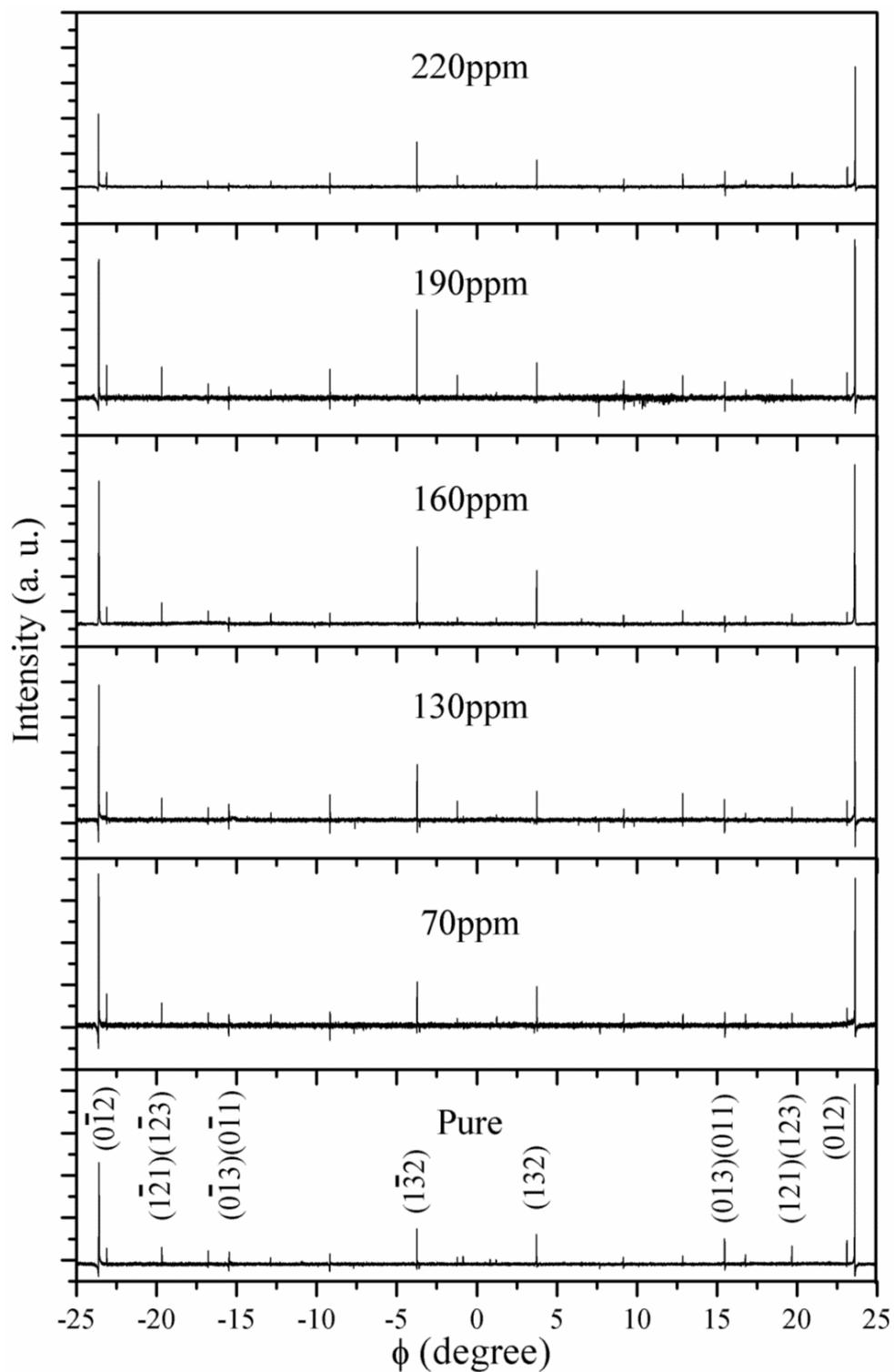


Figure 7.1 Renninger Scans using (004) primary reflection around $\phi=0$ for various samples, i.e. pure NaClO_3 , 70ppm, 160ppm, 190ppm and 220ppm $\text{S}_2\text{O}_6^{2-}$ -doped NaClO_3 . The broad similarity reveals that the symmetry of the four samples did not change much by the presence of $\text{S}_2\text{O}_6^{2-}$ impurity.

enter and leave the Ewald's sphere³. Therefore, for the NaClO₃ RSs, using the (004) primary reflection, there are two distinct mirror types which are repeated each 90° (360°/2(2-fold)/2(additional rotational mirror) = 90°). By examining the peak positions and the amount of peaks among different RSs in Figure 7.1, the overall profiles are satisfactorily consistent, hence implying that the lattice parameters and the crystal symmetry of the pure and doped crystals were not disturbed by the impurity incorporation.

However, a close examination of the peak profiles reveals features at the atomic level related to the incorporation of the impurity. Figure 7.2 shows a much closer view of the RSs around $\phi = 0^\circ$ symmetry mirror. The RS of the pure sample clearly shows four sets of four-beam case secondary peaks, i.e. ($\bar{3}\bar{4}3$)($\bar{3}\bar{4}1$), (343)(341), ($\bar{1}\bar{3}3$)($\bar{1}\bar{3}1$) and (133)(131). Each of the peaks was generated under multiple diffraction conditions involving one incident beam, one primary reflection beam and two secondary reflection beams. However, for the RSs of doped samples, the ($\bar{3}\bar{4}3$)($\bar{3}\bar{4}1$) and (343)(341) peaks almost disappeared, in other words, they became asymmetric peaks with very small intensity. In the meantime, there seems to be no obvious variation of intensity among the peaks of ($\bar{1}\bar{3}3$)($\bar{1}\bar{3}1$) and (133)(131) cases, except some normal fluctuation in intensity due to different sample perfection. This result clearly shows that the S₂O₆²⁻ impurity affected these atomic planes, the reason for which will be discussed in the discussion section of this chapter.

³ Geometry of XRMD was described using Ewald's sphere in Figure 2.20 in section 2.6.3.2.

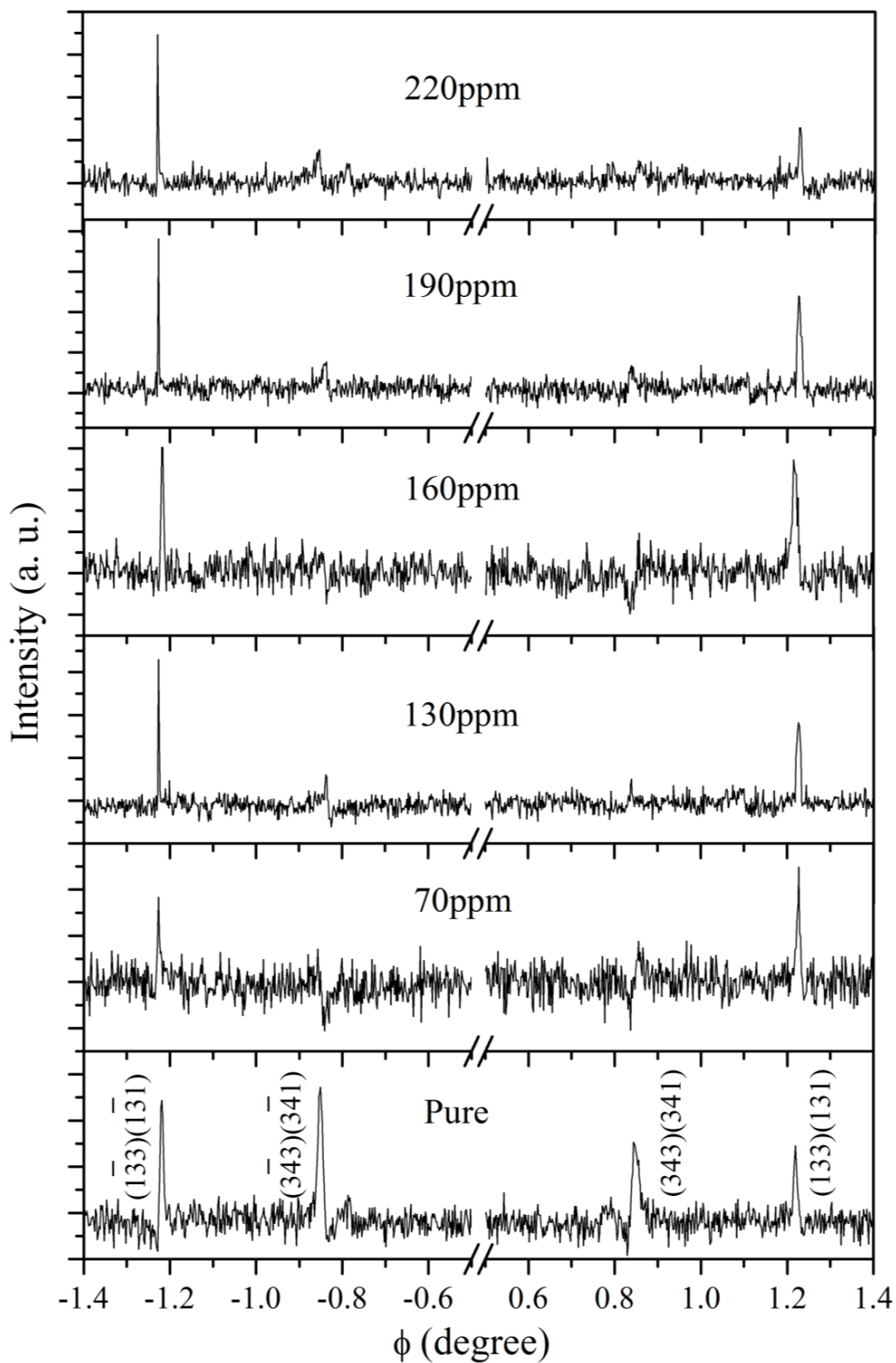


Figure 7.2 Expanded view around 0° of the RSs showing four peaks of different four-beam cases. Two of the four-beam peaks $(\bar{3}\bar{4}3)(\bar{3}\bar{4}1)$ and $(343)(341)$, were seriously suppressed in the doped samples.

7.3 Different Strain at the Impurity Affected / Unaffected Regions

Based on crystal habit observation (cf. section 5.8), the growth of $(1\bar{1}1)$, $(11\bar{1})$, $(\bar{1}11)$ and $(\bar{1}\bar{1}\bar{1})$ faces were affected by doping with $S_2O_6^{2-}$ impurity (Figure 7.3b), but the $(\bar{1}1\bar{1})$, $(\bar{1}\bar{1}1)$, $(1\bar{1}\bar{1})$ or (111) faces were not (Figure 7.3a). By choosing the (002) primary reflection for Renninger Scan, the aim is to explore the structural information from the affected planes $(1\bar{1}1)$ and $(\bar{1}11)$ as well as the non-affected planes (111) and $(\bar{1}\bar{1}\bar{1})$.

Figure 7.4 shows the measured and calculated (by UMWEG program (Rossmannith, 2003)) Renninger Scans of the (111) and $(\bar{1}\bar{1}\bar{1})$ three-beam secondary reflections around the $\phi = 45^\circ$ symmetry mirror, under Bragg-surface diffraction (BSD) conditions. At the same time, Figure 7.5 shows the measured and calculated Renninger Scans of the $(1\bar{1}1)$ and $(\bar{1}11)$ three-beam secondary reflections around the $\phi = 135^\circ$ symmetry mirror. As one can see, these peaks in both Figure 7.4 and 7.5 are negative peaks (aufhellung). This occurs because the intensity of the (002) primary reflection is reasonably strong while that of the secondary reflection is weak, thus, the secondary beam will interact with the primary beam by receiving intensity from it and cause a decrease in the total intensity of diffracted beams.

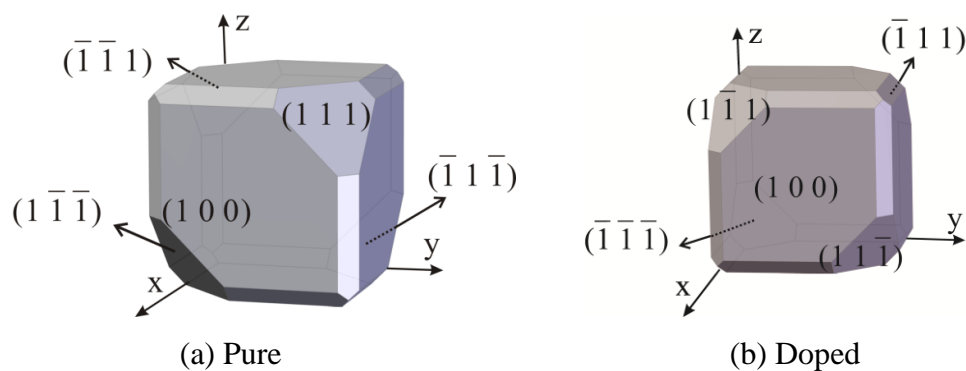


Figure 7.3 Schematic illustration for the tetrahedral faces of pure crystal in (a) and doped crystal in (b).

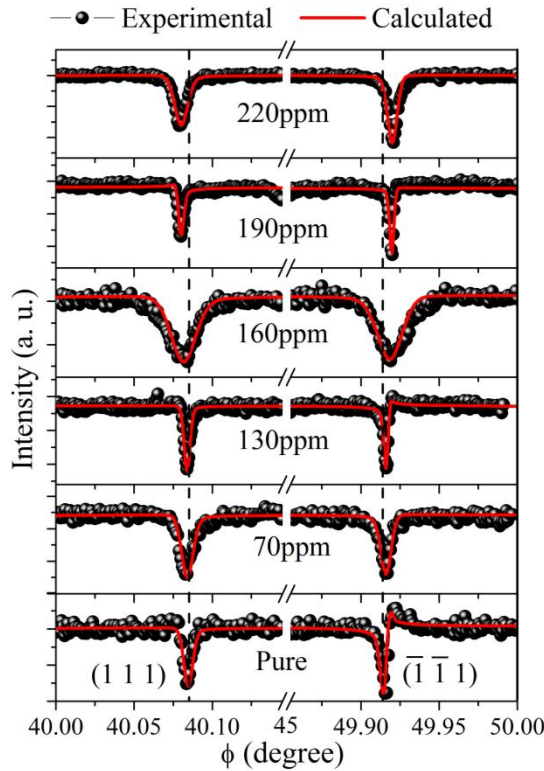


Figure 7.4 Calculation fitting of the BSD peaks (111) and ($\bar{1}\bar{1}\bar{1}$) in the 002 RS for all crystals of various doping concentrations.

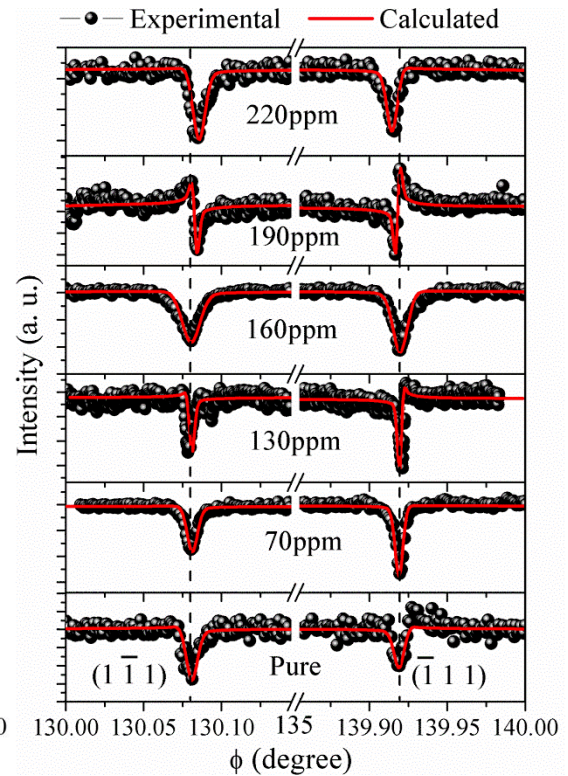


Figure 7.5 Calculation fitting of the BSD peaks ($1\bar{1}\bar{1}$) and ($\bar{1}\bar{1}\bar{1}$) in the 002 RS for all crystals of various doping concentrations.

By careful examination of the secondary peak positions of various RSs in Figure 7.4, it can be noticed that the angular distance between the paired peaks on each side of the mirror is increasing with the increase of impurity concentration. Besides, oppositely, a decrease to the angular distance between the paired peaks with the increase of impurity concentration is observed in Figure 7.5. It is worth emphasizing that, these secondary reflections were BSD cases which are very sensitive to the properties of the sample surface, thus suitable for the detection of surface strains. In an unstrained crystal of the cubic system, the behaviour of these peaks should be the same, which means that the distances from the (111) and ($\bar{1}\bar{1}\bar{1}$) secondary peaks to the $\phi = 45^\circ$ symmetry mirror is equal to the distances from the ($1\bar{1}\bar{1}$) and ($\bar{1}\bar{1}\bar{1}$) secondary peaks to the $\phi = 135^\circ$ symmetry mirror. The experimentally observed distinct behaviour of these peaks

indicates the presence of different strained regions in the sample surface. The secondary beams diffracted by the (111) and ($\bar{1}\bar{1}1$) secondary planes propagate approximately along the [110] and [$\bar{1}\bar{1}0$] in-plane directions, respectively, and these two directions are corresponding to the same region in the sample surface. The secondary beams diffracted by the ($1\bar{1}1$) and ($\bar{1}11$) secondary planes propagates approximately along the [$1\bar{1}0$] and [$\bar{1}10$] in-plane directions, respectively, and these two directions are corresponding to the same region in the sample surface. The beam paths in the crystal for the two sets of peaks are shown in Figure 7.6. It can be seen that the regions in the crystal correspond to the beam paths of the two different pairs of peaks are rotated by 90° around ϕ (normal to the sample surface). Since the position of the secondary peak under XRMD conditions depends on the diffraction plane and lattice parameter, among which the former is fixed and the latter is the only variable term here. Thus, the lattice parameters obtained from the simulation program UMWEG during the fitting of the 002 RSs will be discussed (Figure 7.7).

Figure 7.7 shows the lattice parameters as a function of impurity concentration from the dynamic calculation of 002 RSs and Rietveld analysis of X-ray powder diffraction. The results from the Rietveld analysis have not revealed much difference between the samples, but the XRMD results presented fluctuation at a more precise level. As one can see, the pure sample presents two different strained regions, since, the lattice parameter obtained from the (111) and ($\bar{1}\bar{1}1$) secondary peaks is different from that obtained from the ($1\bar{1}1$) and ($\bar{1}11$) secondary peaks. Furthermore, the lattice parameters obtained from these two strained regions have opposite variation tendencies with the increasing impurity concentration, i.e. for one region the lattice parameter is decreasing with the increasing impurity concentration but for the other region the lattice parameter is increasing. A similar behaviour to these results had been seen in the NaClO_3 crystal doped with about 50ppm $\text{Na}_2\text{S}_2\text{O}_6$, where the interferogram of the curved $\{\bar{1}\bar{1}\bar{1}\}$ faces showed that this surface has a geometrically complicated form having the two main radii (in the a and b crystallographic directions) not equal and changing along the surface (Ristic et al., 1994). In addition, the 160ppm sample lattice

parameters showed a discontinuity (Figure 7.7), this can be attributed to the highly defective sample surface discussed in the next section.

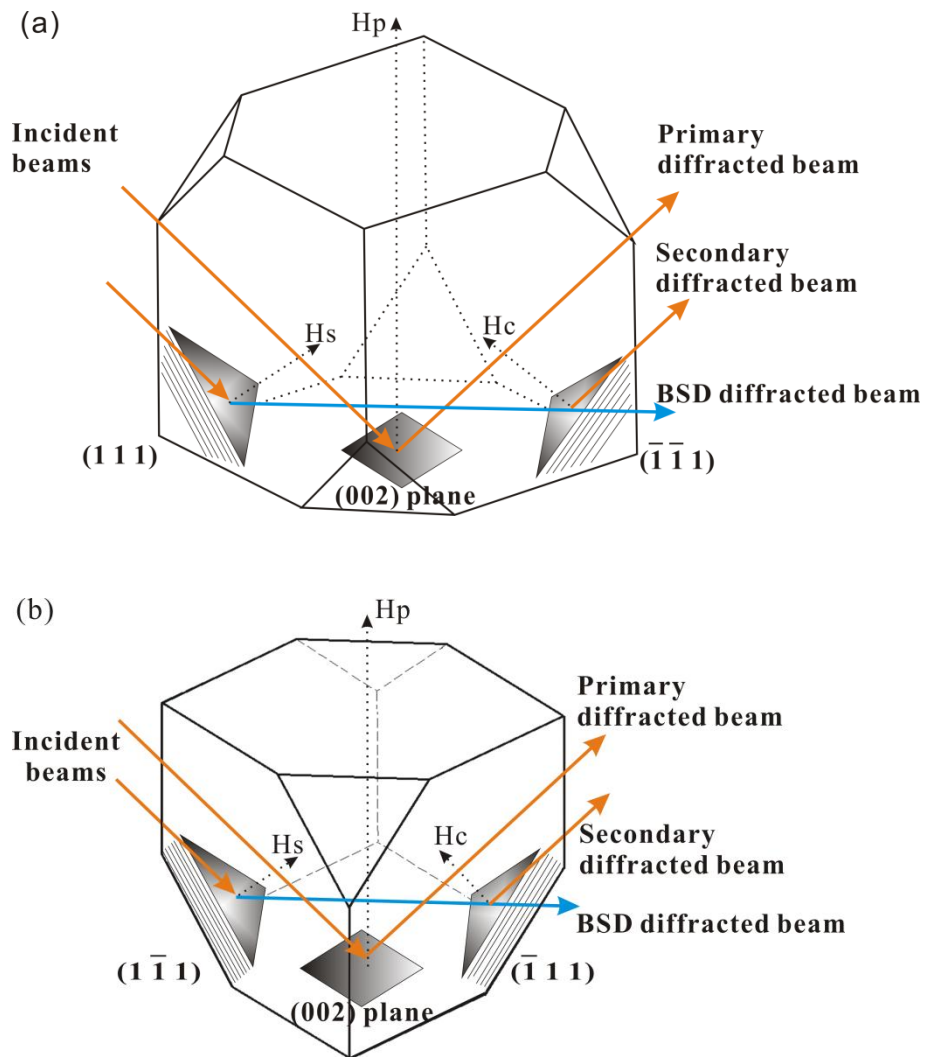


Figure 7.6 Illustration of the beam transmission path for the BSD cases. (a) Beam path of (111) BSD, which is the reversed beam path of ($\bar{1}\bar{1}\bar{1}$). (b) Beam path of ($1\bar{1}\bar{1}$) BSD, which is the reversed beam path of ($\bar{1}\bar{1}\bar{1}$).

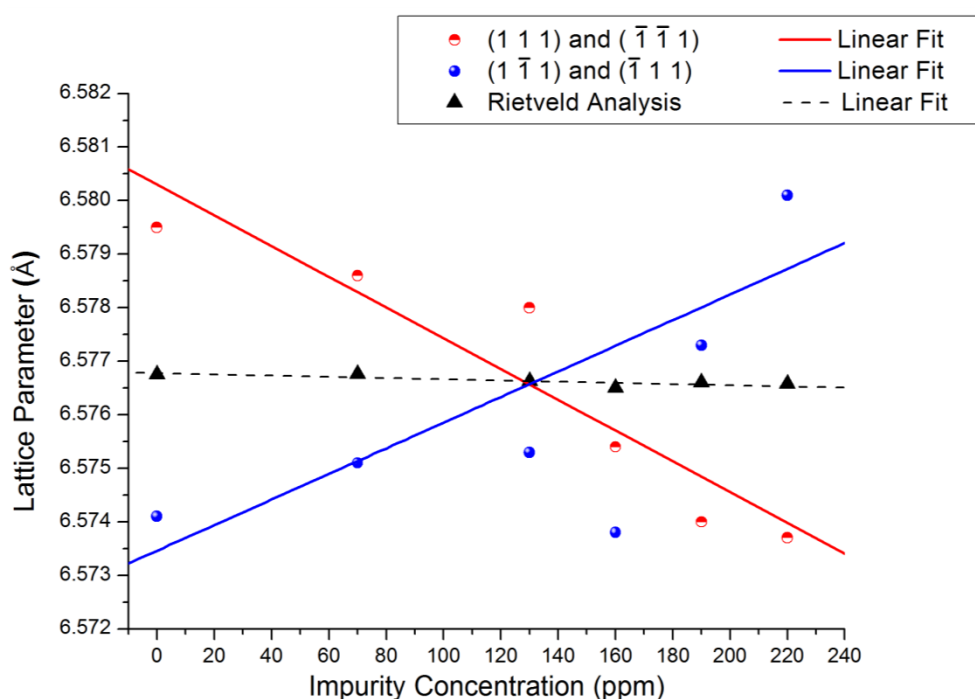


Figure 7.7 Lattice parameters as a function of impurity concentration obtained from the XRMD four-beam cases and the Powder-XRD Rietveld analysis. Results from different XRMD four-beam peaks indicated an opposite variation tendency, while the Rietveld analysis values did not show much difference among the samples.

7.4 Evaluation of Crystal Quality by $\omega:\phi$ Mapping

One can use the $\omega:\phi$ maps under XRMD conditions to study the strain distribution close to the sample surface. However, it is not possible for this case to map the reflection of $\{111\}$ or $\{\bar{1}\bar{1}\bar{1}\}$ type, because they are aufhellung (negative peak) and are of weak intensity. To study the strain distribution on the sample surface, the (012) secondary reflection as a BSD reflection (using the (004) as primary reflection) was chosen for $\omega:\phi$ mapping, due to its strong reflection capability. Figure 7.8 shows the (012) $\omega:\phi$ maps for both pure and doped crystal for various impurity concentrations including 70ppm, 130ppm, 160ppm, 190ppm and 220ppm. The ω and ϕ width of the centre area on the maps gives an indication of the crystal quality. Normally, the

smaller widths in both ϕ and ω directions corresponds to better quality, and the ω width is usually bigger than the ϕ width for crystal of good quality. As one can see, the ω and ϕ widths of the pure and 70ppm samples are relatively small and those of the 220ppm sample are even a little bit smaller than the pure and 70ppm samples, whilst the 130ppm and 190ppm samples presented intermediate widths. However, the 160ppm sample presented a larger width in both the ω and ϕ directions, while the ω width was big.

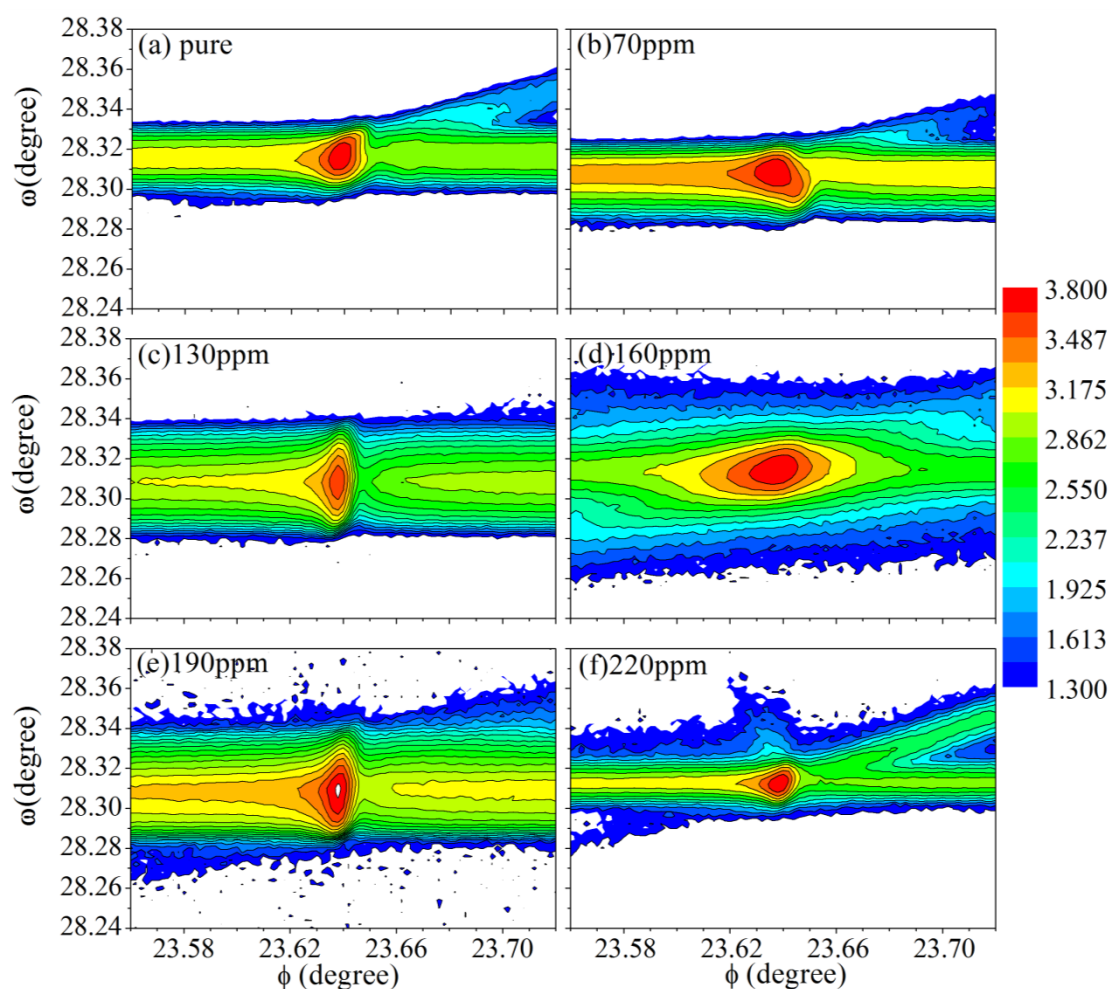


Figure 7.8 High-resolution ω : ϕ mapping of (012) BSD reflection using the 004 reflection as primary diffraction. (a) pure crystal, (b) 70ppm doped crystal, (c) 130ppm doped crystal, (d) 160ppm doped crystal, (e) 190ppm doped crystal and (f) 220ppm doped crystal. The profile of these maps reveals mainly the crystalline quality of the examined crystal surface.

Using the ω and ϕ widths, obtained by applying Gaussian fit to the data of the ω : ϕ maps, one can calculate the mosaic spread in the perpendicular (η_{perp}) and the in-plane ($\eta_{\text{in-plane}}$) directions, respectively, which are associated with the crystalline perfection. Figure 7.9 shows the η_{perp} and $\eta_{\text{in-plane}}$ obtained from the (012) BSD ω : ϕ mappings. On comparing to the pure crystal, the η_{perp} and $\eta_{\text{in-plane}}$ both increased for the 70ppm and 160ppm samples and both decreased for the 220ppm sample. But for the 130ppm and 190ppm samples the η_{perp} had increased while the $\eta_{\text{in-plane}}$ had decreased. It is worth noticing that the $\eta_{\text{in-plane}}$ of 160ppm sample shows a huge increase. Therefore, the overall quality of all the crystals is basically at the same level, except that of 160ppm doped crystal, which showed a huge rise in the $\eta_{\text{in-plane}}$ curve, thus it was concluded to be defective.

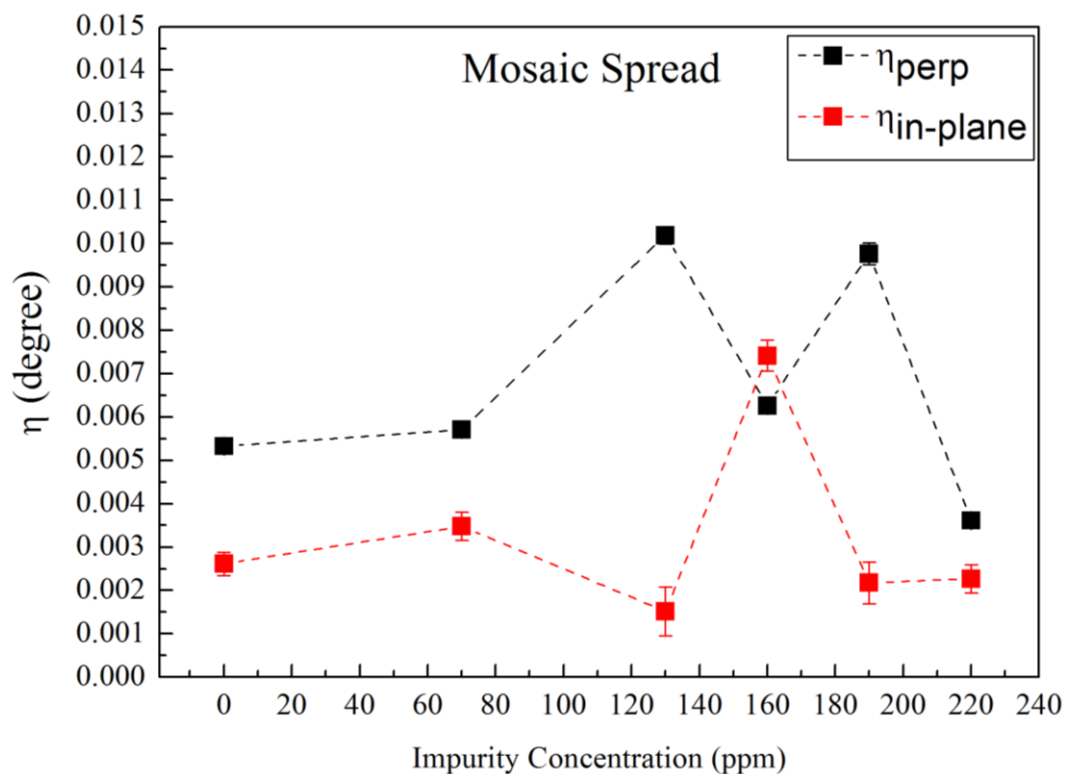


Figure 7.9 Mosaic spread for the perpendicular and in-plane directions as a function of impurity concentration. The dotted line in the figure is not fitted lines, but just used to guide the eye for better visualization.

7.5 Discussion

The peaks of the $(\bar{3}\bar{4}3)(\bar{3}\bar{4}1)$ and $(343)(341)$ secondary reflections from 004 RS of doped crystals were severely suppressed (Figure 7.2), implying that these atomic planes have been disturbed by the incorporation of $\text{S}_2\text{O}_6^{2-}$ impurity. Here it would be useful to interpret this phenomenon based on a structural model for the incorporation of $\text{S}_2\text{O}_6^{2-}$ in NaClO_3 crystals, which is described in a later chapter of this thesis (cf. section 9.2.3, Figure 9.4 and 9.5). It is worth stating that, the establishment of this model was not based on a result of 004 RS. According to the structural model (Figure 9.4), the $\text{S}_2\text{O}_6^{2-}$ can incorporate into the growth front of the $(\bar{1}\bar{1}\bar{1})$ face by substituting one ClO_3 with one SO_3 group while the other SO_3 group protrudes outside the crystal surface. After the impurity incorporation at the growing front, it is found that the O of the protruding SO_3 group will be too close (approximately 0.50\AA) to the O of ClO_3 ions of the next sub-layer (Figure 7.10). As a result, the O of the depositing ClO_3 molecules will suffer a strong repulsive force from the impurity and be dislocated. Thus, the dislocated O is speculated to have affected the phase of the secondary reflections of the $(\bar{3}\bar{4}3)(\bar{3}\bar{4}1)$ and $(343)(341)$ four-beam cases, resulting in a decrease in the intensity of the corresponding peaks. This type of intensity decrease on secondary peaks has already been detected in interstitial Ni-doped L-histidine hydrochloride monohydrate crystals (Miranda et al., 2008). Moreover, a study by Morelhão et al. (2011) on the phase change of the $(11\bar{2})$ and $(15\bar{2})$ secondary reflections of Mn-doped KDP crystals showed that the Mn^{2+} impurity interacts with the nearest PO_4 groups and the structure factor phases of the above reflections were sensitively changing according to the displacement of the PO_4 groups. Therefore, in order to understand the suppressed peaks of $(\bar{3}\bar{4}3)(\bar{3}\bar{4}1)$ and $(343)(341)$ in 004 RS, it is necessary to investigate the structure factors of these secondary planes by considering the displacement of the O atoms.

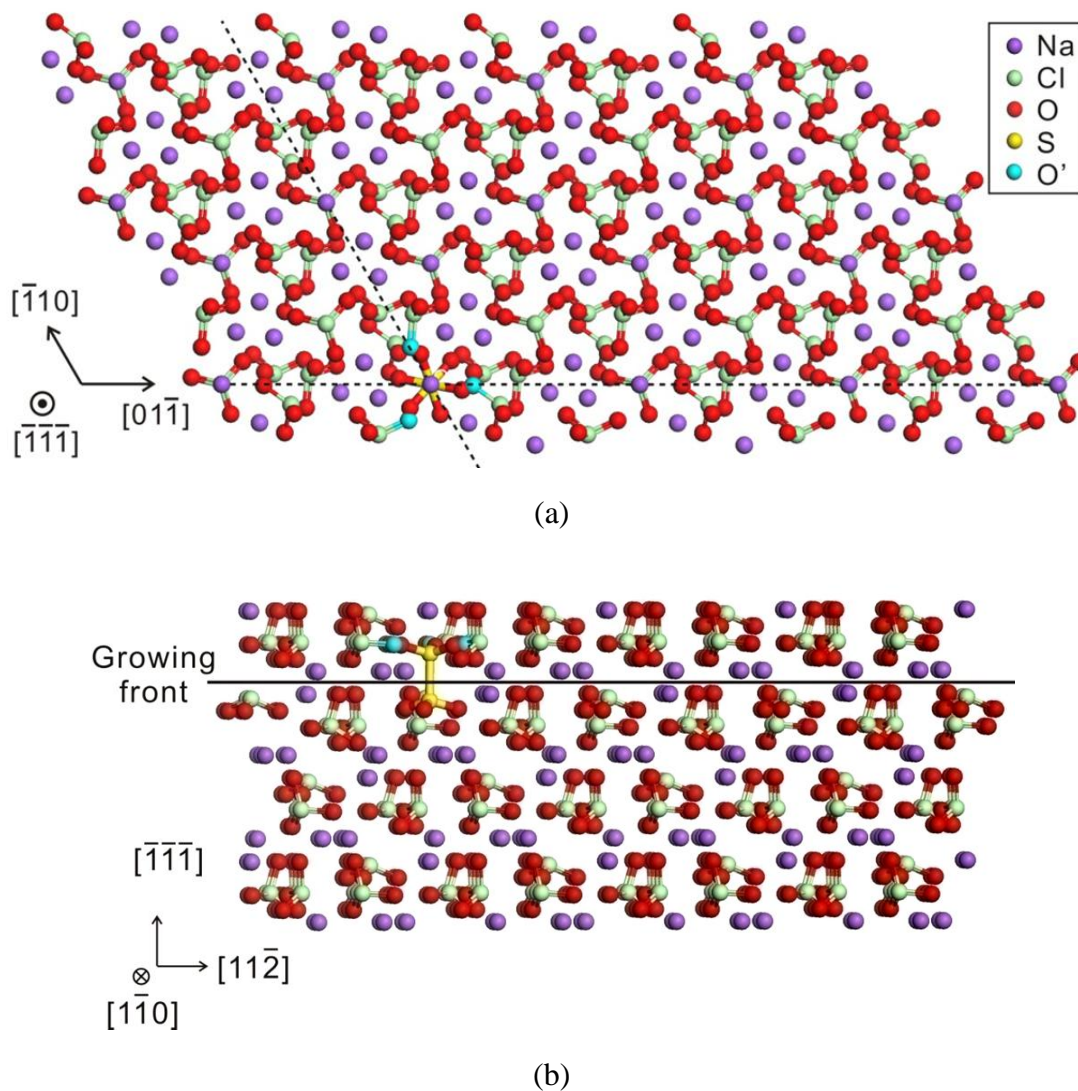


Figure 7.10 Proposed molecular model of $S_2O_6^{2-}$ incorporation on the $(\bar{1}\bar{1}\bar{1})$ face of $NaClO_3$ crystal, with an extra sub-layer above the surface where incorporation occurred. The model is applicable to all equivalent faces of $\{\bar{1}\bar{1}\bar{1}\}$ type. (a) Projection along $[111]$. The impurity locates at the cross point of the two dashed lines. The disturbed oxygen atoms are highlighted in blue. (b) Projection along $[1\bar{1}0]$. The $S_2O_6^{2-}$ has incorporated into the growing front, at which location one of the SO_3 group is protruding outside the crystal surface.

The structure factor for the four lattice planes involved in the cases of (343)(341) and (133)(131) had been calculated as a function of the displacement of the O atoms (Figure 7.11) (Lan et al., 2014). The trend of the four curves reveals that the structure factor of the (343) plane is much more sensitive to the displacement of the O atom than the other three planes, where its structure factor decrease rapidly with the increase of oxygen displacement. As a result, the (343)(341) case (thus the reflection intensity) will be more sensitive to the displacement of the O atom than the (133)(131) case. For example, a displacement of 0.20Å will result in approximately 45% and 20% loss to the structure factor of the (343) and (341) planes, respectively, but only approximately 15% to both the (133) and (131) planes. Thus, the displacement of O atoms induced by impurity incorporation will strongly decrease the reflection intensity of the (343)(341) case but will only affect that of (133)(131) slightly. Furthermore, the situation of the $(\bar{3}\bar{4}\bar{3})(\bar{3}\bar{4}\bar{1})$ and $(\bar{1}\bar{3}\bar{3})(\bar{1}\bar{3}\bar{1})$ peaks is the same with the case discussed above, due to their symmetric relationship. To sum up, the suppression of the (343)(341) and $(\bar{3}\bar{4}\bar{3})(\bar{3}\bar{4}\bar{1})$ secondary diffractions was caused by the displacement of O induced by the $\text{S}_2\text{O}_6^{2-}$ incorporation at the $(\bar{1}\bar{1}\bar{1})$ face of NaClO_3 . In turn, since the model provided suitable evidence to explain the experimentally observed results, the correctness of the model is also confirmed.

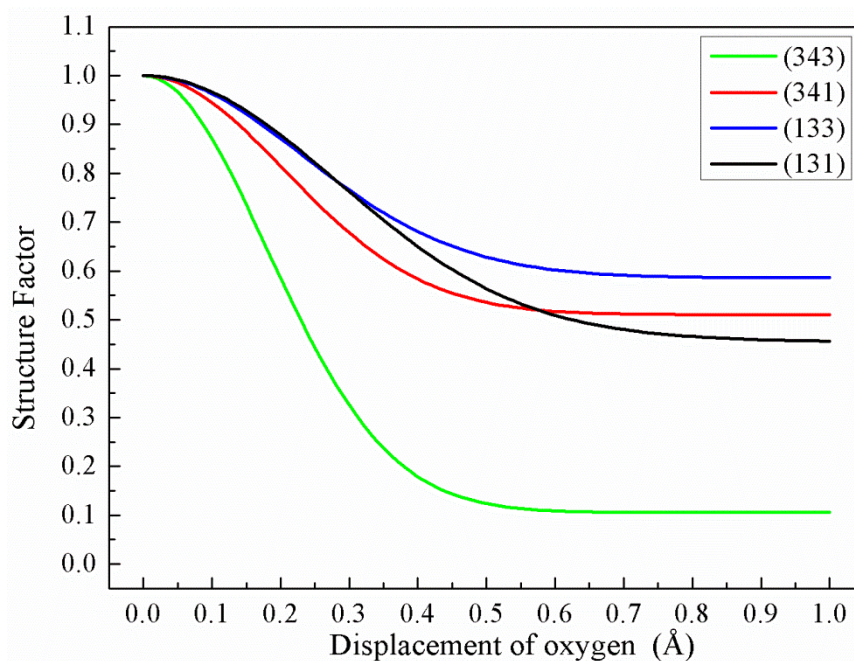


Figure 7.11 The variation of structure factor of particular reflection planes as a function of the displacement of specific oxygen atoms in the NaClO_3 sample. (Lan et al., 2014).

Two different strained regions in both the pure and doped crystals have been revealed by the 002 Renninger Scans. These two regions, which are rotated relatively by 90° along ϕ axis (normal to the (001) surface), are corresponding to the propagating path of the $(1\bar{1}1)$ and $(\bar{1}11)$ secondary diffractions, and (111) and $(\bar{1}\bar{1}1)$ secondary diffractions, respectively (Figure 7.6). According to the observation on habit modification described in Chapter 5, the $(1\bar{1}1)$ and $(\bar{1}11)$ are the planes affected by the doping of $\text{S}_2\text{O}_6^{2-}$ while the (111) and $(\bar{1}\bar{1}1)$ planes are not affected. Since the lattice parameter obtained from the secondary reflections of $(1\bar{1}1)$ and $(\bar{1}11)$ on the doped samples was larger than that obtained from pure sample (Figure 7.7), it is believed that the impurity incorporation at the $(1\bar{1}1)$ and $(\bar{1}11)$ planes has induced tensile strain to the corresponding region and stretched the crystal lattice, resulting in an enlarged lattice parameter. In addition, the tensile strain increases with the increase of doping concentration, indicating that the tensile strain will increase with the increase of doping concentration. At the same time,

due to the stretching effect at the $(1\bar{1}1)$ and $(\bar{1}11)$ planes, the (111) and $(\bar{1}\bar{1}\bar{1})$ planes which were located at 90° (rotation around normal to the sample surface) to the stretched planes have been compressed, to keep the volume of the lattices as constant. Thus, the decreasing lattice parameters obtained from the planes of (111) and $(\bar{1}\bar{1}\bar{1})$ (Figure 7.7) are related to the increasing compressive force.

From Figure 7.9 it can be seen, the overall quality of most of the crystals was not varying much, except the 160ppm sample which presented a huge raise of $\eta_{\text{in-plane}}$ in the curve. The same phenomenon can also be seen in Figure 7.8 which showed the broad width in ϕ . This led to the conclusion that 160ppm crystal contained a large quantity of defects concentrated in the in-plane direction. In turn, it explains the irregular sudden change in lattice parameter of the 160ppm crystal (Figure 7.7), which can be attributed to the defects and associated local strain. However, no correlation was found between the crystal quality and the impurity concentration.

Generally, the doped crystals doped with 70, 130, 160, 190 and 220ppm impurity were good representative for the general cases of this habit modification system. This can be seen from the results of the 002 Renninger Scan (002RS) and the lattice parameter calculated from that. The point of crossing among the different fitted lines was approximately at around 130ppm, which is an intermediate doping concentration among the chosen range. Besides, the result mentioned above also showed good variation tendency with the increase of doping concentration.

7.6 Conclusions

This chapter first discussed the 004 RS results of both pure and doped crystals of various doping concentrations. It was concluded that the incorporation of $\text{S}_2\text{O}_6^{2-}$ has distorted the secondary planes of the $(3\bar{4}3)(3\bar{4}1)$ and $(343)(341)$ cases resulting in a decrease of their reflection intensity. The 002 RS revealed that the variation trends in

lattice parameter as a function of doping concentration were opposite in two different regions of the crystal. The impurity incorporation in the $\{\bar{1}\bar{1}\bar{1}\}$ growth sectors generated tensile strain in the region corresponding to the beam path of the $(1\bar{1}1)$ and $(\bar{1}11)$ secondary reflections, and the lattice parameter obtained from these second reflections was increasing with the increase of impurity concentration. At the same time, it generated compressive strain in the region corresponding to the beam path of the (111) and $(\bar{1}\bar{1}\bar{1})$ secondary diffractions, and lattice parameter obtained from these second reflections was decreasing with the increase of impurity concentration. These strains were later found to have contributed to the inhibiting effect of $S_2O_6^{2-}$ on the growth rate of $(\bar{1}\bar{1}\bar{1})$ faces (cf. section 9.3.2).

At last, the perfection of the crystals was determined qualitatively using the $\omega:\phi$ maps and quantitatively using the calculated mosaic spread from maps. The overall quality of most crystals was not changing much, except that the 160ppm crystal contained large quantity of defects concentrated in the in-plane direction. No correlation was found between the crystal quality and the impurity concentration. In addition, since the results of the 004 RSs were satisfactorily interpreted by the proposed model of impurity incorporation, in turn, the correctness of the model was also confirmed. The lack of information about the local structure of the $S_2O_6^{2-}$ impurity in the bulk crystal will be explored in the next chapter.

CHAPTER 8

Determination of the Local Structure of Dithionate Impurity in NaClO₃ Crystal Using Polarized XAFS

Summary:

This chapter investigates the local structure of the impurity ion within the host crystal to provide structural information for approaching the molecular model for impurity incorporation.

8.1 Introduction

Although the various effects of dithionate ($S_2O_6^{2-}$) impurity on the crystal growth of sodium chlorate ($NaClO_3$) have been discussed in previous chapters, where the $\{\bar{1}\bar{1}\bar{1}\}$ faces were confirmed to be preferred for impurity incorporation, there is still a lack of direct results on the local structure of the $S_2O_6^{2-}$ impurity on these faces. This chapter aims to determine the three-dimensional orientation of the $S_2O_6^{2-}$ ion on the $\{\bar{1}\bar{1}\bar{1}\}$ faces of the $NaClO_3$ crystal and to attempt to explore the molecular structure of the $S_2O_6^{2-}$ in the $NaClO_3$ single crystal. The polarized extended X-ray absorption fine structure (P-EXAFS) was measured for 190ppm doped crystal at two orientations, in order to primarily determine the orientation of the S-S bond of $S_2O_6^{2-}$ (which coincides with the three-fold axis of $S_2O_6^{2-}$) on the $\{\bar{1}\bar{1}\bar{1}\}$ faces of the $NaClO_3$ crystal. In addition, as a secondary objective, by the same measurement it tried to explore the actual structure of $S_2O_6^{2-}$, including S-O bond length and bond angle. The polarized X-ray absorption near edge structure (P-XANES) was measured for the 800ppm sample at 4 orientations, in order to discuss the orientation of $S_2O_6^{2-}$ around its three-fold axis. Also, the isotropic X-ray absorption fine structure (XAFS, including XANES and EXAFS) was measured for a powder crystalline $Na_2S_2O_6$ for comparison purposes. The X-ray fluorescence map of sulphur element was scanned for the 190ppm sample, to investigate the impurity distribution in growth sectors of $\{001\}$ and $\{\bar{1}\bar{1}\bar{1}\}$ types, for the purpose of discussing the coefficient of impurity adsorption in different types of growth sectors.

8.2 Quantitative Determination of the Molecular Orientation and the Structure of S₂O₆²⁻ by EXAFS

8.2.1 EXAFS Data and the Fitting Model

Prior to the measurement of the polarized EXAFS, the isotropic EXAFS was measured using the powder crystalline Na₂S₂O₆ (Figure 8.1), which is considered as the standard compound for discussion on EXAFS. Polarized EXAFS spectra were measured on the sample plate cut parallel to the ($\bar{1}10$) plane from the 190ppm doped crystal at two orientations (c.f. definition in Figure 4.13), with beam polarization either parallel or perpendicular, to the S-S bond axis. At orientation I (c.f. Figure 4.13), the S-S bond of S₂O₆²⁻ was speculated to be parallel to the electric vector of X-ray beam (i.e. $\vec{e} // \text{S-S}$), according to the proposed model (Figure 8.2) by Ristic (1993; 1994). At orientation II the S-S bond was speculated to be perpendicular to the electric vector (i.e. $\vec{e} \perp \text{S-S}$) (for technical details see section 4.10.2). By fitting and analyzing the spectra at the two orientations, the orientation of the S-S bond of S₂O₆²⁻ on the $\{\bar{1}\bar{1}\bar{1}\}$ type face can be obtained.

It is worth noting that, although the XAFS measurements aim to determine the S₂O₆²⁻ on the surface of $\{\bar{1}\bar{1}\bar{1}\}$ type, the X-ray beam actually was illuminating both on the surface and in the growth sectors (see technical details in section 4.10.2). But, this does not affect the result, since the orientation and structure of S₂O₆²⁻ in the $\{\bar{1}\bar{1}\bar{1}\}$ growth sectors is identical to that on the $\{\bar{1}\bar{1}\bar{1}\}$ surfaces.

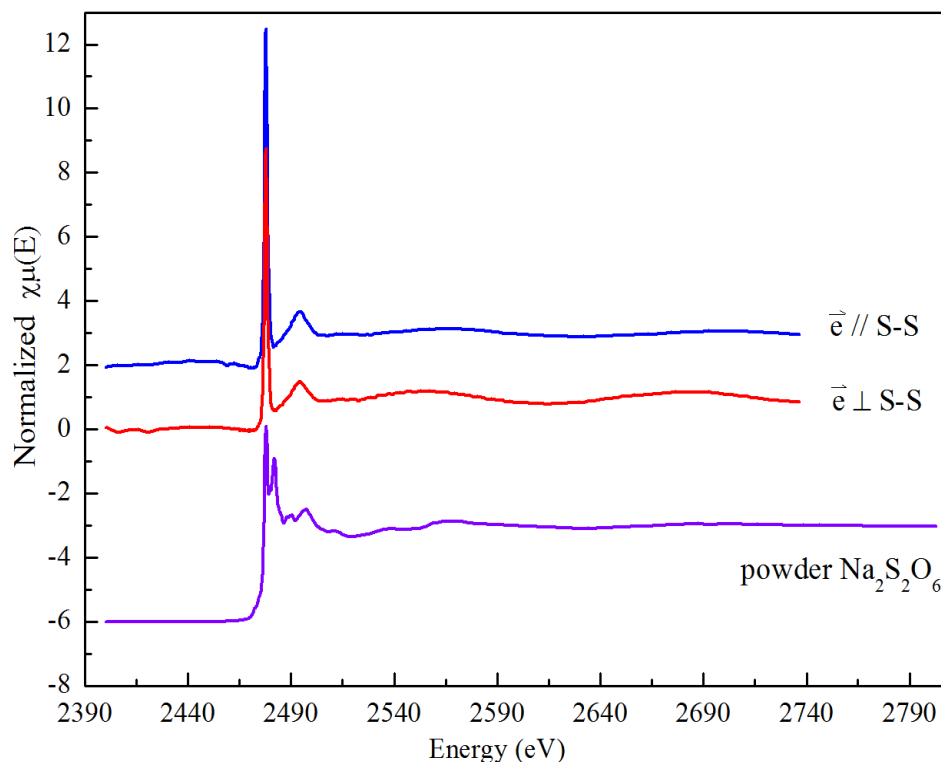


Figure 8.1 The isotropic EXAFS spectra of Na₂S₂O₆ powder and the polarized EXAFS spectra of 190ppm doped crystal collected at the two orientations. The spectra also covered the XANES part. The spectrum at $\vec{e} // \text{S-S}$ was plotted with a vertical translation of +2 in $\chi\mu(E)$. The spectrum of powder Na₂S₂O₆ was multiplied by 3 to enhance the peak height for better observation, and vertically translated by -6 in $\chi\mu(E)$.

Figure 8.1 shows the isotropic EXAFS spectra measured on the Na₂S₂O₆ crystalline powder and the polarized EXAFS spectra measured on the 190ppm doped single crystal. The isotropic EXAFS was fitted using the calculated EXAFS based on the crystal structure of Na₂S₂O₆ (ICSD-26326, Kirfel et al., 1980). The polarized EXAFS spectra of 190ppm doped sample measured at the two geometries (Figure 8.1) present different oscillations in $\chi\mu(E)$, but further analysis requires a quantitatively calculated fit. The isotropic EXAFS and the polarized EXAFS were fitted using the calculated EXAFS based on the molecular structure of the crystal structure of Na₂S₂O₆ (ICSD-26326, Kirfel et al., 1980) and the $(\bar{1}\bar{1}\bar{1})$ surface of S₂O₆²⁻-doped NaClO₃ crystal (Figure 8.2), respectively. The surface structure was created by considering the

proposed model by Ristic (1993; 1994), where the $\text{S}_2\text{O}_6^{2-}$ ($\text{O}_3\text{S-SO}_3^{2-}$) ion was incorporated into the surface by substituting one ClO_3 site with one of its SO_3 groups. This molecular scale model adopted crystal structures of NaClO_3 from Abrahams and Bernstein (1977) and $\text{Na}_2\text{S}_2\text{O}_6$ from Kirfel et al. (1980). One of the two sulphur atoms was selected as the core atom (i.e. absorber) for computing the EXAFS, since the spectra were measured at the sulphur K-edge. The $\text{S}_2\text{O}_6^{2-}$ is composed of two SO_3 groups, both of which are of the same shape of a trigonal pyramid (Figure 8.3). The two SO_3 groups of a $\text{S}_2\text{O}_6^{2-}$ ion were considered as identical for the fitting process for EXAFS.

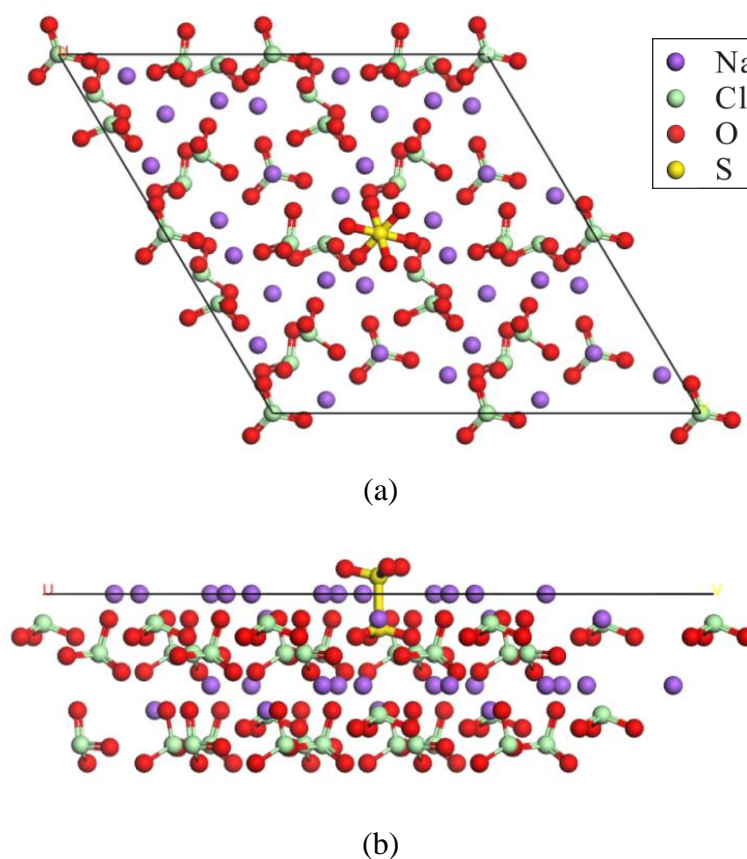


Figure 8.2 Molecular structure of the model used in fitting EXAFS. (a) Projection view of the $\text{S}_2\text{O}_6^{2-}$ -doped NaClO_3 structure at the $(\bar{1}\bar{1}\bar{1})$ surface (Ristic, 1993). The incorporation mechanism of $\text{S}_2\text{O}_6^{2-}$ was presumed to be a half part of the $\text{S}_2\text{O}_6^{2-}$ ion (i.e. SO_3 group) substituting the ClO_3 whose Cl was sitting on the O_3 base and facing outside the surface in the normal direction. The substituting SO_3 group retains the orientation of the ClO_3 , which will result in the S-S bond being aligned along $[\bar{1}\bar{1}\bar{1}]$. (b) Side view of the structure in (a).

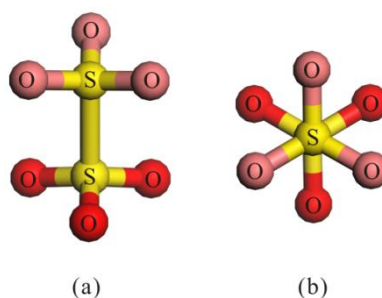
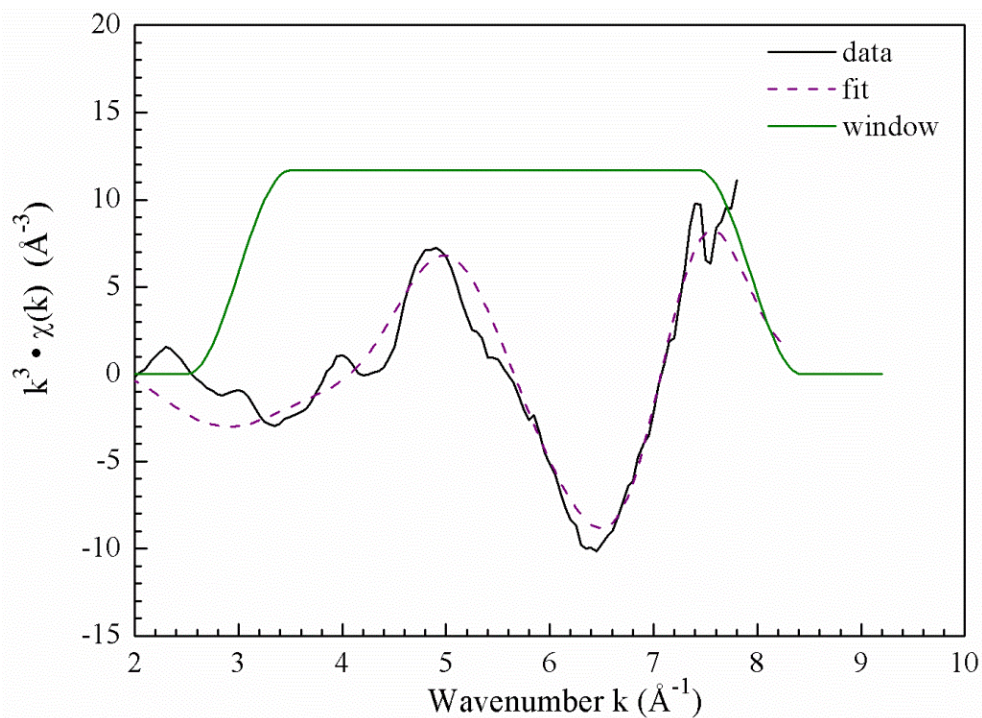


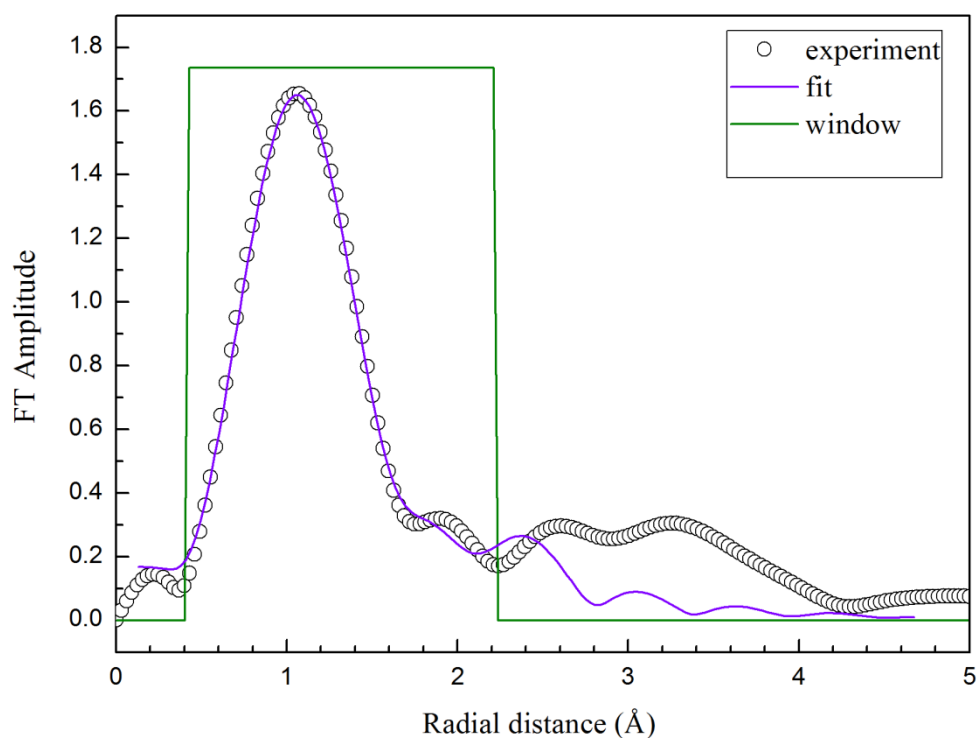
Figure 8.3 Illustration of the structure of the S₂O₆²⁻ ion. (a) Side view of the ion. (b) Projection view of the ion along the S-S bond. Note: The oxygen atoms were coloured with different types to distinguish their connected sulphur for stereo vision.

8.2.2 Fit the isotropic EXAFS of powder crystalline Na₂S₂O₆

The isotropic EXAFS was fitted by calculation based on the crystal structure of Na₂S₂O₆ (ICSD-26326, Kirfel et al., 1980). Figure 8.4 shows the best-fit for the isotropic EXAFS in the k-space and the Fourier transformed R-space, and the EXAFS paths and parameters used are tabulated in Table 8.1. There were 4 independent parameters applied, including the deviation of edge energy, the amplitude reduction for all paths and the variation of absorber-scatterer distance (1st shell and 2nd shell). The fit by the coordination of the first shell oxygen and the second shell sulphur are good in both k-space and R-space. The real coordination number (N_{real}) for the first two shells are 2.92 and 0.94 (Table 8.1), respectively, which are closely consistent to the expected values of 3 and 1. The distances between the scatters on these two shells and the absorber are found to be shorter than that in the published crystal structure of Na₂S₂O₆, where the differences are -0.02826 Å and -0.04200 Å for the first shell and the second shell, respectively. This can be attributed to the acceptable error of measurement for the EXAFS technique, and also the effect of the limited k-range available which was affected by the chlorine k-edge after the sulphur k-edge.



(a)



(b)

Figure 8.4 The $k^3\chi$ curve, Fourier transformed $k^3\chi$ curve and the best-fit for powder Na₂S₂O₆. (a) The $k^3\chi$ curve measured on powder Na₂S₂O₆ sample and the best-fits by calculation based on its crystal structure. (b) Fourier transform of the $k^3\chi$ curve and the best-fit by calculation using Na₂S₂O₆ crystal structure.

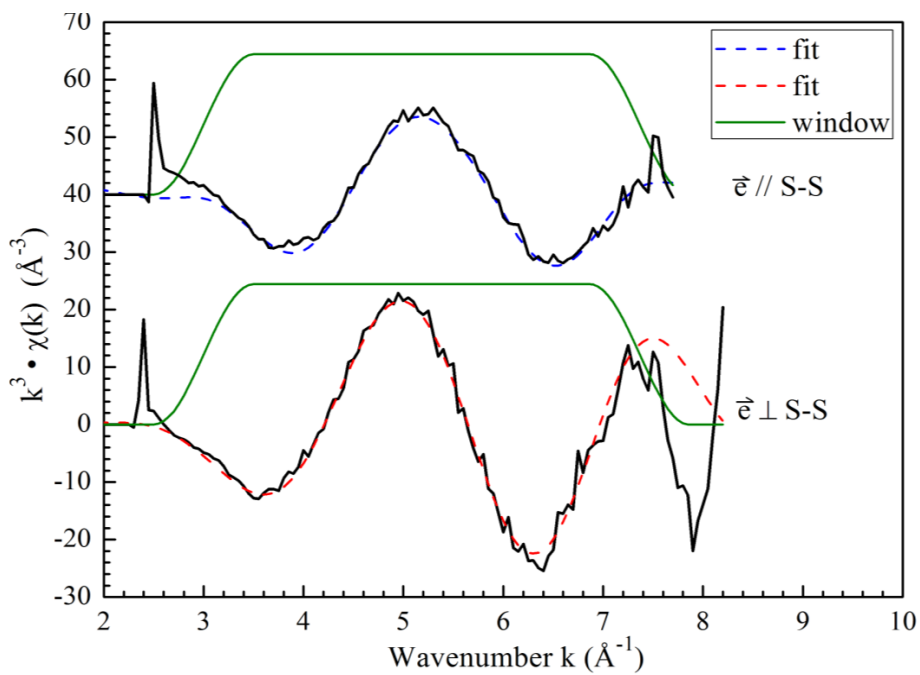
Shell no.	Shell atom	Scattering path	N _{real}	R _{theo.}	ΔR (Å)	R _{exp.} (Å)	σ ² (Å ²)
1st	O1	@→O1→@	2.92	1.4512	-0.02826(±0.002)	1.4229	0.001
2nd	S2	@→S2→@	0.94	2.1399	-0.04200(±0.004)	2.0979	0.001

Table 8.1 Results of the fit to the isotropic EXAFS measure on powder Na₂S₂O₆ sample “@” represents the absorber where the EXAFS begins. The oxygen atoms were labelled by their shell sequence as O1. The sulphur on the second shell was labelled as S2 to distinguish it from the core atom. N_{real} refers to the coordination numbers of the atoms on a shell. R_{theo.} and R_{exp.} are the theoretical path length and the corresponding experimental value from best-fit, respectively. The path length is equal to the aimed bond length. ΔR is the difference between the above two values. σ² represents the “mean square displacement” between the absorber and backscatter due to thermal vibration. Note: The correlation⁴ between ΔR and energy (E, ev) was 0.9266. All other unreported correlations were below 0.4.

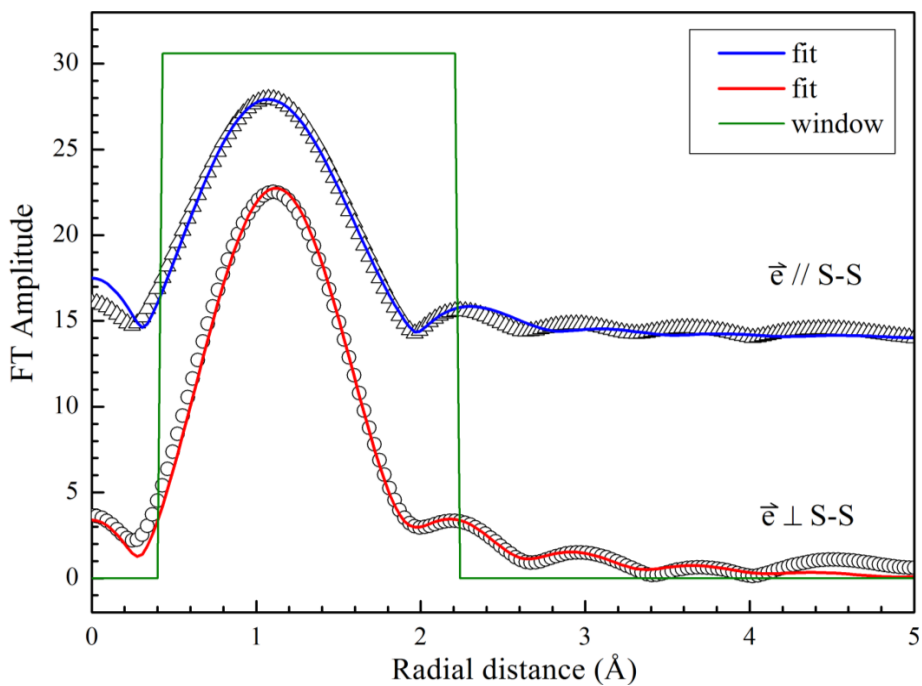
⁴ Here it used correlation to indicate the goodness of the fit, rather than co-variance.

8.2.3 Fit the 190ppm Polarized EXAFS

During the fitting process for the 190ppm polarized EXAFS data measured at the two orientations, the two SO₃ groups of the S₂O₆²⁻ ion were considered to be identical (cf. Figure 8.3), i.e. they possess identical S-O bond lengths and O-S-S bond angles. The least-squares method was applied to fit the 190ppm EXAFS spectrum simultaneously in the k-space and the Fourier transformed R-space. The best-fits for the two spectra are shown in Figure 8.5 and the EXAFS paths and parameters used are tabulated in Table 8.2. Due to the noise in the data and the limited energy range of the collected EXAFS up to about 260 eV above the sulphur K-edge, the signal from the oxygen scatters on the 3rd shell was not reliably fitted and will not be presented here.



(a)



(b)

Figure 8.5 The $k^3 \chi$ curve, Fourier transformed $k^3 \chi$ curve and the best-fit for 190ppm doped Na₂S₂O₆. (a) The $k^3 \chi$ curves of 190ppm sample at the two orientations and the best-fits in k -space. (b) Fourier transforms of the $k^3 \chi$ curves and the best-fits in R -space. Notes: The green window limits the fitting range. The FT does not include phase-shift corrections, thus the plotted peak positions here will be different from the actually measured bond lengths.

Orientation	Shell no.	Shell atom	Scattering path	N _{effective}	R _{theo.}	ΔR (Å)	R _{exp.} (Å)	σ ² (Å ²)
$\vec{e} // \text{S-S}$	1st	O1	@→O1→@	3.7	1.4512	-0.0209(±0.003)	1.4303	0.0003
	2nd	S2	@→S2→@	2.9	2.1399	0.0920(±0.005)	2.2296	0.0025
$\vec{e} \perp \text{S-S}$	1st	O1	@→O1→@	4.0	1.4512	-0.0232(±0.003)	1.4280	0.004
	2nd	S2	@→S2→@	0.1	2.1399	-0.014	2.1259	0.0005

Table 8.2 Results of the best-fit to 190ppm doped crystal EXAFS at orientation I (i.e. $\vec{e} // \text{S-S}$) and at orientation II (i.e. $\vec{e} \perp \text{S-S}$). “@” represents the absorber where the EXAFS begins. The oxygen atoms were labelled by their shell sequence as O1. The sulphur on the second shell was labelled as S2 to distinguish it from the core atom. N_{effective} refers to the total effective coordination numbers of all the atoms on a shell under the enhancement of polarized beam. R_{theo.} and R_{exp.} are the theoretical path length and the corresponding experimental value from best-fit, respectively. The path length is equal to the aimed bond length. ΔR is the difference between the above two values. σ² represents the “mean square displacement” between the absorber and backscatter due to thermal vibration. Note: The number of independent parameters applied for both the above fittings was 4. The correlation between ΔR and energy (E, ev) was 0.8308 and 0.8658 for orientation I and orientation II, respectively. All other unreported correlations were below 0.4.

From Table 8.2, it can be clearly observed that the most striking difference between the results of the two polarized EXAFS appears on the effective coordination number ($N_{\text{effective}}$) of the sulphur (S) scatterer on the 2nd shell. At orientation I ($\vec{e} // \text{S-S}$), the $N_{\text{effective}}$ of the 2nd shell S is 2.9, which implies a significant contribution to the EXAFS from the S on the 2nd shell. Contrarily, the best-fit for EXAFS at orientation II ($\vec{e} \perp \text{S-S}$) showed tiny value of 0.1 for the $N_{\text{effective}}$ of the 2nd shell S, i.e. the S on 2nd shell was practically not probed by the EXAFS and did not contribute to the spectrum.

8.2.4 Discussion on the Orientation of S₂O₆²⁻

The 190ppm sample was of moderate doping concentration among the as-grown doped crystals and good crystal perfection (section 7.4), thus can be considered as representative of the general case of NaClO₃ grown in the presence of S₂O₆²⁻. Its EXAFS result is used to discuss the orientation of S₂O₆²⁻ in NaClO₃ crystals below.

According to the structural model (Figure 8.2) used for fitting the polarized EXAFS, at orientation I ($\vec{e} // \text{S-S}$) the S-S scattering path possesses $\theta = 0^\circ$ (θ is the angle between the absorber-scatterer vector and the electric vector of the X-ray beam), while it is $\theta = 90^\circ$ at orientation II. By utilizing Equation 2.40, the calculated $N_{\text{effective}}$ of the 2nd shell S is 3 at orientation I ($\vec{e} // \text{S-S}$) (Equation 8.1) and is 0 at orientation II ($\vec{e} \perp \text{S-S}$) (Equation 8.2). The calculations mentioned are :

$$\text{When } \vec{e} // \text{S-S} \quad N_{\text{effective}} = \frac{\chi(\text{pol})}{\chi(\text{iso})} = 3 \cos^2 \theta = 3 \times \cos^2(0^\circ) = 3 \quad (8.1)$$

$$\text{When } \vec{e} \perp \text{S-S} \quad N_{\text{effective}} = \frac{\chi(\text{pol})}{\chi(\text{iso})} = 3 \cos^2 \theta = 3 \times \cos^2(90^\circ) = 0 \quad (8.2)$$

where χ_{pol} is the polarized EXAFS, χ_{iso} is the isotropic EXAFS contribution of the S scatterers on the 1st shell.

One of the problems in analyzing the data lies in the limited k-range of c.a. 8 Å⁻¹ available during the experiment. This reflects the fact that the Cl and S k-edge are

only separated by 150 eV. Nonetheless, the polarized data provides direct evidence for the orientation of the S₂O₆²⁻ impurity within the NaClO₃ crystal lattice. The data shown in Figure 8.5 and Table 8.2 reveals that when the \vec{e} is parallel to $[\bar{1}\bar{1}\bar{1}]$ then the effective co-ordination number of 2nd shell S is 2.9, consistent with the theoretical effective coordination number of 3 (Equation 8.1) when allowing for the polarization enhancement of 0.97. This is consistent with the S-S bond orientation parallel to $[\bar{1}\bar{1}\bar{1}]$ direction. In contrast, when \vec{e} is perpendicular to $[\bar{1}\bar{1}\bar{1}]$ then the effective coordination number from experimental fit is 0.1, which is consistent with the theoretical value of 0 (Equation 8.2) at this orientation within acceptable error range. Furthermore to confirm this analysis, the sulphur enhanced ($\vec{e} // \text{S-S}$) data (Figure 8.6 (a)) was Fourier filtered to remove the S-S coordination (b) which showed good agreement with the data of $\vec{e} \perp \text{S-S}$ in (c) and the data of Na₂S₂O₆ powder reference sample in (d). By comparing a-c it can be seen that the amplitude of EXAFS under polarization enhancement was larger, comparing to (d) which was magnified by 3 times. In total, the data provide compelling evidence for the orientation of the dithionate S₂O₆²⁻ ion's S-S axis parallel to $[\bar{1}\bar{1}\bar{1}]$ direction.

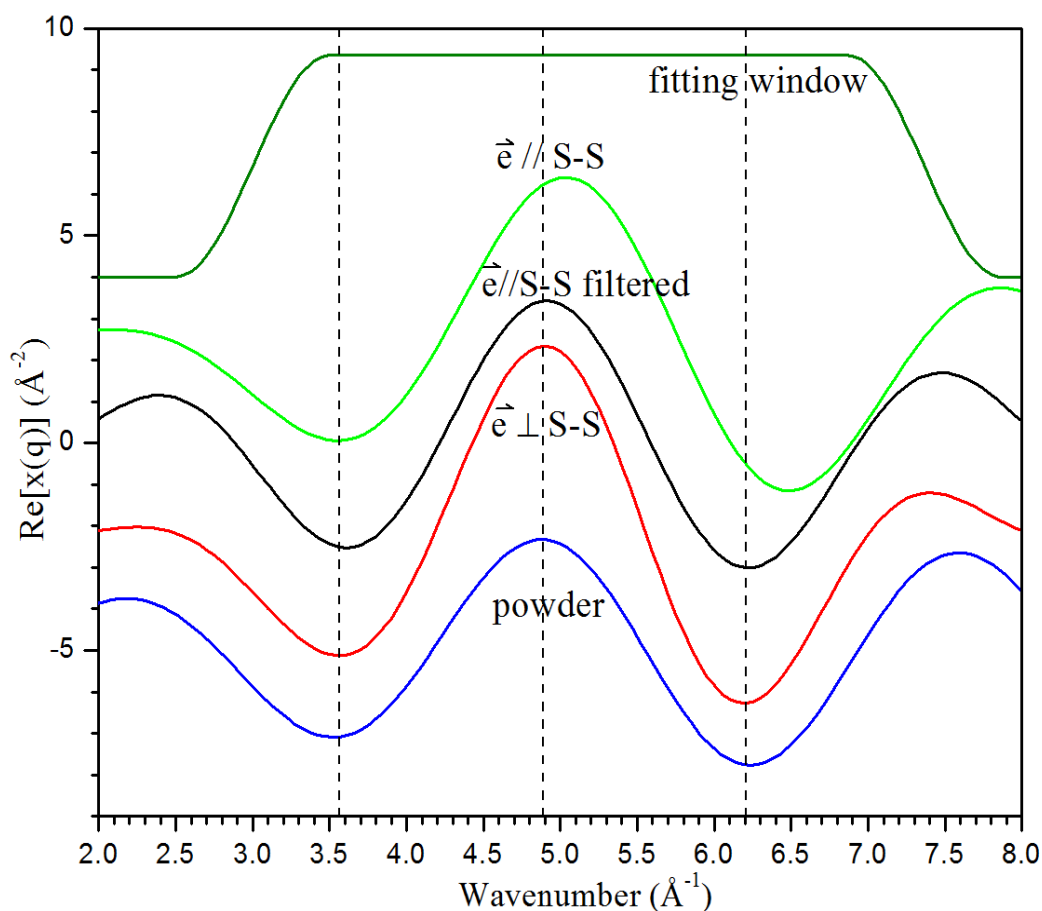


Figure 8.6 The back Fourier Transformed (FT) spectra of different EXAFS. (a) Back FT spectrum of the EXAFS ($R = 2.0$) at orientation I, i.e. $\vec{e} // \text{S-S}$. (b) Back FT spectrum of the EXAFS ($R = 1.35$) at orientation I, i.e. $\vec{e} // \text{S-S}$. (c) Back FT spectrum of the EXAFS ($R = 2$) at orientation II, i.e. $\vec{e} \perp \text{S-S}$. (d) Back FT spectrum of the EXAFS ($R = 2$) for powder sample. Note: The amplitude of powder data was multiplied by 3 for convenient visualization. The three dotted vertical lines are used as reference position to observe the overlap ratio among the spectra.

8.2.5 Discussion on the Local Structure of the S₂O₆²⁻

In addition to the determination of the S-S bond direction from the polarized EXAFS, in this section it will try to explore the actual structure of S₂O₆²⁻, including the bond length and the bond angle, from the best-fits of the polarized EXAFS.

Detailed examination of the bond lengths of 1st shell S-O provided an acceptable value of about 1.4229 Å (Table 8.1) to the reference standard compound which was obtained from powder EXAFS, while that is 1.4292 Å (see Table 8.2, averaged from 1.4280 Å and 1.4303 Å) in the analysis of the polarized data of doped single crystals. Thus, the bond length of 1st shell S-O obtained for S₂O₆²⁻ in doped single crystals can be considered as consistent with that for powder crystalline Na₂S₂O₆. Given the limited k-range available (c.a. 8 Å⁻¹), it is not really feasible to do better fit for both the powder EXAFS and the polarized EXAFS.

According to Equation 8.3, in the analysis of EXAFS the bond angle <S-O,S-S> is directly related to the N_{effective} of the 1st shell O.

$$\theta_{s-o} = \arccos \left(\sqrt{\frac{\chi_{pol} \div \chi_{iso}}{3 \times n}} \right) \quad (8.3)$$

where χ_{pol} is the polarized EXAFS, χ_{iso} is the isotropic EXAFS contribution of one O scatterers on the 2nd shell, n refers to the number of equivalent scatters on the same shell. Here χ_{pol}/χ_{iso} is equal to the N_{effective} of all equivalent scatterer on the same shell.

From the results of the best-fits of polarized data (Table 8.2), the N_{effective} of the 1st shell O has two distinct values from the two different experiments, i.e. 3.7 and 4.0 (Table 8.3a), respectively. Thus, in order to explore the bond angle <S-O,S-S> in this system, the one-to-one correspondence between the angle <S-O,S-S> and the N_{effective} of 1st shell O was tabulated in Table 8.3b (calculation see Appendix III). However, the angles <S-O,S-S> calculated from the experimental values of the N_{effective} at the two different orientations respectively, i.e. parallel and perpendicular, do not match each other. The N_{effective} = 3.70 at the parallel orientation corresponds to <S-O,S-S> = 50 °, while N_{effective} = 4.00 at the perpendicular orientation approximately corresponds to <S-O,S-S> = 70 °.

N _{effective} (experiment)		Angle <S-O,S-S>	Angle <S-O,S-S>	N _{effective} (theoretical)	
$\vec{e} // S-S$	$\vec{e} \perp S-S$			$\vec{e} // S-S$	$\vec{e} \perp S-S$
3.70	4.00	unknown	80	0.27	4.36
			70	1.00	3.97
			65	1.61	3.70
			60	2.25	3.40
			55	3.00	3.02
			50	3.70	2.68

Table 8.3 The experimental and the theoretical values of the N_{effective} and the angle <S-O,S-S>. (a) The experimental result of the N_{effective}. (b) The theoretical values of the N_{effective} calculated from its corresponding angle <S-O,S-S> according to Equation 8.3.

As a result, there is a need to evaluate the two different values obtained above. There are a series of RO₃ and RO₄ ions presenting the molecular configuration of trigonal pyramid similar to that of the S₂O₆²⁻. A detailed investigation over the bond angle of such ions was carried out, in order to compare with the experimental results. Consulting the angle <S-O,S-S> of S₂O₆²⁻, the angle between the R-O bond and the three-fold axis (Figure 8.7) of the investigated ion were tabulated in Table 8.4. From Table 8.4 it can be seen that, the angles <S-O,S-S> of most RO₃ and RO₄ ions are around 70°. This suggests that such molecular configuration prefers a bond angle <S-O,S-S> of 70°, which indirectly supports the experimental value of N_{effective} = 4.00 at the perpendicular orientation which corresponds to <S-O,S-S> = 70°. However, the experimental N_{effective} = 3.70 at the parallel orientation is quite different with the theoretical value of 1.00.

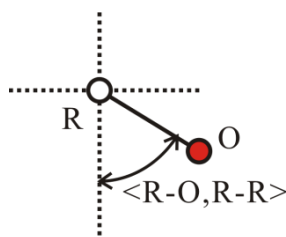


Figure 8.7 The measuring method for bond angle <R-O,R-R> of RO₃ and RO₄ ions.

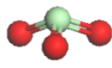
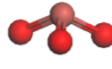
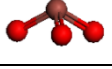
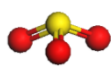

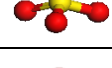
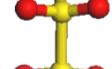
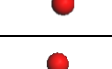
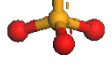
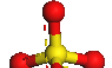
Formula	Measured angle	R-O bond length	Ion	Reference
ClO ₃ ⁻	68.1	1.485		(Abrahams & Bernstein 1977)
BrO ₃ ⁻	66.02	1.648		(Abrahams & Bernstein 1977)
IO ₃ ⁻	57.68	1.811		(Svensson & Ståhl 1988)
SO ₃ ²⁻	66.96	1.505		(Larsson & Kierkegaard 1969)
S ₂ O ₃ ²⁻	71.48	1.473		(Teng et al. 1984)
S ₂ O ₆ ²⁻	74.2	1.451		(Kirfel et al. 1980)
SeO ₄ ²⁻	70.53	1.654		(Kámán & Cruickshank 1970)
SO ₄ ²⁻	68.82	1.476		(Nord 1973)
ClO ₄ ⁻	69.45	1.43		(Wartchow 1978)
Cr ₂ O ₇ ²⁻	74.4	1.62		(Panagiotopoulos & Brown 1973)

Table 8.4 The angle between the R-O bond and the three-fold axis of the investigated ion (note: R represents the non-oxygen element).

Therefore, it was an ambitious idea to explore the bond angle between the S-O bond and the S-S bond $\langle \text{S-O}, \text{S-S} \rangle$ for the S₂O₆²⁻ in doped single crystal, by calculation based on the $N_{\text{effective}}$ of the 1st shell oxygen. However, mindful of the strong correlation among the $N_{\text{effective}}$, bond length and amplitude reduction factor (S_0^2), caution should be taken in terms of over-analyzing the data. In particular, the

theoretically expected variation in $N_{\text{effective}}$ could be even more than $\pm 10\%$ for a data of a short k-range. Clearly, further work is needed for more fully understand the atomic arrangement association with the measured S-O correlation.

To sum up, at this stage with the most effort, the experimental S-O bond length obtained is 1.4292Å, and the bond angle $\langle \text{S-O}, \text{S-S} \rangle$ is approximately 70° . These results lead to the reconstruction of an experimentally measured structure of $\text{S}_2\text{O}_6^{2-}$ ion shown in Figure 8.8.

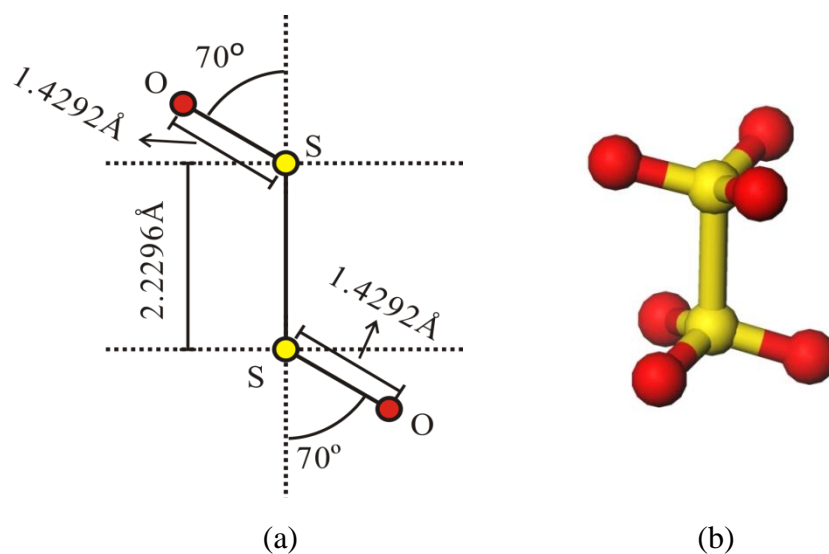


Figure 8.8 Illustration of the the structure of $\text{S}_2\text{O}_6^{2-}$. (a) Schematic illustration of the structure of $\text{S}_2\text{O}_6^{2-}$ with dimensions obtained from 190ppm EXAFS. (b) Stereo illustration of an $\text{S}_2\text{O}_6^{2-}$ ion.

8.3 Qualitative Determination of the Molecular Orientation of S₂O₆²⁻ around Its 3-Fold Axis by Polarized XANES

8.3.1 Polarized XANES of 800ppm S₂O₆²⁻-doped NaClO₃ Crystal

In order to fully understand the three-dimensional orientation of the S₂O₆²⁻ during the impurity incorporation process, besides the above discussion on the orientation of S-S bond of S₂O₆²⁻, the orientation of S₂O₆²⁻ around its three-fold axis within the plane of the crystal surface of $(\bar{1}\bar{1}\bar{1})$ is discussed in this section. On one hand, the P-XANES spectra were measured by aligning the 800ppm doped crystal at 4 different orientations with respect to the beam \vec{e} vector (Figure 8.9, cf. section 4.10.2 for technical details). This allows the enhancement of specific electron transitions along certain crystallographic directions and these directions can be known according to the speculative structural model of impurity incorporation (Figure 8.2). On the other hand, the partial density of states (PDOS) and the unoccupied molecular orbitals of S₂O₆²⁻ had already been simulated in a certain energy range of the XANES (Lan et al., 2014). The theoretical unoccupied molecular orbitals can be plotted with respect to the energy range where transition enhancement was experimentally observed. A slice across the orbitals with respect to the orientation of S₂O₆²⁻ under experimental geometry was created (since the ion is on the $(\bar{1}\bar{1}\bar{1})$ surface, to judge its orientation under experimental geometry it also needs to consider the surface model), and the experimental direction of beam \vec{e} vector was introduced into the sliced map. Thus, the correctness of the molecular orientation of S₂O₆²⁻ as in the proposed model of the $(\bar{1}\bar{1}\bar{1})$ surface can be verified if the XANES result is consistent with the result from judging the enhancement of electron transition by \vec{e} vector in the map of the orbitals.

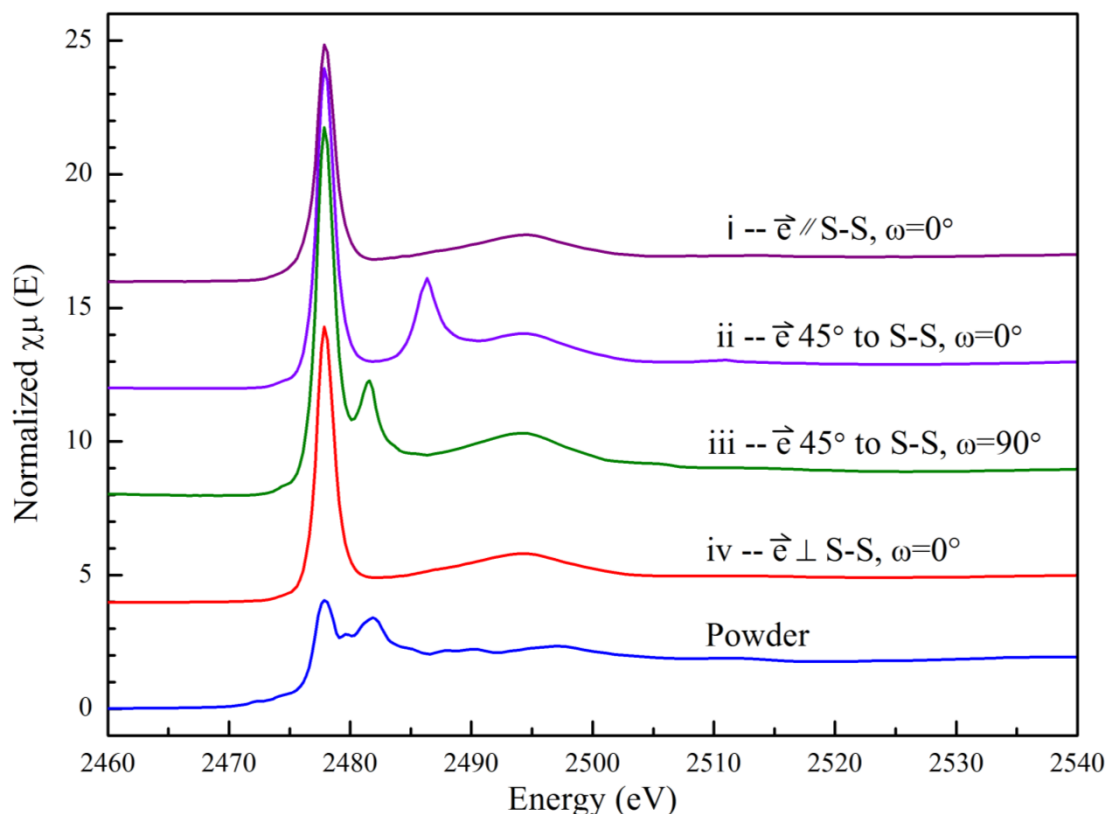


Figure 8.9 The XANES spectra of 800ppm doped crystal sample at various orientations, together with that measured on powder Na₂S₂O₆. The spectrum of powder Na₂S₂O₆ was multiplied by 2 to enhance the peak height for better observation.

Figure 8.9 shows the 800ppm polarized XANES spectra together with the XANES measured on Na₂S₂O₆ powder for comparison. It can be seen that the sulphur K-edge in the spectra (indicated by the strong white-line peaks) are all at 2477.85 eV. The identical peak position implies that, the sulphur element exists in the single crystal sample is of the same oxidation-state as that in the powder sample. Thus, the sulphur element in both the samples is in the format of S₂O₆²⁻ ion. In other words, the S₂O₆²⁻ entered the NaClO₃ crystals keeping its ionic form unchanged as S₂O₆²⁻. The S K-edge peak position of S₂O₆²⁻ was reported by Sekiyama et al. (1986) and Filipponi et al. (1993) to be at 2476.5 eV and 2480.9 eV, respectively. The S K-edge at 2477.85 eV measured in the current study can be considered as consistent with that reported by Sekiyama et al. (1986).

Besides, by observing the overall spectral shape among the spectra in Figure 8.9, the polarized spectra at the 4 orientations present a smoother curve with less oscillation than the isotropic spectrum (i.e. powder spectrum). In addition, some specific peaks at different energy positions were significantly enhanced in the polarized spectra of ii and iii (e.g. the peaks at 2486.35 eV on ii and at 2481.60 eV on iii, in Figure 8.9) compared to the other polarized spectra of i and iv. These characteristics are attributed to the effect of the orientational beam \vec{e} vector, which have weakened some transitions at specific orientation and enhanced some others in the polarized XANES measurements.

The absorption peaks in the sulphur K-edge XANES are caused by the intensive electron transition from the 1s initial state to the unfilled final state of p-symmetry (dipole selection rules) which absorbs the beam energy. Since the p-symmetry PDOS (partial density of states) is able to present the transition possibility for K-edge XANES at specific energy levels, thus it can be used for comparing with the XANES to interpret the absorption peaks. Unoccupied molecular orbitals calculated simultaneously with the PDOS are presented to discuss the polarization-enhanced peaks. The p-symmetry PDOS and the corresponding unoccupied molecular orbitals of S₂O₆²⁻ had been calculated by Dr. C. Seabourne (Lan et al., 2014) using CASTEP pseudopotential DFT code (Pickard, 1997; Clark et al., 2005; Gao et al., 2008; Gao et al., 2009), based on the crystal structure of Na₂S₂O₆ (Kirfel et al., 1980). These results will be cited here for interpreting the XANES.

8.3.2 The Isotropic XANES and the PDOS

Figure 8.10 shows the isotropic XANES of Na₂S₂O₆ powder and the theoretical p-symmetry PDOS. The white-line peak labelled “A” and the two resonance peaks labelled “B” and “C”, respectively, are in good agreement with the PDOS peaks within the specific energy ranges. The white-line peak correlates to three adjacent

PDOS peaks, which can explain its high intensity. The energy ranges of resonance peak “C” and its correlated PDOS peak are slightly shifted with respect to each other. This might be ascribed from the unknown many-body effects of XANES which were not considered in the calculation. Besides, although there is a PDOS peak within the range of 2485.3 – 2486.9 eV, on the isotropic XANES no corresponding peak appeared, the reason for which is unclear. To sum up, the overall features of the isotropic XANES are mostly consistent with the theoretical PDOS.

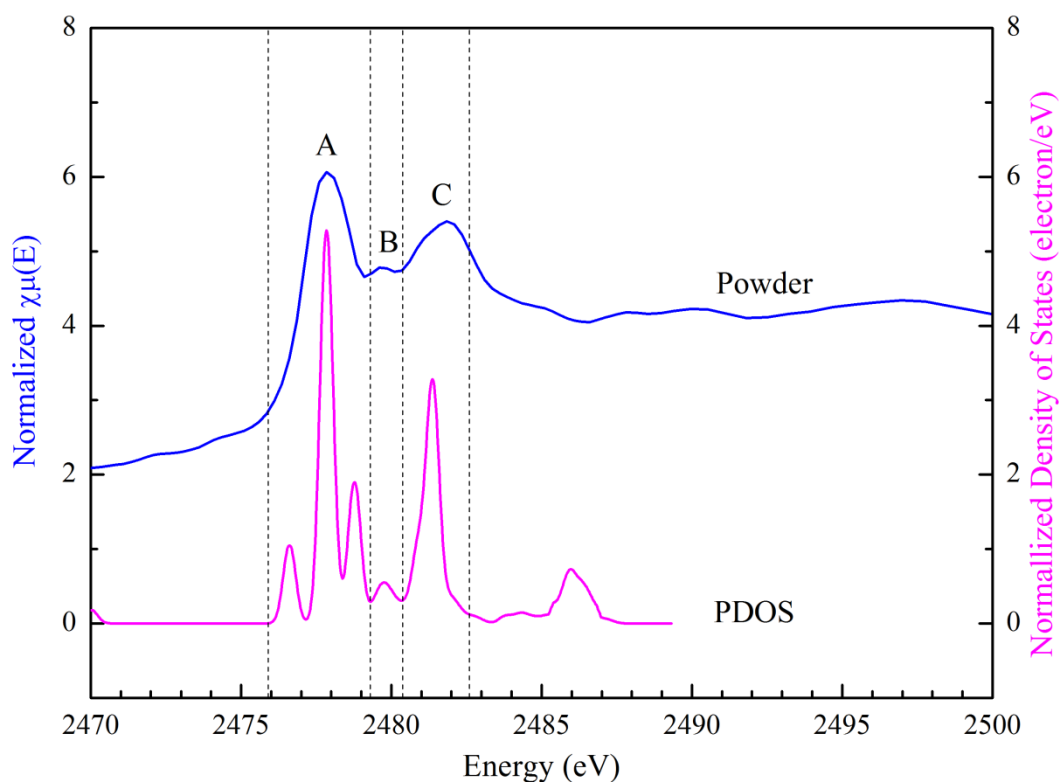


Figure 8.10 The S K-edge XANES of Na₂S₂O₆ powder and the theoretical p-symmetry PDOS. The white-line peak of XANES is labelled as “A”, and there are two other resonance peaks which were labelled “B” and “C”, respectively. The dotted vertical lines define the energy range of the correlated peaks from the XANES and the PDOS.

8.3.3 The Polarized XANES and the PDOS

Figure 8.11 shows the p-symmetry PDOS and the polarized XANES of 800ppm doped crystal measured at four orientations. Both the spectra of ii and iii presented largely enhanced peaks, whereas spectra i and iv showed no such peaks. The reasons will be discussed with the aid of the p-symmetry PDOS and the unoccupied molecular orbitals.

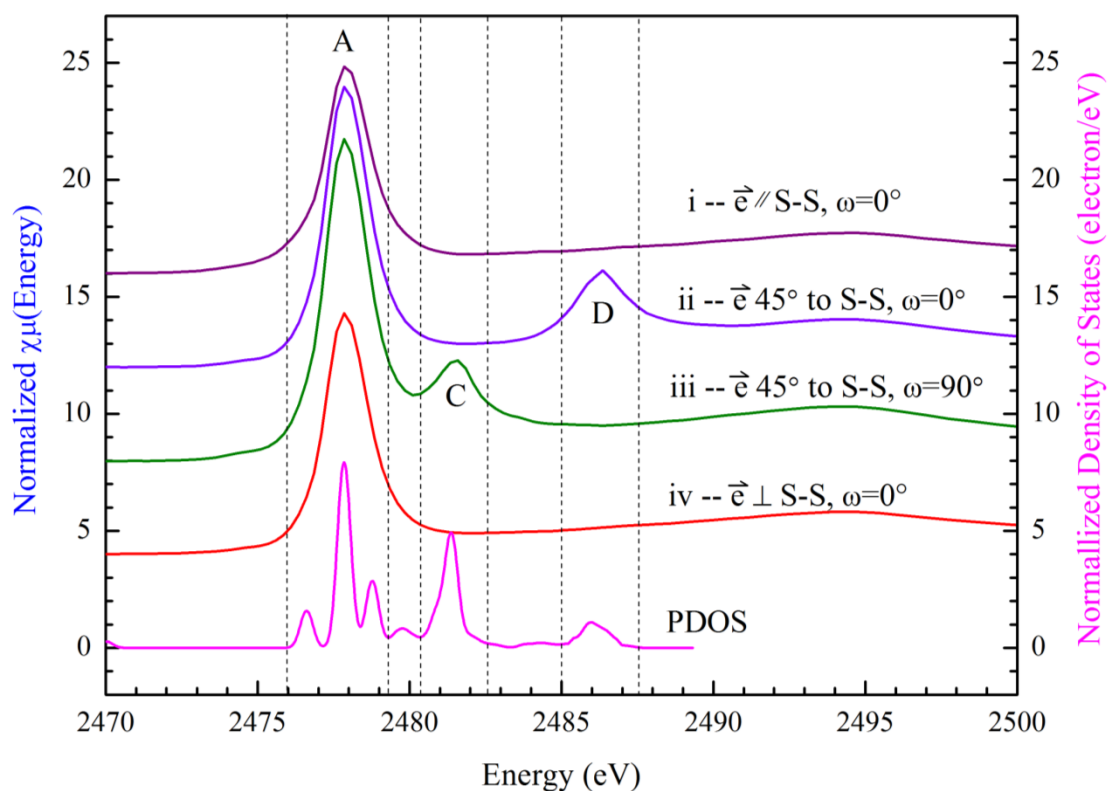


Figure 8.11 The S K-edge XANES of 800ppm doped crystal at various orientations and the unoccupied p-symmetry PDOS (magenta line). The dotted vertical lines define the energy regions of the correlated peaks from the XANES and the PDOS. ω is the angle rotated along the S-S axis (looking along the [111] direction clockwise is “+” and anticlockwise is “-”) (cf. section 4.10.2), 0° started from the position where an edge of the $(\bar{1}\bar{1}\bar{1})$ surface is vertically aligned on the left hand side when looking along the beam incident direction.

The XANES spectrum iii in Figure 8.11 presents a resonance peak within the energy range of 2479.30 – 2480.37 eV. This energy range is the same as that of peak “C” in Figure 8.10. Thus, this peak in spectrum iii is also labelled “C”. A corresponding peak in the PDOS can be identified, whose high intensity implies a high transition probability underpinning the occurrence of the XANES peak.

The unoccupied theoretical orbitals within the energy range of peak “C” were extracted from the calculation and plotted as a projection map in Figure 8.12a, which was created by slicing across the density plot of the orbitals according to the orientation of S₂O₆²⁻ under experimental geometry based on speculated model. The map shows that these orbitals retain a significant density at the opposite side of the S-O bond, around each of the SO₃ groups. As a result, the line direction from the S absorber to the area of highest density (opposite to the S-O bond direction) is approximately collinear with the beam \vec{e} vector (which was 45° to the S-S bond), which implies that the electron transition at the current geometry can be maximally enhanced⁵. This has satisfactorily interpreted the peak “C” of spectrum iii in Figure 8.11. In addition, by considering the same principle and consulting the orientation of \vec{e} vector applied for spectra i and iv (Figure 8.12a and b), it is simple to understand that there were no peaks in the same energy range of “C” on spectra i and iv, since there were no suitable areas of high density of unoccupied states for the \vec{e} vector to enhance.

⁵ Transition is maximally enhanced when the \vec{e} vector is collinear with the line direction from the core atom to the area of highest density of unoccupied states.

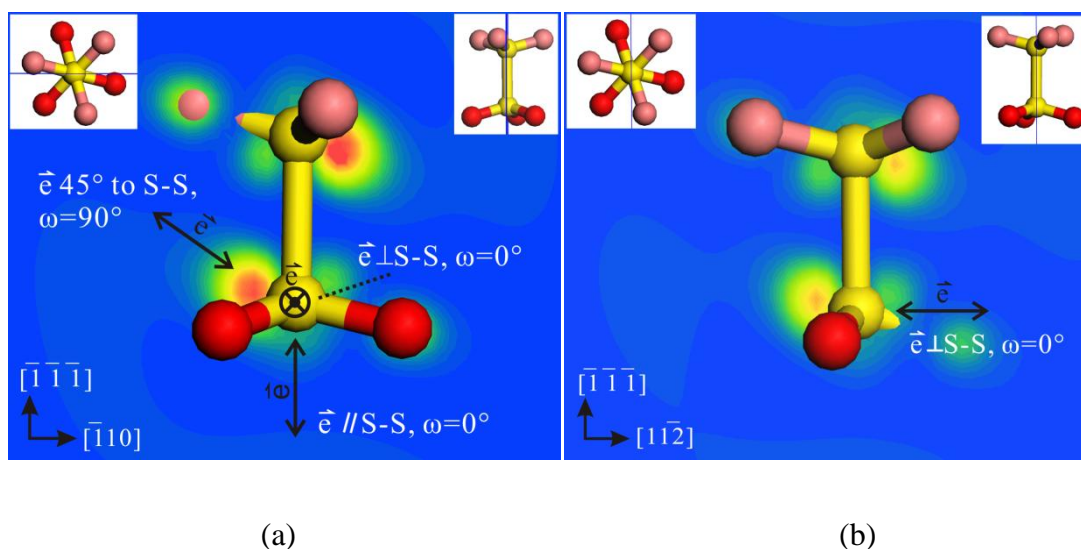


Figure 8.12 Projection map of the unoccupied orbitals of $S_2O_6^{2-}$ ion within specific energy region “C”, i.e. 2479.30 – 2480.37 eV. (a) Orbital slice created through the S-S axis of the $S_2O_6^{2-}$ ion. The slicing direction is indicated by the line position indicated on the top corners of the figure. The bottom SO_3 group was orientated with respect to that of the substituted ClO_3^- on the $(\bar{1}\bar{1}\bar{1})$ surface (Figure 8.2) under the applied experimental conditions (e.g. the X-ray beam direction). In the map, “ \vec{e} 45° to S-S” was the electric vector used in the detection of peak “C”, while the other two were used for the spectra i and iv. (b) Orbital slice created normal to the slice in (a), for assisting the depiction of the electric vector perpendicular to the first slice (a).

For the absorption peak “D” of spectrum ii in Figure 8.11, its corresponding unoccupied orbitals have also been projected as a map (Figure 8.13) to depict the area of high density of unoccupied states. Around each of the SO_3 groups, the line direction from the S absorber to the area of high density is approximately collinear with the \vec{e} vector (\vec{e} is 45° to S-S) in the current map. As a result, with the suitable relative position the \vec{e} vector can enhance the corresponding electron transition to produce peak “D”. In addition, within the energy region “D”, the spectra i and iv did not show any absorption peak. This can also be explained by consulting the orientation of \vec{e} vector applied for spectra i ($\vec{e} // S-S$) and iv ($\vec{e} \perp S-S$) (Figure 8.13a and b). In the direction of these \vec{e} vectors the corresponding density of unoccupied

orbitals is too low to produce a strong peak.

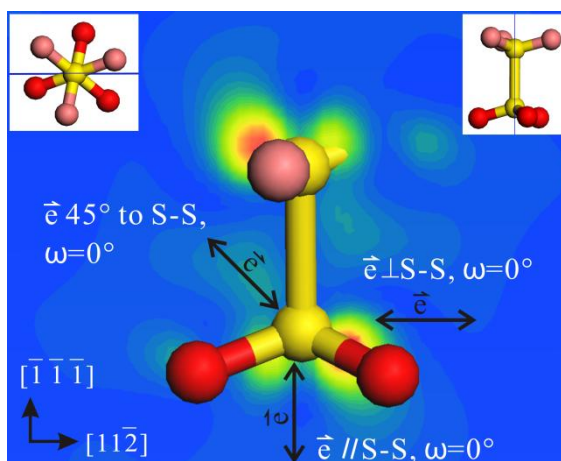


Figure 8.13 Projection map of the unoccupied orbitals of $S_2O_6^{2-}$ ion within specific energy range “D”. The slice was created by slicing through the S-S axis of the $S_2O_6^{2-}$ ion whose orientation was adjusted identically to that of the ClO_3^- on the $(\bar{1}\bar{1}\bar{1})$ crystal face under the actual experimental conditions. Three electric vectors have been indicated in the figure, all of which are of orientation within the slice.

To sum up, for the P-XANES spectra of the 800ppm sample, the specific absorption peaks of “C” and “D” on spectra ii and iii have been satisfactorily interpreted by applying the experimental \vec{e} vector into the map of the unoccupied molecular orbitals. Since the creation of the orbital maps was based on judging the orientation of $S_2O_6^{2-}$ with respect to the proposed structural model, the above successful interpretation in turn proves the correctness of the model. In addition, it proved that the $S_2O_6^{2-}$ substituted the ClO_3^- on the surfaces of $\{\bar{1}\bar{1}\bar{1}\}$ type by one SO_3 group and retained the orientation of ClO_3^- in the plane of the surface.

8.4 Determination of S₂O₆²⁻ Distribution in Different Types of Growth Sectors by XRF-Mapping

To determine the distribution of S₂O₆²⁻ in the growth sectors of different types of doped crystal, X-ray fluorescence mapping (XRF-mapping) was performed to detect the distribution of the sulphur element since all sulphur element in the doped crystal is from the impurity S₂O₆²⁻. Figure 8.14a shows a sulphur XRF-map scanned on part of the crystal plate ($\bar{1}10$) cut from 190ppm doped crystal. By comparing the map to the X-ray topographic image of the sample (Figure 8.14b), it can be seen that the sulphur distribution significantly varied according to the type of the growth sector. The fluorescence intensity (i.e. sulphur K α photon counting) at the four points in growth sectors of different types on the map (Figure 8.14a) can give clear indication of sulphur distribution since the intensity is proportional to the concentration of sulphur.

It is not surprising to see that the sulphur concentration in the $\{\bar{1}\bar{1}\bar{1}\}$ type sector is twice as much as that in the growth sectors of $\{001\}$ type. However, although the sulphur concentrations are low in growth sectors of $\{001\}$ type, the existence of sulphur in these sectors implies that S₂O₆²⁻ impurity can adsorb onto the surface of $\{001\}$ type during growth.

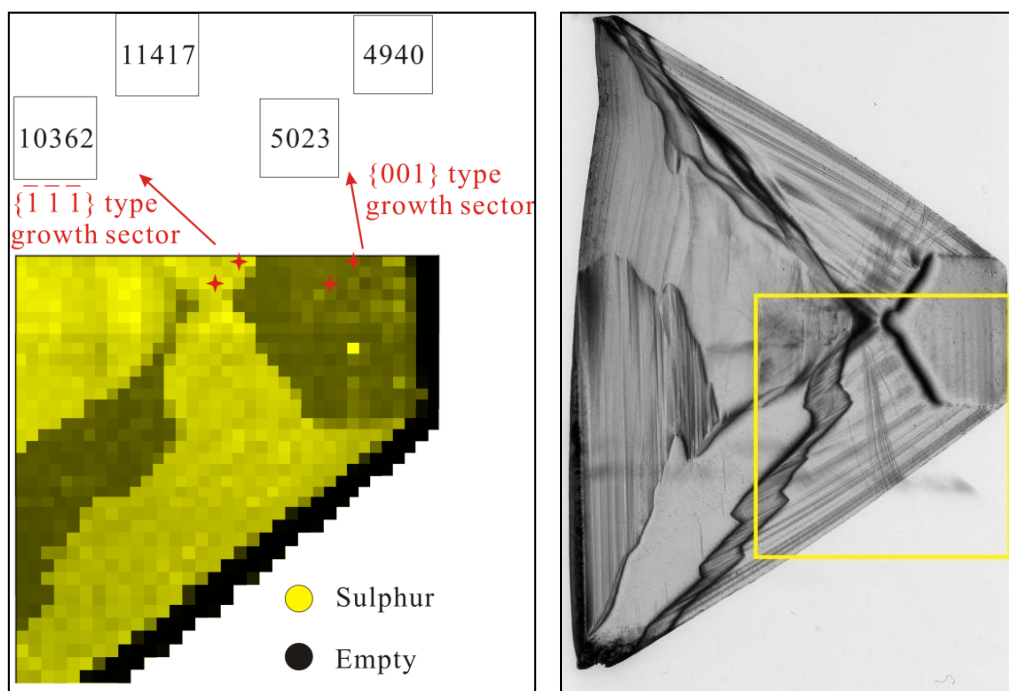


Figure 8.14 (a) XRF-map of sulphur across part of the 190ppm doped crystal plate. A bright yellow point in the sector of the {001} type was caused by surface scattering of the X-ray beam during measurement. (b) The topograph for the same plate used for XRF-mapping. Note: The yellow box defined in (b) is the sampling section used in the XRF-mapping.

Therefore, for the elemental map scanned for the 190ppm sample, the sulphur signal recorded in the sector of $\{\bar{1}\bar{1}\bar{1}\}$ type was approximately twice as much as that in the sector of {001} type. From this it can be concluded that during the growth of the crystal, the incorporation of $S_2O_6^{2-}$ impurity occurred intensively on the $\{\bar{1}\bar{1}\bar{1}\}$ faces, and also, $S_2O_6^{2-}$ impurity can also adsorb or incorporate on the {001} faces at a much lower probability. The incorporation mechanism of $S_2O_6^{2-}$ on the $\{\bar{1}\bar{1}\bar{1}\}$ faces have been experimentally explored and will be concluded at the end of this thesis, but that on the {001} faces is outside the scope of this thesis.

8.5 Conclusions

This chapter discussed the three-dimensional orientation of S₂O₆²⁻ impurity on the { $\bar{1}\bar{1}\bar{1}$ } faces of NaClO₃ crystal, and attempted to explore the bond length and bond angle of the impurity in the host crystal. The EXAFS results indicated that, the S-S bond of S₂O₆²⁻ aligns parallel to the growth direction of { $\bar{1}\bar{1}\bar{1}$ } faces, i.e. along the $\langle\bar{1}\bar{1}\bar{1}\rangle$ directions. Nevertheless, according to the XANES results, the substituting SO₃ of S₂O₆²⁻ was confirmed to have retained the orientation of the substituted ClO₃⁻ in the { $\bar{1}\bar{1}\bar{1}$ } surface. Thus, the three-dimensional orientation of S₂O₆²⁻ in the growth sectors of { $\bar{1}\bar{1}\bar{1}$ } type has been confirmed. Furthermore, the determined orientation of S₂O₆²⁻ was unique, implying that there is only one unique orientation of ClO₃⁻ which facilitates the substitution of ClO₃⁻ by the S₂O₆²⁻. The results agree with the previously proposed model by Ristic et al. (1993; 1994). This work also attempted to explore the bond angle for the incorporated S₂O₆²⁻ impurity, where the two measurements at different geometries did not show good consistence, due to the short k-range of the EXAFS data and the strong correlation of N_{effective} to other parameters.

Additionally, the XAF-mapping revealed that the concentration of impurity incorporated in growth sectors of { $\bar{1}\bar{1}\bar{1}$ } type is approximately twice that in growth sectors of {001} type. This indicates different incorporation/adsorption probabilities in the growth sectors of different types.

CHAPTER 9

A Structural Model for the Habit Modification of NaClO₃ by Na₂S₂O₆

Summary:

A comprehensive discussion based on both experimental and molecular modelling results is presented, aiming at to consummate the structural model of the impurity incorporation in the NaClO₃/Na₂S₂O₆ (host/impurity) system. The effect Na₂S₂O₆ impurity on the growth mechanism of NaClO₃ during the habit modification process is also discussed.

9.1 Introduction

This chapter aims to approach the mechanism of the habit modification of sodium chlorate (NaClO₃) by sodium dithionate (Na₂S₂O₆) from the molecular level, after its macroscopic features have been experimentally characterized from different aspects in previous chapters. Since the impurity Na₂S₂O₆ is also a sodium salt as is NaClO₃, the impurity under discussion is thus only S₂O₆²⁻. By comparing the structure and the atomic charges between the molecules of the impurity and the host crystal, this chapter investigates the molecular similarity between them to discuss the possibility for substitution of ClO₃⁻ by S₂O₆²⁻ to occur. In order to compare the suitability for S₂O₆²⁻ incorporation among different types of growing faces, the surface structure of various faces of NaClO₃ is analyzed. Then, the rational structural model for this habit modification system is established and correlated with the experimental results from previous chapters. Based on the molecular model and other experimental results, the habit-modifying effect of S₂O₆²⁻ on the NaClO₃ crystal is discussed. Finally, the nature of the twinning origin and the structure of the twin boundary are addressed.

9.2 Molecular Model of Impurity Incorporation

9.2.1 Molecular Similarity between ClO₃⁻ and S₂O₆²⁻

To understand the possibility for substitution of ClO₃⁻ by S₂O₆²⁻ (also written as (SO₃)₂²⁻) to occur, the molecular similarity between the ClO₃⁻ from the host crystal and the S₂O₆²⁻ impurity ion will be discussed, in terms of structure and atomic charge distribution. The crystal structures of the NaClO₃ and the Na₂S₂O₆ used in this chapter were derived from the crystal structures deposited in the Inorganic Crystal Structure Database (ICSD) under reference code icsd-1301 (Abrahams and Bernstein, 1977) and icsd-26326 (Kirfel et al., 1980), respectively.

The structure of the ClO₃⁻ and S₂O₆²⁻ ions are shown in Figure 9.1 and Figure 9.2. On one hand, the ClO₃⁻ presents a trigonal pyramidal shape with the Cl on the apex and

three O separated 2.386 Å at the corners of the trigonal base (Figure 9.1a and b, Figure 9.2c). On the other hand, the S₂O₆²⁻ constitutes two identical trigonal pyramids twisted by 60° along its three-fold symmetry axis (which is coincident with S-S bond) (Figure 9.1c and d). Each pyramid has the S on the apex and three O separated 2.430 Å at the corners of the trigonal base (Figure 9.2d). Therefore, it can be seen that, the ClO₃⁻ and the SO₃ of S₂O₆²⁻ possess the similar trigonal pyramidal shape, and, the difference of 0.044 Å (approximately 1.8%) between the side lengths thus the sizes of their bases is very small. Consequently, in terms of structure, the substitution of ClO₃⁻ in NaClO₃ crystal by half of S₂O₆²⁻ can occur without much obstruction.

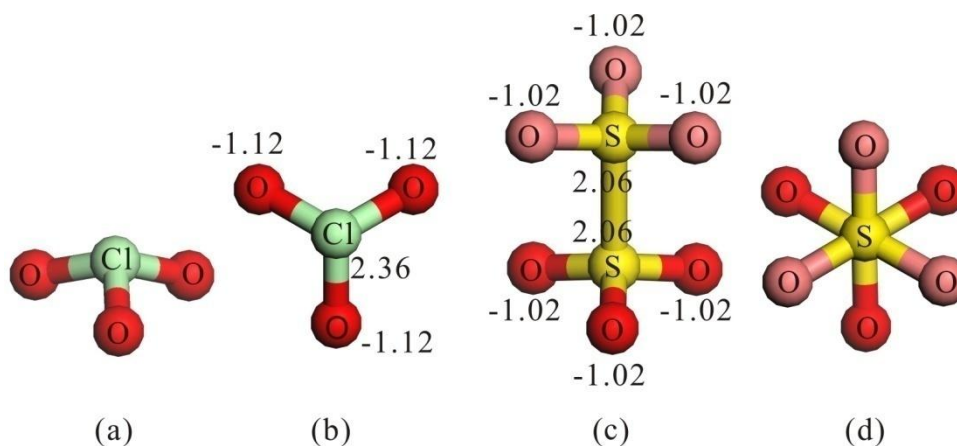


Figure 9.1 The structure and the atomic charges of the ClO₃⁻ and the S₂O₆²⁻. (a) Side view of ClO₃⁻ ion; (b) Projection view of ClO₃⁻ ion along its three-fold axis; (c) Side view of S₂O₆²⁻ ion; (d) Projection view of S₂O₆²⁻ ion along its three-fold axis, where the two SO₃ groups are at staggered positions twisted by 60°

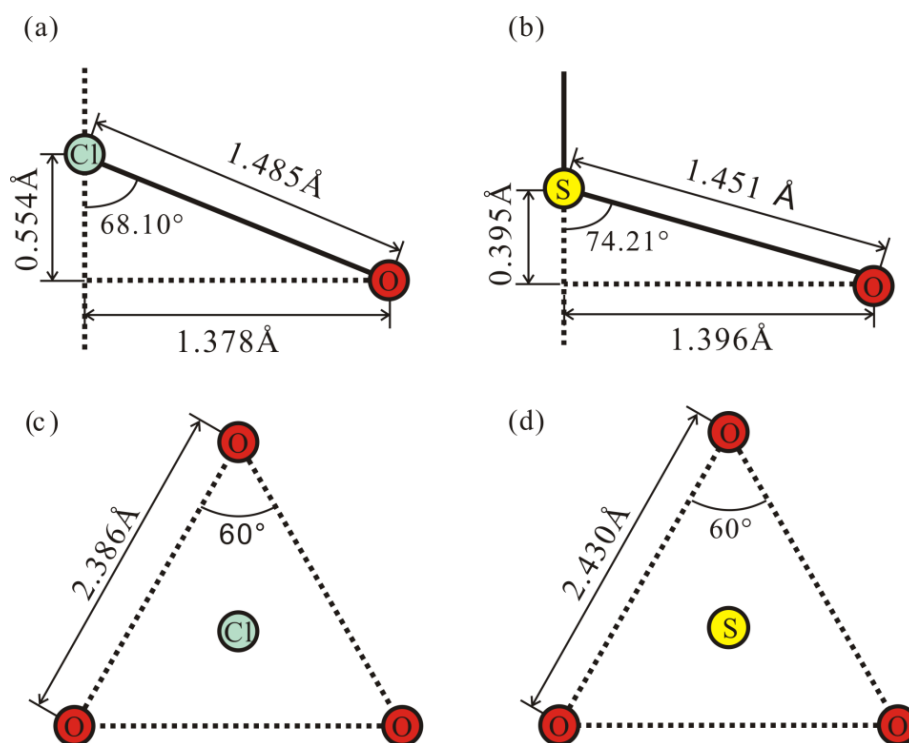


Figure 9.2 The dimensions of chlorate and dithionate ions. (a) The chlorate ion viewed along the normal to its three-fold axis. (b) The dithionate ion viewed along the normal to its three-fold axis. (c) The chlorate ion viewed along its three-fold axis. (d) One SO_3 group of the $\text{S}_2\text{O}_6^{2-}$ ion viewed along its three-fold axis.

The atomic charges were calculated for the two ions using the semi-empirical PM6 method in the MOPAC code, results are shown in Figure 9.1b and c. It can be seen that, the ClO_3 and one SO_3 of the S_2O_6 have a similar charge distribution and the total charges of the ClO_3 and one SO_3 of the S_2O_6 are both -1. Here it is more important to discuss the charge on the O rather than the shielded charges on the Cl or S. The negative charges on the O of the ClO_3 and the SO_3 are -1.12 and -1.02, respectively, resulting in an acceptable difference of about 10%. Therefore, it can be concluded that, the similar charge distribution and the different charge on O within reasonable range would enable the substitution of ClO_3 by one SO_3 of S_2O_6 .

Consequently, since the ClO_3^- and the SO_3 of $\text{S}_2\text{O}_6^{2-}$ are similar in terms of structure and atomic charge distribution, it is believed that one SO_3 of $\text{S}_2\text{O}_6^{2-}$ is capable of mimicking the ClO_3^- and incorporating into the lattice of the NaClO_3 crystal.

9.2.2 Surface Structure of NaClO₃ and Suitable Sites for Impurity Incorporation on the $\{\bar{1}\bar{1}\bar{1}\}$ Faces

To understand the selective incorporation of S₂O₆²⁻ in NaClO₃ crystals, it is necessary to analyze the packing structure of the surfaces of different type to evaluate the more favourable ones for impurity incorporation. The surfaces under discussion are from the most important growth forms of {001}, {110}, {111} and $\{\bar{1}\bar{1}\bar{1}\}$. All the packing structures of the surfaces were derived from crystal structures stated in last section.

NaClO₃ single crystals crystallize in the non-centrosymmetric space group P2₁3, with four molecules in one unit cell (Abrahams and Bernstein, 1977). The four ClO₃⁻, in the shape of a trigonal pyramid, have their apex Cl atoms pointing to a corresponding Na atom 3.981 Å away, respectively, along the three-fold axes of ClO₃⁻. The three-fold axes of the ClO₃⁻ are coincident with the crystal axes <111>.

Figure 9.3a shows the structure of a {001} surface of NaClO₃. The structure shows that the three-fold axis of each ClO₃⁻ group is at an angle of about 54.7° against the surface, with the apex Cl either pointing outwards the surface or inwards the bulk. By comparison, it can be possible that the one SO₃ of S₂O₆²⁻ will substitute the ClO₃⁻ whose Cl apex is aligned towards the surface, while the other SO₃ of S₂O₆²⁻ protrudes outside the surface (Figure 9.3a). However, after the substitution, an O of the protruding SO₃ locates too close (approximate 0.50 Å) to the O of a pre-existing ClO₃⁻ in the surface (circled by dots in Figure 9.3a). This short distance is unacceptable due to too strong a repulsive force. Nevertheless, the S₂O₆²⁻ can deposit onto the surface before that “pre-existing” ClO₃⁻, but the probability of this case occurring is reduced by 50% compared to that if there were no obstruction occurring in the above case. Therefore, the impurity incorporation on the {001} surfaces could occur, but with a low probability.

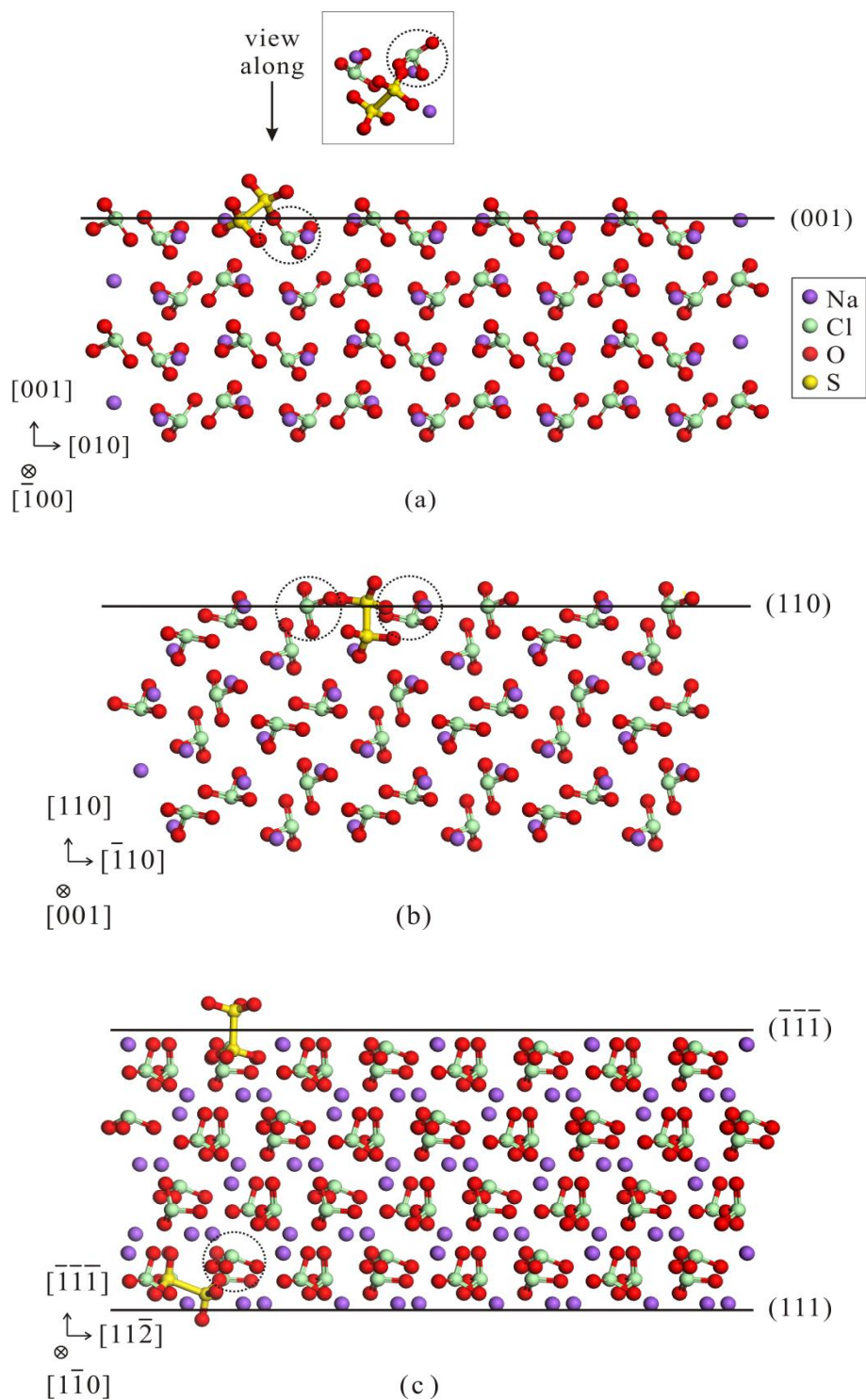


Figure 9.3 The visualization of the molecular arrangement on different surfaces of NaClO_3 . (a) Surface structure of the $\{001\}$ faces. (b) Surface structure of the $\{110\}$ faces. (c) Surface structure of the $\{\bar{1}\bar{1}\bar{1}\}$ faces and their geometrically opposite faces of $\{111\}$. Note: In the figures, the $\text{S}_2\text{O}_6^{2-}$ was inserted into the crystal by replacing the most suitable ClO_3^- for substitution on the surfaces.

On the (110) surface (belonging to the {110} type), the only possible ClO₃⁻ for impurity substitution is shown in Figure 9.3b, whose three-fold axis lies at 35.27° to the [110] direction. By incorporating into this site, the S₂O₆²⁻ impurity would interact with two vicinal ClO₃⁻ (circled by dots in figure) by strong repulsive force due to the distance of about 0.50 Å between their O atoms being too close. It is likely the two ClO₃⁻ are from the subsequent layers and should not produce much resistance to the impurity incorporation process. However, after further observation, it can be seen that the two layers of the ClO₃⁻ packing structure are not distinctively separated, and can even be considered as mixed into one layer. In turn, this feature of mixed layer could lead to great obstruction on the impurity incorporation by causing repulsive force between the ions.

Crystal faces of ($\bar{1}\bar{1}\bar{1}$) and (111) are a pair of Friedel opposite facets, possessing different surface structure (Figure 9.3c). From Figure 9.3c it can be seen, the situation on (111) is similar to that of (001), where the impurity incorporation is difficult due to the obstruction from a “pre-existing” ClO₃⁻. On the ($\bar{1}\bar{1}\bar{1}$) surface shown in Figure 9.3c, one in every four ClO₃⁻ is aligned with its Cl apex pointing outwards the surface along [$\bar{1}\bar{1}\bar{1}$] while its O₃ base pointing to the opposite direction [111]. It can be seen that, the incorporation of S₂O₆²⁻ at this site by one SO₃ of S₂O₆²⁻ while the other SO₃ of S₂O₆²⁻ protruding outside the surface, will not be obstructed by any vicinal molecules. Furthermore, due to the special orientation of the substituted ClO₃⁻ that its basal O atoms are in the same plane parallel to the surface, the three O of the substituting SO₃ of the S₂O₆²⁻ can simultaneously contact the crystal surface and stabilize the position of the S₂O₆²⁻ during the incorporation process. This is difficult to achieve in all the other cases. Thus, it can be concluded that the S₂O₆²⁻ impurity can easily incorporated into the ($\bar{1}\bar{1}\bar{1}$) surface of NaClO₃ by substituting the specific ClO₃⁻.

To sum up the above analysis, it is only the { $\bar{1}\bar{1}\bar{1}$ } type faces of NaClO₃ crystal

which can accommodate the S₂O₆²⁻ by providing suitable ClO₃⁻ sites for substitution with no obstructing effects (Figure 9.3c). Contrarily, incorporation of S₂O₆²⁻ on faces of {001} or {110} types would encounter great repulsion. In general, from the above discussions it is concluded that, whether the molecular arrangement of the host crystal surface can provide proper space for accommodating the impurity without obstruction should be considered during the investigation of the habit modification of crystals by impurity.

9.2.3 The Structural Model and Its Correlations to All the Experimental Results

The discussion in the previous sections covers the similarity of the structures and atomic charges between the ClO₃⁻ and the S₂O₆²⁻ and the surface structure of the { $\bar{1}\bar{1}\bar{1}$ } type faces of NaClO₃. This section summarizes the structural model, shown in Figure 9.4. The S₂O₆²⁻ has incorporated into the { $\bar{1}\bar{1}\bar{1}$ } type faces of NaClO₃, using one of its SO₃ to mimic and substitute the ClO₃⁻. Only those ClO₃⁻ with their three-fold axis pointing in the $\langle \bar{1}\bar{1}\bar{1} \rangle$ directions can be substituted by the impurity. During the incorporation process, the structure of impurity S₂O₆²⁻ varied according to the local environment. The incorporation mechanism of S₂O₆²⁻ in the NaClO₃ crystal discussed in this thesis agrees with the proposed model by Ristic et al. (1993; 1994) where he speculated that S₂O₆²⁻ incorporated into the { $\bar{1}\bar{1}\bar{1}$ } faces due to structural similarity between the molecules of the impurity and the host.

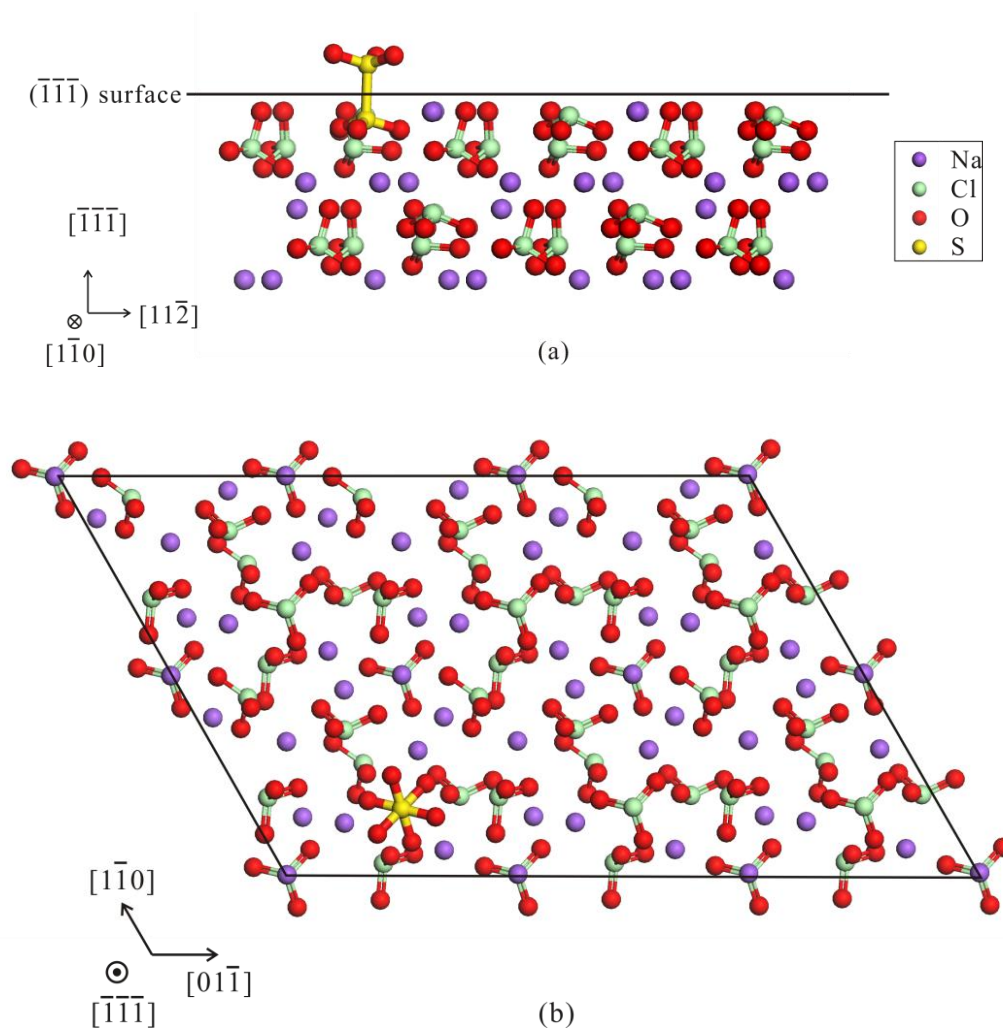


Figure 9.4 The structural model of the incorporation of $\text{S}_2\text{O}_6^{2-}$ on the $\{\bar{1}\bar{1}\bar{1}\}$ type faces of NaClO_3 .

In the investigation by X-ray topography (Chapter 6), the intensive impurity incorporation in the $\{\bar{1}\bar{1}\bar{1}\}$ growth sectors of doped crystals was clearly revealed by the growth striations which appeared quasi-periodically in the growth sectors of only $\{\bar{1}\bar{1}\bar{1}\}$ type on the topographic images, rather than any growth sectors of others types (cf. section 6.2.2). This is consistent with the modelling results that it is only the $\{\bar{1}\bar{1}\bar{1}\}$ faces which can accommodate the $\text{S}_2\text{O}_6^{2-}$ without causing any obstruction. However, it does not exclude the incorporation of $\text{S}_2\text{O}_6^{2-}$ on the other faces, since light incorporation would not induce growth striations in topographic images. Nevertheless,

by XRF-mapping (cf. section 8.4), the ratio between the impurity concentration determined in the $\{\bar{1}\bar{1}\bar{1}\}$ sector and the $\{001\}$ sector was 2:1, implying that impurity could get into $\{001\}$ sectors but with low probability compared to $\{\bar{1}\bar{1}\bar{1}\}$ sectors. This is consistent with the analysis in section 9.2.2 that the incorporation of S₂O₆²⁻ in $\{001\}$ type sectors would encounter great obstruction. Anyway, the incorporation mechanism or structural model on the $\{001\}$ faces of NaClO₃ is out of the scope of this thesis.

In the results by X-ray multiple-wave diffraction (XRMD) (section 7.5), the suppression of $(3\bar{4}3)(3\bar{4}1)$ and $(343)(341)$ secondary diffractions was attributed to the displacement of atoms induced by the incorporation of S₂O₆²⁻ at the specific sites on the $\{\bar{1}\bar{1}\bar{1}\}$ surfaces. Those results were successfully interpreted based on the structural model shown in Figure 9.4, which in turn proved the proposed model.

Finally, the most direct proof underpinning the structural model is from EXAFS measurements. According to the EXAFS results concluded in section 8.5, the S-S bond of the S₂O₆²⁻ ion aligns along the $\langle\bar{1}\bar{1}\bar{1}\rangle$ directions on the $\{\bar{1}\bar{1}\bar{1}\}$ faces. This strongly supports the structural model. Besides, the orientation of the S₂O₆²⁻ around its three-fold axis on the $\{\bar{1}\bar{1}\bar{1}\}$ faces was confirmed by the XANES results, which was identical to that shown in the structural model (section 8.3).

9.2.4 Charge Compensation Associated with Impurity Incorporation

Since the total electronegative charge of a S₂O₆²⁻ is -2 whereas that of ClO₃⁻ is -1, the ready substitution of one ClO₃⁻ by one S₂O₆²⁻ on the { $\bar{1}\bar{1}\bar{1}$ } faces would require further charge compensation to maintain the electroneutrality of the crystal. Figure 9.5 presents the surface structure of the ($\bar{1}\bar{1}\bar{1}$) face⁶, including one hypothetical sub-layer after the layer which the impurity incorporated into. It can be seen that, each O atom of the protruding SO₃ of S₂O₆²⁻ locates very close (approximately 0.50Å) to an O atom of one of the three ClO₃⁻ in the sub-layer (dotted circle in Figure 9.5), respectively. This short distance can cause strong repulsive force between the S₂O₆²⁻ in the crystal face and the depositing ClO₃⁻ from solution. As a result, during the crystal growth, the deposition of ClO₃⁻ ions into these three sites would probably be disturbed. To maintain electroneutrality of the crystal after the incorporation of S₂O₆²⁻, it is likely that one of these ClO₃⁻ in the sub-layer will be absent without affecting its corresponding Na⁺, whereas the other two ClO₃⁻ are present but dislocated from their original sites in the sub-layer. Therefore, during the impurity incorporation process the impurity S₂O₆²⁻ (with charge -2) has substituted one ClO₃⁻ (with charge -1) in the growing surface, and after incorporation it rejected another ClO₃⁻ (with charge -1) in the sub-layer. As a result, the electroneutrality of the doped crystal is maintained after the incorporation of S₂O₆²⁻ on the { $\bar{1}\bar{1}\bar{1}$ } faces.

⁶ All other { $\bar{1}\bar{1}\bar{1}$ } faces are equivalent to ($\bar{1}\bar{1}\bar{1}$).

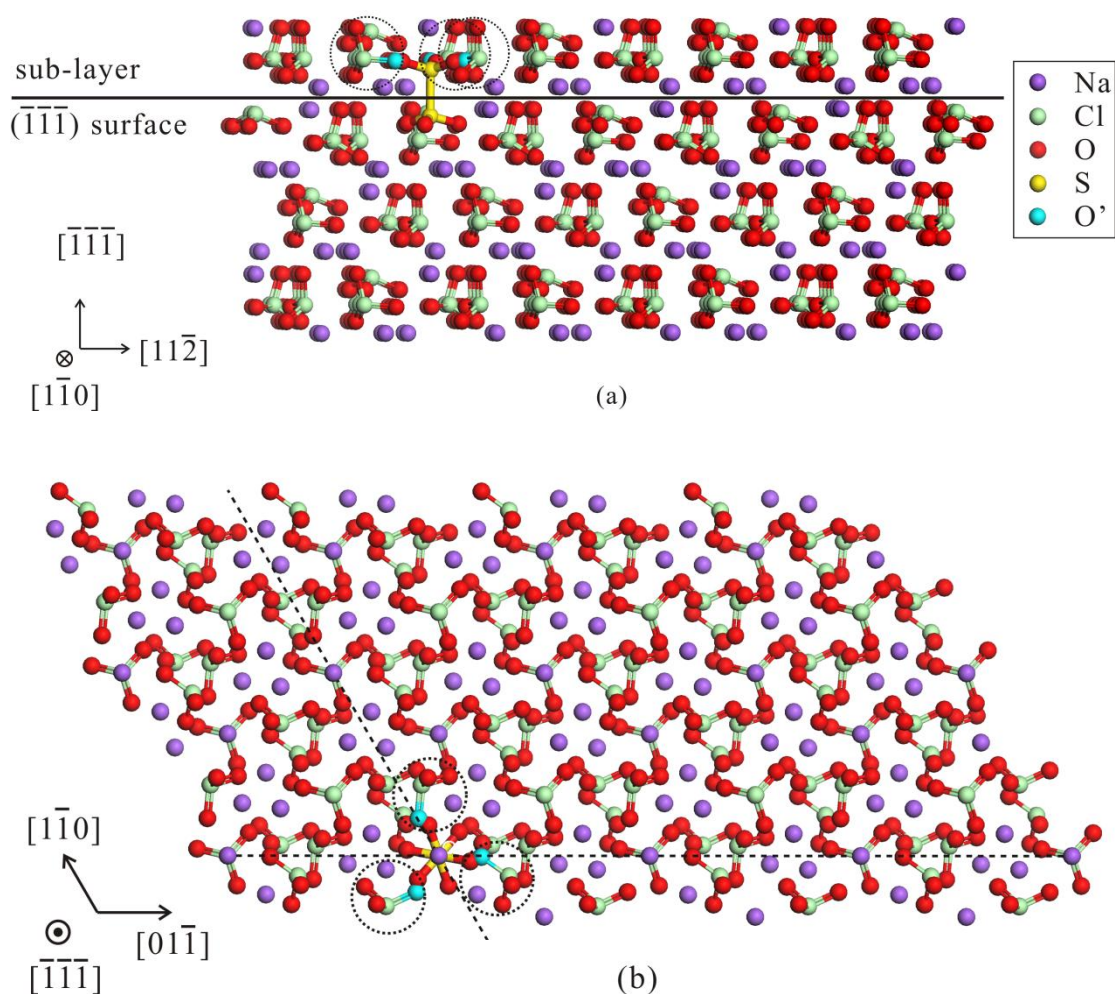


Figure 9.5 The structure of the $(\bar{1}\bar{1}\bar{1})$ face after impurity incorporation, showing the surface where impurity incorporation occurred and one sub-layer after that. The structure of the sub-layer was only for illustration and it was concluded to have been disturbed. For emphasis, the disturbed O atoms of the ClO_3^- in the sub-layer are highlighted by blue colour, and the disturbed ClO_3^- ions are circled by dotted line.

9.3 Habit-modifying Effect of S₂O₆²⁻ on the Crystal Growth of NaClO₃

In the current study, the relative supersaturation of solution used for the crystal growth was below 4% at the cooling rate of 0.5 °C/12 hours. But it would be confusing to judge the growth mechanism based on the supersaturation range, since this range corresponds to different reported growth mechanisms (cf. section 3.3.4). However, based on the results of X-ray topography in Chapter 6 of this thesis, it was concluded that the growth mechanism of the {001} and $\{\bar{1}\bar{1}\bar{1}\}$ faces is spiral growth relying on screw dislocations or screw components of mixed dislocations, i.e. the crystal grows at the growth steps or kink sites. After the establishment of the structural model, the inhibiting effect of S₂O₆²⁻ on the growth rate of $\{\bar{1}\bar{1}\bar{1}\}$ faces of NaClO₃ can be explored below.

9.3.1 Blocking Effect at the Growth Steps or Kink Sites

On the growing surfaces of $\{\bar{1}\bar{1}\bar{1}\}$ type, the S₂O₆²⁻ ions will inevitably incorporate at the growth steps or kink sites. Serving as blocker tailor-made impurity (Clydesdale et al., 1994), once after the incorporation the S₂O₆²⁻ can impede the growth of the face by its protruding SO₃ group. It can be seen from Figure 9.5, the three O atoms of the protruding SO₃ group are at a distance of only 0.50 Å to the O atoms of the depositing ClO₃⁻ ions at three positions, respectively. The electrostatic repulsion between the electronegative O atoms at such a short distance is too strong. Thus, it is likely that the depositing ClO₃⁻ ions in the sub-layer would be dislocated, either they will deposit at distorted positions or be absent from the sub-layer. To sum up, the incorporation of S₂O₆²⁻ at the $\{\bar{1}\bar{1}\bar{1}\}$ faces can prevent the oncoming molecules from getting into their proper positions and disrupt the proper packing structure of the $\{\bar{1}\bar{1}\bar{1}\}$ faces of NaClO₃, thus decreasing the growth rate of these faces.

9.3.2 The Effect of Impurity-Induced Strain

The results of 002 Renninger Scans (RSs) using X-ray multiple-wave diffraction revealed that the impurity incorporation in the $\{\bar{1}\bar{1}\bar{1}\}$ growth sectors have induced different types of strain into two different regions, i.e. the tensile strain at the region corresponding to the beam path of the $(1\bar{1}1)$ and $(\bar{1}11)$ secondary reflections and the compressive strain at the region corresponding to the beam path of the (111) and $(\bar{1}\bar{1}1)$ secondary reflections. It is worth emphasizing that, these secondary reflections were BSD cases which are very sensitive to the properties of the sample surface, thus suitable for the detection of surface strains. Previous studies have reported that externally induced strain can affect the crystal growth from two aspects (Ristic et al., 1997a; Ristic et al., 1997b). Firstly, the strain existing on the crystal surface can increase the surface-free energy, which will cause obstruction to the generation of growth steps and also retard their propagation over the surface. Secondly, the strain will increase the chemical potential (μ_s , the chemical potential of the solid phase) of the surface, which can decrease the driving force for crystal growth ($\Delta\mu=\mu_l-\mu_s$, where μ_l is the chemical potential of the liquid phase). Since it was observed that the incorporation of S₂O₆²⁻ on the $\{\bar{1}\bar{1}\bar{1}\}$ faces of NaClO₃ has induced strains on these growing surfaces, thus the reduced growth velocity of these faces can be interpreted according to the above two effects of strain on the crystal growth.

9.4 The Origin of Twinning and the Structure of the Twin Boundary

9.4.1 Origin of the Twinning

Although NaClO₃ crystals were frequently grown from pure solution, twinning of NaClO₃ in pure solution has never been observed. This implies that, the formation of

the twinned crystal was induced by the presence of S₂O₆²⁻ impurity in the solution. For the current case of NaClO₃, in principle the twinning could occur according to two different mechanisms, i.e. surface nucleation at the S₂O₆²⁻ site on a modified habit face (Ristic et al., 1993) and S₂O₆²⁻-induced twinned nucleation in the solution.

Upon the incorporation of S₂O₆²⁻ on the faces of the $\{\bar{1}\bar{1}\bar{1}\}$ type (Figure 9.4), the SO₃ of S₂O₆²⁻ which protrudes out of the surface could provide a local environment for the depositing ClO₃⁻ to attach. If the density of the S₂O₆²⁻ ions on the surface is adequate to attract a sufficient amount of ClO₃⁻, then a surface nucleation for the second domain can occur. The second domain is in the opposite direction to the first domain (Figure 9.6). However, such a process is expected to happen at a very low probability. Furthermore, due to the 60° twisting between the two SO₃⁻ groups of S₂O₆²⁻ (cf. Figure 9.1), the second domain of the twinned crystal has a 60° rotation with respect to the first domain along the <111> type axes, as observed from the twinned crystals (cf. section 5.4.2).

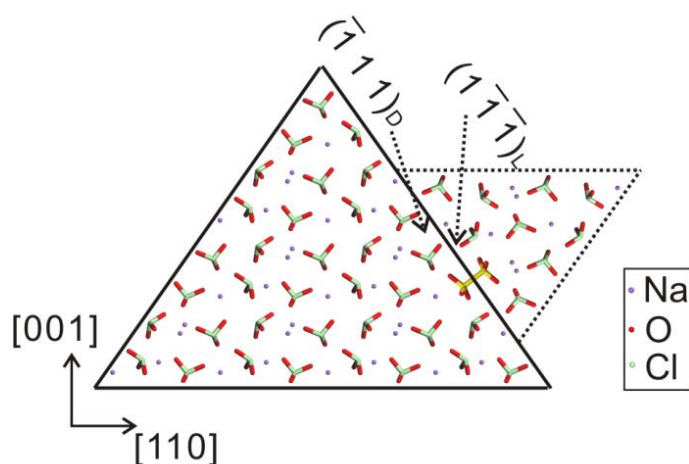


Figure 9.6 Projection of the structure of surface epitaxial twinning NaClO₃ along the cube diagonal [110]. On one tetrahedral surface of the D- crystal, the S₂O₆²⁻ ion (yellow and red in the figure) substitutes one ClO₃⁻ at the specific orientation of normal to the surface and induced the generation of the epitaxial L- crystal.

Penetration or intergrowth twins from the centre were frequently observed (*e.g.*

diamond, Machado et al. (1998) and iron borate, Diehl et al. (1984)). The twinning mechanism due to the twinned nucleation would result in the macroscopic penetration twins (Senechal, 1980). In the case of NaClO₃, the presence of S₂O₆²⁻ in the growth solution could lead to twinned NaClO₃ nuclei, and hence result in the formation of penetration twinned crystals. Although the surface-nucleation can induce the second twin domain, which then grows over the edge of the first domain face onto the adjacent faces, giving rise to the final habit of penetration twins (e.g. Figure 5.11), this could not exclude the twinning formation at the nucleation stage.

There are two possible types of combinations for the twin domains, i.e. D-&L-, D-&D- (equivalent to L-&L-). By applying twin law $m(001)$ to the two cases, the relative positions of the ClO₃⁻ ions at the interface between domains were obtained by symmetry operation. At the $\{\bar{1}\bar{1}\bar{1}\}$ interfaces of the D-&L- twinned crystal, a pair of ClO₃⁻ ions from the growing surface of each domain are oppositely aligned and twisted 60° to each other (Figure 9.7a and b), which is consistent with the configuration of S₂O₆²⁻ (Figure 9.1). Thus, this pair of ClO₃⁻ ions can be substituted by the S₂O₆²⁻. However, for the D-&D- or L-&L- cases, at the $\{\bar{1}\bar{1}\bar{1}\}$ interfaces the twist angle between the oppositely aligned ClO₃⁻ ions is 34.44° (Figure 9.7c and d), which is different from the staggered angle of 60° in the configuration of S₂O₆²⁻. To sum up, it is only the D-&L- combination which is suitable to provide the geometry for S₂O₆²⁻ to substitute a pair of ClO₃⁻ and structurally link the two domains at the interface between the $\{111\}_L$ face and the $\{\bar{1}\bar{1}\bar{1}\}_D$ face.

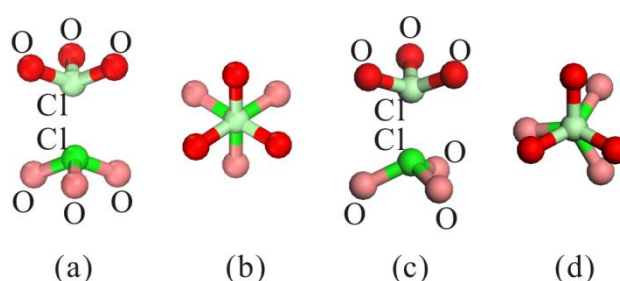


Figure 9.7 Schematic illustration of a pair of ions on the interface between the twin domains. (a) Sideview of the D-&L- combination. (b) Projection view of the D-&L- combination. (c) Sideview of the D-&D- or the quavalent L-&L- combination. (d)

Projection view of the D-&D- or the quavalent L-&L- combination.

9.4.2 The Structure of The Twin Boundary

The twin boundaries, starting approximately from the centre of the twinned crystal, propagated briefly along the {001} type planes which are theoretically the growing path of the re-entrant edge between the {111}_L and $\{\bar{1}\bar{1}\bar{1}\}$ _D type faces (e.g. $(\bar{1}1\bar{1})$ _L and $(\bar{1}\bar{1}1)$ _D faces in Figure 6.20, topograph of twin 110 plate, p.64). The curved interface implies a varying ratio between the growth rates of the twin domains. Following the surface structural model (Figure 9.6), S₂O₆²⁻ can enter at the (001) re-entrant edge by substituting a pair of oppositely aligned ClO₃⁻ ions from the L- and D- domains (Figure 9.8), respectively. For such an incorporation at a twin boundary, there can be two orientations of S₂O₆²⁻ with their S-S bonds normal to the {111}_L or $\{\bar{1}\bar{1}\bar{1}\}$ _D faces respectively (e.g. see the solid circles on the ClO₃⁻ ion pairs in Figure 9.8). In the case that the twin domain combination is L-&L- or D-&D-, the two paired ClO₃⁻ ions in the opposite domains at the twin boundary do not have the relatively staggered angle of 60°, and hence cannot be substituted by the S₂O₆²⁻. During the incorporation process of S₂O₆²⁻ at the re-entrant edge, a local cavity will be created by excluding a NaClO₃ from its lattice site in the D- domain (e.g. see dotted-circled pairs of ClO₃⁻ ions in Figure 9.8), due to the distance from the ClO₃⁻ to an O of the S₂O₆²⁻ being too close. The paired ClO₃⁻ ions that are not substituted by the S₂O₆²⁻ have their separation distance as close as 2.14 Å and hence could not co-exist at the twin boundary. This would exclude a NaClO₃ resulting in a cavity in the L- domain (see dotted circle in Figure 9.8). Whatever the case is, in this imperfect twin boundary the S₂O₆²⁻ impurity could incorporate into the boundary and act as a bridge linking the two domains together to help stabilizing the boundary. Therefore, the twin boundaries become more stabilized with the bridging effect of S₂O₆²⁻ between the L-&D- domains, although producing some cavities around the interface.

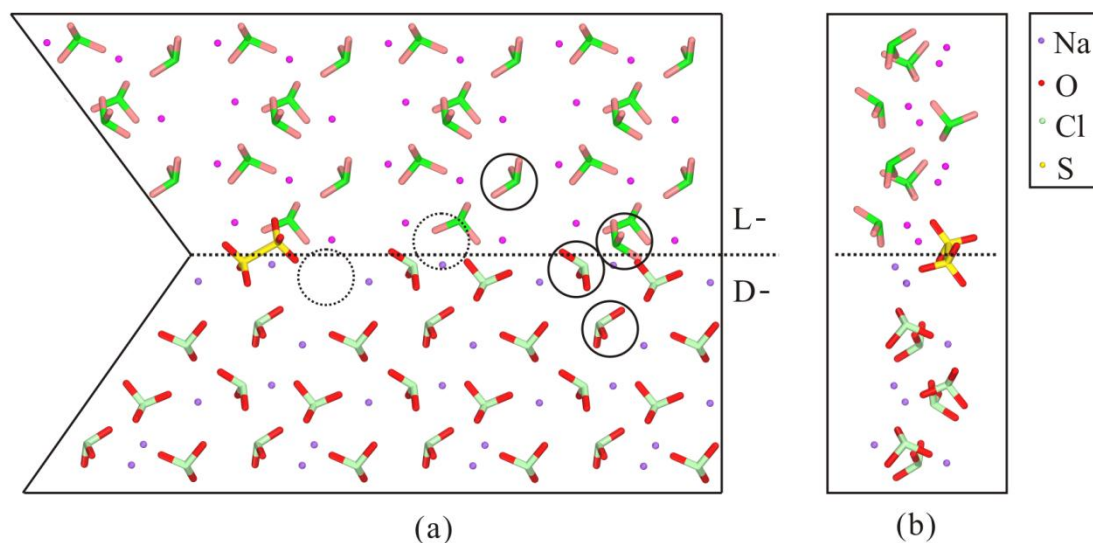


Figure 9.8 Projected views of the (001) twin boundary, where the S₂O₆²⁻ impurity is incorporated. (a) [110] projection of a S₂O₆²⁻ ion substituting one ClO₃⁻ from each domain respectively. The lower domain is D- and the upper one is L-. (b) The side view of the projection in (a).

9.5 Conclusions

This chapter firstly discussed the similarity between the impurity S₂O₆²⁻ and the host crystal composition ClO₃⁻, and analyzed the surface structure of the important habit faces of NaClO₃. It was concluded that the similar structure and atomic charges between the SO₃ group of S₂O₆²⁻ and the ClO₃⁻ ion makes it possible for S₂O₆²⁻ to substitute ClO₃⁻. The special surface structure of { $\bar{1}\bar{1}\bar{1}$ } faces, where one in four ClO₃⁻ (of trigonal pyramidal shape) is aligned with its Cl apex pointing perpendicularly outwards the surface, made these faces the preferred interface for the incorporation of S₂O₆²⁻. Whereas, incorporation on the faces of the {001} and {110} types could encounter great obstruction. Since the S₂O₆²⁻ has substituted one ClO₃⁻ and can probably reject a ClO₃⁻ in the sub-layer, the electroneutrality of the host crystal was maintained. After considering all the above results, the structural model for S₂O₆²⁻ on the { $\bar{1}\bar{1}\bar{1}$ } faces of NaClO₃ was established. The structural model

showed good consistency with the experimental results in this thesis including X-ray topography, XRF-mapping, XRMD and XAFS (section 9.2.3).

The S₂O₆²⁻ has retarded the growth rate of { $\bar{1}\bar{1}\bar{1}$ } faces of NaClO₃ from two aspects. On one hand, the incorporated impurity can disrupt the proper packing structure of these faces resulting in a slow growth rate. On the other hand, the incorporation of S₂O₆²⁻ has induced strain into the { $\bar{1}\bar{1}\bar{1}$ } growing surfaces which will obstruct the generation and propagation of growth steps and also decrease the driving force for crystal growth.

The impurity-induced twinning of NaClO₃ originated from either surface-nucleation at an existing face or spontaneous twinned nucleation in the solution. At the twin boundary, the S₂O₆²⁻ impurity has incorporated into the boundary and act as a bridge linking the two domains to help stabilizing the twin boundary.

CHAPTER 10

Conclusions and Future Work

Summary:

This chapter summarizes all the main findings and outcomes from this research work together with the recommendations for future work.

10.1 Conclusions

The aim of this research was to examine the structural role of the impurity sodium dithionate ($\text{Na}_2\text{S}_2\text{O}_6$) in the habit modification of sodium chlorate (NaClO_3) and to explore the influences associated with the impurity incorporation. This has been attained through the successful characterization of the habit-modified NaClO_3 crystals grown from aqueous solution doped with $\text{Na}_2\text{S}_2\text{O}_6$ compared to the NaClO_3 crystals grown from non-doped solution, and the molecular modelling analysis on the structures of the impurity and the host crystal.

Chapter 2 presented a comprehensive description on the fundamental knowledge of crystalline solid and the important theories of the crystallization and crystal growth science. Especially, it reviewed the essential principles of the characterization methods used in this research. Chapter 3 compiled a literature review of the previous studies on the habit modification of crystals and the related mechanisms. It summarized the literature from a wider scale of inorganic systems to the specific case of NaClO_3 doped with $\text{Na}_2\text{S}_2\text{O}_6$. Studies of the pure habit of NaClO_3 were also reviewed for comparison purposes. Both chapters provided relevant theoretical principles and scientific background to underpin the current research work. Chapter 4 described the material and the experimental and modelling work in detail. It is worth mentioning that, the extended explanations on the operation methods of some techniques are available in the Appendix of this thesis.

The habit of pure NaClO_3 crystal was a simple $\{001\}$ cube at the relatively higher cooling rate of $1.0\text{ }^\circ\text{C}/\text{day}$, but $\{110\}$ and $\{111\}$ faces can appear on the final habit under relatively lower cooling rates of $0.5\text{ }^\circ\text{C}/\text{day}$ and $0.125\text{ }^\circ\text{C}/\text{day}$, respectively. In the presence of $\text{S}_2\text{O}_6^{2-}$, the $\{\bar{1}\bar{1}\bar{1}\}$ faces developed rapidly with the increasing impurity concentration, implying an inhibiting effect of the impurity. The non-affected faces of the $\{001\}$ and $\{110\}$ types could only appear on the final habit of crystal grown from solution doped with very low concentration of 40ppm of $\text{S}_2\text{O}_6^{2-}$. At 70ppm doping

concentration and above, the crystal habit will be dominated by the $\{\bar{1}\bar{1}\bar{1}\}$ faces. Occasionally, the $\{001\}$ faces can appear as small facet on the edges of the tetrahedron. Twinned crystal can form in the solutions doped with 800ppm $S_2O_6^{2-}$ and above, although at a low probability. The habit of the twinned crystals was either a small tetrahedral crystal formed on the existing large face of the $\{\bar{1}\bar{1}\bar{1}\}$ type or two large inter-grown tetrahedra. In addition, it was concluded that both the presence of $S_2O_6^{2-}$ and the high cooling rate can enhance the MSZW of $NaClO_3$ in aqueous solution. Also, the segregation coefficient ($S_{bulk}/S_{solution}$) of $S_2O_6^{2-}$ in $(\bar{1}\bar{1}\bar{1})$ sector was more than twice of that in the (001) and (110) sectors, showing strong impurity incorporation in the specific growth sectors of $\{\bar{1}\bar{1}\bar{1}\}$ type compared to the others. With the increase of doping concentration in different crystals, the segregation coefficient was determined to be fluctuating around 1.2.

By the feasibility of X-ray topography, the grown-in dislocation lines of straight profile in the $\{001\}$, $\{110\}$ and $\{\bar{1}\bar{1}\bar{1}\}$ growth sectors of both pure and $S_2O_6^{2-}$ -doped $NaClO_3$ crystals were characterized and compared to the theoretical calculations. The line directions of most dislocations were consistent with the preferred line direction obtained from calculations (Hooper et al., 1983). However, two extra types of dislocation lines were observed in the $\{\bar{1}\bar{1}\bar{1}\}$ growth sectors of doped crystals (i.e. $3c^*$ and $3u$ types), which were defined as intermediate dislocations with relatively high energy. More importantly, growth striations were observed in the growth sectors of only the $\{\bar{1}\bar{1}\bar{1}\}$ type of doped crystals, implying that impurity had intensively incorporated into these faces during crystal growth, whereas no growth striations were observed in growth sectors of other types. The growth history of habit-modified crystal (i.e. doped crystal) was reconstructed and interpreted with respect to the inhibiting effect of $S_2O_6^{2-}$ (cf. section 6.4). Nevertheless, the growth mechanism of the $\{001\}$ and $\{\bar{1}\bar{1}\bar{1}\}$ faces was concluded to be spiral growth.

In the 004 Renninger Scan results by XRMD, it was concluded that the incorporation of $S_2O_6^{2-}$ has distorted the secondary planes of the $(\bar{3}\bar{4}3)(\bar{3}\bar{4}1)$ and $(343)(341)$ cases resulting in a decrease of their reflection intensity. The 004RS was interpreted based on the proposed structural model of impurity incorporation on $\{\bar{1}\bar{1}\bar{1}\}$ faces, which, in turn, proved the proposed model. The impurity incorporation has induced different types of strain into the $\{\bar{1}\bar{1}\bar{1}\}$ growth sectors at two different regions, i.e. tensile strain at the region corresponding to the beam path of the $(1\bar{1}1)$ and $(\bar{1}11)$ secondary diffractions and compressive strain at the region corresponding to the beam path of the (111) and $(\bar{1}\bar{1}1)$ secondary diffractions. Besides, the strains were found to be increasing along with the increasing impurity concentration. These strains contributed to the inhibiting effect of $S_2O_6^{2-}$ on the growth rate of $(\bar{1}\bar{1}\bar{1})$ faces. The perfection of the pure and doped crystals was examined by the $\omega:\phi$ mapping associated with the mosaic spread calculation, where the quality of most crystals was not changing much, except that the 160ppm crystal contained a large quantity of defects concentrated in the in-plane direction.

The three-dimensional orientation of $S_2O_6^{2-}$ impurity on the $\{\bar{1}\bar{1}\bar{1}\}$ faces of $NaClO_3$ crystal was revealed by the polarized XAFS, and this thesis also tried to explore its actual structure after incorporation. The S-S bond is aligned along the $\langle\bar{1}\bar{1}\bar{1}\rangle$ direction on these faces and the substituting SO_3 retained the orientation of the substituted ClO_3^- in the plane of the growing surface. Further work is needed to fully understand the actual structure of the $S_2O_6^{2-}$, due to the limited data quality in the current study. Moreover, the XRF-map revealed that the concentration of impurity in growth sectors of $\{\bar{1}\bar{1}\bar{1}\}$ type is approximately twice that in the growth sectors of the $\{001\}$ and $\{110\}$ types, showing strong impurity incorporation in the specific growth sectors of $\{\bar{1}\bar{1}\bar{1}\}$ type rather than the others. This is consistent with the segregation coefficient measurements in this thesis.

The structural model for the incorporation of $S_2O_6^{2-}$ on the $\{\bar{1}\bar{1}\bar{1}\}$ faces of $NaClO_3$ has been established based on both the experimental results and the molecular modelling analysis. The $S_2O_6^{2-}$ incorporated into the $\{\bar{1}\bar{1}\bar{1}\}$ type faces of $NaClO_3$, using one of its SO_3 group to mimic and substitute the ClO_3^- . Only those ClO_3^- (in the shape of trigonal pyramid) with their Cl apex pointing to the $\langle\bar{1}\bar{1}\bar{1}\rangle$ directions (outwards the crystal surface) can be substituted by $S_2O_6^{2-}$. The structural model has been correlated with the experimental results in this thesis including X-ray topography, XRF-mapping, XRMD and XAFS (section 9.2.3), and the model showed very good consistency with the results.

The inhibiting effect of $S_2O_6^{2-}$ on the growth of the $\{\bar{1}\bar{1}\bar{1}\}$ faces of $NaClO_3$ was implemented in two ways. Firstly, the protruding SO_3 of the incorporated $S_2O_6^{2-}$ can cause strong repulsive force to the depositing ClO_3^- from solution, thus disrupting the proper packing structure of these faces and correspondingly reducing their growth rate. Secondly, the incorporation of $S_2O_6^{2-}$ induced strain into the $\{\bar{1}\bar{1}\bar{1}\}$ growing surfaces, leading to the obstruction on the generation and propagation of growth steps and the decrease of driving force (i.e. supersaturation) for crystal growth.

In the twinned crystal, the optical activities of the two twin domains were found to be opposite, i.e. one is dextro- (D-) and the other one levo- (L-). Through validation by X-ray topography, the morphologies of the two domains was confirmed to be opposite in polarity. Based on these two facts it was concluded that this twinning case follows twin law of $m\{100\}$ (or equivalently the inversion $\bar{1}$). The twinning of $NaClO_3$ was concluded to be originated from either surface-nucleation at an existing face or spontaneous twinned nucleation in the solution, under the influence of the impurity $S_2O_6^{2-}$. At the twin boundary, the $S_2O_6^{2-}$ impurity incorporated into the boundary and acted as a bridge linking the two domains to help stabilizing the twin boundary.

In general, this research project has successfully worked out a comprehensive

framework to reveal the structural role of the impurity sodium dithionate in the habit modification of sodium chlorate and the influences associated with the impurity incorporation, in terms of habit modification observation, characterization of growth history and defect configuration, determination of lattice distortion and strain, exploration of three-dimensional orientations of the impurity in the host crystal, and analysis of the probability of accommodating impurity by different types of crystal faces.

10.2 Review of the Aims and Objectives

The key objective of this PhD work was to explore the structural role of $\text{Na}_2\text{S}_2\text{O}_6$ in the habit modification of NaClO_3 and the influences associated with the impurity incorporation. The experimental work has obtained good success in determining the local structure of $\text{Na}_2\text{S}_2\text{O}_6$ in NaClO_3 and revealing the effects of impurity on the crystal habit, defect structure and micro-crystallography of the host crystal. However, this work also has fallen short of developing the correlation between the chirality and the dislocation configuration of the crystals.

10.3 Recommendations for Future Work

To the author's best knowledge, there are several suggestions for consideration in the extensive studies after the current work :

- Investigate the habit modification of NaClO_3 as a function of cooling rate at fixed moderate doping concentration of $\text{S}_2\text{O}_6^{2-}$. The various supersaturation resulting from the different cooling rates might significantly affect the growth rate of different habit faces, thus such experiments could reveal the impact of supersaturation on the habit modification of $\text{Na}_2\text{S}_2\text{O}_6$ -doped NaClO_3 . Furthermore, by comparing the results of the above work to the results in this thesis, the competition relationship between the impurity

concentration and the supersaturation of growth solution in affecting the habit of NaClO_3 can be established.

- Perform X-ray standing wave (XSW) to study the impurity location. The XSW is capable of determining the position of the sulphur atoms of $\text{S}_2\text{O}_6^{2-}$ with respect to the lattice planes of the $\{\bar{1}\bar{1}\bar{1}\}$ type. This enables us to further confirm the structural model of $\text{S}_2\text{O}_6^{2-}$ in the $\{\bar{1}\bar{1}\bar{1}\}$ type faces of NaClO_3 .
- Explore the structure of the twin boundary with the aid of Transmission electron microscopy (TEM), in order to reveal the role played by the impurity in the formation of the twin boundary. The structure of the twin boundary so far is still only a speculation, due to a lack of experimental observation.
- To explore the local structure of $\text{S}_2\text{O}_6^{2-}$ impurity on the faces of $\{001\}$ and $\{110\}$ types, to understand whether the $\text{S}_2\text{O}_6^{2-}$ impurity also incorporated into these faces and affected the growth of them, especially the $\{001\}$ faces.
- To utilize molecular modelling to predict the habit modification of this system. Molecular modelling work is needed to investigate the effect of the impurity after its incorporation, especially to strengthen the understanding on how exactly the impurity has affected the growth of the sub-layers, since the mechanism is just speculation so far.

References:

- ABRAHAMAS, S.C. and J.L. BERNSTEIN 1977. Remeasurement of optically active NaClO_3 and NaBrO_3 . *Acta Crystallographica Section B*. **33**(11),pp.3601–3604.
- AOKI, Y. 1979. No Title. *Mem. Fac. Sci., Kyushu Univ., D*. **24**,p.75.
- AVANCI, L.H., L.P. CARDOSO, J.M. SASAKI, S.E. GIRDWOOD, K.J. ROBERTS, D. PUGH and J.N. SHERWOOD 2000. Synchrotron-radiation X-ray multiple diffraction applied to the study of electric-field-induced strain in an organic nonlinear optical material. *Physical Review B*. **61**(10),pp.6507–6514.
- AVANCI, L.H., M.A. HAYASHI, L.P. CARDOSO, S.L. MORELHA, S.L. MORELHÃO, F. RIESZ, K. RAKENNUS and T. HAKKARAINEN 1998. Mapping of Bragg-surface diffraction of InP / GaAs (1 0 0) structure. *Journal of Crystal Growth*. **188**(1–4),pp.220–224.
- BARRETT, N.T.T., G.M.M. LAMBLE, K.J.J. ROBERTS, J.N.N. SHERWOOD, G.N.N. GREAVES, R.J.J. DAVEY, R.J.J. OLDMAN, D. JONES and A. CHEMISTRY 1989. Glancing angle EXAFS investigation of the habit modification of ADP by the incorporation of iron. *Journal of Crystal Growth*. **94**(3),pp.689–696.
- BELL, D.J., M. HOARE and P. DUNNILL 1983. The formation of protein precipitates and their centrifugal recovery. *Advances in Biochemical Engineering/Biotechnology*. **26**(Downstream Process.),pp.1–72.
- BENNEMA, P. 1967. Interpretation of the relation between the rate of crystal growth from solution and the relative supersaturation at low supersaturation. *Journal of Crystal Growth*. **1**(5),pp.287–292.
- BENNEMA, P. 1984. Spiral growth and surface roughening: Developments since Burton, Cabrera and Frank. *Journal of Crystal Growth*. **69**(1),pp.182–197.
- BENNEMA, P. 1968. Surface diffusion and the growth of sucrose crystals. *Journal of Crystal Growth*. **3-4**,pp.331–334.
- BERG, W.F. 1938. Crystal growth from solutions. *Proceedings of the Royal Society of London, Series A: Mathematical, Physical and Engineering Sciences*. **164**,pp.79–95.
- BERTHOUD, A. 1912. No Title. *Journal of Chemical Physics*. **10**,pp.624–635.
- BONNIN-MOSBAH, M., N. METRICH, J. SUSINI, M. SALOME, D. MASSARE and B. MENEZ 2002. Micro X-ray absorption near edge structure at the sulfur and iron K-edges in natural silicate glasses. *Spectrochimica Acta, Part B: Atomic Spectroscopy*. **57B**(4),pp.711–725.

- BUCKLEY, H.E. 1951. *Crystal Growth*. New York: John Wiley.
- BUCKLEY, H.E. 1949. No Title. *Discussions of the Faraday Society*. (5),pp.243–254.
- BUCKLEY, H.E. 1930a. The Crystallization of Potash-alum and the Effect of Certain Added Impurities on its Habit. *Zeitschrift für Kristallographie*. **73**,pp.443–464.
- BUCKLEY, H.E. 1932a. The growth of KClO_3 crystals in the presence of ionic impurities. *Zeitschrift für Kristallographie*. **72**,pp.37–46.
- BUCKLEY, H.E. 1932b. The influence of RO_4 and related ions on the habit of potassium sulphate crystals. *Zeitschrift für Kristallographie*. **81**,pp.157–168.
- BUCKLEY, H.E. 1930b. The Influence of RO_4 and Related Ions on the Crystalline Form of Sodium Chlorate. *Zeitschrift für Kristallographie*. **75**,pp.15–31.
- BUNKER, B. 2010. *Introduction to XAFS*. Cambridge: Cambridge University Press.
- BUNN, C. 1961. *Chemical Crystallography*. Oxford: Clarendon Press.
- BURKE-LAING, M.E. and K.N. TRUEBLOOD 1977. Sodium Chlorate: Precise Dimensions for the ClO_3^- ion. *Acta Crystallographica*. (B33),pp.2698–2699.
- BURRILL, K.A. 1972. No Title. *Journal of Crystal Growth*. **12**,p.239.
- BURTON, W.K., N. CABRERA and F.C. FRANK 1951. The Growth of Crystals and the Equilibrium Structure of their Surfaces. *Philosophical Transactions of the Royal Society of London. Series A, Mathematical and Physical Sciences*. **243** (866),pp.299–358.
- CHANG, S.L. 2004. *X-Ray Multiple-Wave Diffraction*. Berlin: Springer-Verlag Berlin Heidelberg.
- CHERNOV, A.A. 1984. *Modern Crystallography III: Crystal Growth*. Berlin: Springer-Verlag.
- CHERNOV, A.A. 1993. Present-day understanding of crystal growth from aqueous solutions. *Progress in Crystal Growth and Characterization of Materials*. **26**,pp.121–151.
- CLARK, S.J., M.D.S. II, C.J.P. II, P.J.H. III, M.I.J.P. IV and K.R. V 2005. First principles methods using CASTEP. *Zeitschrift für Kristallographie*. **220**,p.567.
- CLYDESDALE, G., R.B. HAMMOND and K.J. ROBERTS 2003. Molecular Modeling of Bulk Impurity Segregation and Impurity-Mediated Crystal Habit Modification of Naphthalene and Phenanthrene in the Presence of Heteroimpurity Species. *The Journal of Physical Chemistry B*. **107**(20),pp.4826–4833..

- CLYDESDALE, G., K.J. ROBERTS and R. DOCHERTY 1996. HABIT95 — a program for predicting the morphology of molecular crystals as a function of the growth environment. *Journal of Crystal Growth*. **166**(1–4),pp.78–83.
- CLYDESDALE, G., K.J. ROBERTS and R. DOCHERTY 1994. Modelling the morphology of molecular crystals in the presence of disruptive tailor-made additives. *Journal of Crystal Growth*. **135**(1–2),pp.331–340.
- CLYDESDALE, G., K.J. ROBERTS, K. LEWTAS and R. DOCHERTY 1994. Modelling the morphology of molecular crystals in the presence of blocking tailor-made additives. *Journal of Crystal Growth*. **141**(3–4),pp.443–450.
- CLYDESDALE, G., K.J. ROBERTS, G.B. TELFER, V.R. SAUNDERS, D. PUGH, R.A. JACKSON and P. MEENAN 1998. Prediction of the Polar Morphology of Sodium Chlorate Using a Surface-Specific Attachment Energy Model. *Journal of Physical Chemistry*. **102**,pp.7044–7049.
- COLE, H., F.H. CHAMBERS and H.M. DUNN 1962. Simultaneous diffraction. Indexing unwegangeregung peaks in simple cases. *Acta Crystallographica*. **15**(2),pp.138–144.
- CRABB, T.A., K.J. ROBERTS and P.N. GIBSON 1992. Application of X-ray absorption near-edge spectroscopy at the S k-edge to the structural characterisation of surface reacted metallic alloys. *Japanese Journal of Applied Physics*.
- CUNNINGHAM, D. a. H., D.R. ARMSTRONG, G. CLYDESDALE and K.J. ROBERTS 1993. Investigation into the structural chemistry of Cu²⁺ ions in doped nearly perfect single crystals of ammonium sulfate with reference to their role in habit modification. *Faraday Discussions*. **95**,p.347.
- CURIE, P. 1885. No Title. *Bulletin de la Societe Francaise de Mineralogie et de Cristallographie*. **8**,pp.145–150.
- DAVEY, R.J. 1976. The effect of impurity adsorption on the kinetics of crystal growth from solution. *Journal of Crystal Growth*. **34**(109-119).
- DAVEY, R.J., J.W. MULLIN and T. PLACE 1974. Growth of the {100} faces of ammonium dihydrogen phosphate crystals in the presence of ionic species. *Journal of Crystal Growth*. **26**(1),pp.45–51.
- DEER, W.A. 1961. Memorial of Harold Eugene Buckley. *The American Mineralogist*. **46**,pp.481–484.
- DHANARAJ, G., K. BYRAPPA, V. PRASAD and M. DUDLEY 2010. Crystal Defects and Characterization In: G. DHANARAJ et al., eds. *Springer Handbook of Crystal Growth*. New York: Springer-Verlag Berlin Heidelberg, pp. 15–16.

- DIEHL, R., W. JANTZ, B.I. NOLAENG and W. WETTLING 1984. Growth and properties of iron borate, FeBO₃. *Current Topics in Materials Science*. **11**,pp.241–387.
- DONNAY, J.D. and G. DONNAY 1962. Structural Hints from Crystal Morphology *In: Twentieth Annual Diffraction Conference*. Pittsburgh, p. 17.
- DONNAY, J.D.H. and D. HARKEI 1937. A new law of crystal morphology extending the law of Bravais. *American Mineralogist*. **22**,pp.446–467.
- ELWELL, D. and H.J. SCHEEL 1975. *Crystal Growth from High-temperature Solutions*. London: WILEY-VCH Verlag.
- FIEBIG, A., M.J. JONES and J. ULRICH 2007. Predicting the Effect of Impurity Adsorption on Crystal Morphology. *Journal of Crystal Growth and Design*. **7**(9),pp.5–9.
- FILIPPONI, A., T. TYSON, K. HODGSON and S. MOBILIO 1993. KL edges in X-ray-absorption spectra of third-period atoms: Si, P, S, and Cl. *Physical Review A*. **48**(2), pp.1328-1338.
- FLEET, M.E. 2005. Xanes Spectroscopy of Sulfur in Earth Materials. *The Canadian Mineralogist*. **43**(6),pp.1811–1838.
- FRANK, F.C. 1949. The influence of dislocations on crystal growth. *Discussions of the Faraday Society*. **5**(0),pp.48–54.
- FREUND, A. K., A. MUNKHOLM, AND S. BRENNAN, 1996. X-ray diffraction properties of highly oriented pyrolytic graphite. *Proc. SPIE, Optics for High-Brightness Synchrotron Radiation Beamlines II*, **2856**, pp. 68–79.
- GAO, S.-P., C.J. PICKARD, M.C. PAYNE, J. ZHU and J. YUAN 2008. Theory of core-hole effects in 1s core-level spectroscopy of the first-row elements. *Physical Review B*. **77**(11),p.115122.
- GAO, S.-P., C.J. PICKARD, A. PERLOV and V. MILMAN 2009. Core-level spectroscopy calculation and the plane wave pseudopotential method. *Journal of physics. Condensed matter : an Institute of Physics journal*. **21**(10),p.104203.
- GIBBS, J.W. 1948. *Collected works, vol.1, Thermodynamics*. New Haven: Yale University Press.
- GOLDSCHMIDT, V.M. 1929. Crystal structure and chemical constitution. *Transactions of the Faraday Society*. **25**(0),pp.253–283.
- HAHN, T. and H. KLAPPER 2003. Twinning of crystals. *In: Int. Tables Crystallogr.* Kluwer Academic Publishers, pp. 393–448.

- HARTMAN, P. 1987. Modern PBC Theory *In*: I. SUNAGAWA, ed. *Morphology of Crystals, Part A*. Tokyo: Terra Scientific, pp. 269–319.
- HARTMAN, P. 1973. Structure and Morphology *In*: P. HARTMAN, ed. *Crystal Growth: An Introduction*. Amsterdam: North Holland, pp. 367–402.
- HARTMAN, P. and P. BENNEMA 1980. The attachment energy as a habit controlling factor: I. Theoretical considerations. *Journal of Crystal Growth*. **49**(1),pp.145–156.
- HARTMAN, P. and W.G. PERDOK 1955. The relations between structure and morphology of crystals. I. *Acta Crystallographica*. **8**,pp.49–52.
- VON HAUER, C. 1877. No Title. *Verh. geol. Reichsanst. Wien*. **58**.
- HAYASHI, M. a., S.L. MORELHÃO, L.H. AVANCI, L.P. CARDOSO, J.M. SASAKI, L.C. KRETLY and S.L. CHANG 1997. Sensitivity of Bragg surface diffraction to analyze ion-implanted semiconductors. *Applied Physics Letters*. **71**(18),p.2614.
- HOOVER, R.M., K.J. ROBERTS and J.N. SHERWOOD 1983. X-ray topographic investigations of dislocations in sodium chlorate. *Journal of Materials Science*. **18**(1),pp.81–88.
- HOSOYA, S., M. KITAMURA and T. MIYATA 1978. Growth mechanisms of NaClO₃ and KBr from aqueous solutions under relatively high supersaturation ranges. *Mineralogical Journal*. **9**(3),pp.147–168.
- HULL, D. and D.J. BACON 2001. *Introduction to dislocations*. Oxford: Butterworth-Heinemann.
- HUNT, J.D. and K.A. JACKSON 1966. Nucleation of solid in an undercooled liquid by cavitation. *Journal of Applied Physics*. **37**(1),pp.254–257.
- JACKSON, K.A. 1975. Theory of melt growth. *In*: *Cryst. Growth Charact., Proc. Int. Spring Sch. Cryst. Growth, 2nd*. North-Holland, pp. 21–32.
- KALMAN, A. & D. W. J. CRUICKSHANK, (1970). A note on the structure of Na₂SeO₄. *Acta Crystallographica Section B*, 26(4),p. 436.
- KERN, R. 1965. *Bulletin de la Societe Francaise de Mineralogie et de Cristallographie*. **78**,p.497.
- KIRFEL, A., G. WILL and A. WEISS 1980. No Title. *Acta Crystallographica Section B*. **36**,pp.223–228.
- KITO, I. and N. KATO 1974. X-ray topographic studies of sodium chlorate crystals grown from aqueous solutions. *Journal of Crystal Growth*. **24-25**(0),pp.544–548.

- KLAPPER, H. 2010. Generation and Propagation of Defects During Crystal Growth
In: G. DHANARAJ et al., eds. Springer Handbook of Crystal Growth SE - 4 .
Springer Berlin Heidelberg, pp. 93–132.
- KLAPPER, H. 2000. Generation and propagation of dislocations during crystal growth. *Materials Chemistry and Physics*. **66**(2-3),pp.101–109.
- KLAPPER, H. 1980. Post-growth defects *In: B. K. TANNER and D. K. BOWEN, eds. Characterization of Crystal Growth Defects by X-Ray Methods*. New York and London: Plenum Press, p. 156.
- KLAPPER, H., T. HAHN and S.J. CHUNG 1987. Optical, pyroelectric and X-ray topographic studies of twin domains and twin boundaries in KLiSO₄. *Acta Crystallographica Section B Structural Science*. **43**(2),pp.147–159.
- KLAPPER, H., H. KÜPPERS and H. KUPPERS 1973. Directions of dislocation lines in crystals of ammonium hydrogen oxalate hemihydrate grown from solution. *Acta Crystallographica Section A*. **29**(5),pp.495–503.
- KONINGSBERGER, D.C. and R. PRINS 1988. *X-ray Absorption: Principle, Applications and Techniques of EXAFS, SEXAFS and XANES*. New York.
- KOSSEL, W. 1936. No Title. *Annals of Physics*. **25**,p.512.
- KOSSEL, W. 1934. The energetics of surface procedures. *Annals of Physics*. **21**,pp.457–480.
- KUBOTA, N., J. FUKAZAWA, H. YASHIRO and J.W. MULLIN 1994. Pseudo-solubilities of potassium sulfate caused by traces of chromium(III) salts under controlled pHs. *Journal of Crystal Growth*. **143**(3-4),pp.287–293.
- KUBOTA, N., I. UCHIYAMA, K. NAKAI, K. SHIMIZU and J.W. MULLIN 1988. Change of solubility of potassium sulfate in water caused by traces of chromium(III). *Industrial & Engineering Chemistry Research*. **27**(6),pp.930–934.
- LAHAV, M., Z. BERKOVITCH-YELLIN, J. VAN MIL, L. ADDADI, M. IDELSON and L. LEISEROWITZ 1985. No Title. *Israel Journal of Chemistry*. **25**,p.353.
- LAI, X. 1998. *The Molecular Scale Mechanism Involved in the Habit Modification of KDP by Trivalent Transition Metal Cations* Ph.D Thesis. University of strathclyde.
- LAI, X., K.J. ROBERTS, L.H. AVANCI, L.P. CARDOSO and J.M. SASAKI 2003. Habit modification of nearly perfect single crystals of potassium dihydrogen phosphate (KDP) by trivalent manganese ions studied using synchrotron radiation X-ray multiple diffraction in Renninger scanning mode. *Journal of Applied Crystallography*,pp.1230–1235.

- LAI, X., K.J. ROBERTS, M.J. BEDZYK, P.F. LYMAN and M. SASAKI 2005. Structure of Habit-Modifying Trivalent Transition Metal Cations (Mn^{3+} , Cr^{3+}) in Nearly Perfect Single Crystals of Potassium Dihydrogen Phosphate As Examined by X-ray Standing Waves , X-ray Absorption Spectroscopy , and Molecular Modeling. *Chem. Mater.* **47**(4),pp.4053–4061.
- LAN, Z., X. LAI, K.J. ROBERTS, A.S. DE MENEZES, A.O. DOS SANTOS, G.A. CALLIGARIS and L.P. CARDOSO 2014. Determination of the Lattice Distortion in Dithionate-doped Sodium Chlorate Crystals using XRMD. *Crystal Growth and Design*,p.Manuscript in preparation.
- LAN, Z., X. LAI, C.R. SEABOURNE, A.J. SCOTT and K.J. ROBERTS 2014. Determination of the Local Structure of the Orientational Dithionate Impurity in the Sodium Chlorate Crystals using Polarized XAFS. *Crystal Growth & Design*,p.Manuscript in preparation.
- LANG, A.R. 1959. The projection topograph: a new method in X-ray diffraction microradiography. *Acta Crystallographica.* **12**,pp.249–250.
- LARSSON, L. O., & P. KIERKEGAARD (1969). The crystal structure of sodium sulphite. *Acta Chemica Scandinavica*, **23**, 2253–2260.
- LEHMANN, O.Z. 1891. No Title. *Physicalische Chemie.* **8**,p.543.
- LI, D., G.M. BANCROFT, M. KASRAI, M.E. FLEET, X. FENG and K. TAN 1995. S K- and L-edge X-ray absorption spectroscopy of metal sulfides and sulfates: applications in mineralogy and geochemistry. *Canadian Mineralogist.* **33**(5),pp.949–960.
- LIAO, J.C. and K.C. NG 1990. Effect of ice nucleators on snow making and spray freezing. *Industrial & Engineering Chemistry Research.* **29**(3),pp.361–366.
- LONSDALE, K. 1947. Divergent-beam X-ray photography of crystals. *Trans. Roy. Soc. (London).* **A240**,pp.219–250.
- MACHADO, W.G., M. MOORE and A. YACOOT 1998. Twinning in natural diamond. II. Interpenetrant cubes. *Journal of Applied Crystallography.* **31**(5),pp.777–782.
- MANN, S. and R.B. FRANKEL 1989. No Title In: S. MANN, J. WEBB and R. J. P. WILLIAMS, eds. *Biomineralization: Chemical and Biochemical Perspectives.* Weinheim: Vch Pub, pp. 389–426.
- MANN, S., R.B. FRANKEL and R.P. BLAKEMORE 1984. Structure, morphology and crystal growth of bacterial magnetite. *Nature.* **310**(5976),pp.405–407.
- MARC, R. 1910. No Title. *Z. Phys. Chem.* **73**,p.685.

- MATSUNAKA, M., M. KITAMURA and I. SUNAGAWA 1980. Dislocations in NaClO_3 crystals in relation to growth mechanism from aqueous solution. *Journal of Crystal Growth*. **48**,pp.425–434.
- MCCABE, W.L. and R.P. STEVENS 1951. Rate of growth of crystals in aqueous solution. *Chemical Engineering Process*. **47**,pp.168–174.
- MEYER, P. 1972. Polymorphism of sodium chlorate. *Comptes Rendus des Seances de l'Academie des Sciences, Serie C: Sciences Chimiques*. **274**(9),pp.843–845.
- MEYER, P. and M. GASPERIN 1973. Structural study of an unstable, high-temperature, sodium chlorate phase. *Bulletin de la Societe Francaise de Mineralogie et de Cristallographie*. **96**(1),pp.18–20.
- MIERS, H.A. 1927. Growth of crystals in supersaturated liquids. *Journal of the Institute of Metals*. **37**,pp.331–350.
- MIERS, H.A. 1904. The concentration of the solution in contact with a growing crystal. *Philosophical Transactions*. **A202**,pp.492–515.
- MIERS, H.A. and F. ISAAC 1908. The Spontaneous Crystallization of Binary Mixtures. Experiments on Salol and Betol. *Proceedings of the Royal Society of London, Series A: Mathematical, Physical and Engineering Sciences*. **79**,pp.322–351.
- MIERS, H.A. and F. ISAAC 1906. XLVII. The refractive indices of crystallising solutions, with especial reference to the passage from the metastable to the labile condition. *Journal of the Chemical Society, Transactions*. **89**,p.413.
- MIRANDA, C.M.R.R. and W.P. and J.A.L.J. and P.T.C.F. and J.M.-F. and F.E.A.M. and A.S. de M. and A.O. dos S. and L.P.C. and M.A.R., C.M.R. REMÉDIOS, W. PARAGUASSU, J. a LIMA JR, P.T.C. FREIRE, J. MENDES-FILHO, F.E. a MELO, a S. DE MENEZES, a O. DOS SANTOS, L.P. CARDOSO and M. a R. MIRANDA 2008. Effect of Ni(II) doping on the structure of L-histidine hydrochloride monohydrate crystals. *Journal of Physics: Condensed Matter*. **20**(27),p.275209.
- MONKHORST, H.J. and J.D. PACK 1976. Special points for Brillouin-zone integrations. *Physical Review B*. **13**(12),pp.5188–5192.
- MORELHÃO, S.L. and L.P. CARDOSO 1993. Structural properties of heteroepitaxial systems using hybrid multiple diffraction in Renninger scans. *Journal of Applied Physics*. **73**(9),p.4218.
- MORELHÃO, S.L. and L.P. CARDOSO 1996. X-ray Multiple Diffraction Phenomenon in the Evaluation of Semiconductor Crystalline Perfection. *Journal of Applied Crystallography*. **29**(4),pp.446–456.

- MORELHÃO, S.L., C.M.R. REMÉDIOS, R.O. FREITAS, A.O. DOS SANTOS, S.L. MORELHAO and C.M.R. REMEDIOS 2011. X-ray phase measurements as a probe of small structural changes in doped nonlinear optical crystals. *Journal of Applied Crystallography*. **44**(1),pp.93–101.
- MULLIN, J.W. 1992. *Crystallization*. London: Wiley.
- MUSSARD, F. and S. GOLDSZTAUB 1972. Sur la croissance du chlorate de sodium en solution. *Journal of Crystal Growth*. **13–14**(0),pp.445–448.
- MYERSON, A. 2002. *Handbook of industrial crystallization* (A. Myerson, ed.). Oxford: Butterworth-Heinemann.
- NERNST, W. 1904. No Title. *Zeitschrift für Physikalische Chemie*. **47**(52-55).
- NEWVILLE, M. 2004. *Fundamentals of XAFS*. Chicago: University of Chicago.
- NIINOMI, H., H. MIURA, Y. KIMURA, T. KURIBAYASHI, M. UWAHA, S. HARADA, T. UJIHARA and K. TSUKAMOTO 2013. Two Pathways Determining Chirality in NaClO₃ Crystals Grown from Solution via Achiral Precursors. *In: 17th ICCGE.*, pp. 36–37.
- NORD, A. G. (1973). Refinement of the crystal structure of Na₂SO₄. *Acta Chemica Scandinavica*, **27**, 814–822.
- NOYES, A.A. and W.R. WHITNEY 1897. No Title. *Zeitschrift für Physikalische Chemie*. **23**,pp.689–692.
- NYVLT, J. 1971. *Industrial Crystallisation from Solutions*. London: Butterworths.
- ONSAGER, L. 1944. Crystal statistics. I. A two-dimensional model with an order-disorder transition. *Physical Review*. **65**,pp.117–149.
- OSTWALD, W. 1897. No Title. *Zeitschrift für Physikalische Chemie* **22**,pp.289–330.
- PANAGIOTOPOULOS, N. C., & BROWN, I. D. (1973). The crystal structure of [alpha] - Na₂Cr₂O₇ and the [alpha] - [beta] phase transition. *Acta Crystallographica Section B*, **29**(4), PP.890–894.
- PICKARD, C.J. 1997. Ph.D Thesis. University of Cambridge.
- POORNACHARY, S.K., P.S. CHOW, R.B.H. TAN and R.J. DAVEY 2007. Molecular Speciation Controlling Stereoselectivity of Additives: Impact on the Habit Modification in α-Glycine Crystals. *Crystal Growth & Design*. **7**(2),pp.254–261.
- POST, B. 1975. Accurate lattice constants from multiple diffraction measurements. I. Geometry, techniques and systematic errors. *Journal of Applied Crystallography*. **8**(4),pp.452–456.

- POWERS, H.E.C. 1963. Nucleation and early crystal growth. *Industrial Chemist and Chemical Manufacturer*. **39**(7),pp.351–355.
- PRYWER, J. 2004. Explanation of some peculiarities of crystal morphology deduced from the BFDH law. *Journal of Crystal Growth*. **270**(3-4),pp.699–710.
- QUEEN, M.S., B.D. TOWEY, K. a. MURRAY, B.S. VELDKAMP, H.J. BYKER and R.K. SZILAGYI 2013. Electronic structure of [Ni(II)S₄] complexes from S K-edge X-ray absorption spectroscopy. *Coordination Chemistry Reviews*. **257**(2),pp.564–578.
- RAMACHANDRAN, G.N. and K.S. CHANDRASEKARAN 1957. The absolute configuration of sodium chlorate. *Acta Crystallographica*. **10**(10),pp.671–675.
- RAVEL, B. and M. NEWVILLE 2005. ATHENA, ARTEMIS, HEPHAESTUS: data analysis for X-ray absorption spectroscopy using IFEFFIT. *Journal of Synchrotron Radiation*. **12**(4),pp.537–541.
- REHR, J.J., R.C. ALBERS and S.I. ZABINSKY 1992. High-order multiple-scattering calculations of X-ray-absorption fine structure. *Physical Review Letters*. **69**(23),pp.3397–3400.
- REMEDIOS, C.M.R., a. O. DOS SANTOS, X. LAI, K.J. ROBERTS, S.G.C. MOREIRA, M. a. R. MIRANDA, a. S. DE MENEZES, F.P. ROUXINOL and L.P. CARDOSO 2010. Experimental Evidence for the Influence of Mn³⁺ Concentration on the Impurity Incorporation and Habit Modification Mechanism of Potassium Dihydrogen Phosphate. *Crystal Growth & Design*. **10**(3),pp.1053–1058.
- RENNINGER, M. 1937. No Title. *Zeitschrift für Kristallographie*. **106**,p.141.
- RISTIC, R., B.Y. SHEKUNOV and J.N. SHERWOOD 1994. Growth of the tetrahedral faces of sodium chlorate crystals in the presence of dithionate impurity. *Journal of crystal growth*. **139**,pp.336–343.
- RISTIC, R., J.N. SHERWOOD and K. WOJCIECHOWSKI 1993. Morphology and growth kinetics of large sodium chlorate crystals grown in the presence and absence of sodium dithionate impurity. *The Journal of Physical Chemistry*,pp.10774–10782.
- RISTIC, R.I., B.Y. SHEKUNOV and J.N. SHERWOOD 1997. The influence of synchrotron radiation-induced strain on the growth and dissolution of brittle and ductile materials. *Journal of Crystal Growth*. **179**(1–2),pp.205–212.
- RISTIC, R.I., J.N. SHERWOOD and T. SHRIPATHI 1990. Strain variation in the {100} growth sectors of potash alum single crystals and its relationship to growth rate dispersion. *Journal of Crystal Growth*. **102**(1–2),pp.245–248.

- RISTIC, R.I., J.N. SHERWOOD and T. SHRIPATHI 1997. The influence of tensile strain on the growth of crystals of potash alum and sodium nitrate. *Journal of Crystal Growth*. **179**(1–2),pp.194–204.
- RISTIC, R.I., J.N. SHERWOOD and K. WOJCIECHOWSKI 1988. Assessment of the strain in small sodium chlorate crystals and its relation to growth rate dispersion. *Journal of Crystal Growth*. **91**(1–2),pp.163–168.
- ROSSMANITH, E. 2003. UMWEG: a program for the calculation and graphical representation of multiple-diffraction patterns. *Journal of Applied Crystallography*. **36**(6),pp.1467–1474.
- SANGWAL, K. 1996. EFFECTS OF IMPURITIES ON CRYSTAL GROWTH PROCESSES. *Prog. Crystal Growth and Charact.* **32**,pp.3–43.
- SEARS, G.W. 1958. No Title. *Journal of Chemical Physics*. **29**,p.1045.
- SEKIYAMA, H., N. KOSUGI, H. KURODA and T. OHTA 1986. Sulfur K-edge absorption spectra of Na₂SO₄, Na₂SO₃, Na₂S₂O₃, and Na₂S₂O_x (x = 5–8). *Bulletin of the Chemical Society of Japan*. **59**(2),pp.575–579.
- SENARMONT, H. 1854. No Title. *Annals of Physical Chemistry*. **167**,p.491.
- SENECHAL, M. 1980. Origin of twin growth in crystals. *Kristallografiya*. **25**(5),pp.908–915.
- SHAH, B.C., W.L. MCCABE and R.W. ROUSSEAU 1973. Polyethylene vs. stainless steel impellers for crystallization processes. *AIChE Journal*. **19**(1),p.194.
- SIMON, B. 1983. Influence of the direction of the solution flow on the morphology of NaClO₃ crystals. . **61**,pp.167–169.
- SMOLSKY, I.L., A.E. VOLOSHIN, N.P. ZAITSEVA, E.B. RUDNEVA and H. KLAPPER 1999. X-ray topographic study of striation formation. *Phil. Trans. R. Soc. Lond. A*. **357**,pp.2631–2649.
- SOLÉ, V. a. A., E. PAPILLON, M. COTTE, P. WALTER and J. SUSINI 2007. A multiplatform code for the analysis of energy-dispersive X-ray fluorescence spectra. *Spectrochimica Acta Part B: Atomic Spectroscopy*. **62**(1),pp.63–68.
- SOWA, H. 1995. The High-Pressure Behavior of NaClO₃. *Journal of Solid State Chemistry*. **118**(2),pp.378–382.
- STEWART, J.J.P. 2007. Optimization of parameters for semiempirical methods V: modification of NDDO approximations and application to 70 elements. *Journal of molecular modeling*. **13**(12),pp.1173–213.

- STRICKLAND-CONSTABLE, R.F. 1968. *Kinetics and Mechanism of Crystallization*. Academic Press.
- STRICKLAND-CONSTABLE, R.F. 1979. Mechanism of production and growth inhibition of collision crystallites. *Journal of the Chemical Society, Faraday Transactions 1: Physical Chemistry in Condensed Phases*. **75**(0),pp.921–924.
- SUGIURA, C. 1981. Sulfur K X-ray absorption spectra of FeS, FeS₂, and Fe₂S₃. *The Journal of Chemical Physics*. **74**(1),p.215.
- SURENDER, V. and K.K. RAO 1993. Growth and habit modification of sodium chlorate crystals. *Bull. Mater. Sci.* **16**(2),pp.155–158.
- SVENSSON, C., & STAHL, K. (1988). The crystal structure of NaIO₃ at 293 K. *Journal of Solid State Chemistry*, **77**(1), PP.112–116.
- TAKAHASHI, M., H. TANIDA, S. KAWAUCHI, M. HARADA and I. WATANABE 1999. DV-Xalpha MO approach to Zn K-XANES spectra of zinc aqueous solution. *Journal of synchrotron radiation*. **6**(Pt 3),pp.278–80.
- TANNER, B.K. 1976. *X-ray diffraction topography*. Oxford: Pergamon press.
- TAUSON, V.L., J. GOETTLICHER, A.N. SAPOZHNIKOV, S. MANGOLD and E.E. LUSTENBERG 2012. Sulphur speciation in lazurite-type minerals (Na,Ca) and their annealing products: a comparative XPS and XAS study. *European Journal of Mineralogy*. **24**(1),pp.133–152.
- TELFER, G.B., J.D. GALE, K.J. ROBERTS, R. a. JACKSON, P.J. WILDE and P. MEENAN 1997. A Transferable Interatomic Potential for Alkali Chlorates and Bromates. *Acta Crystallographica Section A Foundations of Crystallography*. **53**(4),pp.415–420.
- TENG, S. T., H. FUESS, & J. W. BATS (1984). Refinement of sodium thiosulfate, Na₂S₂O₃, at 120 K. *Acta Crystallographica Section C*, **40**(11), 1785–1787.
Retrieved from <http://dx.doi.org/10.1107/S0108270184009549>
- THOMPSON, A. and D. VAUGHAN 2009. *X-ray data booklet*. Berkeley: Lawrence Berkeley National Laboratory.
- TING, H.H. and W.L. MCCABE 1934. Supersaturation and Crystal Formation in Seeded Solutions. *Industrial & Engineering Chemistry*. **26**(11),pp.1201–1207.
- TITIZ-SARGUT, S. and J. ULRICH 2002. Influence of Additives on the Width of the Metastable Zone. *Crystal Growth & Design*. **2**(5),pp.371–374.
- TYSON, T., A. ROE, P. FRANK, K. HODGSON and B. HEDMAN 1989. Polarized experimental and theoretical K-edge X-ray absorption studies of SO₄²⁻, ClO₃⁻, S₂O₃²⁻, and S₂O₆²⁻. *Physical Review B*. **39**(10),pp.6305–6315.

- VALETON, J.J.P. 1924. No Title. *Z. Kristallogr.* **59**,p.483.
- VIEDMA, C. 2005. Chiral Symmetry Breaking During Crystallization: Complete Chiral Purity Induced by Nonlinear Autocatalysis and Recycling. *Physical Review Letters.* **94**(6),p.065504.
- VIEDMA, C. 2004. Experimental evidence of chiral symmetry breaking in crystallization from primary nucleation. *Journal of Crystal Growth.* **261**(1),pp.118–121.
- VIEDMA, C. 2007. Selective Chiral Symmetry Breaking during Crystallization: Parity Violation or Cryptochiral Environment in Control? *Crystal Growth & Design.* **7**(3),pp.553–556.
- VIEDMA, C. and P. CINTAS 2011. Homochirality beyond grinding: deracemizing chiral crystals by temperature gradient under boiling. *Chemical communications (Cambridge, England).* **47**(48),pp.12786–8.
- VOLMER, M. 1939. *Kinetic der Phasenbildung.* Leipzig: Steinkopff.
- VOLMER, M. and W. SCHULTZ 1931. No Title. *Z. Phys. Chem. A.* **156**,pp.1–22.
- WARTCHOW, R. (1978). Crystal structure of sodium perchlorate. *Zeitschrift fuer Kristallographie, Kristallgeometrie, Kristallphysik, Kristallchemie,* **147**, 307–317.
- WEISSBUCH, I., R. POPOVITZ-BIRO, M. LAHAV, L. LEISEROWITZ and REHOVOT 1995. Understanding and control of nucleation, growth, habit, dissolution and structure of two- and three-dimensional crystals using 'tailor-made' auxiliaries. *Acta Crystallographica Section B.* **51**(2),pp.115–148.
- WOJCIECHOWSKI, K. 1995. Relation between morphology, growth kinetics and quality of sodium chlorate crystals grown from pure and sodium dithionate doped solutions. *S.P.I.E.* **2373**,pp.119–126.
- WULFF, G. 1901. To the question of the velocity of growth and the dissolution of crystal faces. *Zeitschrift fur Kristallographie.* **34**,pp.449–530.
- YANO, J., J. ROBBLEE, Y. PUSHKAR, M. A. MARCUS, J. BENDIX, J. M. WORKMAN, V. K. YACHANDRA (2007). Polarized X-ray absorption spectroscopy of single-crystal Mn(V) complexes relevant to the oxygen-evolving complex of photosystem II. *Journal of the American Chemical Society,* **129**(43), 12989–3000.

Appendix I

Sample alignment on X-ray Topography Camera

1. TURN ON: X-ray, detector reader, motor controller (for topography transmission).
2. Mount crystal in the middle of the sample holder, upload sample holder onto the sample stage.
3. Check the sample stage position on the scale, which should be '0' degree here.
4. Manually by eye to adjust the crystal position by rotating the sample holder, to make the crystal direction to satisfy topography reflection direction (use some instrument edges as reference). Then move sample stage into the middle position.
5. Rotate detector to the calculated 2θ position (at this time the detector is open, without any slit), fix the detector screw.
6. Manually rotate sample stage to the calculated θ position roughly with the lever arm, then rotate sample stage slowly while watching the detector reader, until it is moved to the reflection position roughly (try to get as close as possible to the highest intensity), fix the sample stage screw.
7. Adjust 'fine drum' to make the sample stage 2θ (crystal θ position) at the right position, by making the intensity to the highest #I1. Keep the drum value in mind for following step.
8. Raise detector vertical position up by 1 or 2 cm, so that the detector is receiving X-ray from the upper part of the crystal. Adjust 'fine drum' again, to reach highest intensity #I2 (may be different from the above one, due to different perfection of different part of the crystal).
9. Compare the drum value for intensity I1 and I2. If they are not quite different, then the vertical orientation of the crystal is good. If they are far from each

other, e.g. 3 grids on the drum, then the crystal vertical position should be adjusted.

10. The film slits (beam stopper to stop the direct beam) are mounted together on the same arm of the detector. In order to make beam stopper perpendicular to the diffracted beam accurately, here it used a 0,2 mm slit before the detector to reduce the wideness of X-ray receiving area on the detector. Then, adjust the detector (so that the beam stopper is also moving) to the best position (highest intensity). Now, the beam stopper is at the good position. Don't forget to unload the detector slit (the slit might be narrower than the diffracted beam, might cause fault to the film slit alignment).

11. Adjust topography transmission distance.

- It doesn't matter whether to fix left side or right side firstly.
- A. Fix left side screw (make it close to the middle, in order to save time during the adjustment)
- B. Move right side limit to a preferred position depending on the crystal width.
- C. Open X-ray window and turn on transmission motor controller, then the crystal stage is transmitting horizontally.
- D. Stop the controller when the intensity indicated by detector reader fall down to '0' suddenly. Hence, this is the right edge of the crystal. Fix the right transmission limit to this position.
- E. Move left side limit to a preferred position.
- F. Open X-ray window and turn on transmission motor controller.
- G. Stop the controller when the intensity indicated by detector reader fall down to '0' suddenly. Fix the left transmission limit to this position.
- H. Check both limits.
- I. move crystal to the middle position roughly, for following alignment.

12. Adjust film slits (beam stopper)

-
- The slit on the beam stopping side is more important than the other one, because it is used to stop the direct beam.
 - The other one slit, is for reduce the background on the film, by only let the main diffracted beam go through.
 - Adjust both slits to slightly touch the diffracted beam. (a quarter circle one time on the small fine drum)
13. Adjust film stage, to make it parallel to the film slit. Because the film slit was adjusted to be normal to the diffracted beam, so the film would be normal to it, too.
 14. Upload film into the film holder, in the dark room
 15. Final check the crystal theta position, because the theta position is very sensitive and could be disturbed during the alignment.
 16. Put film holder onto the film stage on the camera.
 17. Run transmission motor
 18. Open X-ray windows (first run motor second open window, to avoid continuous X-ray at the same position on the film)

Appendix II

Crystal Alignment in X-Ray Multiple-wave Diffraction

It is critical to align the primary diffraction plane exactly in the horizontal plane normal to the ϕ axis used for Renninger Scan, so that the primary reflection can be maintained while rotating ϕ for scanning. The alignment procedure to achieve this are listed as below:

1. The upper surface (i.e. (001) planes, which is parallel to the preferred (004) primary diffraction plane) of the crystal was placed perpendicular to ϕ -axis, and the (100) plane of the crystal was approximately rotated to diffraction plane of the primary reflection. The angle ϕ was defined as 0° at this time.
2. Adjust the crystal position to put crystal plate into the middle of the beam, by monitoring the X-ray on X-ray camera at the end of the beamline. Use a metal wire adhered to the stage as indicator.
3. Moved the detector to $2\theta_B$ (θ_B is Bragg angle of (002) reflection, which is strong thus used as the reflection for alignment).
4. Make sure $\phi = 0^\circ$. Scan θ (step size 0.01°) in the range of $(\theta_B \pm 5^\circ)$ to locate the real position of the maximum reflection. Move θ to the position of maximum reflection. Record the θ as θ_1 in labbook.
5. Move ϕ to 180° .
6. Scan θ (step size 0.01°) in the range of $(\theta_B \pm 5^\circ)$ to locate the real position of the maximum reflection; record the θ as θ_2 in labbook.
7. Move θ to $\theta_{\text{average}} = (\theta_1 + \theta_2)/2$. At this point the maximum reflection is lost.
8. Tilt “ax” (fine step size 0.0005°) (which possess the same rotation as θ , $\phi = 0^\circ$) to find the maximum reflection again.

9. Move ϕ to 90° .
10. Scan θ (step size 0.01°) in the range of $(\theta_B \pm 5^\circ)$ to locate the real position of the maximum reflection. DO NOT move θ to the position of maximum reflection, since the angle θ has already been adjusted at $\phi=0^\circ$ and 180° .
11. After the last scan, the θ will return to θ_{average} , where the maximum reflection is not obtained. Thus, at this $\phi = 90^\circ$, tilt “ay” (fine step size 0.0005°) (which possess the same rotation as θ , at the current $\phi = 90^\circ$) to move the crystal until reached the maximum reflection.
12. Repeated steps 4 to 11, until Bragg reflection is always maintained well during rotation of ϕ .

The sample is well aligned if the primary reflection used for alignment is always well maintained when moving ϕ . In addition, the zero position of ϕ will be reset after one Renninger Scan has been done, since the initial resetting was probably not sufficiently accuracy.

Appendix III

This is the calculation for the effective coordination number ($N_{\text{effective}}$) of the three 1st-shell oxygen atoms, under the condition when the electric vector of X-ray beam is perpendicular to the S-S bond. Here the calculation takes $\theta=70^\circ$ for instance.

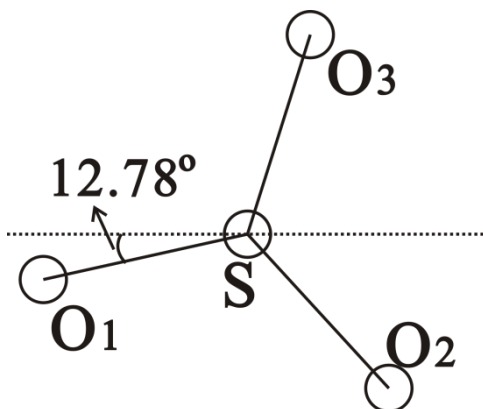
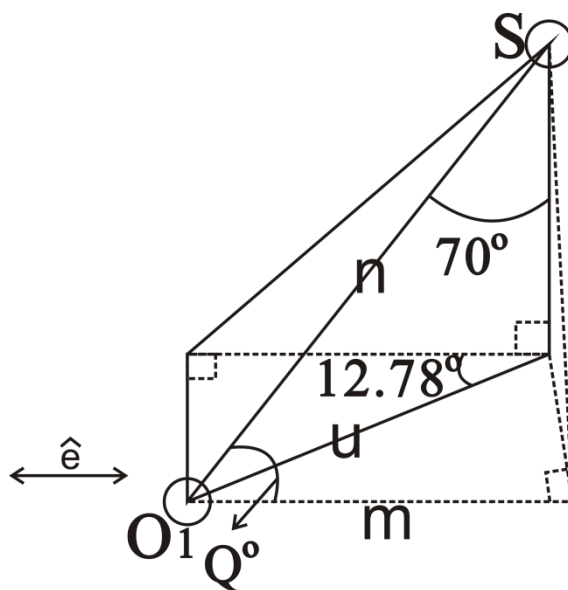
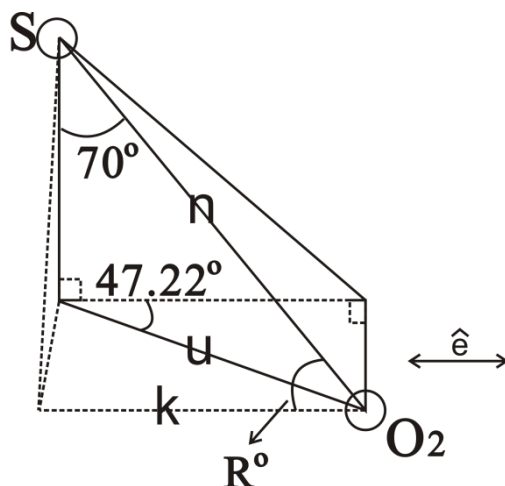


Figure III.1 The projection view of $\text{S}_2\text{O}_6^{2-}$ along its three-fold axis.



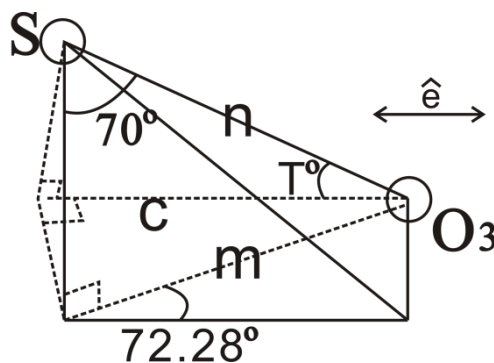
For sulphur 1, because $\cos Q = \frac{m}{n}$, $n = \frac{l}{\sin 70^\circ}$, $m = a$, $l = \frac{a}{\cos 12.78^\circ}$,

thus, $3 \cos^2 Q = 3(\sin 70^\circ \times \cos 12.78^\circ)^2 = 2.52$



For sulphur 2, because $\cos R = \frac{k}{n}$, $n = \frac{u}{\sin 70^\circ}$, $\cos 47.22^\circ = \frac{k}{u}$

Thus $3\cos^2 R = 3(\sin 70^\circ \times \cos 47.22^\circ)^2 = 1.22$



For sulphur 3, because $\cos T = \frac{c}{n}$, $m = \frac{c}{\cos 72.78^\circ}$, $\cos 20^\circ = \frac{m}{n}$

Thus $3\cos^2 T = 3(\cos 20^\circ \times \cos 72.78^\circ)^2 = 0.23$

To sum up all the contributions from the above three calculations, the Neffective f the three 1st-shell oxygen atoms, when the electric vector of X-ray beam is perpendicular to the S-S bond, is equal to 3.97 for $\theta=70^\circ$.